

Experimental Characterization of the Near-Wall Region in
Hall Thrusters and its Implications on Performance and
Lifetime

by

Rohit Shastry

A dissertation submitted in partial fulfillment
of the requirements for the degree of
Doctor of Philosophy
(Aerospace Engineering)
in the University of Michigan
2011

Doctoral Committee:

Professor Alec D. Gallimore, Chair
Professor Iain D. Boyd
Associate Professor John E. Foster
Richard R. Hofer, Jet Propulsion Laboratory

© Rohit Shastry
2011

Acknowledgements

The following dissertation is the culmination of over five years of research in the field of electric propulsion, specifically Hall thrusters. While this document and the research within required quite a personal undertaking, I would be remiss if I did not spend the time mentioning the contributions of all the people who had helped me along the way. If I fail to include anybody within, please accept my apologies and understand it is not done intentionally (unless specifically mentioned via haiku, limerick, or other amusing form).

First acknowledgements have to go to none other than my advisor, Professor Alec Gallimore. While I have not ever had the pleasure of being in one of his classes, Alec was my academic advisor during my undergraduate studies at the University of Michigan; and as I transitioned from an undergraduate to a graduate student, Alec became my research advisor and continued to give me unerring guidance in my academic career. A good friend of mine once told me “your research advisor should be someone for whom you are willing to work hard.” Alec’s pride and commitment to excellence in research and academics is contagious and one can’t help but feel pride and excitement when working in his lab. I am extremely grateful to him for never allowing my research to overwhelm me, for always giving me direction when I needed it, and encouraging me when things went wrong. Oh yeah, and his facilities rock too...

I would also like to thank my other committee members: Professor Iain Boyd, Professor John Foster, and Dr. Rich Hofer. Your advice and comments are greatly appreciated, and have contributed to making this dissertation a better document. Any remaining errors are my own.

Extra thanks go to committee member Rich Hofer, my fellowship sponsor and mentor. I was still a relative newb to the world of experiment and Hall thrusters when I first worked with Rich, and he put up with my constant “sidling” into his office to ask a barrage of questions, thus earning me my first nickname of “Tic Tac.” He has taught me

a lot of what I know about Hall thrusters and related probes, either from discussions or him generously “allowing” me to analyze a large set of data he took shortly before I arrived at JPL in 2007. He is also the source of my knowledge of Endnote and Igor Pro, which sadly may die with my departure, to be replaced with Zotero and Matlab.

On a related note, I’d like to acknowledge the Jet Propulsion Laboratory for funding myself over the past three years with the Graduate Student Research Program. I hope the research contained within this document is useful to you and encompasses some of the promises I made when I first applied for your fellowship.

The Plasmadynamics and Electric Propulsion Laboratory (PEPL) is a great place to work and contains work-class facilities, but is also home to world-class people. My fellow labmates are among the most intelligent, enthusiastic, and amusing people I have met. As per tradition I will acknowledge them in order of decreasing “age” (this is a grad school age and is not necessary correlated with actual age). First on the list is Dr. Tim Smith, Alec’s right-hand man (both figuratively and literally since the seat at Alec’s right during meetings is reserved for him). As someone with extensive technical knowledge and the patience and enthusiasm to teach it to others, he fills this role well. Second is returning PEPL alum Dr. Peter “Pedro” Peterson, whose deep knowledge of Hall thruster design and operation earned him the position of Director of Research at ElectroDynamic Applications (EDA). While Pete spent most of his time picking on me, insisting that “if I pick on you, I like you,” he also found the time to drop nuggets of knowledge and advice when I was struggling in the lab. Taking a little detour, I’d like to thank Dr. Dean Massey, also now part of EDA. Dean, while not strictly part of the PEPL family, is my “nephew” in the extended electric propulsion family. While at JPL and at EDA, Dean taught me a lot about vacuum systems, electrical systems, and how to avoid Bizmuth like the plague. Next on the list are Drs. Josh Rovey and Allen Victor, who sadly graduated soon after I joined the lab. Thanks to my “elder” labmates Drs. Jesse Linnell, Prashant Patel, Dave Kirtley, Dan “DB” Brown, Kristina Lemmer, Sonca Nguyen, Bailo Ngom, and soon-to-be-doctor Ricky Tang for setting great examples on how to be a good member of PEPL, professionally, socially, and personally. Special thanks go to Drs. Bryan Reid, Robert “LT” Lobbia, and Thomas Liu. Bryan was senior grad student at PEPL for me and many others, and his influence continues to be felt at the lab (much to

the chagrin of Pete). He made great sacrifices teaching me, having to deal with my “omens” in the lab which earned me the nicknames of “Damien” and “the cursed.” Every once in a while, I gain the extreme enthusiasm Bryan had when things went well in the lab, and feel the need to get a little...frisky...with the furniture. Robbie is well-known in the lab for doing amazing things with a little wire (also known as a Langmuir probe), and I appreciate all the discussions we’ve had on how to deal with the sometimes ridiculous data that comes from it. Tom, on top of being my roommate and good friend, was always willing to be the “devil’s advocate” and challenge my research arguments, giving me little mini-defenses along the way. That brings us to my cohorts in the lab, Mike McDonald and David Huang. While all of us at PEPL have to share equipment, Mike, David and I had to share one thruster for our research; therefore we got to know each other pretty well, and it’s been an enjoyable ride working with these two. To the ones who are directly my junior, Ray “Monk” Liang, Adam “Shab” Shabselowitz, and Laura Spencer, you are well on your way to becoming great senior grad students, and I hope you learned as much from me as I have from you. To the “babies” of the lab: Roland Florenz, Chris Durot, Kim Trent, and Mike Sekerak, enjoy your time here, the research you do, and appreciate your entrance into a great PEPL family.

Research would have been that much more difficult had it not been for the fantastic staff at the Francois-Xavier Bagnoud (FXB) building. Many thanks to the technical staff, Tom Griffin, Eric Kirk, and Chris Chartier for maintaining PEPL’s great facilities and making themselves available if you just want to chat. I’d also like to thank Denise Phelps, Michelle Shepherd, Suzanne Smith, and Cindy Enoch for helping me make purchases, get paid, and take care of oh-so-much paperwork.

Thanks to Dr. Jorge Cham for writing the amazing PhD comics and showing us all how silly, frustrating, and universal the graduate student experience can be.

Last, but of course not least, is my family: Mom, Dad, and my sister. Their never-ending support was much needed and much appreciated, not just over the past five years, but for my entire life. Thank you for encouraging me to get my degree, always believing I could finish, and making me see the bigger picture of how my degree fits into my life. I can always count on your love, support, and guidance as I move on and transition into the next phase.

Rohit Shastry
Ann Arbor, MI
December 2010

Table of Contents

Acknowledgements	ii
List of Figures.....	x
List of Tables	xxi
List of Appendices.....	xxiii
Nomenclature	xxiv
Chapter 1 Introduction.....	1
1.1 Problem Statement	1
1.2 Motivation and Scope for Research.....	1
1.3 Prior Near-Wall Studies in Hall Thrusters.....	3
1.4 Contributions of Research.....	5
1.5 Dissertation Overview	6
Chapter 2 Background	8
2.1 Rocket Propulsion Fundamentals	8
2.2 Electric Propulsion Systems	9
2.2.1 Gridded Ion Thrusters	10
2.2.2 Hall-effect Thrusters	11
2.3 Summary.....	16
Chapter 3 Experimental Apparatus.....	18
3.1 Vacuum Facility.....	18
3.2 Hall Thruster	19
3.3 Thrust Stand.....	22
3.4 HARP	23
3.5 Helmholtz Coil.....	24
3.6 Flush-mounted Langmuir Probe	26
3.6.1 Coupon Probe.....	26

3.6.2	External Tab Probe	28
3.6.3	Internal Wall-mounted Probe.....	30
3.7	Emissive Probe.....	34
3.7.1	Floating Emissive Probe	34
3.7.2	Swept Emissive Probe.....	35
3.8	Near-field Faraday Probe	38
3.9	Summary	43
Chapter 4 Flush-mounted Langmuir Probe Analysis Studies		44
4.1	Langmuir Probe Theory and Probe Environment.....	44
4.2	Sheath Expansion Model	47
4.2.1	Sheridan's Model	47
4.2.2	Overview of CEX2D.....	49
4.2.3	Method of Expansion Characterization	51
4.2.4	Final Expansion Correction Model.....	53
4.3	Plasma Potential Determination.....	59
4.3.1	Linear Intersection Method.....	59
4.3.2	Derivative Method	60
4.3.3	Shifted Floating Potential Method	61
4.3.4	Swept Emissive Probe Method	62
4.3.5	Comparison of Methods.....	63
4.4	Magnetic Field Effects	65
4.5	Sheath Potential Determination	70
4.5.1	Effects of Secondary Electron Emission.....	71
4.5.2	Implications of Measured Sheath Potentials.....	73
4.5.3	Final Sheath Potential Model.....	74
4.6	Summary	76
Chapter 5 Characterization of the Near-Wall Plasma		77
5.1	Discussion of Data Collection	77
5.1.1	Leakage Current.....	79
5.1.2	Probe Degradation	81
5.2	Prior Internal Measurements.....	83
5.3	Comparison of Plasma Parameters	84

5.3.1	Plasma Potential.....	84
5.3.2	Electron Temperature.....	88
5.3.3	Ion Number Density.....	90
5.4	Electron Energy Distribution Functions	94
5.4.1	Measured Distributions along the Channel Wall	95
5.4.2	Derivation of Potential Electron Distribution Functions	98
5.4.3	Implications of the Measured EEDF Structure	102
5.5	Summary	106
Chapter 6 Thruster Simulations Using HPHall-2.....		107
6.1	General Overview of Hybrid-PIC code	107
6.2	Baseline Simulation Results	110
6.2.1	Plasma Potential.....	110
6.2.2	Electron Temperature.....	112
6.2.3	Ion Number Density.....	114
6.3	Comparison to Experimental Data.....	116
6.4	Summary	120
Chapter 7 Incident Power Deposition onto Channel Walls		122
7.1	Axial Profiles along the Channel Walls.....	122
7.1.1	Incident Ion Current Density	122
7.1.2	Sheath and Beam Energies.....	124
7.1.3	Incident Ion Power Density	129
7.2	Integrated and Averaged Quantities within the Channel	131
7.2.1	Properties within Interrogation Zone	131
7.2.2	Extrapolation of Properties to Entire Channel	136
7.2.3	Estimated Values over Entire Channel Length.....	142
7.3	Correlation with Near-field Ion Current Density Measurements	146
7.3.1	Ion Beam Current.....	146
7.3.2	Plume Divergence.....	148
7.3.3	Comparison between Internal and Near-field Measurements.....	151
7.4	Energy Analysis and Comparison to Prior Measurements	152
7.5	Summary	157
Chapter 8 Sputtering Yield Estimates and Implications.....		159

8.1	Sputtering Yield Overview and Present Models.....	159
8.1.1	Energy-dependent Sputter Yield.....	161
8.1.2	Angle-dependent Sputter Yield.....	163
8.2	Determination of Incident Ion Angles	164
8.3	Calculated Erosion Rates and Profiles	167
8.4	Calculated Sputtering Yield Functions	170
8.5	Suggested Features of Sputtering Yield Model	173
8.6	Summary	174
Chapter 9 Conclusions.....		175
9.1	Dissertation Summary.....	175
9.2	Recommendations for Future Work.....	176
Appendices.....		179
Bibliography		194

List of Figures

Figure 2-1. Schematic of a typical gridded ion thruster, with major components labeled. Not to scale.	11
Figure 2-2. Schematic of a typical Hall thruster with major components labeled. Not to scale.....	13
Figure 2-3. Magnetic field topology of the NASA-173Mv1. The curvature inside the discharge channel is referred to as a plasma lens. Image taken from Ref [24].....	13
Figure 3-1. Photograph of the LVTF with the endcap removed. All seven cryopump shrouds are visible and numbered. Taken by Robert Lobbia.....	19
Figure 3-2. Photograph of the 6-kW laboratory Hall thruster, operating on xenon at 300 V and 20 mg/s anode flow rate. Taken from Ref. [13]......	20
Figure 3-3. Comparison of measured profiles on the original erosion rings with the linear chamfer machined into the new rings (top: inner channel ring; bottom: outer channel ring).....	21
Figure 3-4. Photograph of the inverted-pendulum thrust stand with water-cooled shroud.	22
Figure 3-5. Photograph of the HARP on top of the A-frame within LVTF.	24
Figure 3-6. Left: Side-view of the Helmholtz coil and support structure. Test section is in the center of the two coils. Right: Measured magnetic field contours of the test section with 5 A coil current.	25
Figure 3-7. Schematic showing the position and orientation of the Helmholtz coil relative to the 6-kW Hall thruster. Not to scale.	26
Figure 3-8. Schematic of the coupon probe assembly. Rotation of the probe allows for magnetic field orientation changes.	27
Figure 3-9. Representative Langmuir probe I-V characteristic taken with the coupon probe.	27
Figure 3-10. Schematic of external tab probe design. Not to scale.	28
Figure 3-11. Schematic of the external tab probe placement relative to the 6-kW Hall thruster. Not to scale.	28
Figure 3-12. Electrical diagram of the data collection circuit used with the external tab probe.	29
Figure 3-13. Representative Langmuir probe I-V characteristic taken with the external tab probe at 300 V and 20 mg/s anode flow rate.	30

Figure 3-14. Photograph of the internal wall-mounted Langmuir probes installed into each erosion ring on the 6-kW Hall thruster.	31
Figure 3-15. Schematic showing the locations of each probe relative to the thruster exit plane. Distances are given in units of channel lengths. Not to scale.	32
Figure 3-16. Photograph depicting the azimuthal spacing of the wall-mounted probes on the outer erosion ring. The null probe has no exposed area and is only used to characterize capacitive effects.	32
Figure 3-17. Electrical diagram of the measurement circuit used with the internal wall-mounted probes. Measurements were taken at the inner and outer wall simultaneously at each axial location.	33
Figure 3-18. Representative Langmuir probe I-V characteristics taken with the internal wall-mounted probes at 300 V and 20 mg/s anode flow rate, at $z = -0.071$ channel lengths from the exit plane.	34
Figure 3-19. Schematic of the mechanical design of the swept emissive probe. Not to scale.	36
Figure 3-20. Electrical diagram of the measurement circuit for the swept emissive probe.	37
Figure 3-21. Schematic of the near-field Faraday probe used to measure ion current density. Ceramabond was used to insulate the sides and back of the probe. Not to scale.	39
Figure 3-22. Schematic of the near-field Faraday probe within the stainless steel tube placed on the HARP. Not to scale.	39
Figure 3-23. Electrical diagram of the measurement circuit for the near-field Faraday probe.	40
Figure 3-24. Sample ion current density profile where the left portion of the profile does not drop to $(1/e)$ of its maximum value.	41
Figure 3-25. Method of determining the axial range over which to average calculated values of plume divergence. The range over which the magnitude of the derivative drops below the threshold value is taken as the averaging range.	42
Figure 4-1. Sample sheath boundaries at various probe voltages around a free-floating planar probe. Taken from Ref. [47].	48
Figure 4-2. Sample grid cell showing the locations of calculated potentials and electric fields, along with particle weighting. The relative lengths of r , z , $1-r$, and $1-z$ are used to weight electric fields to particle positions and particle charge to grid nodes.	50
Figure 4-3. Computational domain for ion sheath expansion study using CEX2D. Electric potential boundary conditions are defined at left and right boundaries while electric field boundary conditions are defined at top and bottom boundaries.	51
Figure 4-4. Sample contour plot of equipotentials and ion trajectories (black lines) around a flush-mounted Langmuir probe using CEX2D.	52

Figure 4-5. Schematic representing typical ion trajectories, shown in red, found around a flush-mounted probe. The ion trajectory that reaches the probe edge is the boundary of capture, and can be used to define an equivalent sheath radius.....	53
Figure 4-6. Diagram showing how the sheath boundary becomes perturbed around a flush probe. No perturbation occurs when the probe is biased to the local wall potential, creating a uniform, indistinguishable surface.	54
Figure 4-7. Variation of sheath area expansion with probe bias, found to be highly linear at all values of ρ_p tested. Electron temperature was set to 3 eV.	55
Figure 4-8. Variation of slope b with non-dimensional probe radius, ρ_p , at an electron temperature of 3 eV. A power law function with zero offset was found to fit very well.....	55
Figure 4-9. Variation of the fitting coefficient C with electron temperature, T_e , and floating wall potential, μ_0 . Values are largely constant until the crossover energy is reached, at $T_e = 19.3$ eV or $\mu_0 = 1.02$	56
Figure 4-10. Variation of the fitting coefficient m with electron temperature, T_e , and floating wall potential, μ_0 . Values are roughly constant until the crossover energy is reached, at $T_e = 19.3$ eV or $\mu_0 = 1.02$	57
Figure 4-11. Comparison of corrected and uncorrected ion saturation regimes from a flush-mounted Langmuir probe I-V characteristic. The corrected data is much flatter and the ion saturation current is easily determined.....	58
Figure 4-12. Method of linear intersecting lines to determine plasma potential from Langmuir probe data. A line is fit to the transition and electron saturation regions of the characteristic, and the probe voltage at the intersection of these two lines is taken as the local plasma potential.	60
Figure 4-13. Method of derivatives to determine plasma potential from Langmuir probe data. The probe voltage where the first derivative maximizes, or equivalently where the second derivative reaches zero, is taken as the plasma potential.....	61
Figure 4-14. Sample data from the swept emissive probe using three different filament currents. The voltage at which the traces begin to overlap is taken as the local plasma potential.	62
Figure 4-15. Schematic showing the definition of the magnetic field orientation angle with respect to the coupon and probe. For this particular study, the magnetic field and ion velocity vectors were aligned.....	66
Figure 4-16. Measured floating potentials under various magnetic field magnitudes and orientations. Magnetic field effects are largely negligible, as the slight elevation at 90° is purely an orientation effect.	67
Figure 4-17. Measured plasma potentials under various magnetic field magnitudes and orientations. The presence of the magnetic field appears to have little effect.	67
Figure 4-18. Measured electron temperatures under various magnetic field magnitudes and orientations. Magnetic field effects appear to be largely negligible, as the slight elevation at 90° is purely an orientation effect.	68

Figure 4-19. Calculated electron number density at various magnetic field magnitudes and orientations. An increasing magnetic field appears to create a slight increase in calculated number density..... 68

Figure 4-20. Comparison of sheath potentials in the absence of SEE (left) and when the sheath is in the charge saturation regime (right). In CSR, the sheath potential magnitude is small and the electric field at the surface is reversed. 72

Figure 4-21. Diagram showing the effects of secondary electron fluxes and dependence on electron thermalization processes within the channel. If the two fluxes do not thermalize in the bulk plasma, they can counter-stream to the opposing wall and cancel each other out..... 72

Figure 4-22. Measured sheath potentials as a function of measured electron temperature using internal wall-mounted probes within the 6-kW Hall thruster. Near-ideal sheath potentials indicate a large population of high-energy electrons, which provide evidence of thermalization processes within the bulk plasma. 73

Figure 5-1. Example of leakage current found with a probe along the inner wall at 300 V, 20 mg/s anode flow rate. Compared to the outer wall, which should have similar properties, the floating potential and ion current is reduced along the inner wall due to extra collected current..... 80

Figure 5-2. Measured floating potentials (with respect to ground) along the inner wall at 300 V and 20 mg/s anode flow rate. All data points fit the expected sigmoid function except for the point at $z = -0.095$ channel lengths, which has a significantly reduced floating potential due to leakage current. 80

Figure 5-3. Microscope photograph of an internal wall-mounted probe tip removed from the wall after the end of the test. Preferential sputtering on one side has created a slanted surface such that the probe tip is no longer flat. 81

Figure 5-4. Microscope photograph of an internal wall-mounted probe prior to removal, after the end of the test. A portion of the wall surrounding the probe has been sputtered away, leaving the probe within a “pit.” 82

Figure 5-5. Illustration showing how the sheath boundary can smooth over features of degradation if they are small (less than a few Debye lengths). Not to scale. 83

Figure 5-6. Schematic showing the measurement domain of prior internal measurements taken by Reid. Corner coordinates are given in (z,r) format, with axial location in units of channel lengths and radial location in units of channel widths. Not to scale. 83

Figure 5-7. Axial profiles of plasma potential at three different radial locations within the channel, under the nominal operating condition of 300 V and 20 mg/s. The plasma begins to accelerate further upstream when close to the channel wall. 85

Figure 5-8. Axial profiles of plasma potential at three different radial locations within the channel, under the nominal operating condition of 300 V and 20 mg/s. The plasma begins to accelerate further upstream when close to the channel wall. 85

Figure 5-9. Comparison of axial plasma potential profiles between the inner and outer channel wall near the thruster exit plane at 300 V and 20 mg/s. The plasma at the outer wall accelerates slightly upstream of the plasma at the inner wall.....	86
Figure 5-10. Comparison of expected near-wall and centerline plasma potential profiles, assuming magnetic field lines act as equipotentials. The acceleration zone near the wall moves downstream and contains larger axial electric fields, creating radial electric fields away from the walls (plasma lens topology).....	87
Figure 5-11. Comparison of axial profiles of electron temperature at three different radial locations, under nominal operating conditions of 300 V and 20 mg/s. Peak electron temperatures are comparable but occur slightly downstream close to the wall.....	88
Figure 5-12. Comparison of axial profiles of electron temperature at three different radial locations, under nominal operating conditions of 300 V and 20 mg/s. Peak electron temperatures are comparable at all radial locations.....	88
Figure 5-13. Comparison of axial profiles of electron temperature between inner and outer channel walls near the thruster exit plane at 300 V and 20 mg/s. Peak electron temperatures are consistent between the two walls, with the peak along the outer wall occurring slightly upstream of the peak along the inner wall.....	89
Figure 5-14. Comparison of axial profiles of ion number density at three different radial locations, under nominal operating conditions of 300 V and 20 mg/s. Near the exit plane, the difference between the plasma at centerline and at the wall can approach an order of magnitude.....	91
Figure 5-15. Comparison of axial profiles of ion number density at three different radial locations, under nominal operating conditions of 300 V and 20 mg/s. Near the exit plane, the difference between the plasma at centerline and at the wall can approach an order of magnitude.....	91
Figure 5-16. Comparison of calculated ion number densities along the inner and outer channel walls, under nominal operating conditions of 300 V and 20 mg/s. The density along the inner wall is consistently higher than along the outer wall, with this difference diminishing near the exit plane.....	92
Figure 5-17. Comparison of measured axial profiles of ion number density to those calculated using Boltzmann's relation of thermalized potential at 300 V and 20 mg/s. The calculated values appear to overestimate the plasma density prior to acceleration and underestimate it after acceleration.....	94
Figure 5-18. Measured EEDF at -0.143 channel lengths along the outer wall, under nominal operating conditions of 300 V and 20 mg/s. The Maxwellian distribution based on the measured electron temperature (14 eV) is included for comparison. Distributions are normalized such that their integrals are unity.....	95
Figure 5-19. Measured EEDF at -0.071 channel lengths along the inner wall, under nominal operating conditions of 300 V and 20 mg/s. The Maxwellian distribution based on the measured electron temperature (36 eV) is included for comparison. Distributions are normalized such that their integrals are unity.....	96

Figure 5-20. Measured EEDF at -0.024 channel lengths along the inner wall, under nominal operating conditions of 300 V and 20 mg/s. The Maxwellian distribution based on the measured electron temperature (26 eV) is included for comparison. Distributions are normalized such that their integrals are unity.	96
Figure 5-21. Comparison of EEDFs at various axial locations along the inner channel wall, under nominal conditions of 300 V and 20 mg/s. Distributions are normalized such that their integrals are unity.	97
Figure 5-22. Example of a semi-log plot of an I-V characteristic taken within the acceleration zone inside the channel at 300 V and 20 mg/s. The transition region is composed of a linear and non-linear section. Electron current is less than expected near the plasma potential, where low-energy electrons should be collected.	98
Figure 5-23. Comparison of various potential electron distribution functions within the channel of a Hall thruster. Distributions are normalized such that their integrals are unity.	102
Figure 5-24. Comparison of the measured EEDF to the curve fit of a Maxwellian with velocity shift, at $z = -0.143$ channel lengths along the inner wall, under nominal operating conditions of 300 V and 20 mg/s.	103
Figure 5-25. Comparison of the measured EEDF to the curve fit of a Maxwellian with velocity shift, at $z = -0.048$ channel lengths along the inner wall, under nominal operating conditions of 300 V and 20 mg/s.	103
Figure 6-1. Example of a typical domain space and mesh within HPHall-2, including the channel and near-field plume.	108
Figure 6-2. Computational cycle used to track heavy particle species within HPHall-2.	109
Figure 6-3. Comparison of axial profiles of plasma potential at channel centerline and along the channel walls. The acceleration zone occurs slightly upstream along the walls compared to channel centerline.	111
Figure 6-4. Contour map of plasma potential within the thruster channel. Ion velocity vectors are overlaid on the map to indicate how the electric fields affect the ion motion. Significant radial velocities exist near the wall where radial electric fields defocus the beam.	111
Figure 6-5. Axial profiles of electron temperature at channel centerline and along the walls of the 6-kW Hall thruster. While the plasma is hotter at channel centerline for most of the channel, the maximum electron temperature occurs at roughly the same axial location near the exit plane.	113
Figure 6-6. Contour map of electron temperature within the channel. Lines of constant electron temperature follow magnetic field lines, while maximum electron temperature occurs near the exit plane where the magnetic field lines are nearly radial.	113
Figure 6-7. Axial profiles of ion number density at channel centerline and along the walls of the 6-kW Hall thruster. The plasma density is substantially lower close to the	

walls, and peak density occurs downstream of the peak location along channel centerline.	114
Figure 6-8. Contour map of the ion number density within the channel of the 6-kW Hall thruster. Ion density is 4-6X lower along the walls, with maximum densities occurring significantly downstream of the peak density along channel centerline.	115
Figure 6-9. Contour map of the local ionization rate within the channel of the 6-kW Hall thruster. Elevated rates were found to occur along the inner wall compared to the outer wall.	116
Figure 6-10. Comparison of measured and simulated axial profiles of plasma potential along the channel walls of the 6-kW Hall thruster. The location of the acceleration zone and the electric field strength are in good agreement.	117
Figure 6-11. Comparison of the measured radial recession along the inner and outer channel walls of the 6-kW Hall thruster after 334 hours of operation. Increased erosion is observed along the outer wall, consistent with measured plasma potential profiles.	117
Figure 6-12. Comparison of simulated radial magnetic field profiles along the inner and outer channel walls of the 6-kW Hall thruster. The peak radial magnetic field occurs further upstream along the outer wall compared to the inner wall, consistent with plasma potential measurements.	118
Figure 6-13. Comparison of measured and simulated axial profiles of electron temperature along the channel walls of the 6-kW Hall thruster. While maximum observed temperatures are in good agreement, their axial locations occur slightly upstream in the experimental data.	119
Figure 6-14. Comparison of measured and simulated axial profiles of ion number density along the channel walls of the 6-kW Hall thruster. Peak values are much higher in experiment than simulation, while better agreement is obtained within the acceleration zone close to the exit plane.	120
Figure 7-1. Axial profiles of incident ion current density along the inner channel wall at operating conditions of 150 V and 300 V, 20 mg/s. More ion current appears to reach the wall at 150 V, until the exit plane is approached where the incident currents are more equal.	123
Figure 7-2. Axial profiles of incident ion current density along the outer channel wall at operating conditions of 150 V and 300 V, 20 mg/s. The incident current is roughly equal until the ions begin accelerating at 300 V, at which point the current hitting the walls is reduced.	123
Figure 7-3. Axial profiles of sheath, beam and total ion energy along the inner wall near the exit plane at 300 V, 20 mg/s. The sheath energy is the primary component of ion energy for the majority of the channel, until the acceleration zone is reached. Uncertainty bars are omitted for clarity.	125
Figure 7-4. Axial profiles of sheath, beam and total ion energy along the outer wall near the exit plane at 300 V, 20 mg/s. The sheath energy is the primary component of ion	

energy until the acceleration zone is reached. Uncertainty bars are omitted for clarity.	126
Figure 7-5. Axial profiles of sheath, beam and total ion energy along the inner wall near the exit plane at 150 V, 20 mg/s. The sheath energy remains the dominant component until the exit plane is reached. Uncertainty bars are omitted for clarity.	127
Figure 7-6. Axial profiles of beam, sheath and total ion energy along the outer wall near the exit plane at 150 V, 20 mg/s. The sheath energy remains the dominant component for almost the entire channel. Uncertainty bars omitted for clarity. ...	127
Figure 7-7. Axial profiles of the relative contributions of beam and sheath energies to the total ion energy along the outer wall at 300 V, 20 mg/s. Beam energy does not exceed the sheath energy contribution until the last 8% of the channel.	128
Figure 7-8. Axial profiles of the relative contributions of beam and sheath energies to the total ion energy along the outer wall at 150 V, 20 mg/s. Beam energy does not begin to exceed the sheath energy contribution until the last 2% of the channel.	128
Figure 7-9. Axial profiles of incident ion power density along the inner wall near the exit plane at 150 and 300 V, 20 mg/s. In general, the power density increases as the exit plane is approached, with more power at 300 V.	129
Figure 7-10. Axial profiles of incident ion power density along the outer wall near the exit plane at 150 and 300 V, 20 mg/s. The power density appears to increase as the exit plane is approached, with more power at 300 V.	130
Figure 7-11. Total ion power to the walls within the interrogation zone. While the ion power is fairly linear with discharge power, elevated values were found at 150 V.	132
Figure 7-12. Percent of discharge power that is incident on walls from ion flux. Average power over all operating conditions tested is roughly 6%. Values over 8% were calculated at 150 V, 10 and 20 mg/s.	132
Figure 7-13. Integrated ion current to the channel walls within the interrogation zone. Total ion current appears to increase with anode flow rate and decrease with discharge voltage.	133
Figure 7-14. Total ion current to the channel walls within the interrogation zone, non-dimensionalized by the measured beam current. The decreasing trend with discharge voltage is much more defined, and is present at all flow rates.	133
Figure 7-15. Averaged incident ion energy along the channel walls within the interrogation zone. As expected, the average energy increases with discharge voltage as the channel becomes exposed to higher beam energies.	134
Figure 7-16. Averaged incident ion energy along the channel walls, non-dimensionalized by the discharge voltage. In general, the energy increases with discharge voltage, but decreases at lower voltages.	135

Figure 7-17. Sigmoid curve fits to floating and plasma potential axial profiles along channel centerline within the channel, under nominal conditions of 300 V and 20 mg/s anode flow rate. Data taken from Ref. [13]...... 136

Figure 7-18. Comparison of measured plasma and floating potentials along the outer channel wall and extrapolated sigmoid fits to the entire channel, at 300 V and 20 mg/s anode flow rate. Boundary points at the anode and in the plume are based off prior measurements. Uncertainty bars omitted for clarity. 137

Figure 7-19. Comparison of measured electron temperature along the outer channel wall to the extrapolated axial profile within the channel, at 300 V and 20 mg/s anode flow rate. The extrapolated profile shows reasonable agreement with experimental data, and accurately reproduces the location and magnitude of maximum electron temperature. 139

Figure 7-20. Comparison of functional fits to measured axial profiles of electron temperature and ion number density along the bulk plasma outer bound at 300 V and 20 mg/s anode flow rate. Data taken from Ref. [13]. The electron temperature was found to closely follow a Gaussian profile, while the ion number density most closely resembled a Lorentzian profile. 140

Figure 7-21. Comparison of measured and extrapolated ion current density to the outer channel wall, at 300 V and 20 mg/s anode flow rate. The functional fit is in reasonable agreement with the experimental data. 141

Figure 7-22. Extrapolated plasma potential and ion current density profiles at 300 V and 10 mg/s (left) as well as at 500 V and 10 mg/s (right). In order to ensure the peak current density was captured at 500 V, an artificial data point was created based on the magnitude of the peak at other operating conditions as well as the relative location of this peak along the plasma potential profile. Uncertainty bounds are omitted for clarity. 142

Figure 7-23. Total incident ion power to the walls within the channel. While there is a general increase in wall power with discharge power, elevated values were found at 150 and 500 V. 143

Figure 7-24. Percent of discharge power incident on the channel walls via ion flux. Elevated values are found primarily at 150 V, 10 and 20 mg/s, as well as at 500 V. Average ion power over all operating conditions is 11.5%. 143

Figure 7-25. Total integrated ion current to the channel walls as a function of discharge voltage. As expected, total wall current increases with mass flow rate. In general, wall current drops with increased voltage, but appears to increase at 500 V. 144

Figure 7-26. Total ion current to the channel walls non-dimensionalized by ion beam current. In general, elevated values are found at low voltage due to high divergence and at high voltage due to recession of the acceleration zone. 144

Figure 7-27. Average incident ion energy along the channel walls as a function of discharge voltage. As expected, the average energy increases with discharge voltage, exceeding 100 eV at 400 and 500 V. 145

Figure 7-28. Average ion energy to the channel walls non-dimensionalized by discharge voltage. A minimum occurring at moderate voltages is caused by high sheath energies at low voltage and elevated beam energies at high voltage..... 146

Figure 7-29. Calculated ion beam current as a function of distance from the thruster exit plane, at 300 V and 20 mg/s. Values are very consistent from 0.3 to over 1 mean channel diameter. Horizontal line corresponds to reported beam current value.... 147

Figure 7-30. Comparison of ion current density radial profiles taken by Reid and in this study, 0.3 $D_{T,m}$ downstream of the exit plane at 300 V, 20 mg/s. Elevated current densities are found by Reid far off axis and near thruster centerline..... 148

Figure 7-31. Calculated divergence angle at various axial locations downstream of the thruster exit plane at 300 V, 20 mg/s. Horizontal line corresponds to reported divergence angle. 149

Figure 7-32. Ion current density contour map at 400 V, 10 mg/s anode flow rate. The ion beam exiting the channel is highly collimated, and merging towards thruster centerline does not occur upstream of 1 $D_{T,m}$ from the exit plane..... 150

Figure 7-33. Ion current density contour map at 500 V, 10 mg/s anode mass flow rate. The ion beam exiting the channel is more divergent, and begins to merge towards thruster centerline upstream of 1 $D_{T,m}$ 151

Figure 7-34. Comparison of internal and plume divergence angles for the nine operating conditions tested in this study. A rough linear correlation is found between the two angles. 152

Figure 7-35. Measured ion accommodation factors at various incident ion energies for four different materials. Excellent linear behavior is observed within the energy range tested. Data taken from Kim et al. [84]..... 153

Figure 7-36. Dependence of the electron-to-ion current ratio to the channel wall on local electron temperature. The secondary electron emission characteristics of the wall can increase this ratio from 5 to almost 60 over a short range of temperatures..... 155

Figure 7-37. Calculated axial profiles of incident ion power density, electron power density, and electron temperature along the outer wall at 300 V, 20 mg/s. Around the region where the sheath enters the charge-saturated regime (CSR), the electron power density rises to nearly two orders of magnitude higher than the ion power density. 156

Figure 7-38. Variation of calculated electron power to the channel walls at 300 V, 20 mg/s, depending on the electron temperature at which crossover occurs (onset of CSR), as well as the SEE coefficient at zero incident energy, δ_0 . The calculated electron power drops significantly once the crossover temperature exceeds the maximum observed temperature in the discharge. 156

Figure 8-1. Diagram illustrating the dependence of sputtering yield on incident ion energy, E , and incidence angle, θ , for a given ion species and wall material..... 160

Figure 8-2. Comparison of various fitting functions to experimentally measured values by Rubin et al. While all functions adequately fit the data, the linear and HPHall-2 fits match the best. 162

Figure 8-3. Comparison of the linear fit model to the energy-dependent sputtering yield used in HPHall-2. The values measured by Rubin are much higher than those predicted by HPHall-2, as well as previously measured yields. 162

Figure 8-4. Comparison of the proposed cosine fit to Rubin's data for angle-dependent sputter yield and that presently used in HPHall-2. The experimental data from Rubin predicts a much weaker dependence on sputtering angle. 163

Figure 8-5. Diagram illustrating the effects of an ion beam on the sheath around a planar Langmuir probe. When the probe bias is sufficiently high, the ion beam is repelled. This creates a large space charge layer in the sheath that causes it to bulge out and collect many more electrons. 164

Figure 8-6. Representative second derivative of a probe I-V characteristic. The peak occurring at a voltage above the plasma potential is evidence of an ion beam. 165

Figure 8-7. Diagram illustrating the various variables used to determine the ion incidence angle at the channel wall. 166

Figure 8-8. Comparison of predicted erosion rates using the HPHall-2 sputtering model, based off data from 300 V, 10 mg/s and 300 V, 20 mg/s, to those expected based off the measured erosion profile. The model predicts much higher erosion rates at all locations, but matches the expected profile shape. Uncertainty bounds are omitted for clarity. 168

Figure 8-9. Comparison of predicted erosion rates using the Rubin-based sputtering model, based off data from 300 V, 10 mg/s and 300 V, 20 mg/s, to those expected based off the measured erosion profile. While the Rubin-based model more accurately predicts the very low erosion rates far back in the channel, the predicted erosion rates are much higher near the exit plane than those predicted by the HPHall-2 model. Uncertainty bounds are omitted for clarity. 170

Figure 8-10. Calculated energy-dependent sputter yields using the HPHall-2 model for angle-dependent sputtering yield, given data at 300 V, 10 mg/s and 300 V, 20 mg/s. The data was also weight-averaged by the relative amounts of total charge for each operating condition to represent a more accurate sputtering yield. 171

Figure 8-11. Calculated energy-dependent sputter yields using the Rubin-based model for angle-dependent sputtering yield, given data at 300 V, 10 mg/s and 300 V, 20 mg/s. The data was also weight-averaged by the relative amounts of total charge for each operating condition to represent a more accurate sputtering yield. 172

Figure 8-12. Comparison of calculated charge-averaged energy-dependent sputter yields using HPHall-2 and Rubin-based angle-dependent sputtering yields. Curve fits using the Bohdansky model are also included, showing excellent agreement. 172

List of Tables

Table 4-1. Thruster operating conditions used during plasma potential study.	64
Table 4-2. Comparison of plasma potential results from various analysis techniques. When compared to the swept emissive probe, the derivative method appears to be the most accurate.....	64
Table 4-3. List of magnitudes and orientations tested in magnetic field study. A total of 32 conditions were investigated.....	66
Table 4-4. Characteristic values of pertinent length scales near the walls of the NASA-173Mv1 and within the present study. Properties are based off a 300-V discharge at nominal flow rates.....	69
Table 5-1. List of operating conditions tested using internal wall-mounted probes, spanning a wide range of discharge voltages, mass flow rates, and discharge powers. Shaded operating conditions represent the data presented in this work.	78
Table 5-2. Comparison of number densities along the walls to those along channel centerline at 300 V and 20 mg/s. Reported values use the beam-calculated number density, and location is in units of channel lengths from the thruster exit plane.	92
Table 5-3. Comparison of measured values of electron temperature to those calculated using the measured EEDF at 300 V and 20 mg/s. Prior to acceleration, these values are nearly the same, but within the acceleration zone the effective electron temperature is much higher.....	97
Table 5-4. Comparison of measured values of electron temperature to values determined by the EEDF through distribution curve fitting using a Maxwellian with a velocity shift. The corresponding velocity shift is included for completeness.....	104
Table 5-5. Possible sources of drift velocity for electrons within the Hall thruster channel and calculated typical values.....	105
Table 6-1. Comparison of measured and simulated values of performance at the nominal operating condition.	110
Table 7-1. List of calculated beam currents and current utilization efficiencies for the operating conditions in this work. Values with asterisks denote data taken from Reid [13].	147
Table 7-2. List of calculated plume divergences and divergence efficiencies from near-field ion current density measurements. Values with asterisks correspond to data from Reid [13].....	149

Table 8-1. List of calculated incidence angles along the inner and outer channel walls at 300 V, 20 mg/s. Probe locations are given in units of channel lengths from the exit plane. Incidence angles increase slightly as the exit plane is approached. 167

List of Appendices

Appendix A 6-kW Hall Thruster Performance Data	179
Appendix B Additional Internal Wall-mounted Probe Data.....	181
Appendix C Additional Near-field Faraday Probe Data.....	188

Nomenclature

Physical Constants

e	Elementary charge, 1.6×10^{-19}	[C]
g_o	Gravitational constant at sea level, 9.81	[m/s ²]
k	Boltzmann constant, 1.38×10^{-23}	[J/K]
m_e	Electron mass, 9.1×10^{-31}	[kg]
m_{Xe}	Xenon atom mass, 2.18×10^{-25}	[kg]
ϵ_o	Permittivity of free space, 8.85×10^{-12}	[F/m]

Variables (Latin)

A_p	Physical probe area	[m ²]
A_s	Sheath area	[m ²]
B	Magnetic field	[T]
$D_{T,m}$	Mean thruster diameters	[m]
E	Electric field or incident ion energy	[V/m],[eV]
E_{th}	Threshold energy for sputtering to occur	[eV]
E_l	Incident energy at which secondary electron emission coefficient is unity	[eV]
F	Generalized force	[N]
$f(\epsilon)$	Energy distribution function	[eV ⁻¹]
I_{axial}	Axial ion beam current	[A]
I_b	Ion beam current	[A]
I_d	Discharge current	[A]

I_e	Electron current to probe	[A]
$I_{e,sat}$	Electron saturation current to probe	[A]
$I_{i,sat}$	Ion saturation current to probe	[A]
I_{sp}	Specific impulse	[s]
I_{total}	Total ion current	[A]
I_{walls}	Total ion current to channel walls	[A]
j_b	Ion beam current density	[A/m ²]
j_e	Electron current density	[A/m ²]
j_i	Ion current density	[A/m ²]
j_{se}	Secondary electron current density	[A/m ²]
M_f	Final (dry) spacecraft mass	[kg]
M_i	Ion mass	[kg]
M_o	Initial (wet) spacecraft mass	[kg]
m	Particle mass	[kg]
\dot{m}	Mass flow rate	[kg/s]
\dot{m}_a	Anode mass flow rate	[kg/s]
n	Plasma number density	[m ⁻³]
n_e	Electron number density	[m ⁻³]
$n_{e,ref}$	Reference electron number density	[m ⁻³]
n_i	Ion number density	[m ⁻³]
n_o	Reference number density	[m ⁻³]
n^0, n^i	Initial and i^{th} number density in computational iteration	[m ⁻³]
$P_{electron}$	Incident electron power to channel walls	[W]
P_{ion}	Incident ion power to channel walls	[W]
P_{in}	Thruster input power	[W]

P_d	Discharge power	[W]
r	Radial coordinate location	[m]
$r_{1/e}$	Radial coordinate location where current density drops to (1/e) of its maximum value	[m]
r_{max}	Radial coordinate location where current density is maximum	[m]
r_p	Probe radius	[m]
s	Length coordinate along channel wall	[m]
T	Thrust or temperature	[N],[K]
T_e	Electron temperature	[eV]
T_{eff}	Effective electron temperature	[eV]
T_{\perp}	Electron temperature normal to magnetic field	[eV],[K]
T_{\parallel}	Electron temperature parallel to magnetic field	[eV],[K]
U	Particle speed	[m/s]
u_e	Exit velocity	[m/s]
u_{\perp}	Ion velocity normal to wall	[m/s]
V_a	Acceleration voltage	[V]
V_{anode}	Anode potential	[V]
V_d	Discharge voltage	[V]
V_f	Floating potential	[V]
V_l	Loss voltage	[V]
V_p	Plasma potential	[V]
V_{peak}	Voltage at which ion beam “hump” peaks in probe characteristic second derivative	[V]
V_{sheath}	Sheath potential	[V]
V_{wall}	Potential of channel wall	[V]
ΔV	Velocity change of spacecraft	[m/s]

v	Particle velocity	[m/s]
v_{Bohm}	Bohm velocity	[m/s]
v_d	Drift velocity	[m/s]
v_x, v_y, v_z	Particle velocities in the x , y , and z directions	[m/s]
v_{z_0}	Original particle velocity in the z direction	[m/s]
v_{\perp}	Ion velocity normal to wall surface	[m/s]
v_{\parallel}	Ion velocity parallel to wall surface	[m/s]
Δv	Velocity shift	[m/s]
x	Particle position	[m]
Y	Sputtering yield	[mm ³ /C]
Y_E	Energy-dependent sputtering yield	[mm ³ /C]
Y_{θ}	Angle-dependent sputtering yield	--
Z_i	Charge state of ion species i	--
z	Axial coordinate location	[m]

Variables (Greek)

Γ_e	Electron flux	[m ⁻² s ⁻¹]
Γ_i	Ion flux	[m ⁻² s ⁻¹]
Γ_{se}	Secondary electron flux	[m ⁻² s ⁻¹]
δ_0	Secondary electron emission coefficient at zero incident energy	--
δ_w	Secondary electron emission coefficient	--
δ_w^*	Critical secondary electron emission coefficient	--
ε	Particle energy	[eV],[J]
ε_i	Incident ion energy	[eV]
ε_{total}	Total ion energy	[eV],[J]

ε_{\perp}	Ion energy normal to wall	[eV],[J]
$\bar{\varepsilon}_i$	Average incident ion energy	[eV]
$\Delta\varepsilon$	Energy shift	[eV],[J]
ζ	(Unknown) Proportionality constant	--
η	Total efficiency	--
η_a	Anode efficiency	--
η_b	Current utilization efficiency	--
η_d	Divergence efficiency	--
η_m	Mass utilization efficiency	--
η_p	Non-dimensionalized probe bias with respect to plasma potential	--
η_q	Charge utilization efficiency	--
η_v	Voltage utilization efficiency	--
θ	Ion incidence angle with respect to wall surface normal	[deg]
θ_d	Plume divergence half-angle	[deg]
θ_0	Ion incidence angle upon sheath surface	[deg]
λ_c	Cyclotron radius	[m]
λ_{De}	Debye length	[m]
μ_0	Non-dimensionalized floating wall potential	--
μ_p	Non-dimensionalized probe bias with respect to floating wall potential	--
ρ	Charge density	[C/m ³]
ρ_p	Non-dimensionalized probe radius	--
ϕ	Electric potential	[V]
ϕ_{ref}	Reference electric potential	[V]
ϕ_p	Probe bias with respect to plasma potential	[V]

ψ	Internal divergence half-angle	[deg]
Ω_i	Current fraction of ion species i	--

Chapter 1

Introduction

1.1 Problem Statement

Hall thrusters are electric propulsion devices with moderate specific impulse capabilities, and have been primarily used for orbital station-keeping on Earth satellites. However, there is increasing interest in using these devices for deep space missions, such as those considered by NASA. Such missions have demanding specifications on Hall thruster throughput and lifetime, typically requiring thousands (if not tens of thousands) of hours of operation prior to failure. The present method of qualifying such thrusters is to perform long, expensive life tests where the device is operated to the desired point in life. As mission requirements for Hall thrusters continue to increase, this method of qualification will become prohibitively expensive, thus limiting the ability to use these devices on otherwise appropriate missions.

A more tractable approach towards lifetime qualification is to develop a model that accurately simulates the physics that ultimately lead to thruster failure. Once validated, this model could then be used to estimate the lifetimes of numerous thrusters and desired operating conditions, all at a fraction of the time and cost of a life test. At present, several models are being developed for such purposes, but all require empirical inputs to accurately predict the state of the thruster as observed in experiment. Therefore, the physics models currently being used must be re-evaluated by validating or refining them with experimental data.

1.2 Motivation and Scope for Research

Lifetime of Hall thrusters is currently limited by erosion of the channel wall due to ion bombardment. Once the wall has eroded enough to expose the magnetic circuit to

the plasma, the magnetic material will begin to sputter; this is often considered a “soft” failure point since the thruster will continue to operate, usually with minimal changes in performance [1,2]. The exposure of the magnetic circuit to the plasma has the potential to reduce thruster performance and eventually cause failure, but this has yet to be observed in experiment. The mechanism of erosion due to ion bombardment is complex and requires intimate knowledge of the physics within the thruster channel and along the wall in order to properly simulate its conditions. Sputtering of wall material is dependent upon ion impact energy, incident angle of impact, the properties of the wall material itself, and the flux of ions that reach the wall. A large number of studies have contributed to the understanding of how the plasma inside the thruster interacts with the channel wall, but these studies have largely been limited to theory and simulation [3-9]. Thus, there is presently a lack of experimental data detailing properties relevant to erosion. The aim of this dissertation is to better understand the interaction between the plasma and channel walls within a Hall thruster, and how these interactions affect thruster performance and lifetime. This knowledge can then be used to improve present Hall thruster physics and lifetime models.

Typical internal measurements for Hall thrusters are taken either with physical probes mounted onto high-speed stages [10-13] or through laser-induced fluorescence (LIF) [14]. Since the desired data pertains to wall erosion, measurements must be taken in close proximity to the channel wall (less than one millimeter). Physical probes cannot be injected into the thruster at this proximity due to the necessary probe housing. Laser-induced fluorescence, while having the capability to obtain the required proximity, cannot easily measure ion currents to the wall; furthermore, it lacks the ability to interrogate the electron population and sheath properties at the wall, which is also critical towards understanding the wall physics within Hall thrusters. Due to these restrictions, flush-mounted Langmuir probes were chosen as the diagnostic to use for this study. By imbedding the probes within the channel wall, all relevant properties may be measured with the required proximity. However, use of such probes does not come without certain drawbacks. Analysis of the resulting data can be complex due to the flush-mounted nature of the probe geometry, as well as the fact that the probe material cannot mimic the behavior of the adjacent insulating wall material. Due to the significance of these effects,

a great deal of effort was spent in characterizing them to obtain higher fidelity measurements from flush-mounted Langmuir probes.

The research in this dissertation not only describes the experimental data taken along the channel walls, but the implications and conclusions that can be drawn that are relevant to present erosion and wall physics models. Recommendations are made on improving present models after comparing simulation to experiment.

1.3 Prior Near-Wall Studies in Hall Thrusters

The use of flush-mounted Langmuir probes within Hall thrusters is not a new concept. In particular, groups at Busek Co. Inc. and the Massachusetts Institute of Technology (MIT) as well as the Research Institute of Applied Mechanics and Electrodynamics of Moscow Aviation Institute (RIAME MAI) have measured internal properties of Hall thrusters using Langmuir probes imbedded within the channel walls. While these studies have set the precedence for the diagnostic, they have inherent limitations not only in scope but also in interpretation of the resulting data.

The work done at Busek and MIT was primarily performed by Warner and Szabo [15-17]. Five flush-mounted probes were placed along the outer wall of the BHT-1000 Hall thruster. This was complemented with three external probes near the exit plane of the thruster. Plasma potential, floating potential, electron temperature, and plasma density were acquired at moderate to high discharge voltages (300 – 900 V) using simple Langmuir probe theory. This study laid an excellent foundation for mechanical implementation of flush-mounted Langmuir probes in Hall thrusters. Furthermore, the concept of leakage current was addressed, characterized, and corrected; attempts were made to correct for magnetic field effects on the calculated electron number density; and the transition region of the Langmuir probe traces was analyzed in more detail, leading to preliminary discussion on the electron energy distribution function (EEDF). However, the data were not taken as being representative of the local plasma. Instead, it was assumed that the data represented an average along the intersecting magnetic line of force due to the relatively large conductivity along this path. Therefore, when comparisons were made between simulation and experiment, the data were compared to simulation results along channel centerline. This interpretation limited the usefulness of the study in

regards to wall physics and erosion. A more in-depth comparison between simulation and experiment within this dissertation shows that this assumption is invalid, and that the data from flush-mounted probes are more representative of the local plasma; no plasma properties (with the exception of electron temperature) were found to be constant along magnetic field lines.

The work done at RIAME was performed primarily by Kim [18-21]. Six locations inside the channels of the SPT-100 and PPS-1350 were probed along with two external locations beyond the exit planes, at moderate to high discharge voltages (300 – 700 V). Data were only taken along the outer wall, and symmetry with the outer wall was assumed to determine properties along the inner wall. Plasma potential, floating potential, electron temperature, and ion current density were reported. This particular study used the data to estimate ion and electron power losses to the walls, as well as relate these quantities to the local erosion rate. Comparisons were made to other studies that estimated wall power losses, as well as experimentally determined erosion profiles. Thus, the Kim study provided an excellent basis for using data from flush-mounted Langmuir probes in erosion calculations. However, several limitations prevented this study from reaching full potential:

- mechanical implementation of the probes and analysis of the resulting data was scarcely documented, leading to questionable final results;
- assumptions were made about the inner wall in order to gain values for the whole channel;
- the sheath physics and properties were not analyzed in any detail, leading to the assumption that the potential of the channel wall was the floating potential measured by the probe; and
- direct proportionality was assumed between power to the wall and erosion rate, neglecting the importance of impact angle and non-linear sputtering yield dependence on ion energy.

These limitations motivated a deeper study that would further the use of flush-mounted probes specifically towards better understanding of near-wall physics and Hall thruster erosion.

1.4 Contributions of Research

The contents of this dissertation contain several contributions towards implementing flush-mounted Langmuir probes and understanding near-wall physics and erosion within Hall thrusters, many of which address the issues of previous studies mentioned in Section 1.3. These contributions include:

1. **Development of analysis methods specific towards flush-mounted Langmuir probes.** This mainly includes a new model for sheath expansion in the ion saturation regime, but also includes recommendations for determining plasma potential and ion flow angles in the presence of an ion beam.
2. **Expanded data set along the channel walls, compared to prior measurements.** This includes taking measurements at low (< 200 V), moderate (200 – 400 V), and high (> 400 V) discharge voltage, at a wide range of discharge powers up to 6 kW, and simultaneous data collection at both inner and outer channel walls.
3. **Characterization of the near-wall plasma in comparison to the plasma in the rest of the channel.** Comparison to other internal data shows that the near-wall plasma accelerates further upstream compared to the rest of the plasma, with number densities anywhere from 2-10 times smaller than those found at channel centerline.
4. **Evidence of electron thermalization processes within the channel.** Measured sheath potentials were found to be on the order of five times the electron temperature, indicating the presence of a high-energy electron population. With no thermalization process to replenish this population, it would quickly be lost to the walls. This strongly influences the actual sheath potentials within the thruster; thermalization of secondary electrons emitted from the channel walls regulates the sheath potential, which in turn affects the power deposited to the walls as well as local wall erosion rates.
5. **Measurement of electron energy distribution functions along the channel walls.** Measured distribution functions show a near-Maxwellian structure upstream of the acceleration zone, that transitions into a strongly drifting Maxwellian distribution within the acceleration zone. The corresponding electron

temperatures to these drifting Maxwellian distributions are much lower than those measured using simple probe analysis techniques.

6. **Characterization of the ion power losses to the channel walls as a function of operating condition.** While power losses were found to be largely proportional to discharge power, elevated values were measured at discharge voltages of 150 and 500 V. This trend was caused by large sheath energies and high divergence at low voltage, and large beam energies and additional exposure of the wall to plasma at high voltage.
7. **Derivation of an energy-dependent sputtering model that reproduces observed erosion rates.** Data from the flush-mounted Langmuir probes were used to infer the necessary sputtering yield to produce the observed amount of erosion within a 6-kW Hall thruster. The resulting sputtering yield resembled the model proposed by Bohdanský [22], with an energy threshold for sputtering of at least 25 eV.

1.5 Dissertation Overview

This dissertation is organized into four major sections: an introduction and background section (Chapters 2-3); a data analysis section (Chapter 4); an experimental and computational results section (Chapters 5-6); and a results application and discussion section (Chapters 7-8).

Chapters 2 and 3 give the necessary background information to understand and appreciate the rest of the dissertation. Chapter 2 focuses on the fundamentals of rocket propulsion, electric propulsion, and Hall thruster anatomy and operation. Chapter 3 provides a description of all experimental apparatus used to obtain the results presented in the dissertation.

Chapter 4 covers the studies on developing methods of data analysis for flush-mounted Langmuir probes. Results are presented and then recommendations are made based on conclusions from the studies. Final analysis techniques are summarized.

Chapters 5 and 6 detail the major results from both experimental and computational studies. Chapter 5 covers the data taken using the flush-mounted Langmuir probes within the Hall thruster channel, including all relevant plasma

parameters and their comparison to additional internal data. Chapter 6 describes the baseline simulations run in the hybrid-PIC (particle-in-cell) code HPHall-2 for comparison to the experimental data.

Chapters 7 and 8 discuss the application of the resulting data set towards energy and erosion considerations within the thruster. Chapter 7 details how incident ion power to the channel walls is calculated, how the resulting ion currents and energies are distributed within the channel, how they vary with operating condition, and the implications of the resulting energy loss to the walls. Chapter 8 covers the prediction of erosion rates using the data set and a detailed sputtering model, as well as comparison to expected erosion rates and the resulting implications.

Chapter 9 is the conclusions section. Major findings are summarized, and recommendations are made for future work in this research area.

Chapter 2

Background

This chapter contains a brief summary of the fundamentals of rocket propulsion, electric propulsion and Hall thrusters. While this information is necessary to understand the context of the remainder of the dissertation, it is by no means a thorough review of the broad subject matter. For more details about electric propulsion, as well as Hall thruster operation, design, and analysis refer to Refs. [23-25].

2.1 Rocket Propulsion Fundamentals

Unlike air-breathing gas turbine engines, rocket propulsion devices carry both the necessary fuel and oxidizer (chemical) or propellant (electric), making them ideal for space applications where there is no readily available supply of oxidizer. Energy is imparted to the working fluid to create a high-velocity exhaust out the rocket exit that produces thrust in the opposite direction. Key parameters of any rocket propulsion system are the thrust, specific impulse, and efficiency.

The thrust is the rate of momentum transfer imparted by the rocket onto the object. Due to Newton's third law, this is equivalent to the rate of momentum transferred to the working fluid being ejected out the exit. Since negligible momentum enters the inlet, the thrust is then the rate of fluid momentum exiting the rocket:

$$T = \dot{m}u_e. \quad (2-1)$$

Therefore, the thrust is directly proportional to the mass flow rate, \dot{m} , and velocity of the fluid, u_e , exiting the rocket.

The specific impulse is a measure of how effectively a rocket uses the working fluid mass to produce thrust. In the most general sense, it is the total time-integrated thrust of a rocket per unit propellant weight expelled:

$$I_{sp} = \frac{\int_0^{t_f} T dt}{\int_0^{t_f} \dot{m} g_o dt}. \quad (2-2)$$

If the thrust and mass flow rate are constant over the firing duration, which under most circumstances is a reasonable approximation, then the specific impulse is simplified to:

$$I_{sp} = \frac{u_e}{g_o}. \quad (2-3)$$

Thus the specific impulse to first order is directly related to the exhaust velocity of the working fluid. This is intuitively consistent: if the exhaust velocity is higher, then the rocket can produce the same amount of thrust using less mass flow, and is thus more mass-efficient. When considering the fact that rockets have to carry the necessary propellant mass, the specific impulse becomes a very important factor in mission design; if the rocket is not mass-efficient, it will have to carry much more propellant to impart the necessary impulse or “ ΔV ” to the spacecraft. This is characterized by the Tsiolkovsky rocket equation,

$$\frac{M_f}{M_o} = e^{-\Delta V / g_o I_{sp}}, \quad (2-4)$$

where M_f is the final (dry) spacecraft mass and M_o is the initial (wet) spacecraft mass. It is clear that a high specific impulse is desirable to maximize the final mass of the spacecraft.

The efficiency of a rocket is a measure of how well it converts the input power into thrust. It is defined as the “jet power” divided by the total input power of the device:

$$\eta = \frac{\frac{1}{2} \dot{m} u_e^2}{P_{in}}. \quad (2-5)$$

This equation is more applicable towards electric propulsion devices, as the input power is not readily defined for chemical rockets. The efficiency will be analyzed in more detail in Section 2.2.2.

2.2 Electric Propulsion Systems

In Section 2.1, the importance of high specific impulse was highlighted in terms of propellant mass savings. Traditional chemical rockets are limited in the amount of

energy they can impart to the working fluid, since this energy comes from broken chemical bonds. Thus, while these rockets have enormous mass flow rates and can achieve thrust levels on the order of millions of newtons, their specific impulses are limited to only a few hundred seconds. Electric propulsion systems, on the other hand, impart energy using combinations of electric and magnetic fields, and are thus only limited by the available energy from a power supply. The variety of electric propulsion systems can be broken up into three main categories: electrothermal, electrostatic, and electromagnetic thrusters. A thorough treatment of this broad subject is not given here; further detail can be found in Refs. [23,25]. Instead, brief descriptions of two major electric propulsion systems, the gridded ion thruster and Hall thruster, are provided below.

2.2.1 Gridded Ion Thrusters

A common electrostatic propulsion system is the gridded ion thruster. These devices have significant heritage and have been used on multiple spacecraft including Deep Space 1 and Dawn. In development since the 1960s, these thrusters are a mature, well-understood technology.

A typical ion thruster consists of five major parts: the discharge chamber; discharge cathode; neutralizer cathode; floating screen grid; and accelerating grid (see Figure 2-1). The discharge chamber, which also serves as the anode for the discharge, attracts electrons that are injected into the chamber by the discharge cathode. A ring-cusp magnetic field inhibits the motion of the electrons and traps them within the chamber. This increases the electron residence time in the chamber and facilitates ionization of neutral gas by electron bombardment. The ions in the chamber then migrate towards the screen grid and are subsequently driven out of the chamber by the accelerating grid, creating thrust. The positively-charged beam is then neutralized by electrons emitted by the neutralizer cathode external to the discharge chamber.

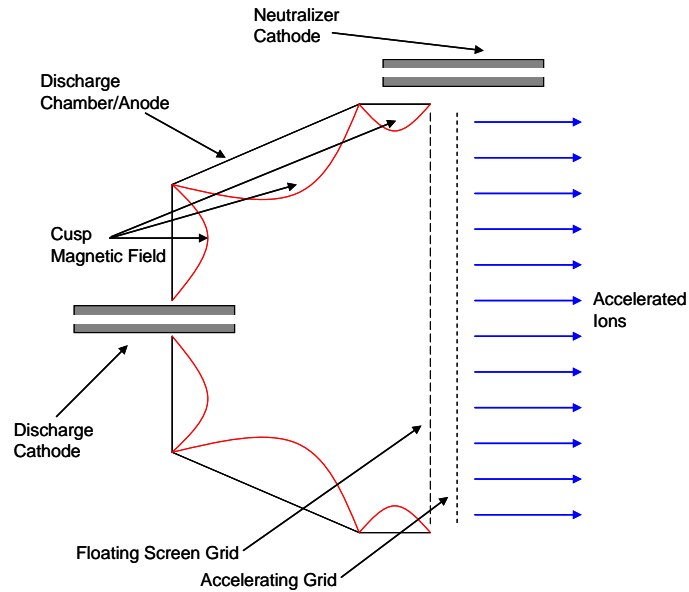


Figure 2-1. Schematic of a typical gridded ion thruster, with major components labeled. Not to scale.

Since the velocity of the exiting ions is dictated by the accelerating voltage, specific impulses well over 3,000 seconds are routinely achieved, making the gridded ion thruster much more mass-efficient than a traditional chemical rocket. However, despite its significant heritage, this thruster remains a complex and expensive device. Required electric fields necessitate a grid gap on the order of a millimeter, making the grids prone to shorting during thermal expansion. Also, while the grids tend to degrade due to ion bombardment, the primary life-limiting mechanism in these devices is cathode erosion. Furthermore, the beam current is not neutralized during the acceleration process; this limits the maximum current drawn out by the device before the fields created by the ions themselves cancel out the accelerating field (known as space-charge-limited current). Thus, the thrust densities of ion thrusters are typically much lower than that of other electric propulsion devices such as Hall thrusters. Despite these limitations, gridded ion thrusters remain a reliable, long-lasting, mass-efficient propulsion device.

2.2.2 Hall-effect Thrusters

Another common electric propulsion device, and the subject of this dissertation, is the Hall thruster. While initially conceived in the United States, significant development of this device occurred in the Soviet Union in the 1960s, 1970s, and 1980s. After the end of the Cold War, in the early 1990s, the technology was brought back to the western

world and research continued on its design and operation. Since then, significant advances have been made on understanding the underlying physics and design of these devices. The following section serves as a brief introduction to the anatomy, physics, and operation of Hall thrusters.

2.2.2.1 Hall Thruster Fundamentals

A typical Hall thruster is composed of four major components: an anode; a cathode; a discharge channel; and a magnetic circuit (see Figure 2-2). Neutral gas, typically xenon due to its large atomic mass and low ionization potential, is injected through the anode, which also serves as the gas distributor. Electrons are emitted from the cathode and are attracted to the positively-biased anode. However, their motion is inhibited by the externally-applied magnetic field. As a result, a strong electric field is generated in this zone to maintain the discharge current and compensate for the increased resistance. The primarily axial electric field and radial magnetic field cause the electrons to drift in the azimuthal direction, giving rise to the Hall current for which the thruster is named. This facilitates the ionization of the neutral gas, creating ions that are subsequently accelerated by the electric field. The magnetic field is of sufficient strength to magnetize the electrons, but has little effect on the ions due to their large mass. The cathode also supplies the necessary electrons to neutralize the ion beam exiting the thruster. The configuration allows for the entire discharge to remain quasi-neutral, thus avoiding any space-charge limitations on the current and thrust densities.

The externally-applied magnetic field is of particular importance to the performance of the thruster, as it dictates the electron motion and resulting electric field responsible for thrust generation. A magnetic field topology typical of modern Hall thrusters in the United States is shown in Figure 2-3. As previously mentioned, the magnetic field is primarily oriented in the radial direction, especially near the exit plane of the thruster. Furthermore, the curvature of the magnetic field lines within the channel is known as a plasma lens. This is due to the high conductivity of the electrons along the magnetic field lines compared to across the lines. Thus, the magnetic field lines are, to first order, equipotential lines; the electric field generated “focuses” the ions away from the walls and towards the channel centerline [26].

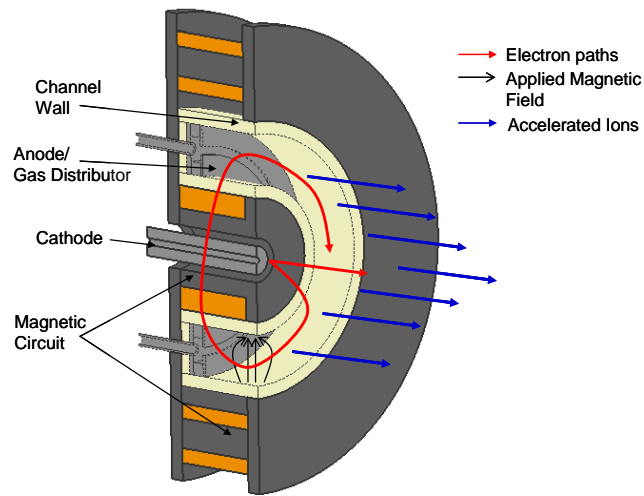


Figure 2-2. Schematic of a typical Hall thruster with major components labeled. Not to scale.

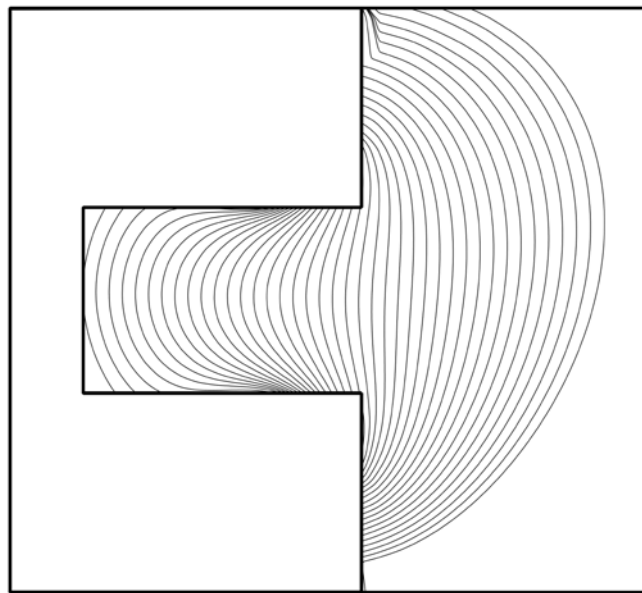


Figure 2-3. Magnetic field topology of the NASA-173Mv1. The curvature inside the discharge channel is referred to as a plasma lens. Image taken from Ref [24].

The channel wall is also an important component of the thruster, and is of particular significance to this dissertation. The wall's primary purpose is to protect the magnetic circuit from the harsh environment of the plasma discharge. However, the properties of the wall can have a large effect on the properties of the discharge; interactions between the wall and the plasma can affect energy losses within the discharge including the electron population responsible for ionization. Furthermore,

these interactions dictate how ions approach the surface, how the wall erodes away, and ultimately how long the thruster will operate prior to failure.

The efficiency of the thruster is defined by Eq. (2-5). Typically this general definition is simplified by neglecting all input power but the discharge power (power to energize magnets is typically 1-2% of the discharge power), as well as the cathode mass flow rate (typically 5-10% of the anode mass flow rate). This results in the often reported “anode efficiency”:

$$\eta_a = \frac{1/2 \dot{m}_a u_e^2}{P_d} = \frac{T^2}{2\dot{m}_a P_d}. \quad (2-6)$$

This gives an overall estimate of the efficiency of the thruster, and can be easily calculated by measuring the thrust at a given operating condition. However, it is advantageous to decompose the anode efficiency into several simpler, more specific efficiencies. A typical model is given in Ref. [27]. This model equates the anode efficiency to the product of five other efficiencies: the mass utilization efficiency, η_m ; the current utilization efficiency, η_b ; the voltage utilization efficiency, η_v ; the charge utilization efficiency, η_q ; and the divergence efficiency, η_d . The mass utilization efficiency is given by

$$\eta_m = \frac{I_d m_{Xe}}{\dot{m}_a e} \frac{I_b}{I_d} \sum_i \frac{\Omega_i}{Z_i}, \quad (2-7)$$

where I_d is the discharge current (equal to the sum of ion and electron currents), m_{Xe} is the mass of a xenon atom, e is the elementary charge, I_b is the ion beam current, Ω_i is the current fraction of ion species i and Z_i is the charge state of ion species i . The mass utilization efficiency is a measure of how effectively the thruster converts the initial anode mass flow into a directed, thrust-producing ion flow. The current utilization efficiency is given by

$$\eta_b = \frac{I_b}{I_d}. \quad (2-8)$$

It is a measure of how much of the discharge current is carried by thrust-producing ions. The voltage utilization efficiency is given by

$$\eta_v = \frac{V_a}{V_d} = 1 - \frac{V_l}{V_d}, \quad (2-9)$$

where V_a is the effective acceleration voltage of ions, V_d is the discharge voltage, and V_l is the loss voltage. Thus the voltage utilization efficiency is a measure of how effectively the discharge voltage is used to accelerate ions. The charge utilization efficiency is defined as

$$\eta_q = \frac{\left(\sum_i \frac{\Omega_i}{\sqrt{Z_i}} \right)^2}{\sum_i \frac{\Omega_i}{Z_i}}, \quad (2-10)$$

and is a measure of the energy loss associated with creating multiply-charged ions within the discharge. Finally, the divergence efficiency is given by

$$\eta_d = \langle \cos \theta_d \rangle^2, \quad (2-11)$$

where θ_d is the plume divergence half-angle. The divergence efficiency is a measure of the loss of thrust due to ion momentum directed in the radial direction rather than the axial direction. These efficiencies will become important when correlating plume properties with discharge channel properties later in the dissertation.

The above description of anatomy, physics and efficiency are all applicable towards Hall thrusters in general. This section will be wrapped up with a brief description of the two main types of Hall thrusters: anode layer thrusters (TAL) and stationary plasma thrusters (SPT).

2.2.2.2 Anode Layer Hall Thruster

The thruster with anode layer, or TAL, is a Hall thruster whose primary characteristics are a conducting channel wall and a channel length that is short compared to the channel width. The channel wall is typically biased to cathode potential to repel electrons and reduce associated energy losses. This leads to larger electron temperatures within the channel, as the electron energy is not regulated by channel wall losses. As a result, the ionization and acceleration zones occur within a thin layer close to the anode, giving the thruster its name.

The secondary electron emission associated with metallic materials is relatively low compared to ceramic materials. Therefore, significant trade between high-energy primary electrons and low-energy secondary electrons at the wall does not occur in this thruster, further leading to high electron temperatures within the discharge. Large sheath

potentials at the walls form due to the potential bias, low secondary electron emission, and large electron temperatures. These sheath potentials can provide significant energy to incoming ions at the wall, making erosion due to ion bombardment a primary concern. However, the primary energy loss mechanism in these devices is at the anode, due to its close proximity to the high-temperature plasma region.

2.2.2.3 Stationary Plasma Hall Thruster

The second type of Hall thruster is the stationary plasma thruster, or SPT. In contrast with the TAL, the SPT has floating ceramic channel walls and a channel length that is long compared to the channel width. Since the channel wall is no longer biased to the cathode potential, energy losses at the wall regulate the electron temperature within these devices, leading to extended ionization and acceleration regions. Consequently, anode power losses are less significant when compared to the TAL since the high-temperature plasma is far downstream of the anode.

Secondary electron emission from the ceramic wall in SPTs is much more prolific and has significant impact on the thruster physics. The exchange of high-energy primary electrons with low-energy secondary electrons affects the electron energy distribution within the discharge, effectively lowering the average electron temperature. Furthermore, the electron emission at the wall strongly affects the resulting wall sheath potentials, which not only regulate the electron energy dynamics but also the energy and angle at which ions approach the wall. All these factors not only affect the performance but also the lifetime of the thruster, since erosion of the channel wall by ion bombardment is a primary concern in SPTs as well.

The subject of this dissertation does not concern TALs, and therefore all mention of Hall thrusters from this point will refer to the SPT. The test article for the study is a 6-kW laboratory model SPT; further details of this thruster can be found in Section 3.2.

2.3 Summary

This chapter described the fundamentals of rocket propulsion, explained the benefits of electron propulsion over traditional chemical propulsion, and introduced the basic anatomy and operation of two major electric propulsion systems, the gridded ion

thruster and Hall thruster. These systems are capable of specific impulses over an order of magnitude higher than chemical systems, allowing them to minimize the required mass of propellant for a given mission.

The plasma-wall interactions within Hall thrusters were identified as a significant factor in thruster performance and efficiency. Various interactions can strongly affect energy losses within the discharge, alter the electron dynamics within the channel, and limit lifetime through erosion. The specifics of these interactions can be highly complex, and are the subject of this dissertation.

Chapter 3

Experimental Apparatus

This chapter describes all experimental apparatus used to obtain the results presented in the remainder of the dissertation. The section begins with a description of all major pieces of hardware, including the vacuum chamber and Hall thruster, and then continues with the mechanical and electrical setup for each probe used in the study. Analysis methods for each diagnostic are also summarized, with the exception of the flush-mounted Langmuir probe; details of the analysis techniques used for this diagnostic are covered in Chapter 4.

3.1 Vacuum Facility

All experimental studies were carried out within the Large Vacuum Test Facility (LVTF) at the Plasmadynamics and Electric Propulsion Laboratory (PEPL). The LVTF is a 6-m-diameter by 9-m-long stainless-steel-clad cylindrical vacuum chamber, equipped with seven CVI model TM-1200 cryopumps as well as liquid-nitrogen-cooled shrouds capable of providing a pumping speed of 245,000 l/s on xenon. Chamber pressure was monitored using two commercially available hot-cathode ionization gauges, one internally-mounted (nude) and one externally-mounted. Reported pressures are obtained by averaging the two gauge readings, which has given chamber pressures consistent with pumping capabilities. Base pressures of 7×10^{-7} torr were routinely achieved, and at a total mass flow rate of 21.4 mg/s, the facility pressure was 1.5×10^{-5} torr, corrected for xenon.

The chamber also contains two large linear stages for movement in the axial and radial directions of the thruster. These stages have stepper motors that are actuated with a commercially available motor controller, and are controlled remotely using either National Instruments Measurement and Automation Explorer or Labview. The “axial”

stage has a range capability of 0.9 m while the “radial” stage has a range capability of 1.5 m. Both stages are capable of placement accuracies better than 0.1mm.

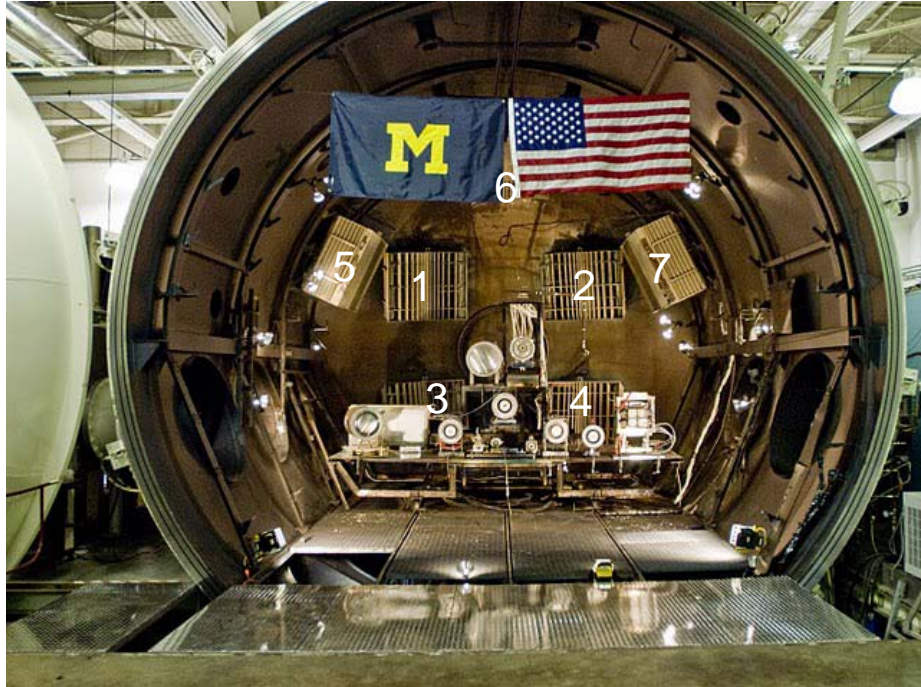


Figure 3-1. Photograph of the LVTF with the endcap removed. All seven cryopump shrouds are visible and numbered. Taken by Robert Lobbia.

3.2 Hall Thruster

The test article used in this work is a 6-kW laboratory model Hall thruster with an approximate throttling range of 100-600 mN thrust, 1000-3000 s specific impulse, and 1-10 kW discharge power. This thruster has been well documented and has undergone extensive performance and probe testing [13,14,28-34]. The magnetic circuit is comprised of a single inner coil, eight outer coils, and an inner trim coil. Magnetic field settings at each operating condition were chosen to maximize anode efficiency, given a symmetric vacuum magnetic field about channel centerline. The trim coil was not energized during any of the studies presented here.

Research-grade xenon propellant (99.999% pure) was supplied using commercially available controllers with an accuracy of $\pm 1\%$ full scale. These controllers were calibrated prior to the experiment using a constant volume method that corrected for compressibility effects. The flow rate through the thruster’s center-mounted LaB_6

cathode [31] was maintained at 7% of the anode mass flow rate for all operating conditions presented.

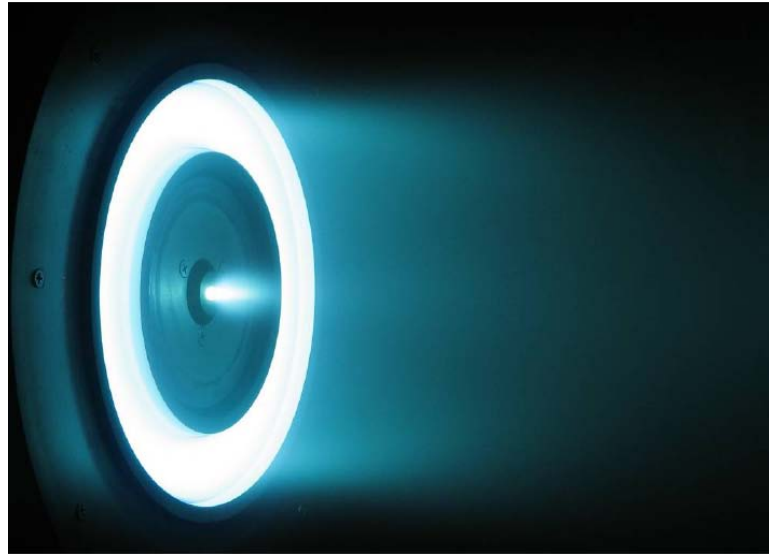


Figure 3-2. Photograph of the 6-kW laboratory Hall thruster, operating on xenon at 300 V and 20 mg/s anode flow rate. Taken from Ref. [13].

The discharge was sustained with a 100-kW power supply capable of outputting 1000 V (with a 400 mV_{rms} ripple) and 100 A. Separate supplies were used to power the magnets, as well as the cathode keeper and heater. The power supplies for the heater and keeper were only used for initial thruster startup, and were turned off during steady-state operation and all subsequent data collection.

The discharge circuit included a single 95- μ F capacitor in parallel with the anode and cathode to filter out high-frequency oscillations. Discharge voltage was monitored across the capacitor using a high-precision digital multimeter. The time-averaged discharge current was measured across a 10-m Ω current shunt placed in series with the circuit on the cathode (low potential) side. Measured discharge currents did not exceed 40 A, which is within the 50-A rating of the current shunt. The time-dependent discharge current was measured across a magneto-resistive current sensor (F.W. Bell NT-50) placed in line with the 10-m Ω current shunt. The 100-kHz bandwidth of this sensor is sufficient to resolve the typical “breathing mode” oscillations found within Hall thrusters, occurring at frequencies on the order of 10 kHz.

The discharge channel is segmented, and includes replaceable “erosion rings” at the end of the channel to facilitate lifetime studies. For the study using internal wall-

mounted probes, a new set of erosion rings were fabricated in order to avoid unnecessary alterations to the original rings. The new rings were machined with a linear chamfer to mimic the erosion pattern present after approximately 334 hours of operation at an average discharge power of 4.6 kW. This was done to match geometries with the original rings such that prior internal measurements could be compared to the present study [13]. Previous studies have shown that pre-machined erosion geometries can give consistent thruster performance to within approximately 2% of the performance at the target point in life [35]. The erosion profile was measured using a MicroVal coordinate measuring system with a ruby ball point probe. Due to the low number of operation hours, a linear chamfer provided an excellent approximation to the erosion profile, with differences not exceeding 250 μm (see Figure 3-3). Prior to the study, the thruster was operated with these rings at the nominal operating condition of 300 V and 20 mg/s anode flow rate until the discharge current and oscillations settled to values that were observed with the original rings, which occurred after approximately two hours.

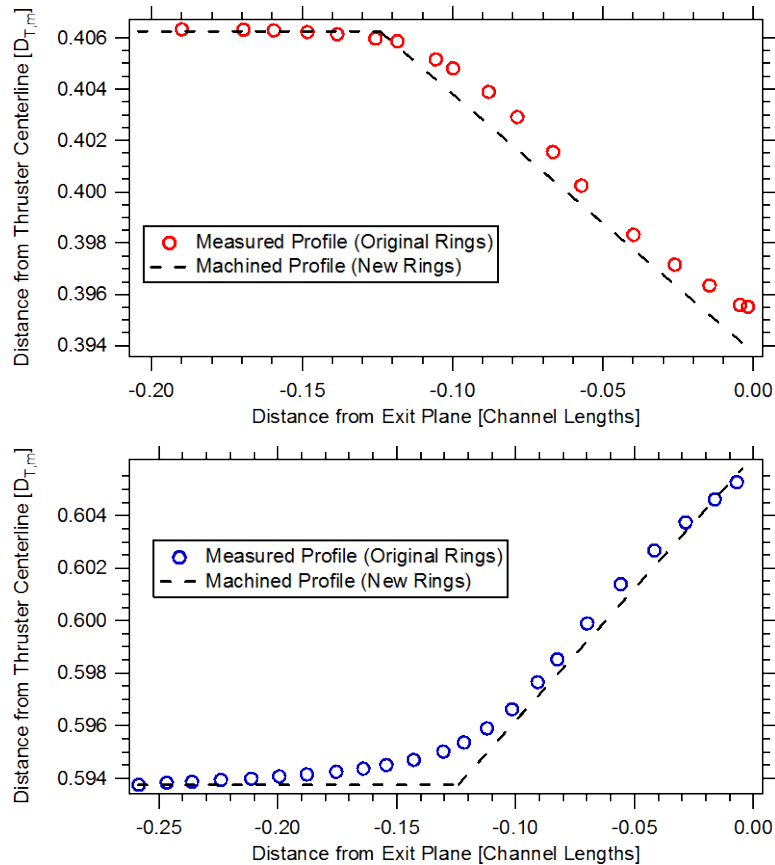


Figure 3-3. Comparison of measured profiles on the original erosion rings with the linear chamfer machined into the new rings (top: inner channel ring; bottom: outer channel ring).

3.3 Thrust Stand

A thrust stand was used to determine the proper magnetic field strength that optimizes the thruster anode efficiency, given by Eq. (2-6). The thrust stand that was used is a NASA Glenn Research Center (GRC) inverted-pendulum design [36,37]. To minimize changes in measured thrust due to thermal expansion of the thrust stand, the shroud, coils, and thruster mount were cooled using a closed-loop refrigeration system (see Figure 3-4).



Figure 3-4. Photograph of the inverted-pendulum thrust stand with water-cooled shroud.

As thrust is produced, the inverted pendulum deflects and this displacement is converted into a voltage signal with a linear voltage displacement transducer (LVDT). The thrust stand electronics take this voltage signal and output the necessary current to the null coil to provide the restoring force required to return the pendulum to its rest position. This technique requires a feedback loop that is controlled using a proportional integral differential (PID) circuit. The final required current to the null coil is proportional to the thrust produced, and was monitored using a high-precision digital multimeter and mechanical “strip chart” plotter.

The thrust stand was calibrated using a series of weights approximately 28.8 g in mass that provided incremental increases in applied force through a low-friction wheel that converted the weights of the masses into a horizontal force on the thrust stand.

Calibrations were first performed in a forward manner by adding each mass successively, followed by a reverse manner where they were removed successively. These calibrations were found to be highly linear and repeatable.

The largest source of uncertainty was found to be the drift of the “zero” thrust value due to the thermal expansion/contraction of the thrust stand. This was characterized by occasionally turning off the thruster (typically while switching operating conditions, once every hour) and noting the new zero with time. The thrust stand inclination, whose drift can also affect thrust stand measurements, was continually monitored and kept constant while data were being collected. Uncertainties in thrust measurements are estimated to be ± 2 mN. Additional details on the thrust stand operation and design can be found in Ref. [13].

3.4 HARP

Internal and near-field measurements typically require rapid injection and removal of probes to increase survivability in the harsh plasma environment. This is accomplished with the High-speed Axial Reciprocating Probe, or HARP. The HARP has been used extensively at PEPL for internal studies [10,11,13], and is capable of accelerations around 70 m/s^2 and velocities up to 2.5 m/s [38]. For this study, the maximum velocity was fixed at approximately 1.8 m/s to minimize the residence time within the plume and increase probe survivability. Dwell times between injection and retraction were held to within 60 ms.

The use of the HARP in this work is limited to near-field current density measurements. Thus, the HARP was oriented such that the direction of motion was normal to the thruster firing axis, while the thruster was placed on the axial stage of LVTF. This configuration allowed radial sweeps to be taken at several axial locations. The HARP was placed on top of a rigid “A-frame” support structure that connected the HARP to the vacuum chamber wall and floor with several steel extrusions. This prevented the HARP from significantly shifting due to the forceful probe reciprocation.

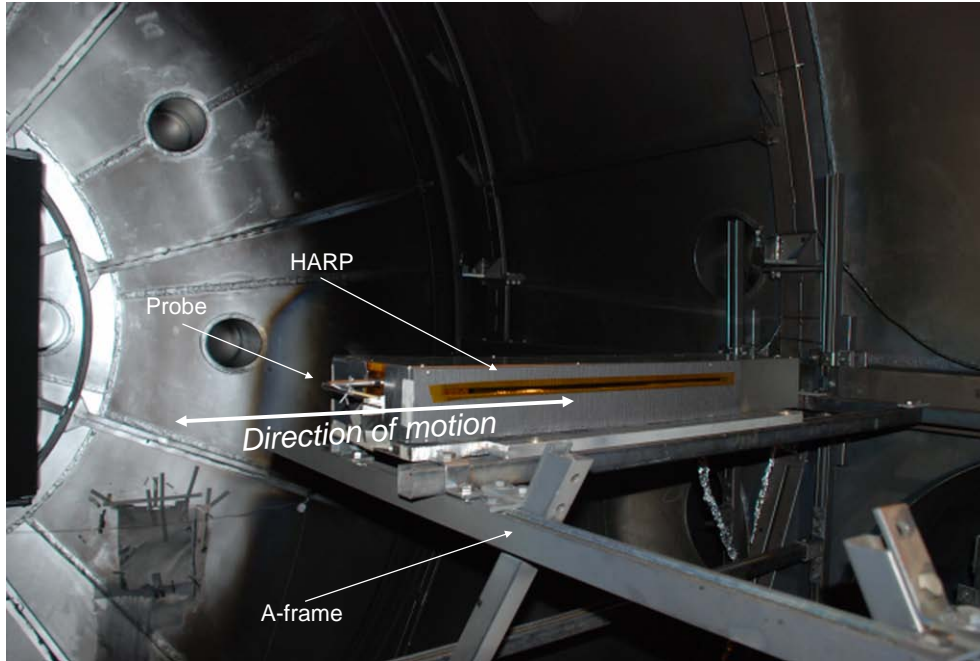


Figure 3-5. Photograph of the HARP on top of the A-frame within LVTF.

3.5 Helmholtz Coil

In order to facilitate studies of magnetic field effects on flush-mounted Langmuir probe data, a Helmholtz coil was designed and fabricated to produce a uniform, well-characterized magnetic field. A coupon probe, described in Section 3.6.1, was placed within the test section of the Helmholtz coil and subjected to various magnetic field magnitudes and orientations. The coil was designed using the simulation program MagNet; each coil consisted of 200 turns of 13-AWG magnet wire wrapped around aluminum spools. In order for plasma to adequately reach the test section, each spool was made hollow with an inner diameter of approximately 5 cm. The coils were held in place using commercially available aluminum extrusions, and had a separation distance of 18.5 mm (see Figure 3-6). A 350-W power supply was used to energize the coils, while a digital multimeter placed in series was used to monitor the supplied current.

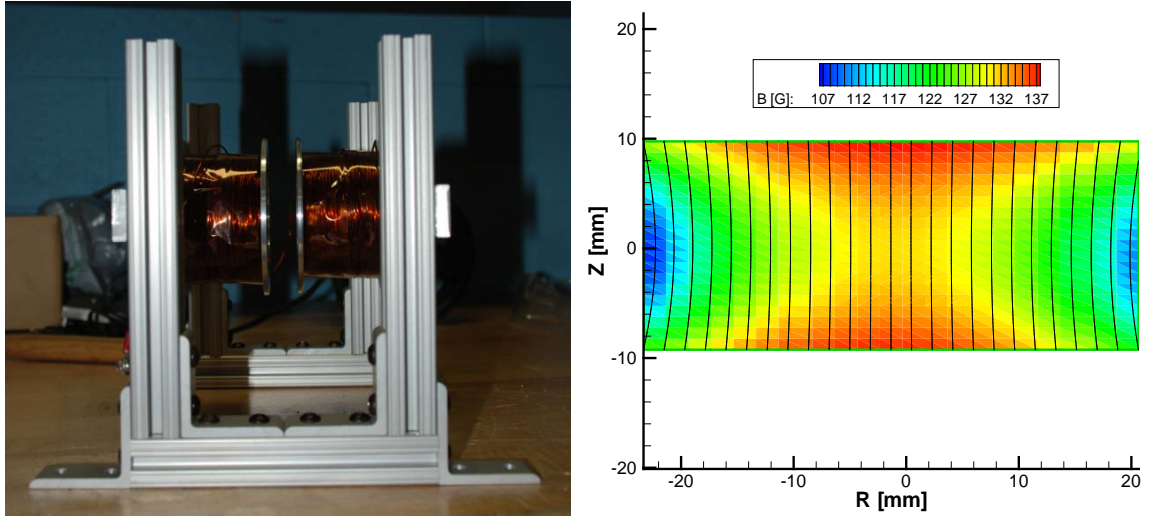


Figure 3-6. Left: Side-view of the Helmholtz coil and support structure. Test section is in the center of the two coils. Right: Measured magnetic field contours of the test section with 5 A coil current.

A 3-axis gaussmeter was used to map the magnetic field along the center plane at several current levels. The ambient magnetic field map was measured and later subtracted out of subsequent data sets. Figure 3-6 shows the test section of the Helmholtz coil as well as the magnetic field map at 5 A of supplied current. A calibration curve was generated for the magnetic field strength at the center of the test section and used to determine the required current for each data point tested. The magnetic field generated was approximately 26 gauss (G) per ampere (A) at the test section center. Magnetic field strengths in excess of 200 G were achieved before the coils began to overheat, which was deemed sufficient for the study.

The coil was placed 3 m downstream of the 6-kW Hall thruster, at an angle of 14° from thruster centerline. The entire assembly was rotated such that the Helmholtz coil axis was aligned with the ion flow, based on a point-source approximation emanating from the thruster center (see Figure 3-7). While this restricted independent control over magnetic field and ion flow orientation, it allowed for constant exposure of the Helmholtz coil test section to plasma. Furthermore, by aligning the ion flow and magnetic field, resistance of the flow through the coil was minimized; had the flow been forced to cross magnetic field lines, strong electric fields may have been created that would lead to undesirable, uncontrolled conditions within the test section.

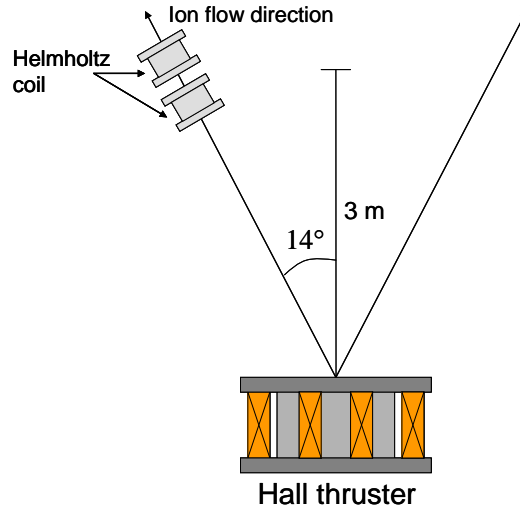


Figure 3-7. Schematic showing the position and orientation of the Helmholtz coil relative to the 6-kW Hall thruster. Not to scale.

3.6 Flush-mounted Langmuir Probe

This section describes the mechanical and electrical setup of the various flush-mounted Langmuir probes used in this work. Three types of probes are included: the coupon probe, which was used for studies on magnetic field effects; the external tab probe, which was used for studies on analysis techniques of flush probes; and the internal wall-mounted probe, which was used for measurement of erosion-relevant properties within the Hall thruster channel.

3.6.1 Coupon Probe

The coupon probe is a flush-mounted Langmuir probe used with the Helmholtz coil for studies of magnetic field effects on measured plasma properties. It was comprised of a tungsten wire 0.5 mm in diameter flush-mounted in the center of a 2.54-cm-diameter boron nitride disc. The probe was insulated and held in place with high-temperature ceramabond (Omega CC HIGH TEMP). The disc was mounted onto an alumina post and mated to a rotational stage with a stainless steel collar (see Figure 3-8). This entire assembly was integrated with the Helmholtz coil such that the probe was in the center of the test section. The probe was mounted such that the position of the face coincided with the axis of rotation. This ensured the probe moved minimally while testing different magnetic field orientations.

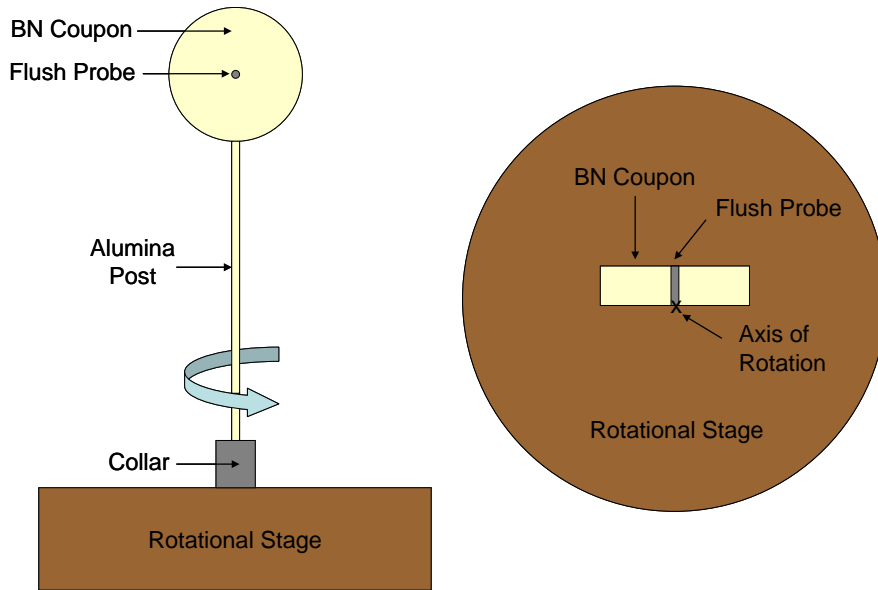


Figure 3-8. Schematic of the coupon probe assembly. Rotation of the probe allows for magnetic field orientation changes.

The probe was operated with a Keithley 2410 sourcemeter that sourced the desired voltage and measured the collected current. Data were collected and stored automatically using Labview. Figure 3-9 shows a representative Langmuir probe trace taken with the coupon probe, illustrating the absence of large current oscillations. Thus, due to the quiescent nature of the plasma in the far-field plume, only one Langmuir probe trace was necessary at each magnetic field configuration tested.

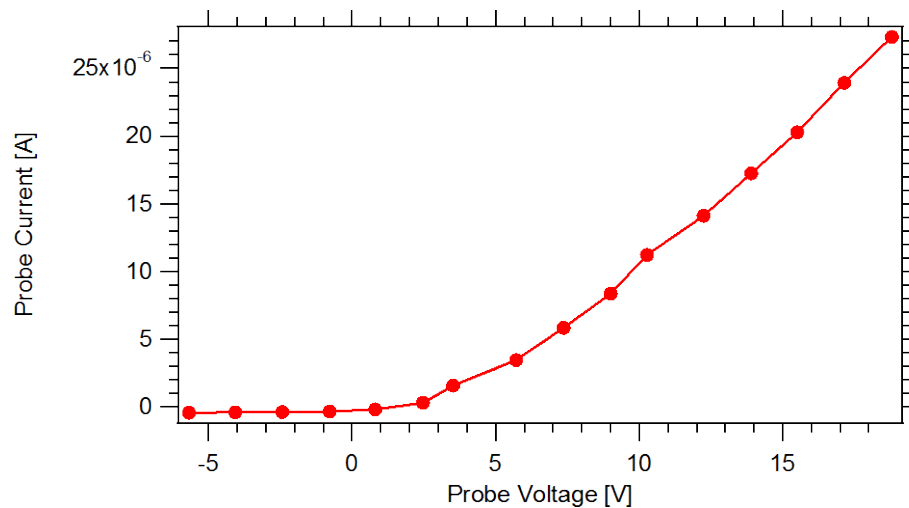


Figure 3-9. Representative Langmuir probe I-V characteristic taken with the coupon probe.

3.6.2 External Tab Probe

In order to obtain a data set representative of the internal Hall thruster environment, an external tab probe was designed and implemented to facilitate studies on analysis techniques for flush-mounted Langmuir probes. The final design is comprised of a 0.381-mm-diameter tungsten wire placed inside a 1.6-mm-diameter alumina tube. This assembly was then inserted into a semi-circular boron nitride (HP grade, from Saint-Gobain) tab such that the tungsten wire was flush with the tab surface (see Figure 3-10). The probe was held in place with a high-temperature ceramabond (Omega CC HIGH TEMP).

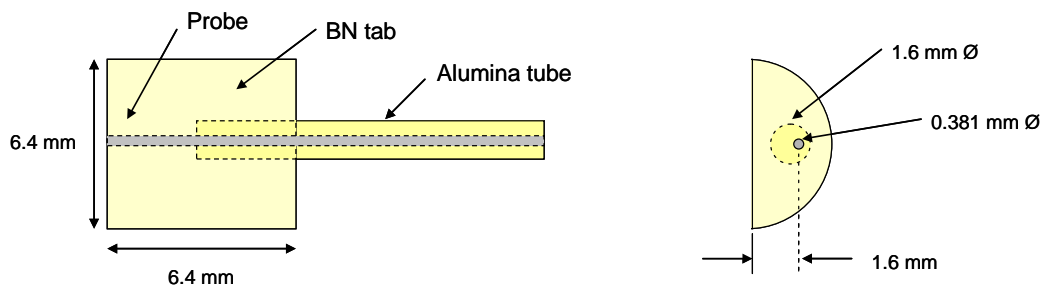


Figure 3-10. Schematic of external tab probe design. Not to scale.

The probe was mounted onto the 6-kW Hall thruster using a stainless steel block and clamp, such that the flat portion of the tab lay adjacent to the thruster exit plane (see Figure 3-11). The final position of the probe was approximately 1.6 mm from the thruster exit plane and 1 mm radially recessed from the outer channel wall. This position was found to be representative of the magnetic field conditions expected internally near the exit plane of the thruster.

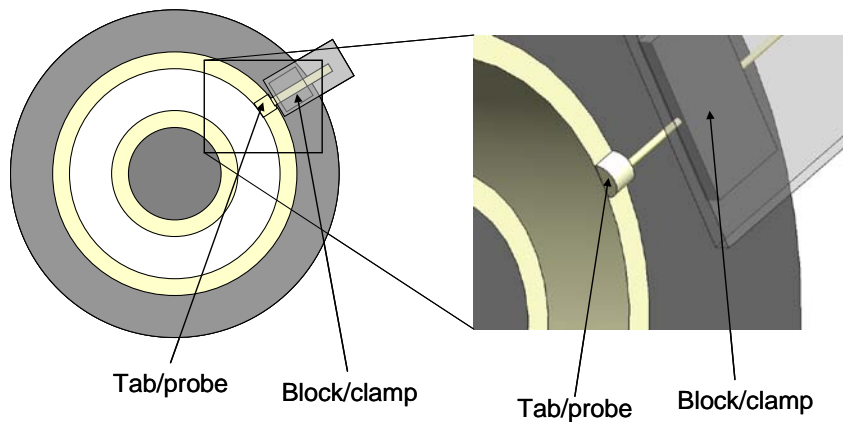


Figure 3-11. Schematic of the external tab probe placement relative to the 6-kW Hall thruster. Not to scale.

Probe current and voltage were collected and stored using a data acquisition system (DAQ) capable of a 500-kHz scan rate across all channels. Figure 3-12 shows a schematic of the measurement circuit used for the Langmuir probe. A function generator was connected to a bipolar power supply that supplied the desired voltage waveform to the probe. The current shunt was comprised of a single 100- Ω thin-film resistor, while the voltage divider used to measure the applied voltage was comprised of 8.18-M Ω and 0.24-M Ω thin-film resistors. The signals were isolated from the DAQ with voltage-following isolation amplifiers, each having a bandwidth of 20 kHz. Blocking diodes were placed in parallel with the current shunt in order to protect the isolation amplifier from large current spikes.

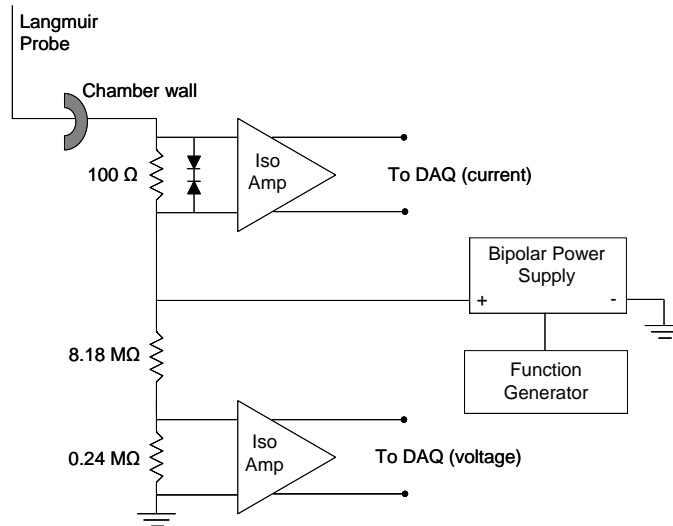


Figure 3-12. Electrical diagram of the data collection circuit used with the external tab probe.

The circuit was calibrated at DC prior to the study, and displayed excellent linearity. The probe was biased using a symmetric triangle wave with a frequency of 20-30 Hz, which is well within the bandwidth of the isolation amplifiers. Each channel was scanned at 40-50 kHz, resulting in approximately 1000 points per I-V characteristic. Capacitive effects were characterized by taking data with no plasma present, and were subtracted out in post processing. Two hundred traces were taken at each operating condition and averaged before any data analysis was performed. Figure 3-13 shows a representative Langmuir probe trace taken with the external tab probe, illustrating the low level of current oscillations in the trace after averaging is performed.

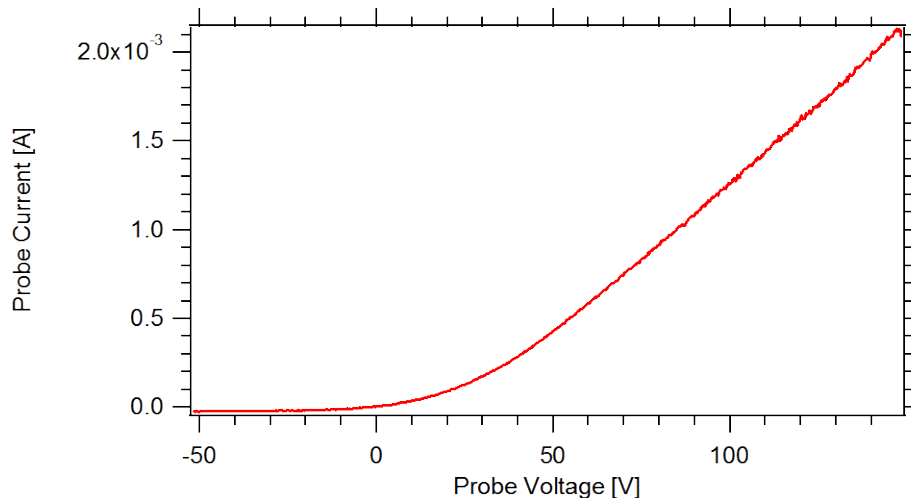


Figure 3-13. Representative Langmuir probe I-V characteristic taken with the external tab probe at 300 V and 20 mg/s anode flow rate.

3.6.3 Internal Wall-mounted Probe

The internal wall-mounted probe is the primary diagnostic of this work, and was used to measure various properties of the plasma near the channel walls of the 6-kW Hall thruster. The final design consisted of five Langmuir probes flush-mounted into each erosion ring (see Figure 3-14). Pure tungsten wire (from Scientific Instrument Services, Inc.) approximately 0.36 ± 0.025 mm in diameter was used for the probe tips. These tips were sanded down to flatten the surface and then inserted into holes within the ring until flush. High-temperature ceramabond (Aremco 813-A) was used to hold the probes in place as well as provide insulation for the first few millimeters of the lead wires. The alumina-based ceramabond was chosen based on its excellent ability to bond boron nitride to tungsten, as well as its maximum rated temperature of over 1900 K. The remaining lead wires were insulated with high-strength fiberglass cloth tape until they were sufficiently beyond the thruster body to avoid large heat loads. The lead wires for the probes on the inner wall were routed to the back of the thruster through the central opening within the inner core used to place the cathode. Ceramic beads were used as extra insulation for portions of the wire in close proximity to the cathode keeper. During operation, there were no noticeable changes to cathode behavior, and insulation of the probe wires was maintained throughout the study.

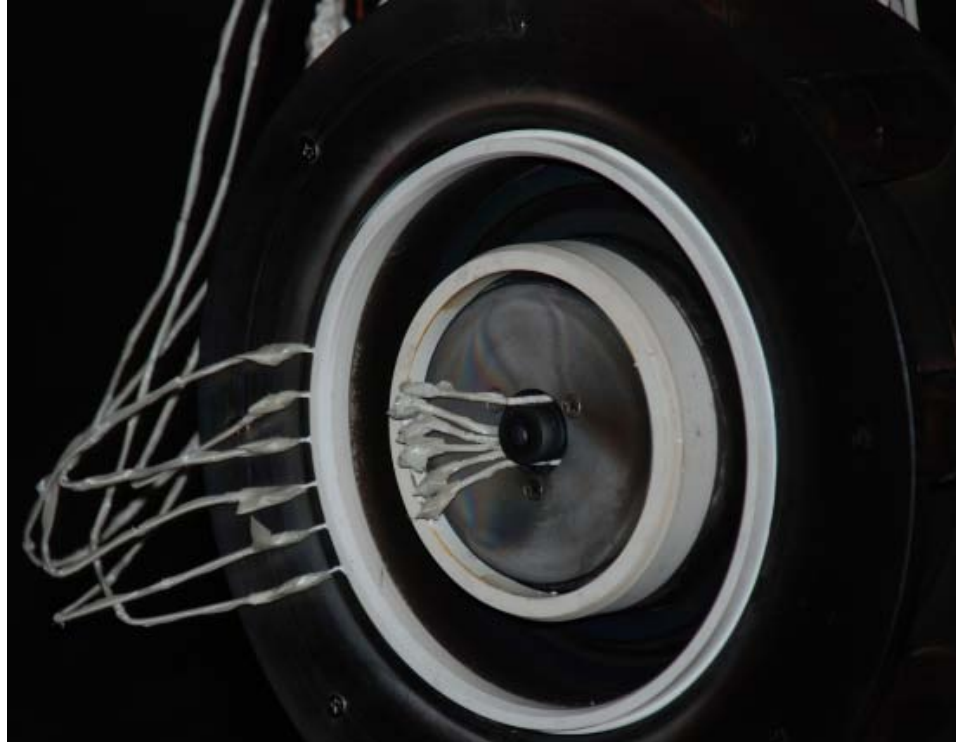


Figure 3-14. Photograph of the internal wall-mounted Langmuir probes installed into each erosion ring on the 6-kW Hall thruster.

Figure 3-15 shows the axial locations of each probe with respect to the thruster exit plane. Since the study was focused on properties relevant to wall erosion, most of the probes were placed close to the exit plane along the chamfer. The probes were spaced azimuthally nine degrees apart to avoid probe-to-probe interactions [15] and facilitate ease of installation (see Figure 3-16). Furthermore, the inner and outer erosion rings were offset azimuthally in order to avoid possible probe-to-probe interactions along magnetic field lines. A sixth probe was placed in each ring to serve as a null probe to characterize capacitive effects [39]. This probe was inserted into a blind hole in order to ensure complete isolation from the channel.

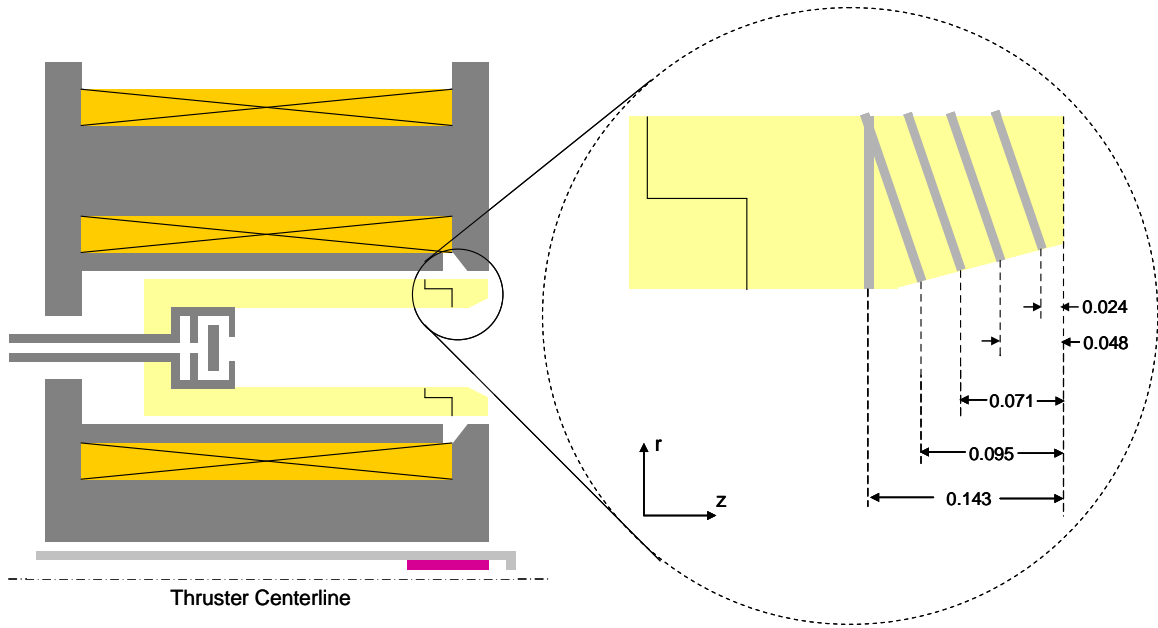


Figure 3-15. Schematic showing the locations of each probe relative to the thruster exit plane. Distances are given in units of channel lengths. Not to scale.

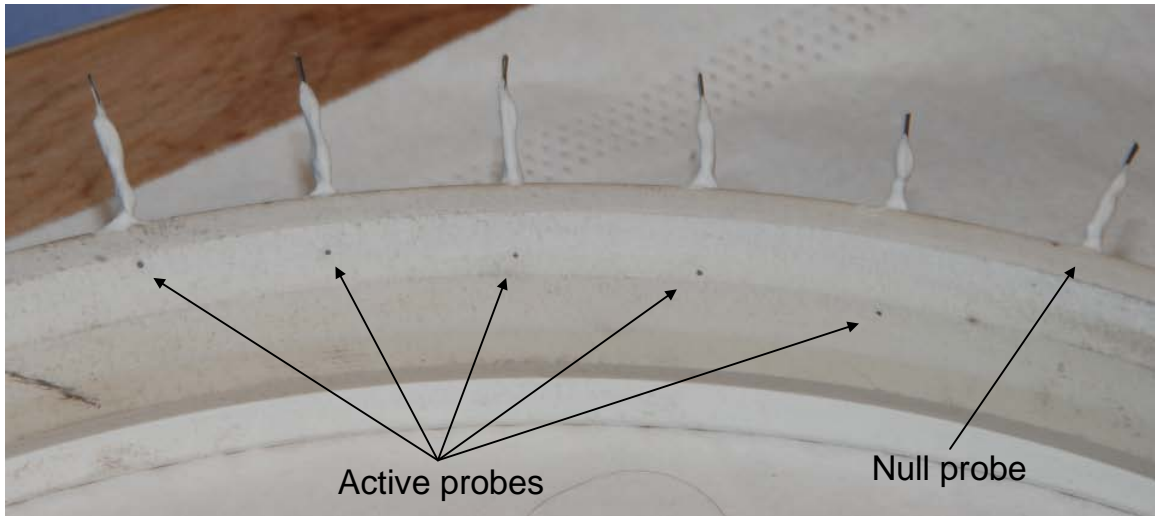


Figure 3-16. Photograph depicting the azimuthal spacing of the wall-mounted probes on the outer erosion ring. The null probe has no exposed area and is only used to characterize capacitive effects.

Since direct comparisons between inner and outer wall probes were desired, a measurement circuit was fabricated that allowed both probes to be run simultaneously. Figure 3-17 shows a schematic of the circuit used to monitor probe voltage and current. Due to the presence of the null probes, four probes needed to be used at once. The current for each probe was measured using a 100- Ω , 500-mW thin-film resistor, while the voltage was monitored using a voltage divider comprised of 10-M Ω and 0.24-M Ω thin-

film resistors. Each signal was isolated from the data acquisition system (DAQ) using voltage-following isolation amplifiers with a bandwidth of 20 kHz. Blocking diodes were used in parallel with the current shunts in order to protect the isolation amplifiers from large current spikes.

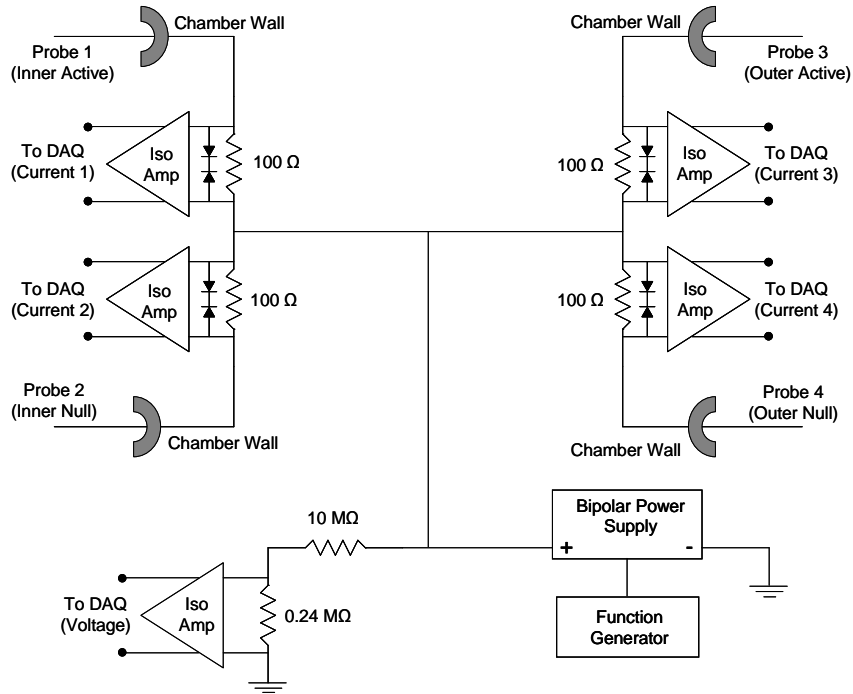


Figure 3-17. Electrical diagram of the measurement circuit used with the internal wall-mounted probes. Measurements were taken at the inner and outer wall simultaneously at each axial location.

The circuit was calibrated at DC prior to and following the study and displayed excellent linearity and repeatability. The probes were operated with a bipolar power supply connected to a function generator. Voltage on the probes was applied using a symmetric triangle wave at a frequency of 20 Hz, which is well within the bandwidth of the isolation amplifiers. Data were collected and stored using an 8-channel DAQ capable of scanning at 2 MHz across each channel. For this study, the scan rate was maintained at 40 kHz per channel, resulting in approximately 1000 data points per I-V characteristic. Two hundred characteristics were taken per probe, per operating condition, and averaged before any analysis was performed. Figure 3-18 shows representative Langmuir probe traces from both inner and outer internal wall-mounted probes, indicating the low level of current oscillations after averaging is performed.

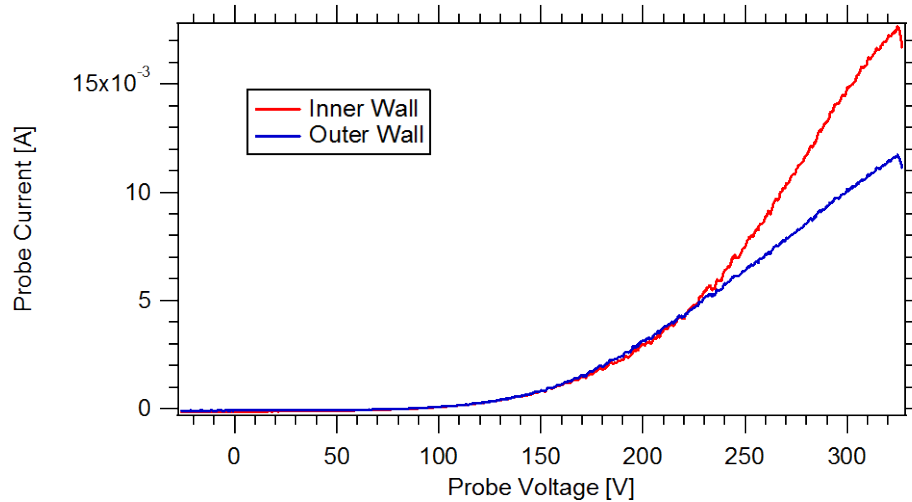


Figure 3-18. Representative Langmuir probe I-V characteristics taken with the internal wall-mounted probes at 300 V and 20 mg/s anode flow rate, at $z = -0.071$ channel lengths from the exit plane.

3.7 Emissive Probe

As part of the study on analysis techniques for flush-mounted probes, an emissive probe was used as a comparative diagnostic that provides a highly accurate measurement of the local plasma potential. While two types of emissive probes are presented here, the floating emissive probe is only briefly discussed as it is not used in this work.

3.7.1 Floating Emissive Probe

The floating emissive probe [40] is the predominant diagnostic used to measure the local plasma potential internally and in the near-field plume of Hall thrusters, and has been used extensively at PEPL with the HARP [10,11,13]. It is a more attractive option than Langmuir probes for measuring plasma potential because it is largely insensitive to the presence of flowing plasma, magnetic fields, and large-amplitude oscillations [41], all of which are present within a Hall thruster. The floating emissive probe also does not require any sweeping of applied voltage, which facilitates rapid measurements to be taken.

Typical floating emissive probes consist of a thin filament that is heated up, usually with applied current, to the point it emits electrons thermionically. As the filament temperature and resulting emission increases, the floating potential of the probe also increases; thermionic emission acts as additional positive current to the probe, thus

reducing the sheath potential (difference between plasma and floating potentials) required for the probe to draw a net zero current. If the emission is strong enough, the floating potential will approach the local plasma potential. However, the thermionic emission required for this to occur in Hall thruster plasmas is quite large, and results in significant space charge effects.

The presence of space-charge effects complicates the use of floating emissive probes and interpretation of the resulting data. Sheath models can be used to calculate the plasma potential from the experimental data, but they usually require the local electron temperature [42]. Thus, a Langmuir probe must be used as well in order to correct for space charge effects. Furthermore, the use of such sheath models can lead to measurement uncertainties on the order of the electron temperature [11]; these uncertainties can be 10% or greater for electron temperatures of 10 – 30 eV and plasma potentials of 100 – 300 V, which are typical values within a 300 V discharge [10,11,13]. Due to these complications, the swept emissive probe was used in this work.

3.7.2 Swept Emissive Probe

Since an independent, highly accurate measurement of plasma potential was desired, the swept emissive probe [41] was used in this work. While this diagnostic is more difficult to implement than the floating emissive probe, the added complexity was minimized due to the stationary nature of the probe during the study. The swept emissive probe is operated like a Langmuir probe: the probe is biased to a range of voltages and the resulting current to the probe is monitored. However, the probe is structured like a floating emissive probe, so that it is capable of thermionic emission. Current-voltage characteristics are taken at various levels of thermionic emission. Once the probe is biased above the local plasma potential, the low-energy (< 0.1 eV) electrons emitted from the probe cannot climb the potential hill formed in the sheath. Thus, all thermionically-emitted electrons return to the probe, nullifying the effects of emission on the I-V characteristic [41]. Therefore, the probe voltage at which all I-V characteristics become identical (to within the noise level) is taken as the local plasma potential. Due to the noise level of the data, uncertainties in plasma potential were estimated at ± 3 V under almost all operating conditions tested; at 600 V discharge voltage and 10 mg/s anode flow rate, the uncertainty increased to ± 15 V due to increased noise levels.

The swept emissive probe mechanical design is based primarily on those from Haas [10], and subsequent modifications by Linnell and Reid [11,13]. A 0.127-mm-diameter filament made of 1% thoriaated tungsten was placed within a 1.6-mm-diameter double-bored alumina tube. Thoriaated tungsten was chosen as the filament material due to its higher emission capabilities; this translates to a lower operating temperature for the required emission currents, thus bringing the filament further away from its melting point. The filament was bent into a loop with a 0.5-mm radius of curvature, and brought into contact with 0.254-mm-diameter copper lead wires. Tungsten filler wires were then placed inside the tube to provide a tight fit between the filament and leads, as well as excellent electrical contact (see Figure 3-19). The probe was mounted to the thruster using a stainless steel block and clamp, similar to the external tab probe. The final position of the probe tip was approximately 1.4 mm from the outer wall radius, and 2.6 mm beyond the exit plane, which was within 1 mm of the location of the external tab probe.

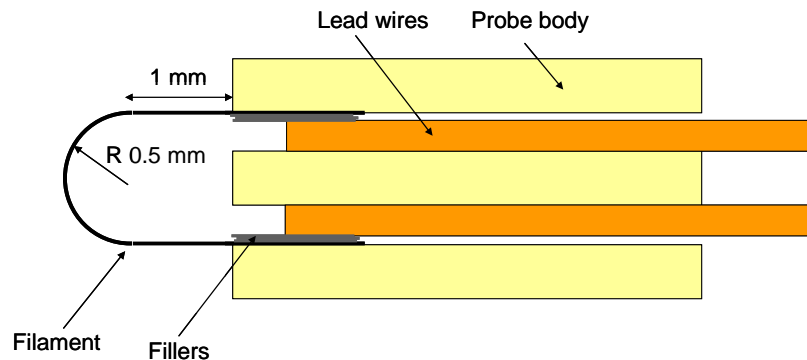


Figure 3-19. Schematic of the mechanical design of the swept emissive probe. Not to scale.

Due to the nature of the swept emissive probe, data were collected in a similar manner to the external tab probe. The probe was biased with a function generator connected to a bipolar power supply, while a floating power supply was used to provide the filament current required for thermionic emission (see Figure 3-20). The floating power supply was isolated from ground by placing an isolation transformer in series with the supplied AC power, and disconnecting the ground line from the back panel of the power supply. A 100- Ω thin-film resistor was used to measure probe current, while probe voltage was measured with a voltage divider comprised of 8.18 and 0.24-M Ω thin-film resistors. Probe current and voltage were collected and stored using a data

acquisition system (DAQ) that scanned each channel at 40 kHz. The DAQ was isolated from each signal using voltage-following isolation amplifiers with a bandwidth of 20 kHz. Blocking diodes were placed in parallel with the current shunt to protect the isolation amplifier from large current spikes.

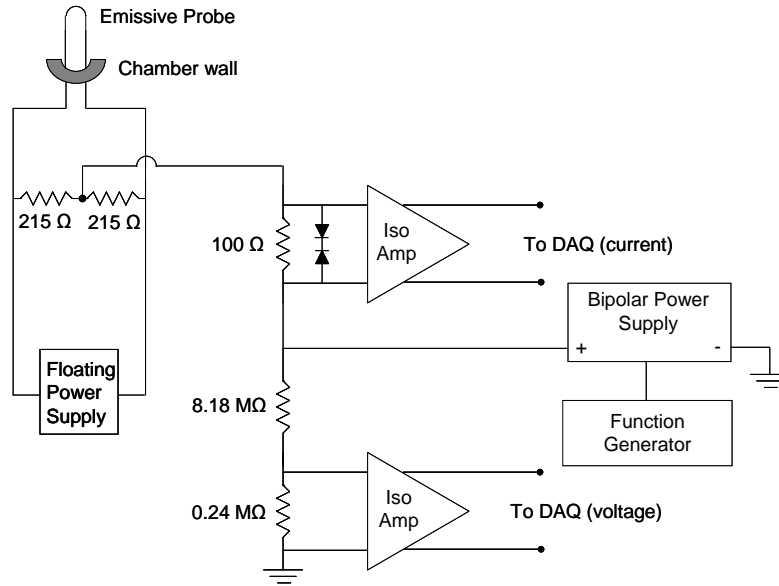


Figure 3-20. Electrical diagram of the measurement circuit for the swept emissive probe.

The circuit was calibrated at DC prior to the study, and displayed excellent linearity. The filament current was slowly increased from zero while the filament was optically monitored. Once the probe showed noticeable signs of emission, I-V characteristics were taken at 2-3 different levels of emission current. A characteristic was taken at zero filament current as well. The probe was biased using a symmetric triangle wave with a frequency of 20 Hz, resulting in approximately 1000 points per I-V characteristic. The probe bias was applied in between a voltage divider placed in parallel with the filament. This voltage divider was comprised of two 215-Ω thin-film resistors and was used to apply probe bias at the center of the filament where most emission should occur [41]. This was done to minimize uncertainties associated with the voltage drop across the filament, which was typically 5 – 10 V. Capacitive effects were characterized by taking data with no plasma present, and were subtracted out in post processing. Furthermore, the voltage drop across the current shunt was taken into account in data analysis when determining probe bias. While this correction is usually negligible, enough current was drawn by the probe to significantly affect a measurement

that would otherwise have uncertainties of only a few volts. Two hundred traces were taken at each operating condition and averaged before any data analysis was performed.

3.8 Near-field Faraday Probe

In order to correlate the internal plasma characteristics of a Hall thruster to those in the plume, measurements of ion beam current and plume divergence are necessary. This was accomplished by using a near-field Faraday probe to measure the ion current density distributions close to the thruster exit plane. Such a diagnostic has been used successfully in the past [13,43,44] to measure beam currents while minimizing facility-induced effects that far-field Faraday probes can be prone to.

The mechanical design of the Faraday probe in this work is derived from the probe used by Reid [13]. A 4.8-mm-diameter molybdenum disc was joined with a 1.6-mm-diameter tungsten rod through an interference “press” fit (see Figure 3-21). The materials were selected based on their low secondary electron emission coefficients [45,46]; significant emission would confound the current measurement and lead to increased uncertainties. The tungsten rod was placed within an alumina tube and held in place using high-temperature ceramabond (Aremco 813-A). The sides and back of the disc were then insulated using the same ceramabond to prevent excess current from being collected on these surfaces. The thickness of the ceramabond layer on the sides of the disc was approximately 100 μm , and thus did not significantly add to the cross-section of the probe. No guard ring was used in this design due to the impractical gap size required at distances close to the thruster exit plane (< 0.1 mm). The probe was placed within a stainless steel tube 9.5 mm in diameter and held in place using six set screws (see Figure 3-22).

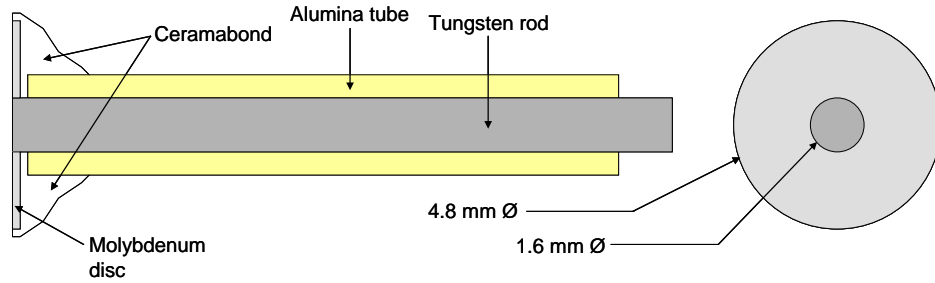


Figure 3-21. Schematic of the near-field Faraday probe used to measure ion current density. Ceramabond was used to insulate the sides and back of the probe. Not to scale.

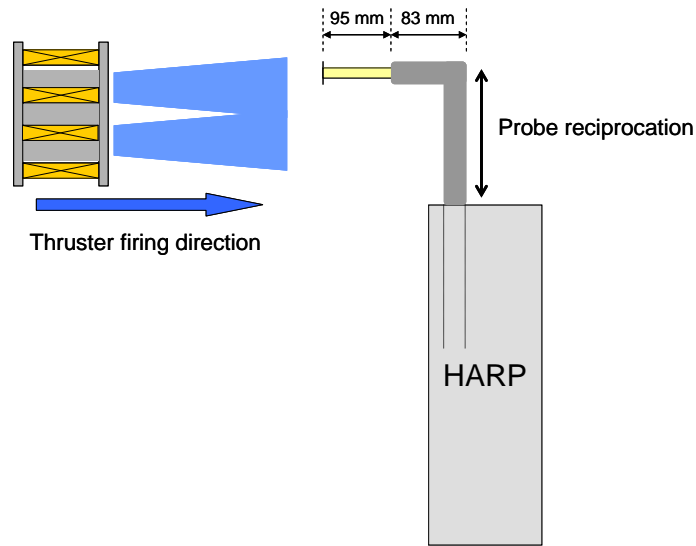


Figure 3-22. Schematic of the near-field Faraday probe within the stainless steel tube placed on the HARP. Not to scale.

Probe current was collected using a 47- Ω , 500-mW thin-film resistor, and the probe was biased approximately 60 V below ground using a commercially available power supply (see Figure 3-23). This bias was typically 70 – 80 V below the local plasma potential, and was sufficient to repel electrons (with electron temperature around 10 eV) from the probe [13,44]. The signal was sent to a 14-bit data acquisition system (DAQ) capable of a total scan rate of 500 kHz. The DAQ was isolated from the signal using a voltage-following isolation amplifier with a bandwidth of 100 kHz. The circuit was calibrated at DC both prior to and following the study, and exhibited excellent linearity and repeatability.

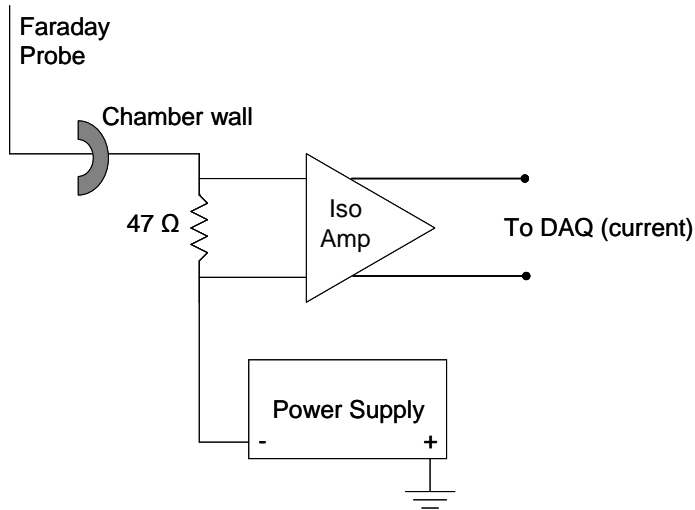


Figure 3-23. Electrical diagram of the measurement circuit for the near-field Faraday probe.

The current signal from the probe was monitored along with the probe position and time-dependent discharge current during each injection with the HARP. The discharge current was monitored to verify acceptable perturbations to the thruster during probe injection and removal. Data were sampled at 100 kHz per channel to adequately resolve the 10-30 kHz thruster oscillations.

Data were collected every 5 mm in the axial direction, from $0.188 - 2.0 D_{T,m}$ (mean thruster diameters) downstream of the thruster exit plane. The probe was injected radially into the plume at each of these axial locations, extending from $2.95 D_{T,m}$ to $-0.219 D_{T,m}$ (past thruster centerline). Data collection was triggered by monitoring the HARP position signal; because this resulted in a slightly truncated injection sweep as the probe began to move, only the retraction portion of the data was analyzed. Symmetry was assumed about the thruster centerline during data reduction and analysis.

Prior to analysis, the data were smoothed using boxcar averaging with a 1-mm window. Data analysis techniques largely followed those outlined by Reid [13]. Beam current was calculated at each axial location by integrating the current density profile at each axial location assuming cylindrical symmetry:

$$I_b = 2\pi \int_{r_1}^{r_2} j_b r dr. \quad (3-1)$$

The bounds r_1 and r_2 were chosen based on the locations where the current density fell to $(1/e)$ of its maximum value. At axial distances where the current density did not fall to $(1/e)$ of its maximum value, the local minimum was taken as the left bound (see Figure

3-24). This occurred as the beam currents from each portion of the annular channel began to blend together along the thruster centerline. This method of beam current determination yielded consistent values over a wide range of axial locations.

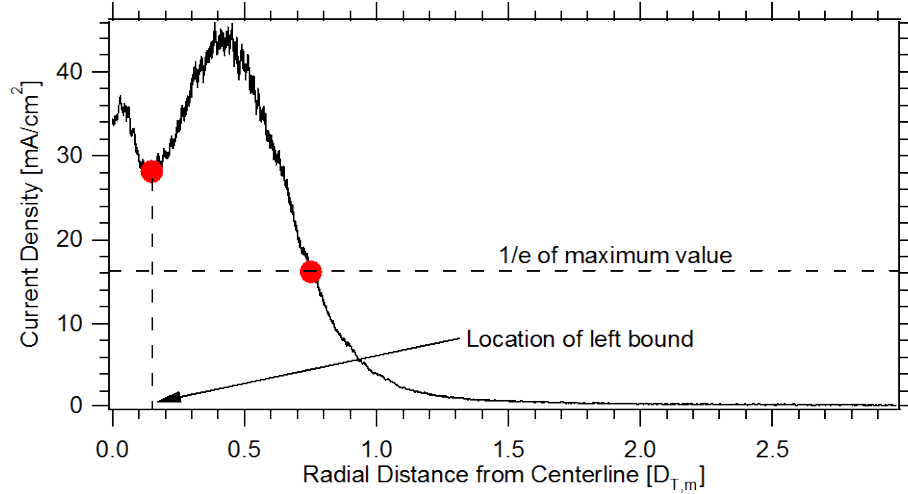


Figure 3-24. Sample ion current density profile where the left portion of the profile does not drop to (1/e) of its maximum value.

The plume divergence angle was calculated at each axial location by forming an angle using the axial distance from the exit plane and the radial distance required for the current density to drop to (1/e) of its maximum value (on the right side of the maximum):

$$\tan(\theta) = \frac{r_{1/e} - r_{\max}}{z}. \quad (3-2)$$

The plume was assumed to be a point source located at the channel centerline and thruster exit plane; thus r_{\max} was taken to be channel centerline, which was found to be a reasonable assumption. This method of plume divergence determination yielded consistent values over a smaller range of axial locations; the point source approximation was found to be invalid at locations very close to the thruster exit plane (typically less than $0.5 D_{T,m}$), while the plume began to blend together at distances beyond $1 D_{T,m}$.

The largest source of uncertainty in measurements of beam current and plume divergence is the collection area of the probe, which was assumed to be equal to the physical probe area. Since the only exposed area of the probe was the front face, edge effects were minimized; a rough analysis of the sheath expansion around the probe indicates that the largest expected increase in collection area is approximately 4%. This analysis used Sheridan's model [47] as a baseline calculation but includes estimates of the effects of flowing plasma and impact parameters on the collection area. While the

selection of probe materials and rapid reciprocation of the probe are expected to minimize effects of secondary electron emission and thermionic emission, respectively, attempts to correct for these effects were not made. Therefore, a conservative estimate of $\pm 10\%$ is used for the uncertainty in the ion beam current and plume divergence.

It was recommended by Reid [13] that beam current and plume divergence values should be averaged over the axial range $0.5 - 1.0 D_{T,m}$, as values tended to be consistent over this range. However, it was found that this range is more dynamic across several operating conditions; how quickly the plume begins to merge past the thruster exit plane dictates the range over which consistent values are found. For this reason, the range over which values were averaged was made more dynamic. The plume divergence was plotted as a function of axial distance from the exit plane. A derivative of this curve was taken, and the axial range over which the derivative fell below a given threshold value was taken as the averaging range (see Figure 3-25). This method allowed for a quantitative measure of the range over which a consistent “plateau” of values was found. The threshold value was chosen from trial-and-error studies of resulting ranges deemed acceptable based on error bounds.

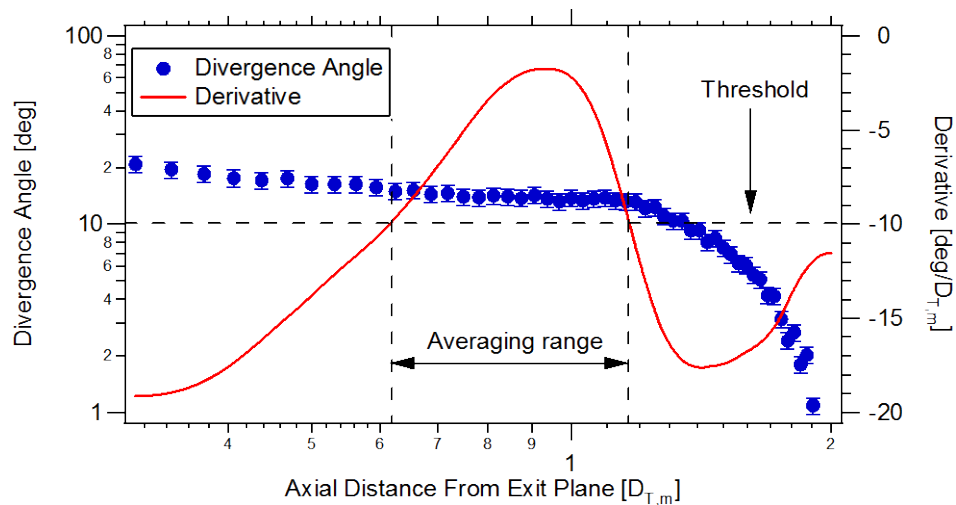


Figure 3-25. Method of determining the axial range over which to average calculated values of plume divergence. The range over which the magnitude of the derivative drops below the threshold value is taken as the averaging range.

It was found that beam current values were also consistent over the averaging range for plume divergence. However, beam current values remained consistent even at distances only $0.188 D_{T,m}$ from the exit plane. This is expected since the beam current calculation is not dependent upon a point source approximation, and therefore should

remain valid even close to the thruster exit plane. Thus, in order to increase the number of measurements included in the reported value, the beam current was averaged from $0.188 D_{T,m}$ to the end of the averaging range for plume divergence.

3.9 Summary

This chapter described the facility, Hall thruster, related hardware, and various diagnostics used within this work. Diagnostics such as the external tab probe and swept emissive probe were used to study and improve data analysis techniques of flush-mounted Langmuir probes, described in Chapter 4. The primary diagnostic, the internal wall-mounted probe, was used within a 6-kW Hall thruster to measure fundamental plasma properties along the channel walls to characterize the near-wall plasma and various plasma-wall interactions. Presentation and discussion of these results can be found in Chapter 5 through Chapter 8.

Chapter 4

Flush-mounted Langmuir Probe Analysis Studies

This chapter describes the various studies performed to improve the fidelity of measurements taken using flush-mounted Langmuir probes in Hall thrusters. A summary of simple Langmuir probe analysis techniques and the complex probe environment of internal wall-mounted probes are first provided. This is followed by studies on sheath expansion in the ion saturation regime, plasma potential determination, and magnetic field effects on the probe characteristic. Finally, determination of the sheath potential along the floating channel wall is proposed and discussed using a combination of theory and measurement.

4.1 Langmuir Probe Theory and Probe Environment

The Langmuir probe is one of the oldest and most often used diagnostics to measure fundamental plasma properties. In its simplest form, it is an electrode placed within the plasma and biased to several voltages. The resulting current to the probe at each voltage is a function of plasma density, electron temperature, and the local plasma potential, all of which can be determined from the probe's I-V characteristic. While the implementation of the Langmuir probe is attractive in its simplicity, analysis and interpretation of the resulting data can be difficult due to numerous deviations from ideal conditions.

Despite frequent deviations from ideal conditions, idealized "simple" Langmuir probe analysis techniques [48,49] are often used to determine estimates of fundamental plasma properties. While using such simple techniques can introduce errors, these errors are often acceptable when compared to the complexities involved in accounting for the non-ideal environment. In simple Langmuir probe analysis techniques, the ion saturation current is first determined. This current is the total current collected by the probe at

highly negative bias voltages, where all electrons are repelled from the probe. This ion current is typically assumed to be constant with probe voltage, and subtracted from the I-V characteristic to determine the electron current to the probe. If the electron population is Maxwellian, the electron current to the probe is expected to vary exponentially with probe voltage:

$$I_e = \frac{1}{4} en_e \sqrt{\frac{8eT_e}{\pi m_e}} A_p \exp\left(\frac{\phi_p}{T_e}\right), \quad (4-1)$$

where A_p is the probe area, ϕ_p is the probe bias with respect to the plasma potential, and the rest of the symbols have their usual meaning. Thus, if the log of the electron current is plotted as a function of the probe bias, a line should result whose slope is the inverse of the electron temperature. Once the probe bias reaches the plasma potential, the electron current is expected to saturate to a constant value, resulting in a sharp change in slope. This “knee” is taken as the location of the plasma potential; however, in practice the electron current does not saturate due to sheath expansion and the knee is rounded due to plasma oscillations. Thus, the linear intersection method of determining plasma potential is typically used, which is further described in Section 4.3.1. Once the plasma potential is found, Eq. (4-1) can be evaluated at $\phi_p = 0$ to determine the plasma number density.

The number density may also be found using the ion saturation current of the probe. If the probe operates in the thin-sheath regime, where the probe radius is much larger than the Debye length, the ion saturation current is set equal to the Bohm current with the assumption that the collection area is equal to the probe area:

$$I_{i,sat} = 0.61en_i \sqrt{\frac{eT_e}{M_i}} A_p. \quad (4-2)$$

The Bohm current results in the necessity for ions to enter the sheath at the Bohm velocity in order to maintain sheath stability [50]. A quasi-neutral layer between the bulk plasma and the sheath, called the presheath, is responsible for accelerating the ions to the Bohm velocity. Because of this acceleration, the ion number density at the sheath edge is approximately 0.61 times the number density in the bulk plasma.

Despite the frequent use of simple Langmuir probe theory, large bodies of work have been performed to characterize the Langmuir probe’s response under various pressures, magnetic field configurations, geometries, plasma densities, and ion and

electron distribution functions [48,51-58]. However, this work has been largely restricted to cylindrical and spherical probe geometries; details on proper analysis techniques for flush-mounted Langmuir probes, under conditions typical for Hall thrusters, are severely lacking.

The combination of the complex Hall thruster environment and the flush-mounted geometry lead to numerous deviations from ideal conditions for Langmuir probes, which could potentially lead to large uncertainties in plasma properties if not accounted for. These include:

1. **Presence of magnetic fields.** The externally-applied magnetic field in Hall thrusters creates a variety of orientations and magnitudes along the channel walls. To further complicate matters, moderate-strength magnetic fields cause typical electron Larmor radii to be of the same order as typical sheath thicknesses (~ 5 Debye lengths).
2. **Presence of flowing plasma.** Simple Langmuir probe theory assumes a stationary plasma with no significant drift component. The large ion velocities created within the Hall thruster channel complicate the determination of plasma densities, as well as determination of plasma potential, which typically relies on a transition between ion-attracting and ion-repelling regimes.
3. **Non-Maxwellian, anisotropic electron energy distributions.** Most Langmuir probe theories assume isotropic Maxwellian distributions for electrons. It is possible that the distributions within the thruster channel are not only non-Maxwellian, but also direction-dependent due to the primarily radial magnetic field.
4. **Floating dielectric material adjacent to probe collection surface.** The geometry of the flush-mounted Langmuir probe can create a complex sheath boundary around the probe that affects the collected current. The sheath expansion characteristics with bias voltage would also be fundamentally different than those for cylindrical, spherical, and free-floating planar probes.

In regards to determination of plasma properties relevant to erosion and power deposition studies, it is important to gain accurate measurements of ion current density, plasma

potential, and wall floating potential. Thus, the studies presented here focus on obtaining high-fidelity measurements of these properties within Hall thruster channels. However, the methods of determining the probe floating potential and electron temperature in this study are retained from simple Langmuir probe analysis techniques. With these methods, the uncertainty in measured floating potential was conservatively estimated at ± 5 V due to probe current fluctuations in the averaged trace; the uncertainty in the measured electron temperature was estimated to be $\pm 15\%$ based on the variation of possible line fits to the transition region of the I-V characteristic on a semi-log scale.

4.2 Sheath Expansion Model

Due to the specific geometry and boundary conditions of the flush-mounted Langmuir probe, a dedicated model was developed to treat the sheath expansion that occurs around the probe in the ion saturation regime (probe biases several electron temperatures below plasma potential). Without such a model, sheath expansion creates a large uncertainty in the collection area of the probe. Thus, the use of this model provides a more accurate determination of the ion saturation current (and thus the ion current density), which is critical for calculations of ion power deposition and related erosion rates. The derivation process for this model is similar to that of Sheridan [47] for free-floating planar probes, and thus will be briefly discussed first. Details of the computational code, derivation process, and final sheath expansion model are then provided.

4.2.1 Sheridan's Model

Sheath expansion around a free-floating planar Langmuir probe has been characterized by Sheridan [47]. A 2-D computational code with particle-in-cell (PIC) ions and Boltzmann electrons is used to solve the ion mass and momentum conservation equations, along with Poisson's equation, around a free-floating pulsed electrode. The steady-state sheath boundary, defined as the location where ions obtain the ion acoustic speed (or Bohm velocity), is tracked as a function of probe bias and Debye length (see Figure 4-1). A number of non-dimensional parameters are defined to obtain an elegant, universal model:

$$\frac{A_s}{A_p} = \frac{\text{sheath area}}{\text{probe area}},$$

$$\rho_p = \frac{r_p}{\lambda_{De}} = \frac{\text{probe radius}}{\text{Debye length}},$$

$$\eta_p = -\frac{\phi_p}{T_e} = -\frac{\text{probe bias}}{\text{electron temperature}}.$$
(4-3)

Using these non-dimensional parameters, a universal power law fit was found relating the sheath expansion ratio (A_s/A_p) to the probe bias. The coefficients of this power-law fit were found to be dependent on the non-dimensional probe radius through additional power law fits:

$$\frac{A_s}{A_p} = 1 + a\eta_p^b,$$

$$a = 2.28\rho_p^{-0.749},$$

$$b = 0.806\rho_p^{-0.0692}.$$
(4-4)

The approach of using such non-dimensional parameters to obtain a more universal model is mimicked in determining the sheath expansion characteristics of a flush-mounted Langmuir probe. It will be shown, however, that due to the difference in geometries and boundary conditions, the sheath boundary shape and expansion is less pronounced around imbedded probes. Thus, Sheridan's model cannot be used to analyze the data from flush-mounted Langmuir probes.

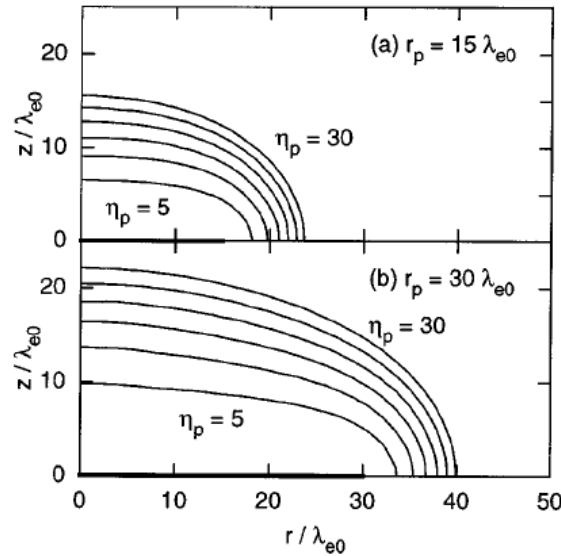


Figure 4-1. Sample sheath boundaries at various probe voltages around a free-floating planar probe. Taken from Ref. [47].

4.2.2 Overview of CEX2D

The code used to derive the sheath expansion characteristics around a flush-mounted Langmuir probe is a two-dimensional hybrid-PIC program developed by Ira Katz at the Jet Propulsion Laboratory (JPL) called CEX2D [59]. The code was designed to simulate ion optics within a gridded ion thruster, including charge-exchange (CEX) ions that play a large part in accelerator grid erosion. Many of the features of CEX2D were disabled for this work since they were not needed, including variable grid spacing and creation of CEX ions.

The basic algorithm of CEX2D involves solving Poisson's equation and tracking ion trajectories on either a Cartesian (x-y) or cylindrical (r-z) grid geometry. Using the input geometry and boundary conditions, Laplace's equation is solved first:

$$\nabla^2 \phi = 0, \quad (4-5)$$

where ϕ is the space potential. Thus, a potential field is first found with no space charge. Ions are then injected through the left boundary at the Bohm velocity, given the input electron temperature and ion mass. These ions are then tracked through the potential field in order to determine the space charge distribution in the domain. Electrons are assumed to follow a Boltzmann distribution:

$$n_e(\phi) = n_{e,ref} \exp\left(\frac{(\phi - \phi_{ref})}{T_e}\right). \quad (4-6)$$

Initially the density of the injected particles is much less than the desired plasma density, and is chosen based on a blending function,

$$\begin{aligned} n^0 &= 0 \\ n^{i+1} &= (1 - \alpha)n^i + an, \end{aligned} \quad (4-7)$$

where α and a are parameters chosen to determine the density step size. Thus, once the space charge distribution is found, Poisson's equation is then solved to determine a new potential field:

$$\nabla^2 \phi = -\frac{\rho}{\epsilon_o} = -\frac{e(n_i - n_e)}{\epsilon_o}. \quad (4-8)$$

Ions are injected once again from the left boundary at a slightly higher density based on Eq. (4-7); this process is repeated until the injected ion density reaches the desired number density defined by the user.

Ion particle positions and velocities are tracked using a leap-frog method found frequently in PIC codes:

$$\begin{aligned}\bar{x}^{t+1} &= \bar{x}^t + \bar{v}^{t+1/2} \Delta t, \\ \bar{v}^{t+1/2} &= \bar{v}^{t-1/2} + \frac{e}{M_i} \vec{E}(\bar{x}^t) \Delta t.\end{aligned}\quad (4-9)$$

Particle positions, the charge density, and electric fields are tracked every timestep, while the particle velocities are calculated every half timestep. Electric field forces are interpolated to particle positions using a conventional bilinear weighting scheme; particle charge is distributed to grid nodes using a similar scheme. While space potentials are defined at grid nodes, the electric fields are defined along the grid edges midway between nodes (see Figure 4-2):

$$\begin{aligned}E_z(i, j + 1/2) &= \frac{\phi(i, j + 1) - \phi(i, j)}{\Delta z}, \\ E_r(i + 1/2, j) &= \frac{\phi(i + 1, j) - \phi(i, j)}{\Delta r}.\end{aligned}\quad (4-10)$$

Particles are created uniformly along the left boundary during the injection process. Particles are removed from the simulation if they exceed the bounds of the simulation in the z direction; they are reflected back into the simulation if they exceed bounds in the r direction.

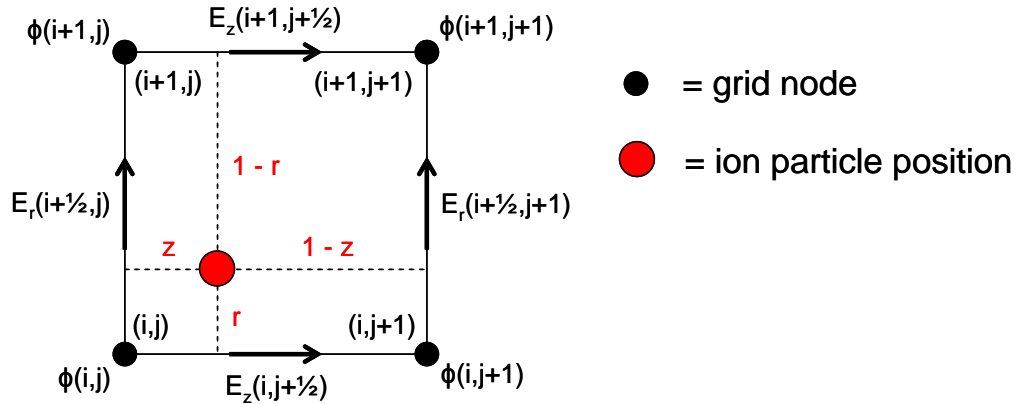


Figure 4-2. Sample grid cell showing the locations of calculated potentials and electric fields, along with particle weighting. The relative lengths of r , z , $1-r$, and $1-z$ are used to weight electric fields to particle positions and particle charge to grid nodes.

The above algorithm was implemented in Fortran 90 and can be run on any standard PC with Windows. The matrix equations were solved using a sparse matrix solver within the Compaq Extended Math Library (CXML) of Compaq Visual Fortran.

This allows the matrices to be solved very efficiently, with ion optics solutions being obtained within tens of minutes; solutions for this study were typically obtained within one minute.

4.2.3 Method of Expansion Characterization

In order to characterize the sheath expansion around a flush-mounted Langmuir probe in ion saturation, a simulation domain was set up in cylindrical space using CEX2D (see Figure 4-3). The left boundary at $z=0$ represents the unperturbed bulk plasma at a defined plasma potential of zero. This boundary also acts as the location where the Bohm current of ions is injected into the simulation domain. The right boundary at $z=z_{max}$ constitutes the probe and adjacent insulating material. The probe is biased to various potentials, while the wall potential is calculated from the electron temperature using the methods described in Section 4.5.3. The bottom ($r=0$, axis of symmetry) and top ($r=r_{max}$) boundaries are reflected boundaries where particles are reflected back into the domain.

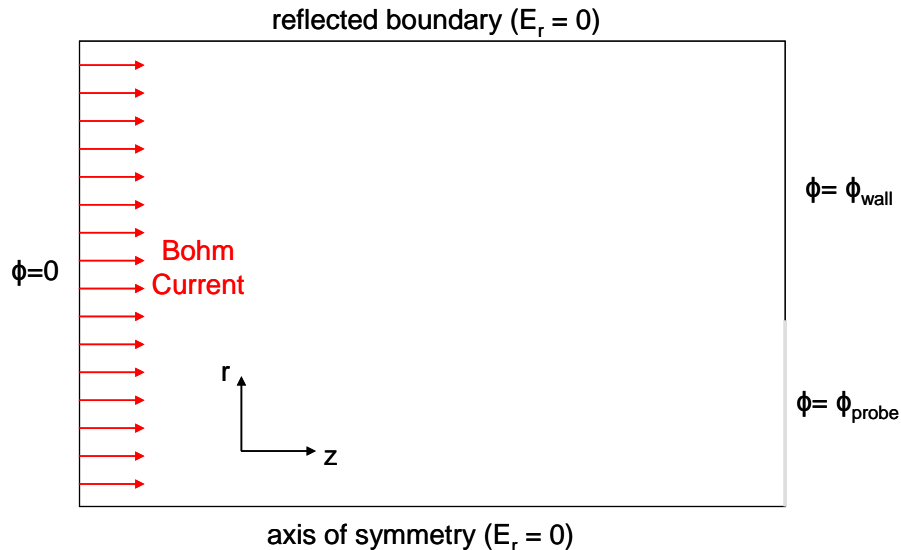


Figure 4-3. Computational domain for ion sheath expansion study using CEX2D. Electric potential boundary conditions are defined at left and right boundaries while electric field boundary conditions are defined at top and bottom boundaries.

A range of simulation conditions were chosen that were representative of the plasma inside the 6-kW Hall thruster. Seven electron temperatures were simulated, ranging from 3 – 30 eV. For each electron temperature, five ρ_p 's (probe radius-to-Debye length ratio) were chosen ranging from 5.5 – 13. The probe radius was held constant for

each of these simulations, and the number density was properly chosen to yield the necessary Debye length. For each ρ_p , six η_p 's (non-dimensional probe bias with respect to plasma potential) were chosen ranging from 5-10. These numbers were chosen to approximately span from the probe floating potential to deep into ion saturation. A typical solution can be seen in Figure 4-4.

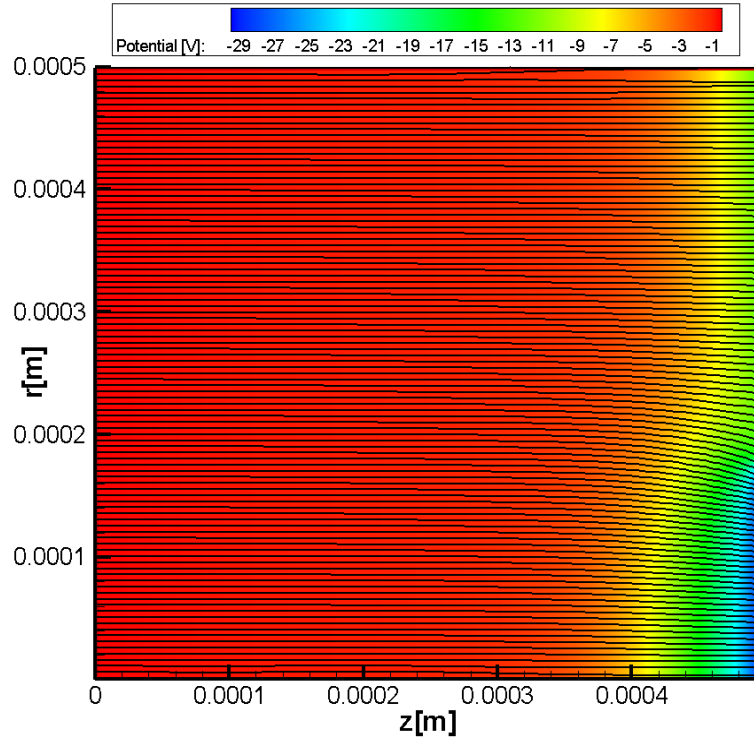


Figure 4-4. Sample contour plot of equipotentials and ion trajectories (black lines) around a flush-mounted Langmuir probe using CEX2D.

The equivalent sheath area for each simulation was found by tracking approximately 100 ion trajectories within the domain; the one that was found to reach the edge of the probe was traced back to $z=0$. This trajectory can be considered the boundary between ions that are and are not collected by the probe. Thus, the radius of this trajectory at $z=0$ can be considered the *radius of capture*, as well as the equivalent sheath radius (see Figure 4-5).

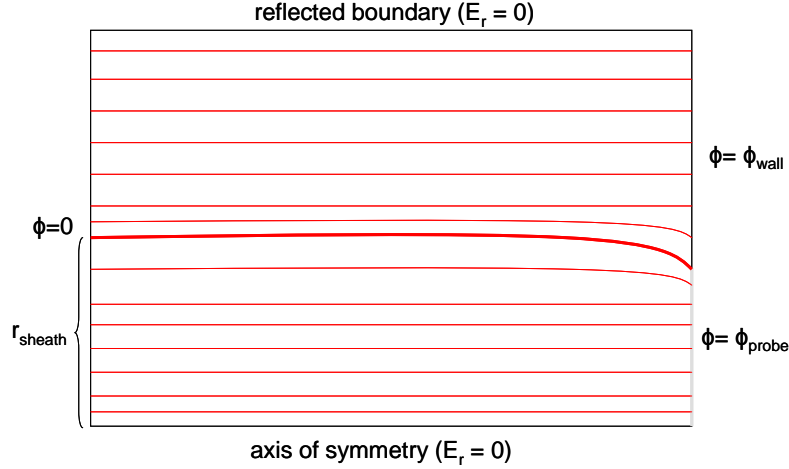


Figure 4-5. Schematic representing typical ion trajectories, shown in red, found around a flush-mounted probe. The ion trajectory that reaches the probe edge is the boundary of capture, and can be used to define an equivalent sheath radius.

The equivalent sheath area was found as a function of η_p , ρ_p , and T_e . Similar to Sheridan's model, sheath expansion was characterized by first comparing A_s/A_p at various probe voltages; the coefficients within the fit functions found are then compared at various values of ρ_p . Finally, the coefficient functions are compared across various electron temperatures to check for universal behavior. The final step was performed due to the dependence of the wall floating potential on electron temperature.

4.2.4 Final Expansion Correction Model

The sheath expansion around a flush-mounted Langmuir probe was first found as a function of the non-dimensional probe bias. However, a new variable is defined for the probe bias in this study:

$$\mu_p = -\frac{\phi_{probe} - \phi_{wall}}{T_e}. \quad (4-11)$$

This new definition is made due to the differing boundary conditions between a flush-mounted probe and a free-floating probe. For a free-floating probe, like in Sheridan's model, the sheath area is equal to the probe area when the probe is biased to the local plasma potential; thus, the area ratio is equal to 1 when $\eta_p=0$. Equivalently, the sheath area around a flush probe is equal to the probe area when the probe is biased to the adjacent wall floating potential; at this point the probe is indistinguishable from the wall, creating a uniform surface (see Figure 4-6). Thus, the area ratio is equal to 1 when $\mu_p=0$.

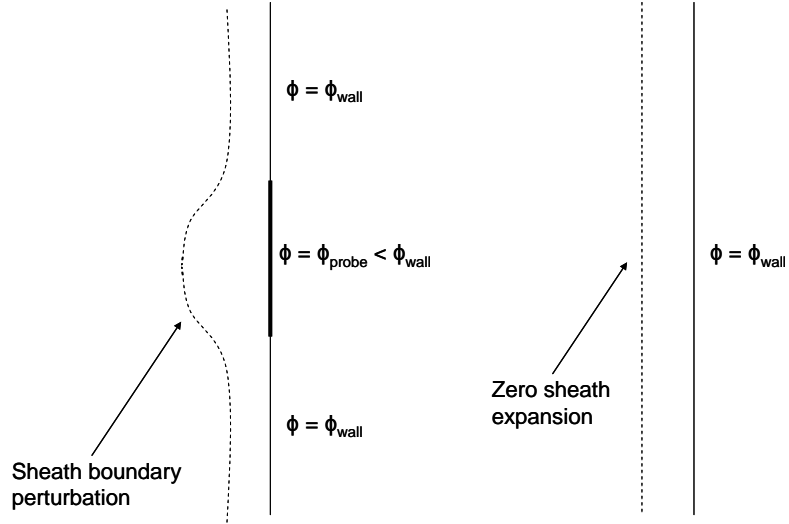


Figure 4-6. Diagram showing how the sheath boundary becomes perturbed around a flush probe. No perturbation occurs when the probe is biased to the local wall potential, creating a uniform, indistinguishable surface.

Figure 4-7 shows variations of the area ratio, A_s/A_p , with probe bias, μ_p , at an electron temperature of 3 eV. The variation is highly linear with a slope that is a function of ρ_p . As expected, all lines intercept $A_s/A_p=1$ when $\mu_p=0$. This trend is consistent across all electron temperatures tested in the study. Thus:

$$\frac{A_s}{A_p} = 1 + b(\rho_p, T_e)\mu_p. \quad (4-12)$$

The variation of the slope b with non-dimensional probe radius, ρ_p , is shown in Figure 4-8 at an electron temperature of 3 eV. Within the range of values tested, the best fit was found to be a power law variation with zero offset. A zero offset was enforced during the fit process since the sheath expansion should naturally fall to zero at an infinite value of ρ_p ; this corresponds to the scenario of an infinite planar probe (or equivalently, a negligible value of Debye length). The power law function was found to be the best fit at all electron temperatures tested. Thus:

$$b(\rho_p, T_e) = C(T_e)\rho_p^{m(T_e)}. \quad (4-13)$$

The coefficients, C and m , were assumed to be functions of electron temperature. However, this is merely due to the dependence of the floating wall potential on the electron temperature. Equivalently, a new non-dimensional variable is defined that characterizes the floating wall potential:

$$\mu_0(T_e) = -\frac{\phi_{wall}(T_e)}{T_e}. \quad (4-14)$$

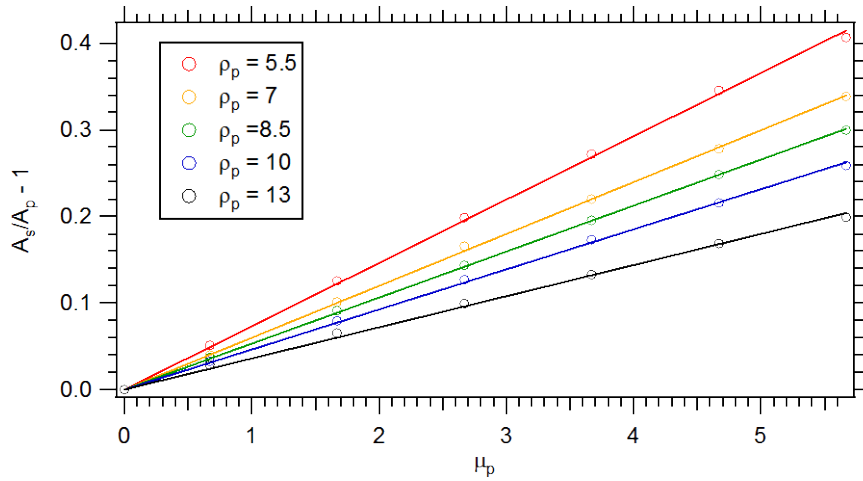


Figure 4-7. Variation of sheath area expansion with probe bias, found to be highly linear at all values of ρ_p tested. Electron temperature was set to 3 eV.

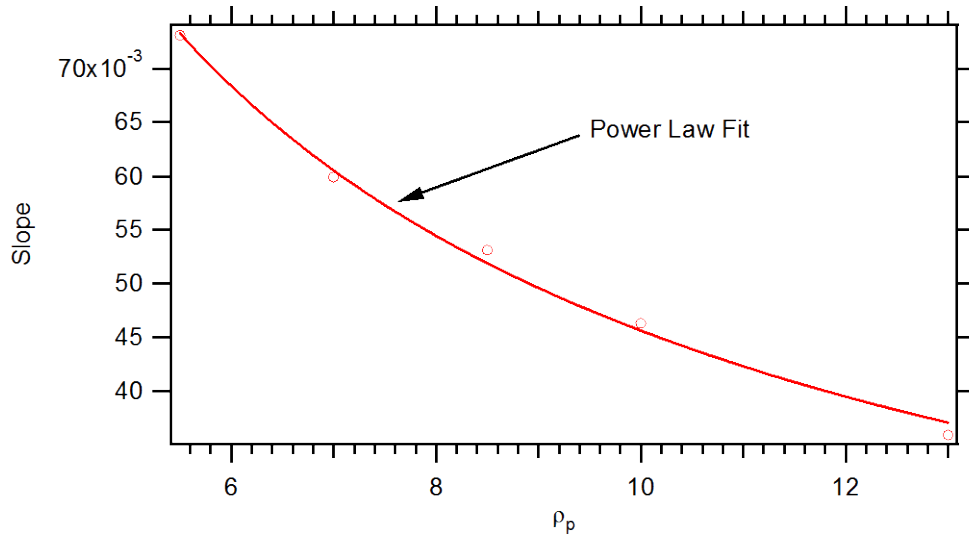


Figure 4-8. Variation of slope b with non-dimensional probe radius, ρ_p , at an electron temperature of 3 eV. A power law function with zero offset was found to fit very well.

The variation of the coefficient C with electron temperature and μ_0 is shown in Figure 4-9. Errors bars are derived from the standard deviations of the power law curve fits to b . The coefficient C appears to be roughly constant in two regions separated at an electron temperature between 18 and 20 eV. This temperature corresponds to the crossover energy of boron nitride, when the sheath becomes space-charge-limited due to

secondary electron emission from the wall (see Section 4.5.3). Thus, an average value is used in each of these two regions:

$$C(\mu_0) = \begin{cases} 0.2985, & \mu_0 > 1.02 \\ 0.4094, & \mu_0 \leq 1.02 \end{cases} \quad (4-15)$$

The non-dimensional wall potential is used here due to its more fundamental nature; the model can then be used for materials other than boron nitride, as long as the secondary electron emission characteristics are known.

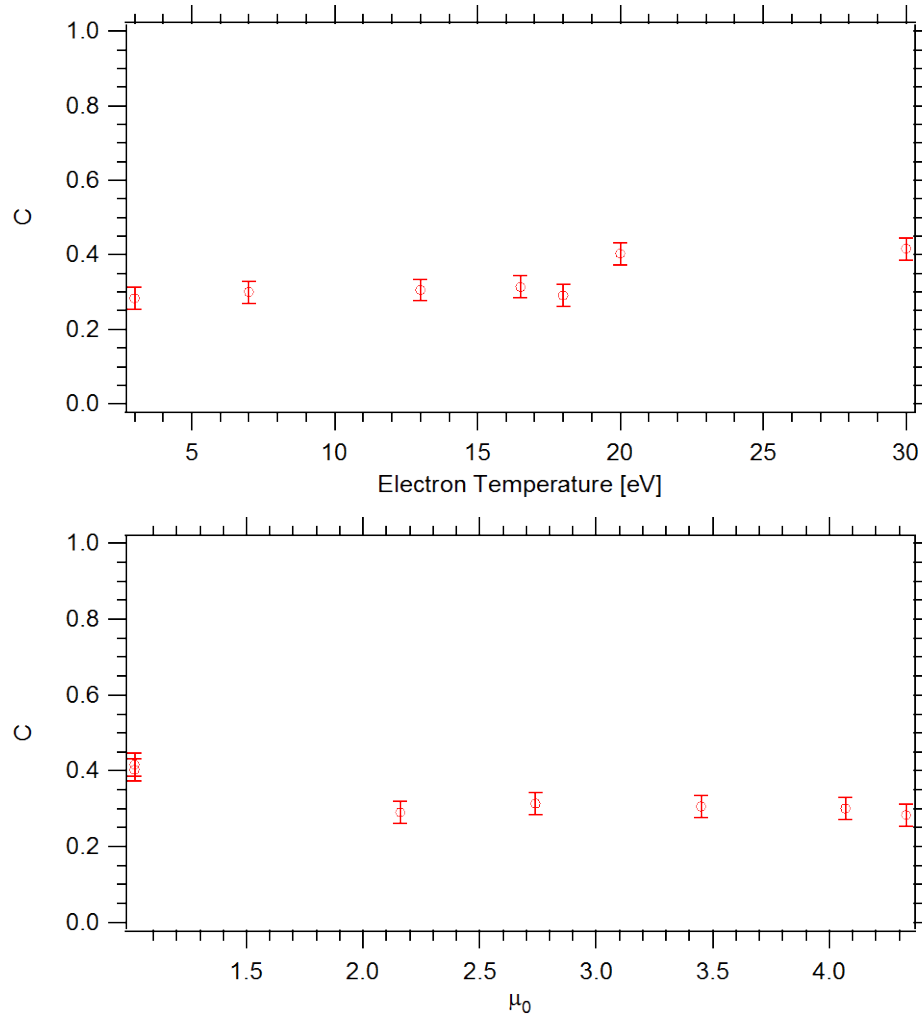


Figure 4-9. Variation of the fitting coefficient C with electron temperature, T_e , and floating wall potential, μ_0 . Values are largely constant until the crossover energy is reached, at $T_e = 19.3$ eV or $\mu_0 = 1.02$.

The variation of the fitting coefficient m with electron temperature and μ_0 is shown in Figure 4-10. Error bars correspond to the standard deviations found for the power law curve fit to the slope b . Similar to the coefficient C , values of m are

approximately constant in two regions separated by the crossover energy at $T_e = 19.3$ eV. Thus, an average value is used in each of these two regions:

$$m(\mu_0) = \begin{cases} -0.7978, & \mu_0 > 1.02 \\ -0.8495, & \mu_0 \leq 1.02 \end{cases} \quad (4-16)$$

As before, μ_0 is used in place of the electron temperature in order to make the model more universal, increasing its applicability to flush-mounted probes in general.

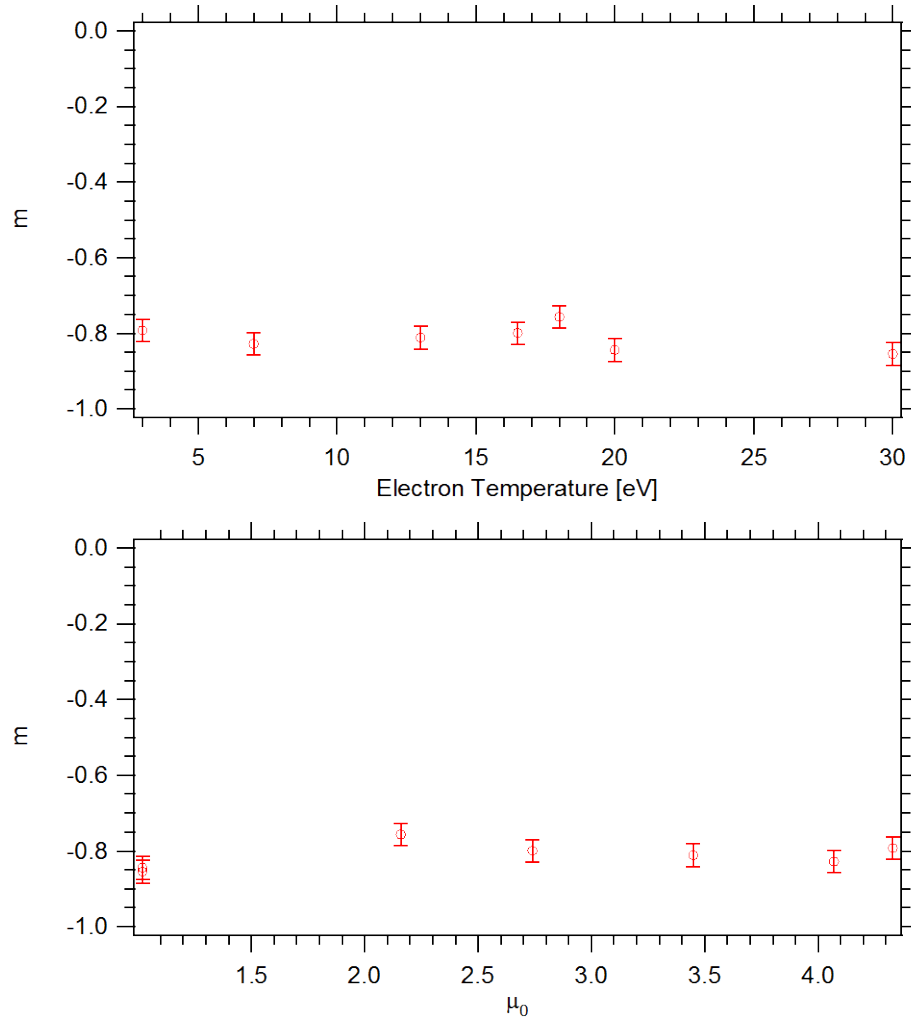


Figure 4-10. Variation of the fitting coefficient m with electron temperature, T_e , and floating wall potential, μ_0 . Values are roughly constant until the crossover energy is reached, at $T_e = 19.3$ eV or $\mu_0 = 1.02$.

The final model is summarized in Eq. (4-17). The secondary electron emission characteristics of the adjacent wall material are required to determine the floating wall potential as a function of the electron temperature (see Section 4.5.3). Other required information includes the local plasma potential, probe radius, and electron temperature;

all of these quantities can either be obtained from the Langmuir probe I-V characteristic or be readily measured. The model can then be used to determine the sheath expansion at each bias voltage of the probe trace. The collected current can be “corrected” for this expansion by accounting for the increased area and solving for the equivalent collected current if there were no sheath expansion. Since the Debye length is a required quantity in the model, which is dependent upon the plasma number density, solving for the correct ion saturation current (and number density) is an iterative process; the model must be used to determine the proper ion number density until a consistent solution is found. Figure 4-11 shows a comparison between corrected and uncorrected data from a flush-mounted Langmuir probe. The derived model does an excellent job of correcting for sheath expansion and recovering a flat ion saturation level. Due to the inherent noise in the data, the ion saturation current is found by averaging values from the lowest bias potential to one electron temperature below the floating potential.

$$\frac{A_s}{A_p} = 1 + C(\mu_0) \rho_p^{m(\mu_0)} \mu_p,$$

$$C(\mu_0) = \begin{cases} 0.2985, & \mu_0 > 1.02 \\ 0.4094, & \mu_0 \leq 1.02 \end{cases}, \quad (4-17)$$

$$m(\mu_0) = \begin{cases} -0.7978, & \mu_0 > 1.02 \\ -0.8495, & \mu_0 \leq 1.02 \end{cases}.$$

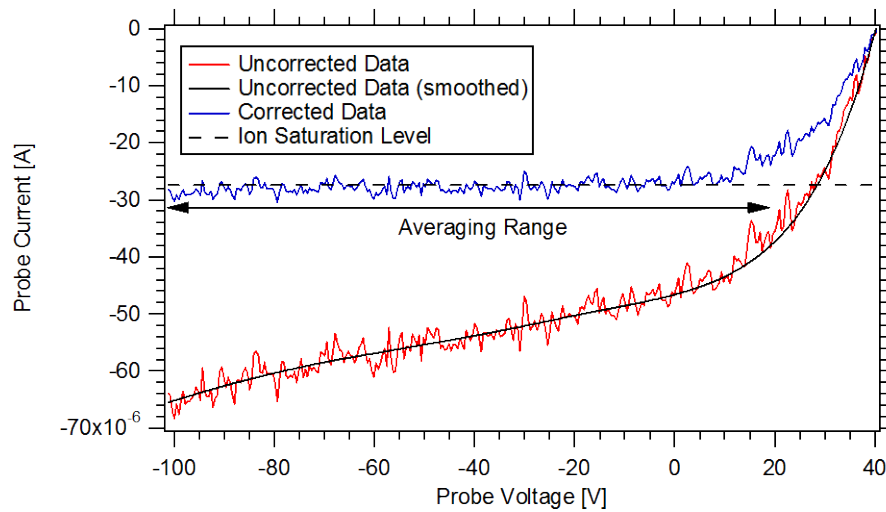


Figure 4-11. Comparison of corrected and uncorrected ion saturation regimes from a flush-mounted Langmuir probe I-V characteristic. The corrected data is much flatter and the ion saturation current is easily determined.

While this model was found to flatten out the ion saturation regime of the I-V characteristic, it did not always result in a highly constant value of ion saturation current. Because of the slight slope in the ion saturation branch and the method of averaging to determine the ion saturation current, the uncertainty associated with this measurement was estimated at $\pm 25\%$. Along with the uncertainty in probe diameter ($\pm 25 \mu\text{m}$), this resulted in a $\pm 40\%$ uncertainty in measured ion current density.

4.3 Plasma Potential Determination

While Langmuir probes have the ability to measure the local plasma potential, the data can be affected by the presence of flowing plasma, magnetic fields, plasma oscillations, and the probe geometry. Since the plasma potential is necessary to calculate proper ion saturation currents, ion beam energies, as well as electron energy distribution functions, it is a critical parameter when dealing with wall power, erosion, and characterization of the plasma. For this reason, a study was done to determine the best technique to obtain plasma potentials from flush probes. A number of analysis techniques were used to determine the plasma potential from data taken with a flush-mounted Langmuir probe, and compared to the more robust diagnostic of a swept emissive probe (see Section 3.7.2). Three analysis techniques for Langmuir probes are described, followed by the analysis for swept emissive probes. All these methods are then compared and a recommendation is made for determining local plasma potential from flush probes.

4.3.1 Linear Intersection Method

This is the standard method of determining plasma potential from Langmuir probe data. The electron current is first calculated from the probe current by subtracting out the ion current, typically assumed to be constant, from the data. The natural log of the electron current is then plotted as a function of probe bias (see Figure 4-12). A line is then fit to the transition (electron repelling) region below the plasma potential, as well as the electron saturation region above the plasma potential. An algorithm was created to find the best line fit that maximized the number of points in the fit while maintaining a reasonable correlation coefficient. The probe voltage at which these two lines intersect is

taken as the local plasma potential. This is based off an ideal Langmuir probe trace, which contains two linear regions in the transition and electron saturation regimes, separated by a sharp change in slope at the plasma potential. This sharp “kink” is typically smoothed out by plasma oscillations, but extrapolating the lines from the extremes of the two regions should recover the location of the plasma potential.

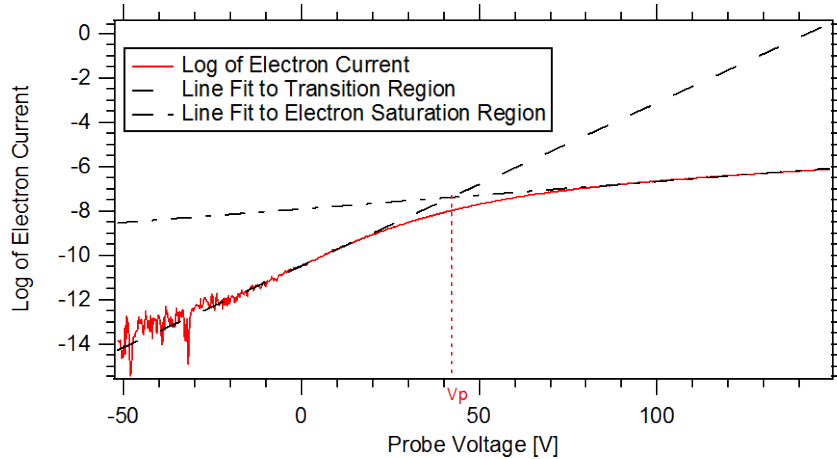


Figure 4-12. Method of linear intersecting lines to determine plasma potential from Langmuir probe data. A line is fit to the transition and electron saturation regions of the characteristic, and the probe voltage at the intersection of these two lines is taken as the local plasma potential.

4.3.2 Derivative Method

The derivative method is a less often used technique to determine plasma potential from Langmuir probe data. A first (and sometimes second) derivative of the probe characteristic is required. Due to the inherent noise level in any experimental data, this typically necessitates smoothing of the raw data. Unfortunately, smoothing data can significantly alter the shapes of the derivatives, leading to larger uncertainties.

For this study, an algorithm was created that starts with negligible smoothing to the raw data and slowly increases the level of smoothing until a satisfactory reduction in noise is achieved, based upon the presence of rapid derivative (dI/dV) changes in the intermediate portion of the I-V characteristic. Smoothing was performed using the Reinsch algorithm available within the analysis program Igor Pro. Each smoothed trace was compared to the original data to ensure the original shape was retained. Due to the fundamental differences in current collected by an electron-repelling probe and an electron attracting probe, an inflection point in the Langmuir probe characteristic is typically found at the plasma potential. Thus, the probe voltage where the first derivative

of the trace is maximized (or equivalently, a zero in the second derivative) corresponds to the local plasma potential.

While in many cases the zero in a second derivative can be easily recognized, in other cases a maximum in the first derivative is not well-defined. Figure 4-13 shows an example of such a case, taken by the external tab probe near the exit plane of the 6-kW Hall thruster. In such circumstances where the second derivative never reaches zero, the primary “hump” is extrapolated linearly to zero to determine an approximate value of the plasma potential.

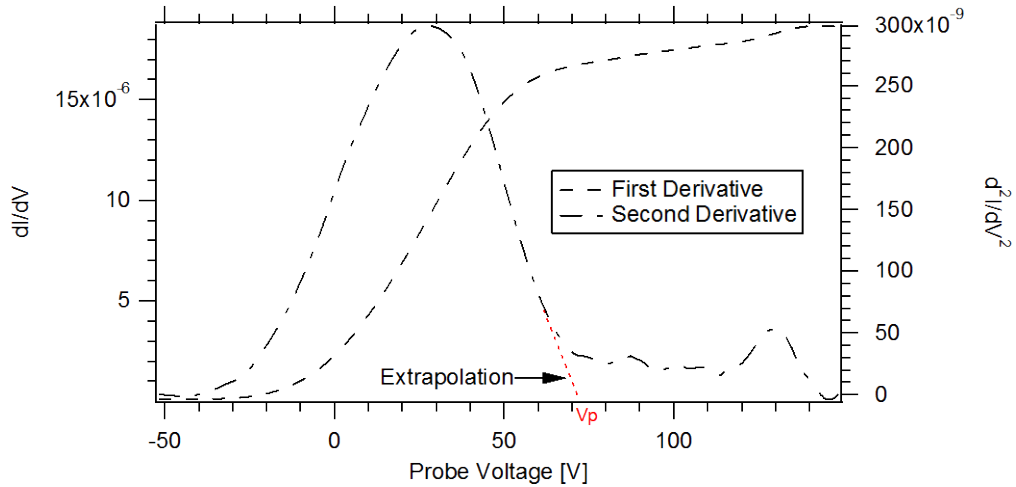


Figure 4-13. Method of derivatives to determine plasma potential from Langmuir probe data. The probe voltage where the first derivative maximizes, or equivalently where the second derivative reaches zero, is taken as the plasma potential.

4.3.3 Shifted Floating Potential Method

Another method for determining plasma potential from Langmuir probes is to take the measured floating potential of the probe and shift it by a certain amount based on the local electron temperature. According to simple Langmuir probe theory [49], the difference between the plasma and floating potentials is given by

$$V_p - V_f = T_e \ln \left(\frac{M_i}{2\pi m_e} \right)^{1/2}, \quad (4-18)$$

where V_p is the plasma potential, V_f is the floating potential, M_i is the ion mass, and m_e is the electron mass. For a xenon plasma, the natural log term equals 5.27; thus, the measured floating potential should be 5.27 electron temperatures below the local plasma potential.

This method includes several assumptions such as a Maxwellian distribution for electrons, ion current equal to the Bohm current, and a 1-D plasma that may not hold within Hall thruster channels. It should be noted that Eq. (4-18) does not include any potential drop from the presheath that accelerates ions to the Bohm velocity. The presheath thickness scales with an ion collisional mean free path, which is typically on the same order as the thruster channel width. Thus, it is not physically justified to include the potential drop associated with the presheath. Despite the assumptions involved in this method, it remains an attractive, simple approach that should give a reasonable estimate of plasma potential.

4.3.4 Swept Emissive Probe Method

The diagnostic used for comparison against the various methods of Langmuir probes is the swept emissive probe (see Section 3.7.2). A filament is biased to various voltages like a Langmuir probe, but under different levels of thermionic emission. Since all thermionically emitted electrons return to the probe when it is biased above the plasma potential, all traces should overlap at probe voltages above the plasma potential. Figure 4-14 shows a typical data set taken near the exit plane of the 6-kW Hall thruster operating at 300 V and 20 mg/s anode flow rate.

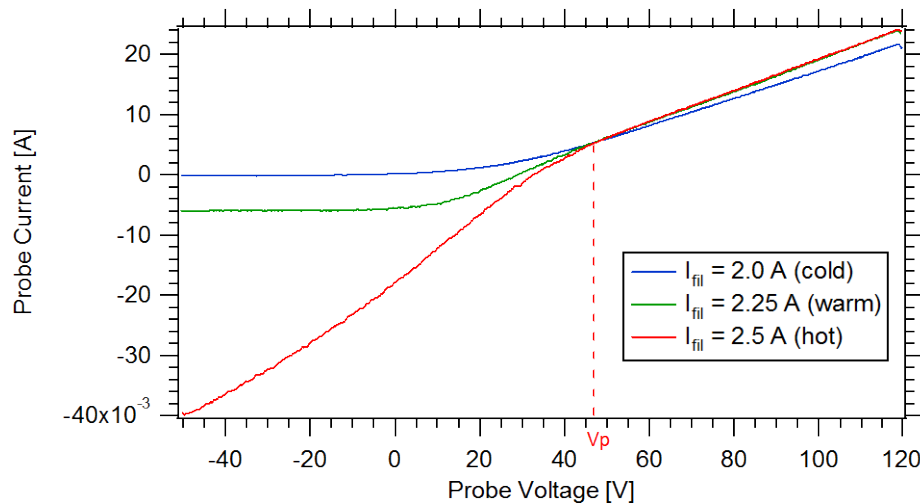


Figure 4-14. Sample data from the swept emissive probe using three different filament currents. The voltage at which the traces begin to overlap is taken as the local plasma potential.

While the warm and hot traces overlapped well at voltages above the plasma potential, the cold trace did not always match well with the other traces. This is possibly due to impurities on the probe that cause variations in the surface work function for the

cold trace [41]; these impurities would burn off when the probe reaches a high enough temperature, thus not affecting the warm and hot traces. For this reason, only the warm and hot traces were used to determine the measured plasma potential.

Despite efforts to match the locations of the external tab probe and swept emissive probe, differences on the order of 1 mm still remained in both axial and radial directions. While this difference seems negligible, the large potential gradients near the exit plane of the thruster could create significantly different plasma properties at each probe location. For this reason, a shifted floating potential method similar to Eq. (4-18) was used to account for the difference in probe location:

$$V_p = V_f + \zeta T_e. \quad (4-19)$$

Since the Hall thruster plasma is non-ideal near the exit plane, ζ is not assumed to be equal to 5.27. However, due to the close proximity of the external tab probe and swept emissive probe, ζ is taken to be a constant between the two probe locations. Thus:

$$\frac{V_{p_1} - V_{f_1}}{T_{e_1}} = \frac{V_{p_2} - V_{f_2}}{T_{e_2}}, \quad (4-20)$$

where the subscript “1” corresponds to the location of the external tab probe and the subscript “2” corresponds to the location of the swept emissive probe. The cold trace from the swept emissive probe is used to determine V_{f_2} and T_{e_2} , while V_{p_1} is left as the unknown variable. In this way, the swept emissive probe data can be used to obtain a measurement of the local plasma potential at the location of the external tab probe.

4.3.5 Comparison of Methods

The three different methods of determining plasma potential from Langmuir probes were compared to the swept emissive probe at seven different thruster operating conditions, shown in Table 4-1. These conditions represent a wide range of discharge voltages, mass flow rates, and discharge powers.

Table 4-1. Thruster operating conditions used during plasma potential study.

Discharge Voltage [V]	Anode Flow Rate [mg/s]	Discharge Current [A]	Discharge Power [kW]
150	10	8.72	1.3
150	20	20.80	3.1
150	30	34.43	5.2
300	10	8.68	2.6
300	20	19.47	5.8
300	30	31.69	9.5
600	10	8.87	5.3

Table 4-2 shows the results of plasma potential near the exit plane of the 6-kW Hall thruster using the four different analysis techniques described above. Percent differences when compared to the swept emissive probe, arguably the most accurate technique, are given in parentheses. Data from the swept emissive probe at 300 V and 30 mg/s anode flow rate is not available due to probe failure.

Table 4-2. Comparison of plasma potential results from various analysis techniques. When compared to the swept emissive probe, the derivative method appears to be the most accurate.

Operating Condition	Swept Emissive Probe Method [V]	Linear Intersection Method [V]	Derivative Method [V]	Shifted Floating Potential Method [V]
150 V, 10 mg/s	63	34 (46)	65 (3)	50 (21)
150 V, 20 mg/s	70	35 (50)	65 (7)	52 (26)
150 V, 30 mg/s	63	34 (46)	61 (3)	43 (32)
300 V, 10 mg/s	70	36 (49)	88 (26)	75 (7)
300 V, 20 mg/s	84	42 (50)	75 (11)	70 (17)
300 V, 30 mg/s	N/A	44	83	74
600 V, 10 mg/s	154	71 (54)	119 (23)	140 (9)

Based on the results, the linear extrapolation method underestimates the local plasma potential by approximately 50%. The derivative and shifted floating potential methods are more accurate, with average relative errors of only 12% and 19%, respectively. Thus, while the linear extrapolation method is the most frequently used analysis technique to determine plasma potential, it does not give accurate results with a flush probe within a Hall thruster discharge plasma. It is surprising that the shifted floating potential method gives such accurate results despite all the assumptions involved

in its derivation. This may indicate that the plasma near the thruster exit plane is more ideal than expected. However, due to the derivative method's independence on electron temperature and its low average error, it is the recommended method for determining plasma potential from flush probes in Hall thrusters. All subsequent presented plasma potentials were determined using this method of analysis.

Based on the results from Table 4-2, the uncertainty associated with the derivative method increases with discharge voltage, being approximately $\pm 5\text{-}10\%$ at 150 V and $\pm 10\text{-}20\%$ at 300 and 600 V. However, the use of these values is applicable only within the acceleration zone where these data were collected, as the derivative method was found to have higher levels of uncertainty due to a poorly defined inflection point. At locations upstream of the acceleration zone, the inflection point of the I-V characteristic was much more defined, leading to reduced uncertainties. Because of this, the uncertainty associated with the derivative method is reported at a fixed value of 6.7% the discharge voltage (e.g. ± 20 V for a 300 V discharge).

4.4 Magnetic Field Effects

The externally-applied magnetic field inside a Hall thruster is of sufficient strength to magnetize the electron population while leaving the ion population relatively unmagnetized (i.e. the ion gyroradius is much larger than the channel dimensions). The presence of such a magnetic field can affect electron motion to a surface, and thus also change the way electrons are collected by a Langmuir probe [48,51,55,58,60-62]. For this reason, a flush-mounted Langmuir probe was placed within a uniform magnetic field (see Sections 3.5 and 3.6.1) in order to characterize the effects of magnetic field conditions representative of Hall thrusters on measurements of floating potential, plasma potential, electron temperature, and electron number density.

In this particular study, a relatively low number of points were taken per I-V characteristic. Due to the low probe voltage resolution (~ 1.5 V), the derivative method of determining plasma potential (see Section 4.3.2) was found to yield large uncertainties. Thus, plasma potentials in this study were determined using the standard linear intersection method (see Section 4.3.1) due to its robustness and independence from other measured properties. This was deemed acceptable due to only needing consistency

across measurements and not absolute accuracy in this study. The electron number density was determined from the electron saturation current collected at plasma potential and assuming a thermal flux:

$$n_e = \frac{4I_{e,sat}}{eA_p} \sqrt{\frac{\pi m_e}{8eT_e}}. \quad (4-21)$$

Eight different magnetic field magnitudes were tested, along with four different angular orientations (see Table 4-3), for a total of 32 conditions. The definition of angular orientation can be seen in Figure 4-15; zero degrees corresponds to a normal incidence of magnetic field. For the data presented here, the thruster was operated at a discharge voltage of 150 V and an anode flow rate of 30 mg/s. This operating condition provided an environment at the probe that was most representative of that within the Hall thruster discharge channel, based on the degree of sheath magnetization characterized by the cyclotron radius-to-Debye length ratio at nominal conditions.

Table 4-3. List of magnitudes and orientations tested in magnetic field study. A total of 32 conditions were investigated.

Magnetic Field Magnitude [G]	Magnetic Field Orientation [deg]
0	0
5	30
10	60
30	90
50	
100	
150	
200	

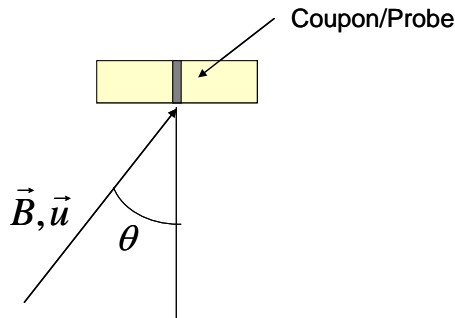


Figure 4-15. Schematic showing the definition of the magnetic field orientation angle with respect to the coupon and probe. For this particular study, the magnetic field and ion velocity vectors were aligned.

Figure 4-16 through Figure 4-19 show the measured floating potentials, plasma potentials, electron temperatures, and electron number densities under various magnetic field magnitudes and orientations. Overall, there is little significant effect on the floating potential, plasma potential, and electron temperature. At an orientation of 90° , the measured floating potential and electron temperature are slightly higher, but this elevation occurs even with no magnetic field present, indicating it is an orientation phenomenon. However, it appears that the calculated number density slightly increases with magnetic field magnitude at all orientations tested. While this is a surprising result since electron current is expected to drop with increasing magnetic field, it is possible that the plasma density actually rose as the magnetic field constricted electrons into close, tight orbits.

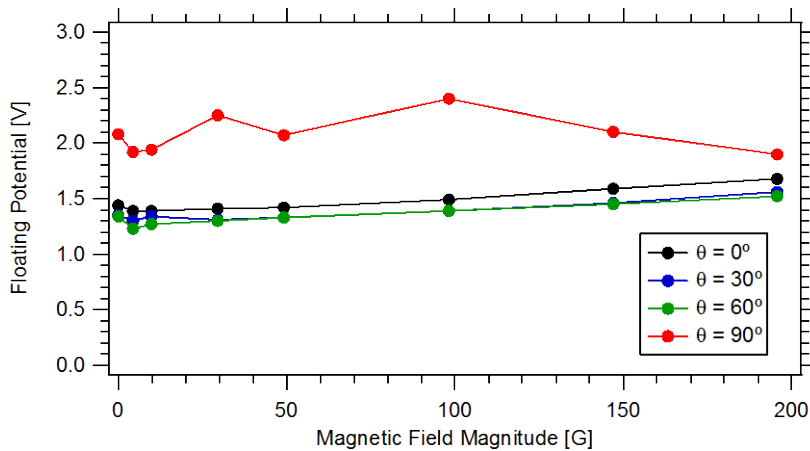


Figure 4-16. Measured floating potentials under various magnetic field magnitudes and orientations. Magnetic field effects are largely negligible, as the slight elevation at 90° is purely an orientation effect.

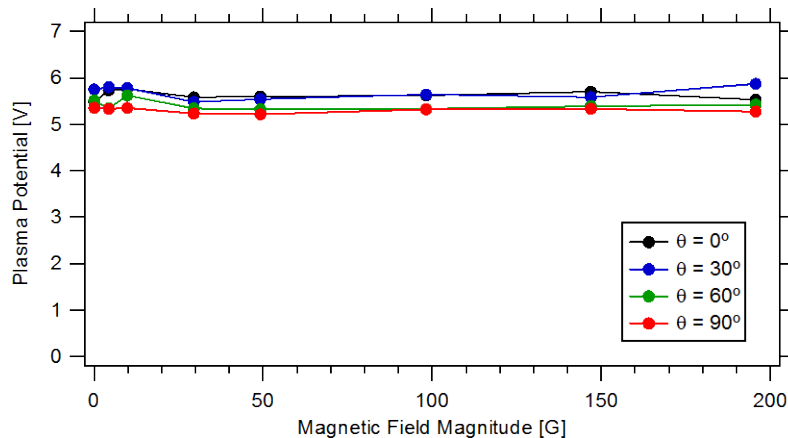


Figure 4-17. Measured plasma potentials under various magnetic field magnitudes and orientations. The presence of the magnetic field appears to have little effect.

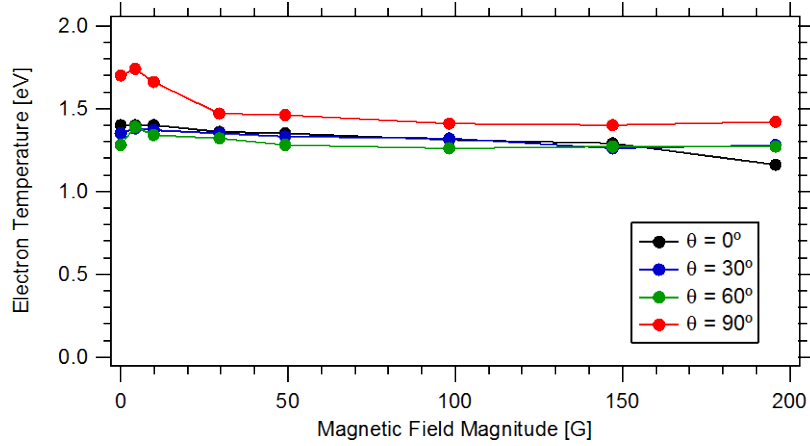


Figure 4-18. Measured electron temperatures under various magnetic field magnitudes and orientations. Magnetic field effects appear to be largely negligible, as the slight elevation at 90° is purely an orientation effect.

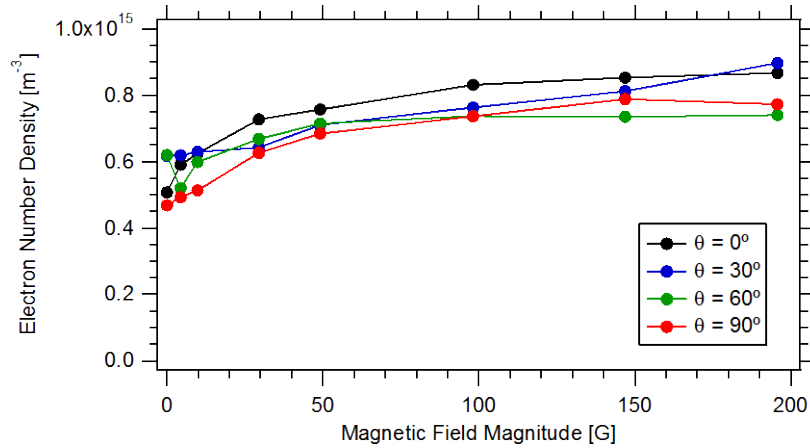


Figure 4-19. Calculated electron number density at various magnetic field magnitudes and orientations. An increasing magnetic field appears to create a slight increase in calculated number density.

The reason behind the negligible observed differences can be explained by considering the changes to the sheath formed around the probe. Ahedo et al. showed that the sheath formation is dictated by the relative magnitudes of the Debye length, λ_{De} , the electron cyclotron radius, λ_c , and the collisional mean free path, λ_m [60-62]. Due to the low number densities involved within this study as well as Hall thruster channels, the collisional mean free path is much larger than the other two scale lengths; thus, sheath formation is dictated by the ratio, λ_c/λ_{De} , given by

$$\frac{\lambda_c}{\lambda_{De}} = \sqrt{\frac{m_e n_e}{\epsilon_0 B^2}}. \quad (4-22)$$

Values representative of the plasma within a Hall thruster channel are compared to values from the present study in Table 4-4. Plasma parameters for the NASA-173Mv1 were taken from Refs. [11,24] for a 300-V discharge at nominal flow rate, and values were measured approximately 0.1 channel widths from each wall. The NASA-173Mv1 was taken as a typical thruster within its power class (5 kW), and while absolute values will vary from thruster to thruster, the ratio λ_c/λ_{De} should remain representative of a large class of Hall thrusters.

Table 4-4. Characteristic values of pertinent length scales near the walls of the NASA-173Mv1 and within the present study. Properties are based off a 300-V discharge at nominal flow rates.

	NASA-173Mv1 Outer Wall	NASA-173Mv1 Inner Wall	Present Study
Number Density [m^{-3}]	$7 \times 10^{17} - 10^{18}$	$7 \times 10^{17} - 10^{18}$	7×10^{14}
Electron Temperature [eV]	10 - 40	10 - 40	1.4
Cyclotron Radius [μm]	450 - 650	335 - 430	140 - 5650
Debye Length [μm]	30 - 40	30 - 40	335
λ_c/λ_{De}	15 - 16	10 - 12	0.4 - 17

For the present study, the transition point where $\lambda_c/\lambda_{De} \sim 1$ occurs at a magnetic field strength of 85 G. For conditions where $\lambda_c/\lambda_{De} \gg 1$, which are typical within Hall thruster channels, Ahedo [60] has shown that the sheath structure is comprised of three layers: a magnetized presheath, an unmagnetized Debye sheath, and a third intermediate layer called the Chodura layer. The purpose of the Chodura layer is to turn the magnetic-field-aligned flow within the presheath to the electric-field-aligned flow within the Debye sheath. Therefore, under these conditions, the magnetic field would have little effect on the sheath and measured properties as their influence is effectively “shielded out” by the Chodura layer.

For conditions where $\lambda_c/\lambda_{De} \leq 1$, the sheath is expected to be partially to completely magnetized and thus greatly affects the electron particle trajectories to the probe. However, these effects are not seen in the experimental data from this study. Since the primary effect of a magnetic-field-aligned flow of electrons would be a change in the effective probe collection area, one would expect only the calculated electron number density to be influenced; but in this particular study this trend is not seen. It is possible there are two competing effects present as magnetic field magnitude is increased: a decrease in calculated number density due to the shrinking probe collection

area; and an increase in calculated number density as the magnetic field confines the electron population into closer orbits. This is plausible since the number density is seen to increase with magnetic field strength until approximately 100 G where it then levels out; this magnitude is where the sheath is expected to become magnetized, thus leading to smaller collection areas.

Based on Table 4-4 and Refs. [11,24], the conditions most relevant for this study are at orientations 0-60° and magnitudes less than 10 G. Within this regime, the measured plasma properties are largely unaffected by the magnetic field. While it is possible that the calculated electron number density will be affected, it is likely that this can be easily corrected by using the projected probe area normal to the magnetic field as the collection area. Furthermore, all other plasma densities in this work are only calculated from the ion saturation current, which should be unaffected by the magnetic field since the ions within Hall thrusters are unmagnetized. It should be noted that a flow orientation of 90° had a slight effect on measured floating potentials and electron temperatures. Since this flow orientation was not observed inside the channel in the present work, its influence is outside the scope of this dissertation. However, such grazing angles may be encountered within the discharge channel in later stages of thruster lifetime, and thus these effects warrant further investigation.

4.5 Sheath Potential Determination

The potential difference formed between the bulk plasma and the floating channel wall is an important quantity that can have significant effects on thruster performance and lifetime. In general, the potential drop is given by

$$V_{sheath} = V_{wall} - V_p. \quad (4-23)$$

This potential difference is formed to attract ions and repel more mobile electrons from the floating wall, in order to balance the flux of positive and negative charge to the wall. Thus, the sheath potential restricts the particle and energy flux of electrons to the wall. Furthermore, the sheath can impart significant energy to incoming ions as they approach the wall, affecting both the ion energy and impact angle at the wall. These factors determine not only the ion energy flux to the wall but also the sputtering capability,

which is relevant to erosion. Equation (4-18) shows that sheath potentials can exceed five electron temperatures in front of an ideal, floating surface. With electron temperatures around 30 eV in a typical 300 V Hall thruster discharge [10-13], the sheath is capable of imparting energies of the same order as the axial electric field. Since the sheath potential has such a significant influence on wall power losses and erosion of the channel, it is important to obtain accurate measurements of the local plasma potential and the floating channel wall.

4.5.1 Effects of Secondary Electron Emission

While it is straightforward to measure the floating potential of a Langmuir probe, a measurement of the floating potential of the adjacent Hall thruster channel wall is complicated by the effects of secondary electron emission. While pure tungsten has a relatively low secondary electron emission (SEE) coefficient [63] in order to avoid complicated analysis of the resulting I-V characteristic, the insulating channel wall materials tend to have much higher SEE coefficients [64]. The SEE properties of the wall material have been shown to significantly affect thruster performance [7,65,66].

Electron emission from the surface acts to increase its potential (making it less negative), thus reducing the magnitude of the sheath potential. Another explanation of this phenomenon is that electron emission is equivalent to ion collection at the surface, thus reducing the necessary potential drop to balance the ion and electron currents to the wall. As secondary electron emission increases, the sheath potential magnitude continues to drop until the emission becomes space-charge-limited at the surface. At this point, the electric field at the surface reverses and prevents further emission from occurring (see Figure 4-20). The energy range over which this occurs is known as the charge saturation regime (CSR).

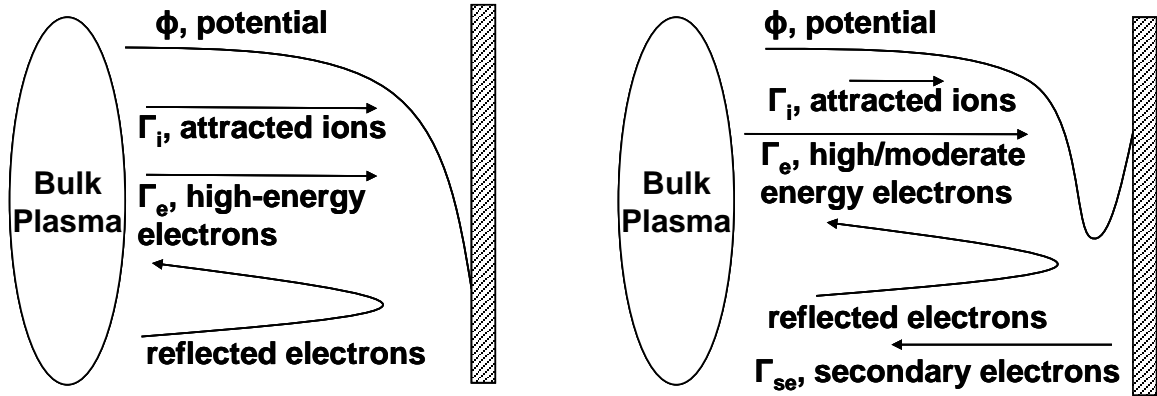


Figure 4-20. Comparison of sheath potentials in the absence of SEE (left) and when the sheath is in the charge saturation regime (right). In CSR, the sheath potential magnitude is small and the electric field at the surface is reversed.

However, the actual effect of SEE from the channel wall on the plasma within the thruster channel is presently under debate. While SEE from the wall can potentially affect sheath potentials and electron populations within the channel, it is possible that SEE from one wall passes through the bulk plasma to be recaptured by the opposing wall (see Figure 4-21). If this occurs, each flux of secondary electrons can cancel the other out by counter-streaming to the opposite wall. Thus, the extent to which SEE affects sheath potentials and the electron population is dependent upon the degree of thermalization within the bulk plasma [3,4].

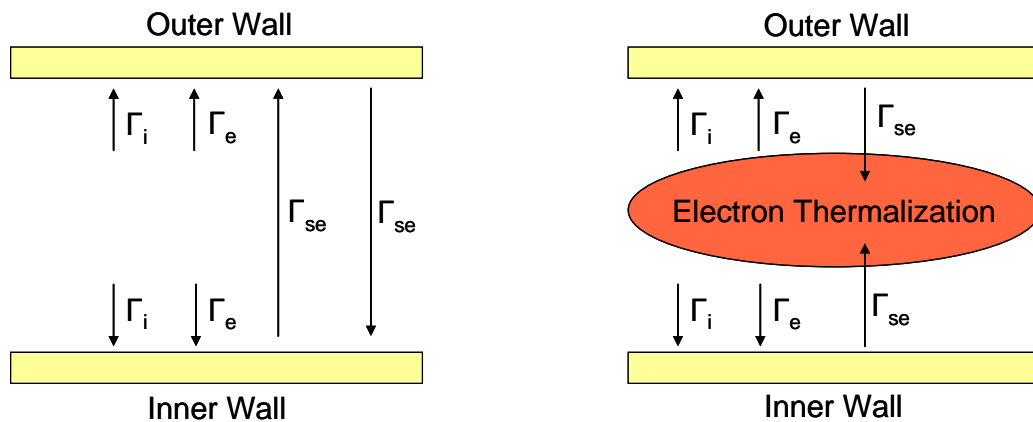


Figure 4-21. Diagram showing the effects of secondary electron fluxes and dependence on electron thermalization processes within the channel. If the two fluxes do not thermalize in the bulk plasma, they can counter-stream to the opposing wall and cancel each other out.

If complete thermalization occurs within the plasma, then the effects of secondary electron emission are described by the Hobbs and Wesson solution of space-charge-limited emission from a surface [42]. This model has already been implemented within

the hybrid-PIC Hall thruster simulation program HPHall-2 at JPL [67]. However, as mentioned before, the effects of SEE on the plasma are still under debate. Kinetic studies performed by Kaganovich et al. [68] have shown that the secondary electron fluxes from each wall move mostly undisturbed through the plasma, thus canceling each other out and having no effect on the sheath potential. However, due to the lack of collisions, a significant portion of high-energy electrons are lost to the walls and not replenished, resulting in reduced sheath potentials on the order of one electron temperature. Thus, determination of the degree of thermalization is critical towards understanding how SEE affects sheath potentials within a Hall thruster.

4.5.2 Implications of Measured Sheath Potentials

The measured sheath potentials of the internal wall-mounted probes can provide information on the electron population within the Hall thruster channel. Figure 4-22 gives the measured sheath potentials as a function of measured electron temperature. The Hobbs and Wesson solution for tungsten (probe material) and boron nitride (channel wall material) are provided for reference. The SEE properties for tungsten were calculated from a power law fit to data taken from Ref. [63], while the data for boron nitride were taken from Refs. [67,69]. The ideal case with no SEE effects, given by Eq. (4-18), is also shown.

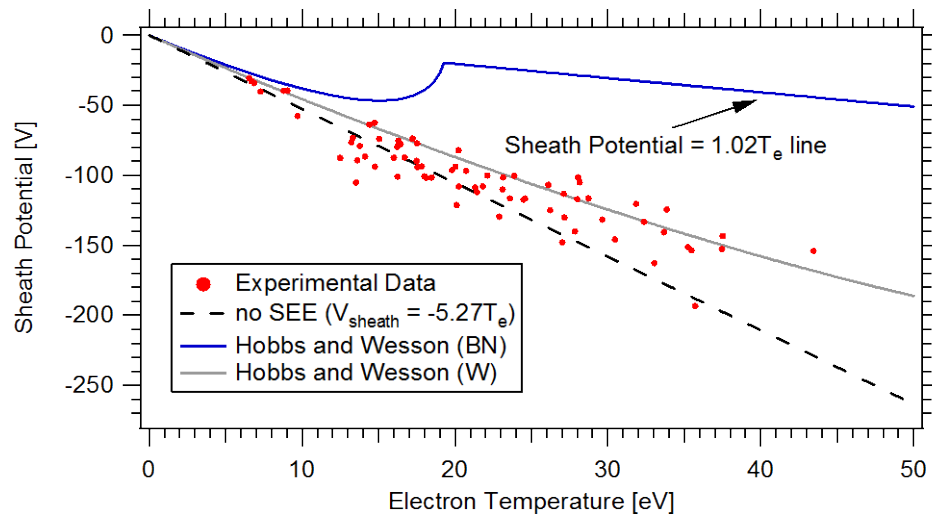


Figure 4-22. Measured sheath potentials as a function of measured electron temperature using internal wall-mounted probes within the 6-kW Hall thruster. Near-ideal sheath potentials indicate a large population of high-energy electrons, which provide evidence of thermalization processes within the bulk plasma.

While the measured potentials do not precisely follow the ideal solution or the Hobbs and Wesson solution for tungsten, most of the data are in between these two curves. A linear fit to the experimental data gives a slope of approximately -4.6, very close to the ideal value of -5.27. Thus, large sheath potentials on the order of five electron temperatures are measured by the imbedded wall probes. This is of critical significance: such large sheath potentials indicate that electron current was still collected by the probe when biased several electron temperatures below plasma potential. This result is clear evidence of the presence of high-energy electrons near the channel walls of a Hall thruster. Furthermore, this shows that high-energy electrons are not depleted but replenished within the plasma, likely by some thermalization mechanism.

The presence of thermalization within the channel is surprising due to the low collision frequency expected in the ionization and acceleration zones. Using an electron collision frequency of 3×10^6 Hz, a typical measured value near the exit plane of the 6-kW Hall thruster [13], a 25 eV electron will have to travel approximately 0.5 m before encountering a collision. This length is much longer than any characteristic length of the thruster, including the channel width. However, simulations performed by King [70] have shown that magnetic mirror effects and radial electric fields allow electrons to bounce between walls while they drift azimuthally around the channel. It is therefore conceivable for the electron path length to greatly exceed the channel width before hitting any walls.

While the exact details of this mechanism are currently unknown, the near-ideal measured sheath potentials are an indication of a high degree of thermalization. To the author's knowledge, this is the first direct experimental evidence of such electron thermalization within a Hall thruster channel. For these reasons, it is reasonable to assume that the SEE effects on sheath potential are significant, and that the Hobbs and Wesson solution can be used to obtain the proper sheath potentials within the Hall thruster channel.

4.5.3 Final Sheath Potential Model

Given the strong experimental evidence of electron thermalization, the method of determining sheath potentials in this study is identical to that found within the HPHall-2 simulation code used by JPL [67,69]. The Hobbs and Wesson model [42] was solved

numerically and a curve fit was created to determine the sheath potential dependence on SEE coefficient:

$$V_{sheath} = \ln(A(1 - \delta_w)) - \frac{B}{(1 - \delta_w)^2} - \frac{C}{(1 - \delta_w)^3} - \frac{D}{(1 - \delta_w)^4}. \quad (4-24)$$

Values of the fitting coefficients A , B , C , and D are 195.7, 1.29×10^{-4} , -3.45×10^{-6} , and 3.69×10^{-8} , respectively. The SEE coefficient, δ_w , is determined from a linear curve fit to experimental data that accounts for backscattered electrons:

$$\delta_w = \delta_0 + (1 - \delta_0) \frac{2T_e}{E_I}, \quad (4-25)$$

where δ_0 is the SEE coefficient at zero electron energy and E_I is the incident energy at which the SEE coefficient is unity. Values used for boron nitride are $\delta_0 = 0.54$ and $E_I = 40$ eV.

The above equations are only valid at incident energies below the crossover energy. At this energy, the sheath becomes space-charge-limited and the sheath potential is reduced to $-1.02T_e$. This occurs at an SEE coefficient of

$$\delta_w = \delta_w^* = 1 - 8.3 \sqrt{\frac{m_e}{M_i}}, \quad (4-26)$$

which is 0.983 for a xenon plasma. For boron nitride, this corresponds to a crossover temperature of 19.3 eV. Thus, for electron temperatures below 19.3 eV, Eqs. (4-24) and (4-25) were used to determine the sheath potential of the floating channel wall. For electron temperatures above 19.3 eV, the sheath potential was set equal to $-1.02T_e$. Corresponding values for various other Hall thruster wall materials can be found in Ref. [23].

Since this method of determining sheath potential is dependent upon the electron temperature, the uncertainty associated with this calculation was found to be within $\pm 15\%$ at almost all temperatures except near the crossover temperature of 19.3 eV. Calculation of the propagation of uncertainty shows that around the crossover temperature the uncertainty can be well over 100%. This sensitivity will be further discussed in Section 7.4, where it is determined to be important towards calculations of electron power to the channel walls. However, due to the small range of electron temperatures where this sensitivity occurs, the uncertainty in sheath potential is reported at $\pm 15\%$ unless otherwise noted.

4.6 Summary

This chapter discussed the various studies performed to improve the data analysis techniques for flush-mounted Langmuir probes. In particular, techniques were developed or proposed to determine the ion saturation current, plasma potential, and wall sheath potential. A hybrid-PIC code, CEX2D, was used to characterize the sheath expansion around a flush probe, and a model was developed that can be applied to experimental data to correct for such effects. The derivative method of determining plasma potential was found to be most accurate when compared to the more robust measurements from a swept emissive probe. Also, magnetic field effects were found to be negligible under the typical conditions expected along Hall thruster channel walls.

Lastly, secondary electron emission was found to strongly affect sheath potentials within Hall thrusters. Measured sheath potentials were found to approach five times the electron temperature, indicating the presence of high-energy electrons. These electrons would be quickly lost to the channel walls if thermalization processes were not present to replenish the population. The thermalization of electrons within the bulk plasma indicates that secondary electrons don't stream collisionlessly across the channel, and thus can strongly influence the sheath potential along the channel walls. For this reason, sheath potentials are assumed to follow the Hobbs and Wesson solution [42] of space-charge-limited emission.

Chapter 5

Characterization of the Near-Wall Plasma

This chapter presents measured values of various plasma parameters along the channel walls of the 6-kW Hall thruster. In an effort to characterize the near-wall plasma and differentiate it from the rest of the bulk discharge, data from the internal wall-mounted probes are compared to measured values inside the channel taken by Reid [13]. Details of the data collection using the internal wall-mounted probes are first provided. A brief summary of the prior internal measurements taken by Reid are then described. Plasma potential, electron temperature, and ion number density along the inner and outer channel walls are then characterized and compared to each other as well as to values within the bulk discharge. Finally, measured electron energy distribution functions are presented, and implications of the structure are discussed.

5.1 Discussion of Data Collection

Table 5-1 provides a full list of the operating conditions tested using the internal wall-mounted probes, spanning a wide range of discharge voltages (150 – 600 V), anode flow rates (5 – 30 mg/s), and discharge powers (0.5 – 10.1 kW). This allowed for various trends to be extracted as a function of all these parameters. The order in which data were collected was driven primarily by priority of desired points; therefore, the nominal operating condition of 300 V and 20 mg/s anode flow rate was first tested. This was then followed by variations in discharge voltage (with focus on 10 mg/s anode flow rate). Higher-power conditions were mixed in with lower-power conditions, since the compact LaB₆ cathode had difficulty sustaining the discharge at low power (< 2 kW) and required intermittent heating at higher-power operating points. The high-power condition of 10.1 kW was tested last due to concerns of probe failure. Data collection for each operating condition took approximately 30 minutes. The thruster was operated for approximately

30 minutes at each operating condition prior to data collection to allow the discharge current to settle. Thus, the total duration for the experiment was approximately 15 hours, with the thruster operating almost continually.

Table 5-1. List of operating conditions tested using internal wall-mounted probes, spanning a wide range of discharge voltages, mass flow rates, and discharge powers. Shaded operating conditions represent the data presented in this work.

Discharge Voltage [V]	Anode Flow Rate [mg/s]	Discharge Current [A]	Discharge Power [kW]	Order of Data Collection
150	5	3.4	0.52	14
150	10	8.9	1.3	3
150	20	21.4	3.2	2
150	30	35.7	5.4	10
200	5	3.5	0.71	13
200	10	8.9	1.8	4
250	5	3.8	0.94	12
250	10	8.7	2.2	5
300	5	4.1	1.2	11
300	10	8.7	2.6	6
300	20	20.1	6.0	1
300	30	33.8	10.1	15
400	10	8.8	3.5	7
500	10	9.0	4.5	8
600	10	9.2	5.5	9

While data were collected at all 15 operating conditions, various issues prevented all the data from being presentable. Data at 300 V and 30 mg/s anode flow rate are not included in this work due to probe failure in the middle of data collection. Data at 600 V and 10 mg/s anode flow rate is also not included because the experimental apparatus was only capable of probe biases up to 420 V (above ground). This maximum bias was chosen to optimize voltage resolution at low and moderate discharge voltages, where most of the data were collected. Thus, measured plasma potentials at 600 V were found to be questionable due to the limitations of the measurement circuit. Finally, all data at 5 mg/s anode flow is not included due to low probe current signal, primarily affecting the measured ion saturation current. Furthermore, data collection at 5 mg/s was difficult due

to inherent thruster instabilities; this was likely caused by insufficient cathode heating at such low discharge power.

Data from the nominal operating condition of 300 V and 20 mg/s anode flow rate will be focused on within Chapter 5 and Chapter 6. The remaining operating conditions will be included in Chapter 7 when discussing trends in incident ion power to the channel walls. Additional data from these operating conditions can be found in Appendix B.

While data collected at the remaining nine operating conditions were found to be presentable, certain issues with the wall-mounted probes found after the end of the test are worth mentioning. In particular, signs of leakage current as well as probe degradation are discussed below.

5.1.1 Leakage Current

The presence and effects of leakage current in wall-mounted probes has been previously documented by Warner [17]. Due to the extreme environment the probe is subjected to, insulation of the probe lead wires are prone to failure. While great care was taken to properly insulate all lead wires, leakage current was found to occur with one of the internal wall-mounted probes along the inner channel wall.

Leakage current occurs when current can be collected from the plasma along any portion of the wire that is normally insulated. This usually results in extra electron current being collected continually along the entire I-V characteristic, causing a reduction in measured floating potential and ion saturation current. Figure 5-1 shows an example of the signs of leakage current with a probe along the inner wall, when compared to an I-V characteristic taken along the outer wall at the same axial location. The increased electron current causes a significant reduction in measured ion current at low probe biases, to the point where the data in the ion saturation branch of the I-V characteristic can not be salvaged with any confidence.

The evidence of leakage current is further substantiated when comparing the floating potential to other values measured along the channel wall. As discussed in Section 7.2.2.1, the floating potential within the channel should follow a sigmoid function when plotted against axial position. Figure 5-2 shows an example of measured floating potential (with respect to ground) as a function of position, with the sigmoid fit included for comparison. It is evident that the data point at $z = -0.095$ channel lengths is much

lower than expected based on the sigmoid function, which fits the remaining data quite well.

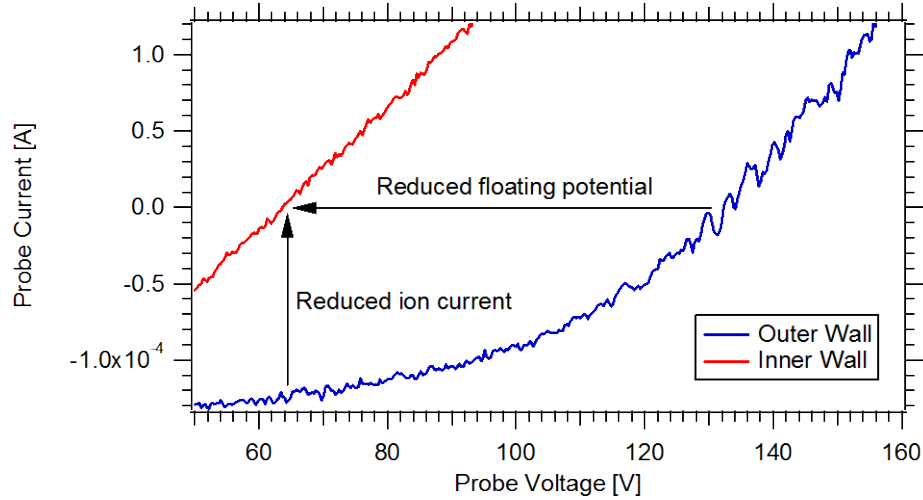


Figure 5-1. Example of leakage current found with a probe along the inner wall at 300 V, 20 mg/s anode flow rate. Compared to the outer wall, which should have similar properties, the floating potential and ion current is reduced along the inner wall due to extra collected current.

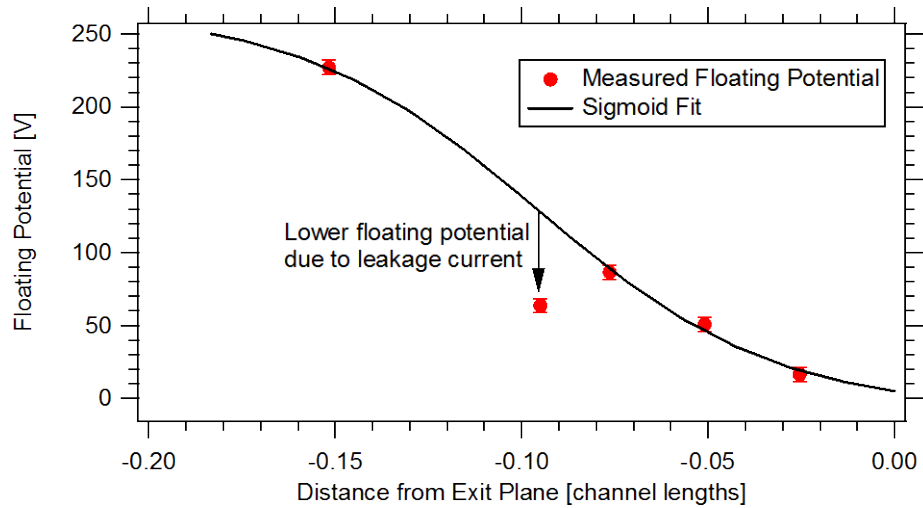


Figure 5-2. Measured floating potentials (with respect to ground) along the inner wall at 300 V and 20 mg/s anode flow rate. All data points fit the expected sigmoid function except for the point at $z = -0.095$ channel lengths, which has a significantly reduced floating potential due to leakage current.

Despite the significant effects of leakage current on the measured floating potential and ion saturation current, values of calculated electron temperature and plasma potential were found to be largely unaffected by the increased electron current. This is likely due to the fact that the ion saturation current and floating potential, found in a region of the I-V characteristic where the probe current and the derivative (dI/dV) are low, are very sensitive to small changes in current. On the other hand, the electron

temperature and plasma potential are measured in a region of the I-V characteristic that is largely insensitive to small changes in current. Therefore, these quantities are presented despite the presence of leakage current, while the floating potential and ion current density are not.

5.1.2 Probe Degradation

The harsh environment of the channel, including exposure to fluxes of high-energy ions and electrons, has the ability to degrade the probe over time. In particular, sputtering of probe material can cause the probe to change shape and recede into the channel wall. Figure 5-3 shows a microscope photograph of one of the internal wall-mounted probe tips after the end of the test. The probe diameter is approximately 350 μm . Portions of the probe have been preferentially sputtered away, leaving a tip that is no longer flat.

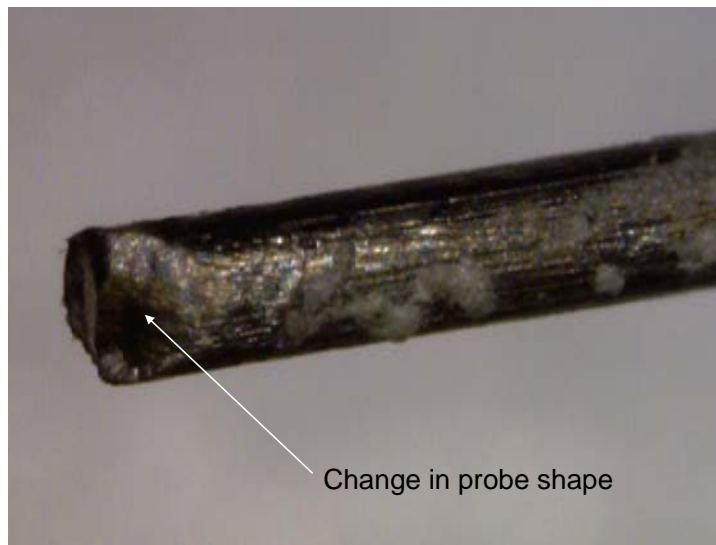


Figure 5-3. Microscope photograph of an internal wall-mounted probe tip removed from the wall after the end of the test. Preferential sputtering on one side has created a slanted surface such that the probe tip is no longer flat.

Figure 5-4 shows a microscope photograph of an internal wall-mounted probe prior to removal, after the end of test. The probe appears to be recessed within a pit created by sputtering of surrounding wall material. This “pitting” phenomenon has been documented previously by Szabo et al. [16]. Most of the probes within this study exhibited some degree of pitting by the end of the test.

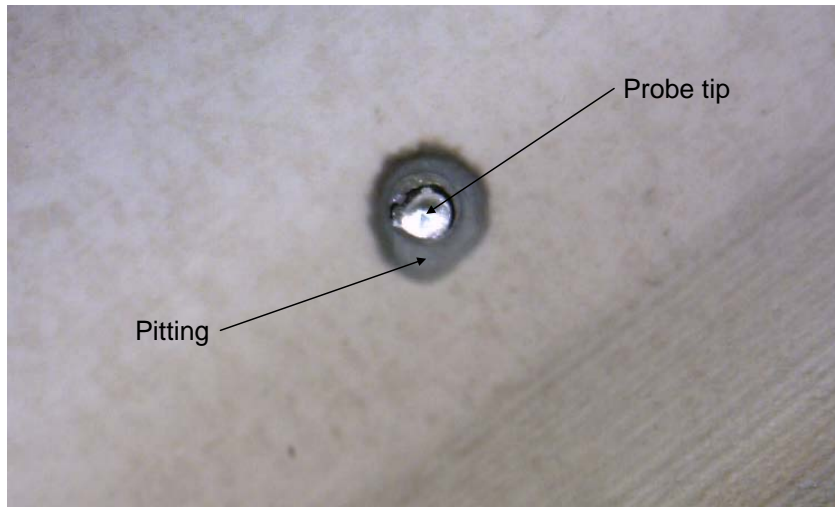


Figure 5-4. Microscope photograph of an internal wall-mounted probe prior to removal, after the end of the test. A portion of the wall surrounding the probe has been sputtered away, leaving the probe within a “pit.”

The significant deterioration of the internal wall-mounted probes is likely the result of extensive testing at high anode flow rates, discharge voltages, and discharge powers. Despite this degradation, the calculated plasma parameters at operating conditions near the end of the test (in particular, at 150 V and 30 mg/s anode flow rate) still appear to be reasonable. There are two possible explanations for this observation. The first is that most of the observed degradation occurred at the end of the test when attempting to take data at 300 V and 30 mg/s anode flow rate, where probe failure occurred due to extreme heat loading. Unfortunately, there is no way to discern whether this is the case, since the probes were not inspected until the end of the 15-hour test. It is recommended for future experiments involving internal wall-mounted probes that either the test be completed in smaller time intervals with probe inspection occurring in between, or having an in-situ apparatus available to closely monitor probe integrity during the test.

The second explanation is that the probe degradation did not significantly affect the data collection. This is possible if the degradation features are relatively small (less than a few Debye lengths); they would then be “smoothed” out by the sheath boundary (see Figure 5-5). Due to reasonable measured values of electron temperature, plasma potential, and floating potential, and the independence of these values on the probe area, no attempts were made to correct these data. The ion current density and corresponding number density, however, are affected by the probe area, which could significantly

change due to probe degradation. Since the probes were recessed within the wall and not protruding out, the increase in probe area is not expected to be significant. Furthermore, the sheath expansion characteristics around the probe are accounted for with the model described in Section 4.2, and appear to reasonably correct the data. For these reasons, the ion saturation current is not corrected for any changes in area due to probe degradation.

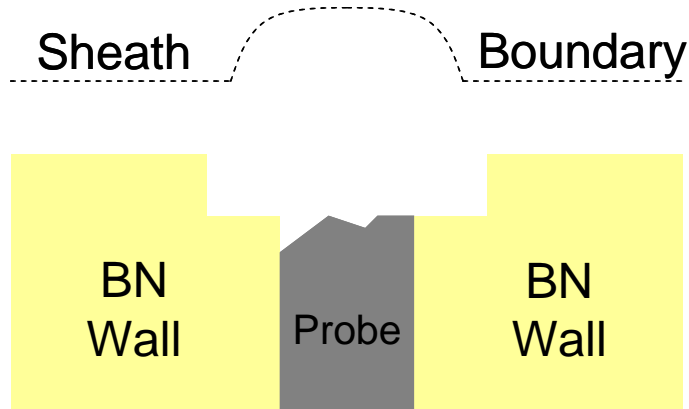


Figure 5-5. Illustration showing how the sheath boundary can smooth over features of degradation if they are small (less than a few Debye lengths). Not to scale.

5.2 Prior Internal Measurements

Spatially-resolved distributions of plasma potential, floating potential, electron temperature, and ion number density have been taken within the channel of the 6-kW thruster by Reid [13]. Figure 5-6 shows the domain of these internal measurements with respect to the thruster anode and channel walls.

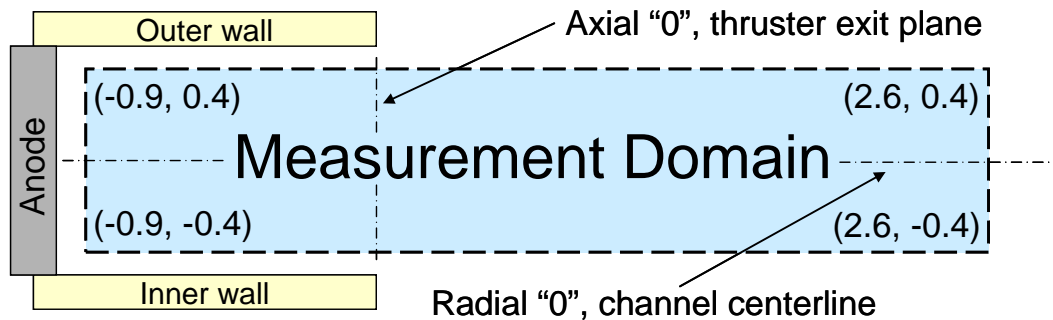


Figure 5-6. Schematic showing the measurement domain of prior internal measurements taken by Reid. Corner coordinates are given in (z,r) format, with axial location in units of channel lengths and radial location in units of channel widths. Not to scale.

Measurements of floating potential, electron temperature, and ion number density were taken with a cylindrical Langmuir probe while plasma potential was measured with

a floating emissive probe. All probes were mounted onto the HARP, and reciprocated in the axial direction at several radial locations. Reid investigated numerous methods of determining ion number density from the ion saturation current, including thin-sheath approximations, orbit-motion-limited (OML) theories, and a blending method that weight-averaged the thin-sheath and OML values based on a self-consistently calculated Debye length. The densities determined from the blending method will be presented here, since it yielded the most physically reasonable density distributions at nominal conditions of 300 V and 20 mg/s anode flow rate.

In order to characterize the plasma near the channel walls, measurements from the internal wall-mounted probes are compared to axial distributions at two different radial locations: channel centerline, and the radial location closest to the channel wall. The distribution along $r = -0.4$ channel widths will be referred to as the “bulk plasma inner bound” while the distribution along $r = 0.4$ channel widths will be referred to as the “bulk plasma outer bound.”

5.3 Comparison of Plasma Parameters

5.3.1 Plasma Potential

The local plasma potential distribution is an important parameter as it determines the strength of the radial and axial electric fields that accelerate ions towards the wall. Thus, these fields can greatly influence the energy and trajectories of ions that ultimately determine the erosion rate of the dielectric wall. Figure 5-7 and Figure 5-8 compare axial profiles of plasma potential at three different radial locations within the discharge channel. The data corresponds to the nominal operating condition of 300 V and 20 mg/s anode flow rate. All values reported are with respect to the cathode; plasma potentials measured with respect to ground were corrected for the cathode-to-ground voltage, typically around -10 V.

The acceleration zone corresponds to the region where the plasma potential significantly drops, and occurs around the thruster exit plane. Upstream of this zone, the plasma potential is uniform not only in the axial direction, but also in the radial direction, with differences less than 5 V. It is interesting to note that this uniformity extends all the

way to the channel walls. This indicates that there are negligible axial and radial electric fields within the plasma for approximately 90% of the channel.

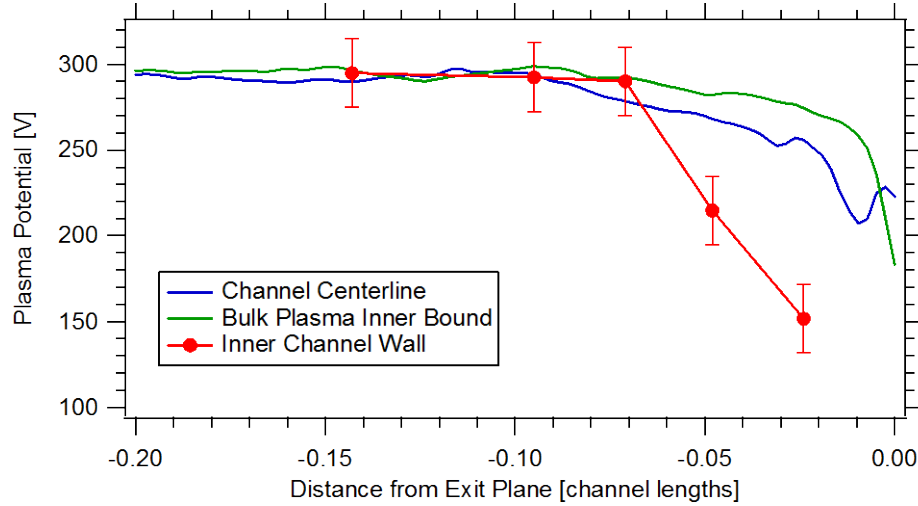


Figure 5-7. Axial profiles of plasma potential at three different radial locations within the channel, under the nominal operating condition of 300 V and 20 mg/s. The plasma begins to accelerate further upstream when close to the channel wall.

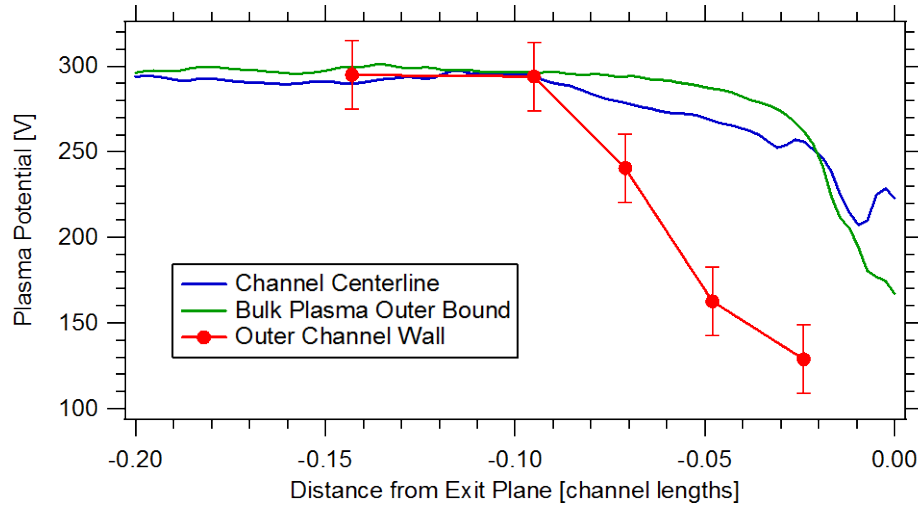


Figure 5-8. Axial profiles of plasma potential at three different radial locations within the channel, under the nominal operating condition of 300 V and 20 mg/s. The plasma begins to accelerate further upstream when close to the channel wall.

At both the inner and outer channel walls, the plasma begins to accelerate further upstream than the bulk plasma. While this difference is only ~ 5% of the channel length, the sharp drop off of the plasma potential in the axial direction creates significant differences in the radial direction. Near the exit plane, these radial electric fields can reach 40-50 V/mm, which are comparable to the axial electric fields set up within the acceleration zone [13]. It is worth noting that this is a lower bound to the radial electric

field, since the distance over which the measured potential difference occurs is uncertain and could be smaller; larger electric fields could potentially exist closer to the channel walls. These electric fields also appear to be restricted to 0.1 channel widths from the walls, as the data taken within the bulk discharge do not indicate significant radial electric fields.

Figure 5-9 compares the measured axial profiles of plasma potential between the inner and outer channel walls at 300 V and 20 mg/s anode flow rate. While the plasma at the outer wall begins to accelerate slightly upstream of the plasma at the inner wall, the electric fields at both walls are roughly equal. The similarity between the inner and outer wall is expected due to the symmetric magnetic field topology used throughout the study; therefore, the magnetic field shape, which heavily influences the plasma potential distribution, should be equivalent along the inner and outer channel wall.

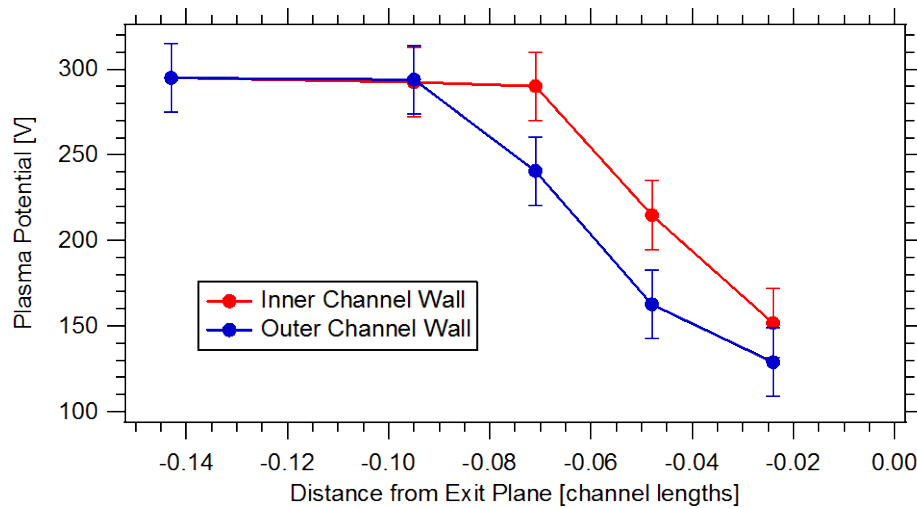


Figure 5-9. Comparison of axial plasma potential profiles between the inner and outer channel wall near the thruster exit plane at 300 V and 20 mg/s. The plasma at the outer wall accelerates slightly upstream of the plasma at the inner wall.

The relative locations of the acceleration zone between the walls and channel centerline is unexpected given the “plasma lens” magnetic field topology. Along magnetic field lines, the electron momentum equation is typically simplified by neglecting inertial terms. Thus, in equilibrium, the electric field and electron pressure forces are balanced and a relation can be derived between the plasma potential and the plasma number density. Under assumption of constant electron temperature, this relation is the well-known Boltzmann relation of thermalized potential [49]:

$$\phi = \phi_0 + T_e \ln\left(\frac{n}{n_0}\right), \quad (5-1)$$

where T_e is the electron temperature in eV, ϕ is the thermalized potential, n is the plasma number density, and ϕ_0 and n_0 are reference values. Therefore, along a magnetic field line, the potential is typically constant to within an electron temperature. For this reason, magnetic field lines are often considered to resemble equipotentials within the thruster. Figure 5-10 shows the expected plasma potential profiles near the wall and at channel centerline under this assumption. Due to the plasma lens configuration, the plasma potential drop-off near the wall should occur downstream of the drop-off at channel centerline. This would create radial electric fields pointed away from the thruster walls, creating the ion focusing effect typical of plasma lens configurations. Furthermore, since the same plasma potential drop occurs over a shorter axial range, the electric field is expected to be stronger at the wall. Neither of these trends is noticed in the experimental data of this study. For the 6-kW Hall thruster, the acceleration zone is close to the exit plane, where the magnetic field lines are mostly radial; thus, these trends are not expected to be highly defined. However, it will be shown in Chapter 6 that large plasma density gradients between channel centerline and the wall cause significant deviations of equipotentials from magnetic field lines, even when the Boltzmann relation is enforced. The concept of the thermalized potential will be further discussed in Sections 5.3.2 and 5.3.3.

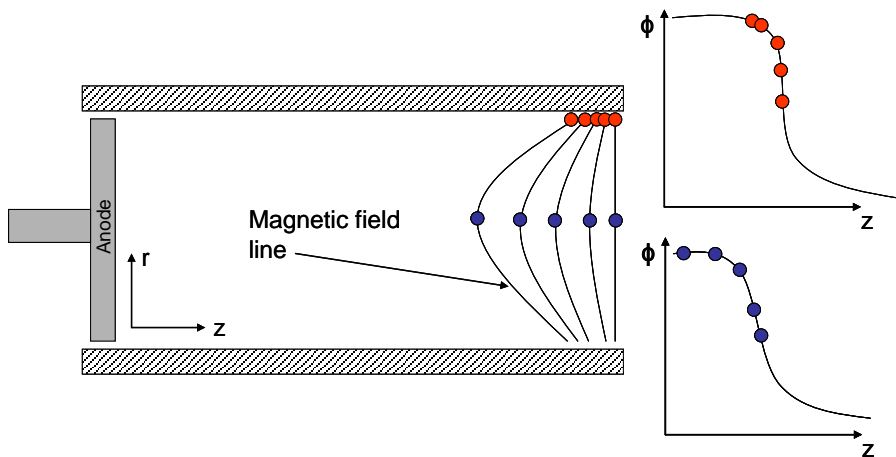


Figure 5-10. Comparison of expected near-wall and centerline plasma potential profiles, assuming magnetic field lines act as equipotentials. The acceleration zone near the wall moves downstream and contains larger axial electric fields, creating radial electric fields away from the walls (plasma lens topology).

5.3.2 Electron Temperature

The electron temperature distribution within a Hall thruster discharge channel is an important parameter that indicates the balance between energy gains via joule heating and energy losses such as those from radiation, ionization, and to the channel walls. Thus, this distribution dictates the levels of ionization within the channel; it also affects the sheath potential distribution along the channel, both of which influence power losses to the wall as well as erosion rates. Figure 5-11 and Figure 5-12 show comparisons of axial distributions of electron temperature at various radial locations within the thruster close to the exit plane. The data corresponds to nominal operating conditions of 300 V and 20 mg/s anode flow rate.

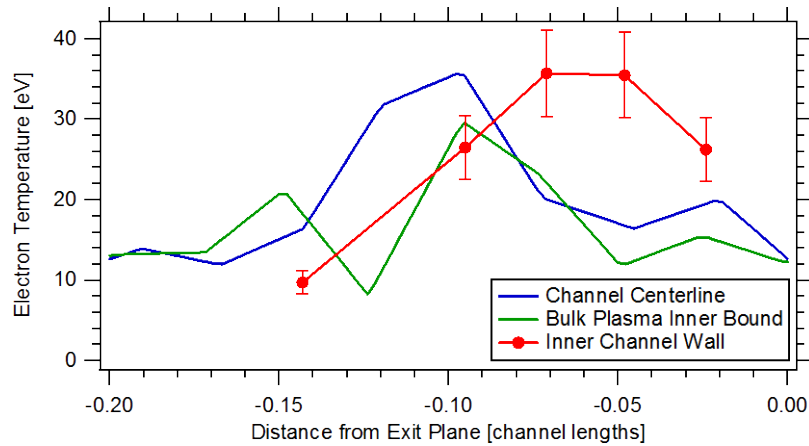


Figure 5-11. Comparison of axial profiles of electron temperature at three different radial locations, under nominal operating conditions of 300 V and 20 mg/s. Peak electron temperatures are comparable but occur slightly downstream close to the wall.

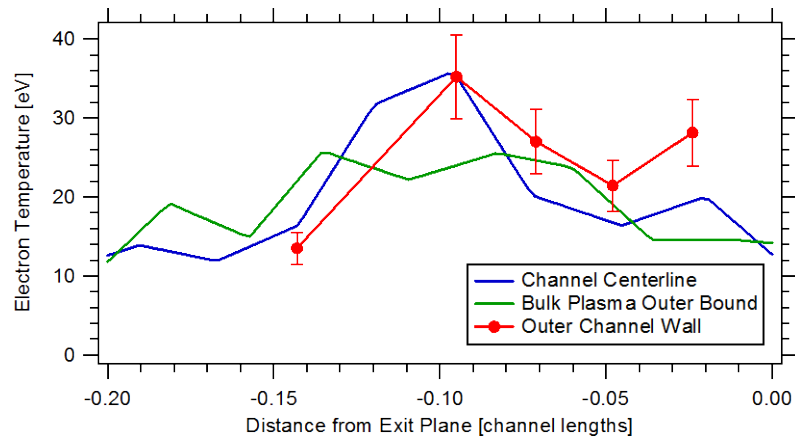


Figure 5-12. Comparison of axial profiles of electron temperature at three different radial locations, under nominal operating conditions of 300 V and 20 mg/s. Peak electron temperatures are comparable at all radial locations.

At both inner and outer channel walls, the peak electron temperature appears to be consistent with measured values within the bulk plasma discharge. The location of this peak is also roughly constant across all radial locations (within 2% of the channel length); however, this location occurs slightly upstream of the acceleration zone in the bulk discharge while occurring slightly downstream of the acceleration zone near the wall. Given the general agreement between bulk plasma and near-wall measurements in terms of both peak location and magnitude, it appears the isothermal approximation along magnetic field lines is valid since they are nearly radial in this region. Also, since the peak magnetic field occurs around the beginning of the acceleration zone near the exit plane, this region (last 10% of discharge channel) is subject to large wall power losses from high-energy electrons as well as high-energy beam ions.

Figure 5-13 compares the axial profile of electron temperature between the inner and outer channel walls. As with prior results, the peak electron temperatures are highly consistent across the channel, further validating the isothermal approximation along magnetic field lines. The peak temperature along the outer wall appears to occur slightly upstream of the peak along the inner wall, consistent with the acceleration zone locations described in Section 5.3.1. A peak electron temperature of 35 eV, roughly 10% of the discharge voltage, is consistent with prior internal measurements [11,13,38].

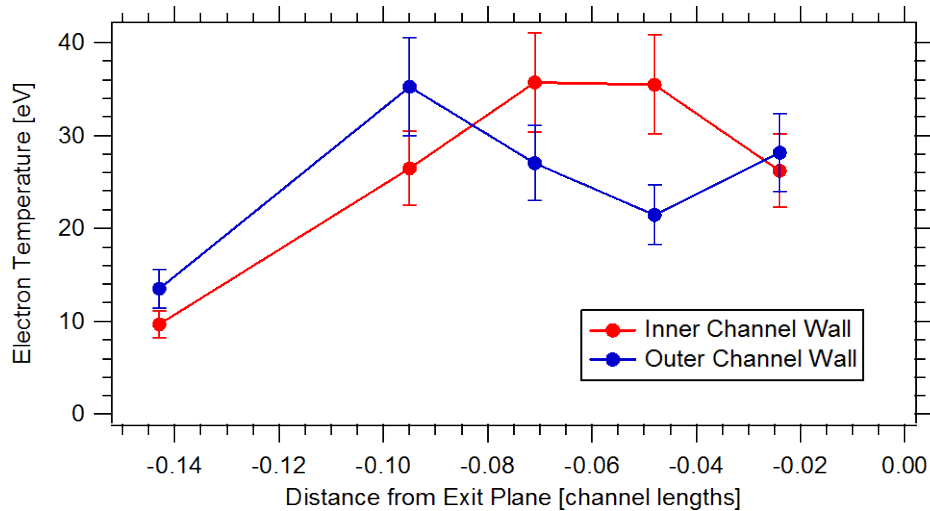


Figure 5-13. Comparison of axial profiles of electron temperature between inner and outer channel walls near the thruster exit plane at 300 V and 20 mg/s. Peak electron temperatures are consistent between the two walls, with the peak along the outer wall occurring slightly upstream of the peak along the inner wall.

5.3.3 Ion Number Density

The ion number density distribution along the channel walls of a Hall thruster is directly proportional to the ion current density to the walls, which affects ion power deposition and sputtering yields of wall material. Therefore, it is important to characterize this distribution in comparison to the bulk plasma within the channel. In this work, the ion number density at the wall was calculated using two different methods. For both techniques, the ion current density was found using the model described in Section 4.2.4. The first method assumes that the ions enter the sheath at the Bohm velocity, calculated using the local electron temperature:

$$j_i = en_i \sqrt{\frac{eT_e}{M_i}}. \quad (5-2)$$

It should be noted that the calculated ion number density is at the sheath edge; this is due to the relatively large presheath lengths expected within the channel, which make it unphysical to calculate a “bulk plasma” ion density beyond the theoretical presheath boundary. Based on the reported $\pm 40\%$ uncertainty in ion current density and $\pm 15\%$ uncertainty in electron temperature, the calculated uncertainty in the number density with this method is $\pm 47.5\%$. The second method takes into account that ions may enter the sheath supersonically when the acceleration zone is reached. Thus, the ion current is taken to be comprised of a beam entering the sheath with a velocity greater than the Bohm velocity:

$$j_i = en_i u_{\perp} = en_i \sqrt{\frac{2e\varepsilon_{\perp}}{M_i}}. \quad (5-3)$$

The normal velocity, u_{\perp} , is calculated using the corresponding normal energy, ε_{\perp} , which is determined using analysis techniques described in Section 8.2. If no normal energy is detected, Eq. (5-2) is used to determine the ion number density. Given a calculated uncertainty in the measured normal energy of $\pm 40\%$, the uncertainty in number density with this method is $\pm 60\%$.

Figure 5-14 and Figure 5-15 show the calculated ion number density axial profiles at several different radial locations within the 6-kW Hall thruster operating at 300 V and 20 mg/s anode flow rate. The data at $z = -0.095$ channel lengths along the inner wall are not included due to the probe at that location showing signs of leakage current (see

Section 5.1.1 for details). The increased electron current to the probe significantly decreased the measured floating potential and ion current, but did not appear to greatly affect the measured electron temperature and plasma potential. Thus, the data from this probe was reported in previous axial profiles but not in the ion density profiles below.

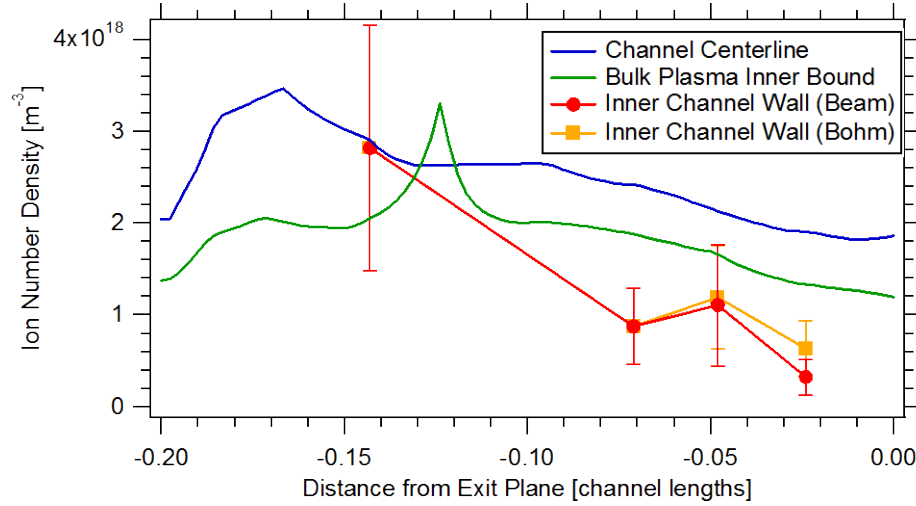


Figure 5-14. Comparison of axial profiles of ion number density at three different radial locations, under nominal operating conditions of 300 V and 20 mg/s. Near the exit plane, the difference between the plasma at centerline and at the wall can approach an order of magnitude.

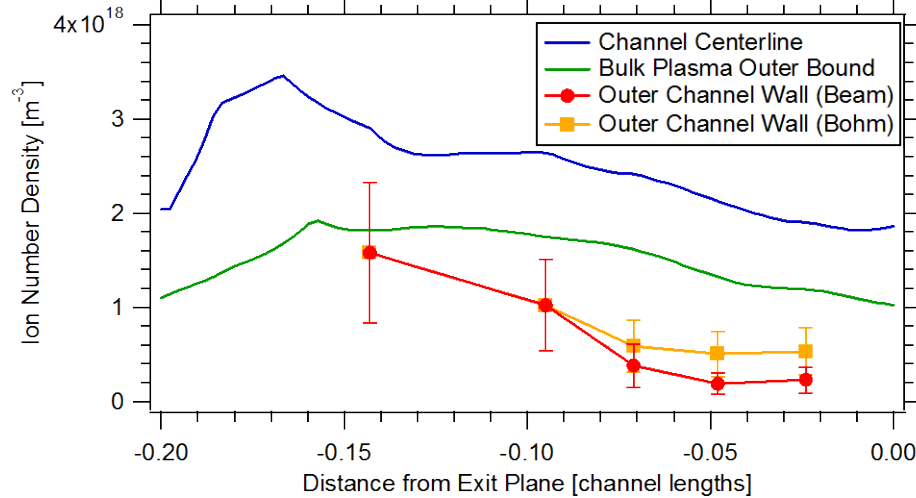


Figure 5-15. Comparison of axial profiles of ion number density at three different radial locations, under nominal operating conditions of 300 V and 20 mg/s. Near the exit plane, the difference between the plasma at centerline and at the wall can approach an order of magnitude.

Along both the inner and outer channel walls the ion number density is lower than within the bulk plasma. Indeed, prior measurements indicate a decrease in density even from channel centerline to the bulk plasma boundaries. Before the plasma accelerates, this decrease is limited to a factor of 2-3X; however, within the acceleration zone near the

exit plane this decrease can approach an order of magnitude (see Table 5-2). It is worth noting that, as expected, the two methods of calculation yield identical answers before the plasma reaches the acceleration zone. Once the plasma accelerates, the ions begin to enter the sheath supersonically, causing the Bohm approximation to differ from the beam calculation by roughly a factor of two.

Table 5-2. Comparison of number densities along the walls to those along channel centerline at 300 V and 20 mg/s. Reported values use the beam-calculated number density, and location is in units of channel lengths from the thruster exit plane.

Location	$n_{\text{wall}}/n_{\text{centerline}}$ (Inner wall)	$n_{\text{wall}}/n_{\text{centerline}}$ (Outer wall)
$z = -0.143$	0.98	0.55
$z = -0.095$	N/A	0.39
$z = -0.071$	0.36	0.16
$z = -0.048$	0.52	0.088
$z = -0.024$	0.17	0.12

Figure 5-16 compares the axial profiles of ion number density between inner and outer channel walls. The measured plasma density is consistently higher along the inner wall, with differences of approximately 1.5-2X before the plasma accelerates. This difference diminishes as the exit plane is approached, and the plasma becomes more symmetric about the channel centerline. The difference between inner and outer channel walls is surprising given the symmetric magnetic field topology used in this study. However, slight asymmetries have already been shown to exist in electron temperature and plasma potential that could influence (or have been influenced by) the differences in plasma density.

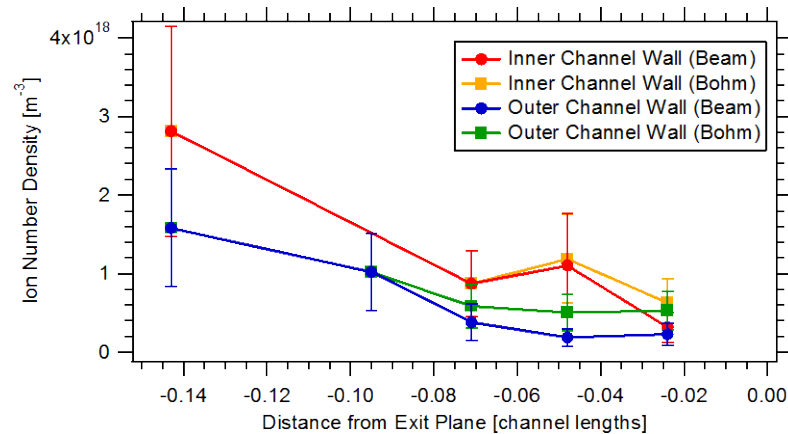


Figure 5-16. Comparison of calculated ion number densities along the inner and outer channel walls, under nominal operating conditions of 300 V and 20 mg/s. The density along the inner wall is consistently higher than along the outer wall, with this difference diminishing near the exit plane.

In order to test the validity of Boltzmann's relation of thermalized potential introduced in Section 5.3.1, Eq. (5-1) was used to determine the plasma number density along the channel walls. Magnetic field lines were traced from the locations of the internal wall-mounted probes to channel centerline, and values of plasma potential, ion number density, and electron temperature were found at these locations from prior internal measurements by Reid [13]. The magnetic field lines were taken from simulations of vacuum conditions performed in MagNet. These values were then used with the measured plasma potentials in this study to determine the expected ion number density along the walls. The electron temperature used was an average between the electron temperature measured at the wall and at channel centerline along the same magnetic field line.

Figure 5-17 shows the comparison of axial profiles between measured values of ion number density and those calculated using Boltzmann's relation. The thermalized potential assumption appears to overestimate the density near the wall prior to plasma acceleration, while underestimating it once the plasma accelerates. The plasma density is overestimated before the acceleration zone because the measured plasma potential at the wall was higher than within the bulk discharge by a few volts (likely due to measurement uncertainty). Due to the low electron temperature within this region, a few volts create a significant plasma density difference, illustrating the sensitivity of Boltzmann's relation. The large radial electric fields created within the acceleration zone, caused by the plasma accelerating further upstream close to the wall, are responsible for the significant density drop. It is uncertain whether this is an indication that Boltzmann's relation is invalid within the thruster or the simulated magnetic field topology differs from the true magnetic field during operation. However, given the measurement uncertainty and the sensitivity of Boltzmann's relation, only minor deviations could cause the trends observed in Figure 5-17. Such minor deviations have been found in studies by Ngom using Zeeman-split laser induced fluorescence spectra [71].

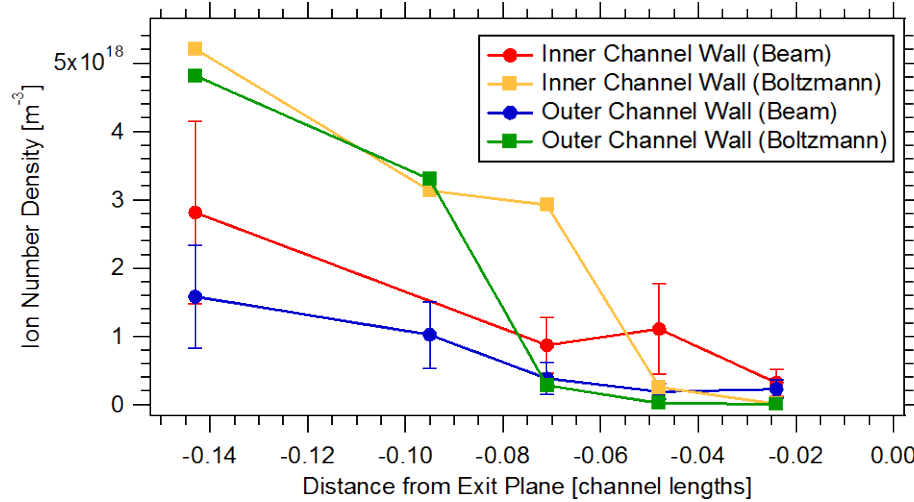


Figure 5-17. Comparison of measured axial profiles of ion number density to those calculated using Boltzmann's relation of thermalized potential at 300 V and 20 mg/s. The calculated values appear to overestimate the plasma density prior to acceleration and underestimate it after acceleration.

5.4 Electron Energy Distribution Functions

The electron energy distribution function (EEDF) is a critical quantity in Hall thrusters, as it describes how energy is distributed within the electron population; thus, the EEDF heavily influences ionization and wall losses, and can provide insight into how the electrons in the discharge are interacting with particles, fields, and the walls. For this reason, EEDFs were measured along the channel walls using internal wall-mounted probes. A smoothed second derivative of the Langmuir probe I-V characteristic was used to determine the EEDF along with the Druyvesteyn formula [49,72]:

$$f(\varepsilon)d\varepsilon = \frac{2m_e}{e^2 A_p} \left(\frac{2e\phi_p}{m_e} \right)^{1/2} \frac{d^2 I_e}{d\phi_p^2}. \quad (5-4)$$

In Eq. (5-4), ϕ_p is the probe bias with respect to the local plasma potential, and the rest of the symbols have their usual meaning. Smoothing techniques are identical to those described in Section 4.3.2.

Distribution functions within the channel are first presented and compared to Maxwellian distributions based on the measured local electron temperature. The structure of the EEDF is then investigated using several distribution functions that are based on physical processes within the discharge.

5.4.1 Measured Distributions along the Channel Wall

Since many of the measured EEDFs share a similar structure, only a few representative distributions are presented here. Figure 5-18 through Figure 5-20 show measured EEDFs along the walls at various axial positions within the channel, at the nominal operating condition of 300 V and 20 mg/s anode flow rate. The Maxwellian distribution based on the measured electron temperature is shown for comparison. All distributions are normalized such that the integral over all energies is unity.

Regardless of whether the plasma is within the ionization or acceleration zone, the EEDF is not consistent with the assumed Maxwellian distribution. At $z = -0.143$ channel lengths, prior to plasma acceleration, the distribution of energies is close to the Maxwellian distribution but is shifted towards slightly higher energies. Once the plasma has accelerated, the EEDF does not resemble the assumed Maxwellian distribution at all and is shifted towards significantly higher energies. In order to characterize this shift, an effective electron temperature is defined using the measured EEDF [49]:

$$T_{eff} = \frac{2}{3} \langle \varepsilon \rangle = \frac{2}{3} \int_0^{\infty} \varepsilon f(\varepsilon) d\varepsilon. \quad (5-5)$$

This definition is based off the fact that the average energy for a Maxwellian distribution is $(3/2)T_e$.

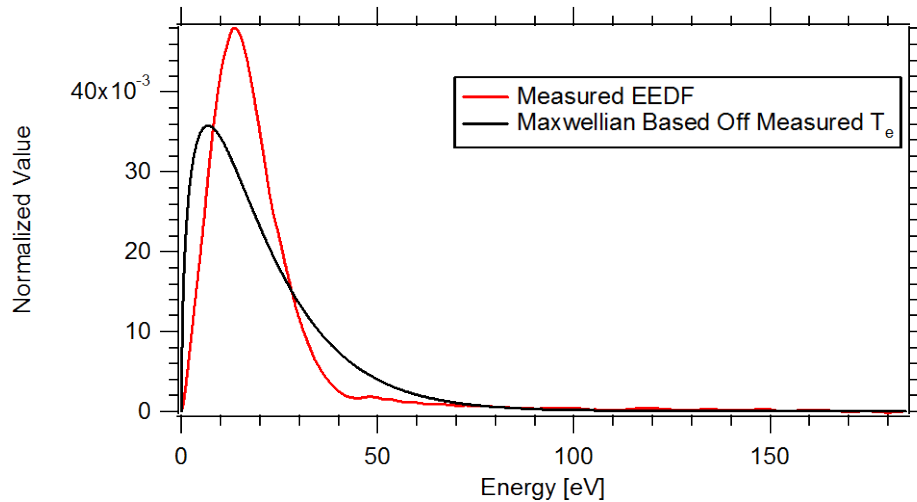


Figure 5-18. Measured EEDF at -0.143 channel lengths along the outer wall, under nominal operating conditions of 300 V and 20 mg/s. The Maxwellian distribution based on the measured electron temperature (14 eV) is included for comparison. Distributions are normalized such that their integrals are unity.

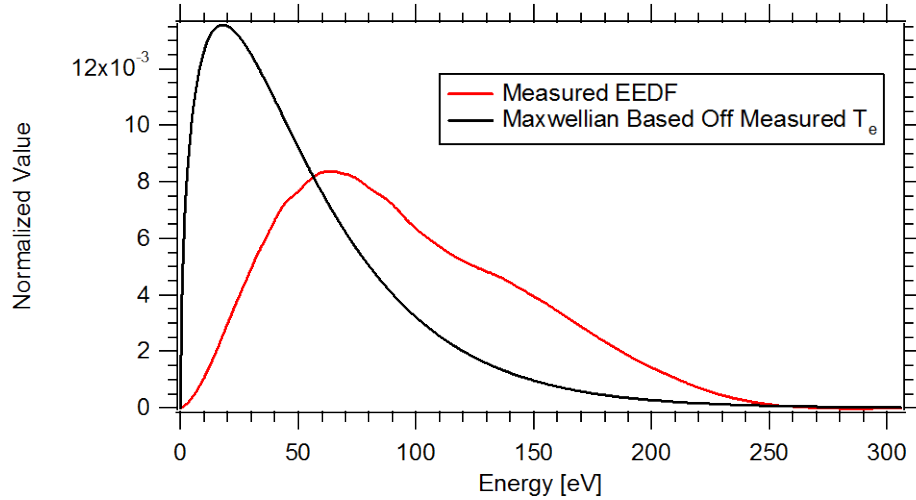


Figure 5-19. Measured EEDF at -0.071 channel lengths along the inner wall, under nominal operating conditions of 300 V and 20 mg/s. The Maxwellian distribution based on the measured electron temperature (36 eV) is included for comparison. Distributions are normalized such that their integrals are unity.

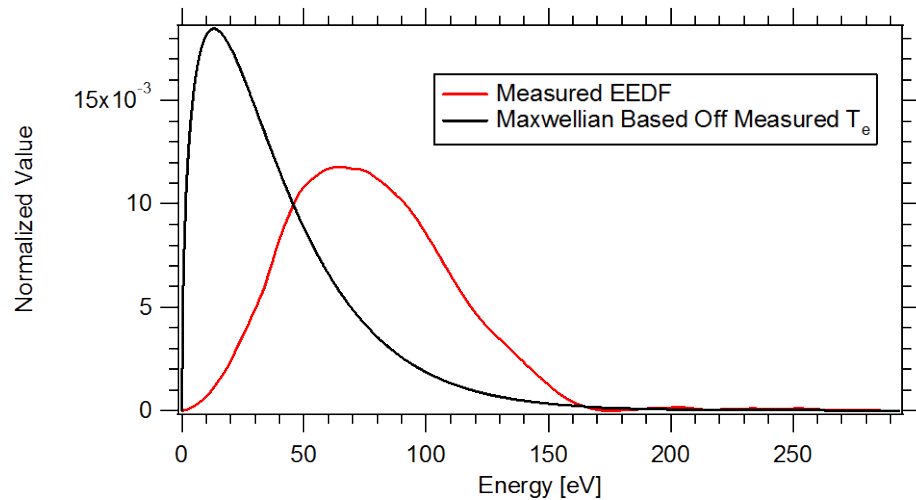


Figure 5-20. Measured EEDF at -0.024 channel lengths along the inner wall, under nominal operating conditions of 300 V and 20 mg/s. The Maxwellian distribution based on the measured electron temperature (26 eV) is included for comparison. Distributions are normalized such that their integrals are unity.

Table 5-3 compares the measured electron temperatures to the effective electron temperatures calculated from the EEDFs at nominal conditions of 300 V and 20 mg/s. As illustrated before, prior to the acceleration zone the measured EEDF is similar to the assumed Maxwellian distribution, and the measured and effective electron temperatures are nearly identical. However, once the acceleration zone is reached, this agreement is gone and the effective temperature is 1.5-2X greater than the measured temperature.

Table 5-3. Comparison of measured values of electron temperature to those calculated using the measured EEDF at 300 V and 20 mg/s. Prior to acceleration, these values are nearly the same, but within the acceleration zone the effective electron temperature is much higher.

Location	Measured T_e [eV]	Calculated $T_{e,eff}$ [eV]	Ratio ($T_{e,eff}/T_e$)
Inner wall, $z = -0.143$	9.7	11	1.1
Inner wall, $z = -0.095$	26	27	1.0
Inner wall, $z = -0.071$	36	64	1.8
Inner wall, $z = -0.048$	35	58	1.7
Inner wall, $z = -0.024$	26	52	2.0
Outer wall, $z = -0.143$	14	14	1.0
Outer wall, $z = -0.095$	35	31	0.9
Outer wall, $z = -0.071$	27	57	2.1
Outer wall, $z = -0.048$	21	44	2.1
Outer wall, $z = -0.024$	28	42	1.5

This distinction is further illustrated in Figure 5-21, which compares EEDFs at various axial locations along the inner channel wall. Upstream of the acceleration zone ($z = -0.143$), the electrons are highly concentrated at low energies due to low temperature and near-Maxwellian structure. Once the acceleration zone is reached, the electrons heat up significantly and obtain energies several times higher than in the region upstream.

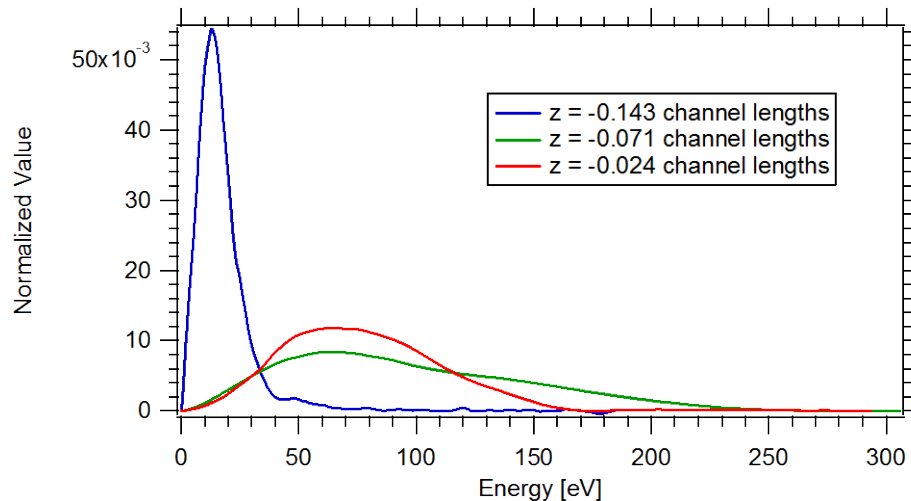


Figure 5-21. Comparison of EEDFs at various axial locations along the inner channel wall, under nominal conditions of 300 V and 20 mg/s. Distributions are normalized such that their integrals are unity.

The non-Maxwellian structure of the measured EEDF is somewhat surprising due to the fairly linear transition region of the Langmuir probe I-V characteristic, whose slope is used to determine the electron temperature. However, a linear transition region does not necessarily indicate that the electron population is Maxwellian [48]. Figure 5-22 shows a typical semi-log plot of an I-V characteristic taken within the acceleration zone inside the channel under nominal operating conditions. While most of the transition region (below the plasma potential) is fairly linear, there is a non-linear section as well, where the collected electron current is less than expected. This region just below the plasma potential contains probe biases that should allow collection of low-energy electrons; the reduction in collected current is an indication that there are fewer low-energy electrons than expected, as evidenced by the EEDF. Had the distribution been Maxwellian, the linear section would continue to the plasma potential; this also explains why the linear intersection method of determining plasma potential consistently underestimated plasma potentials in this region (see Section 4.3.5).

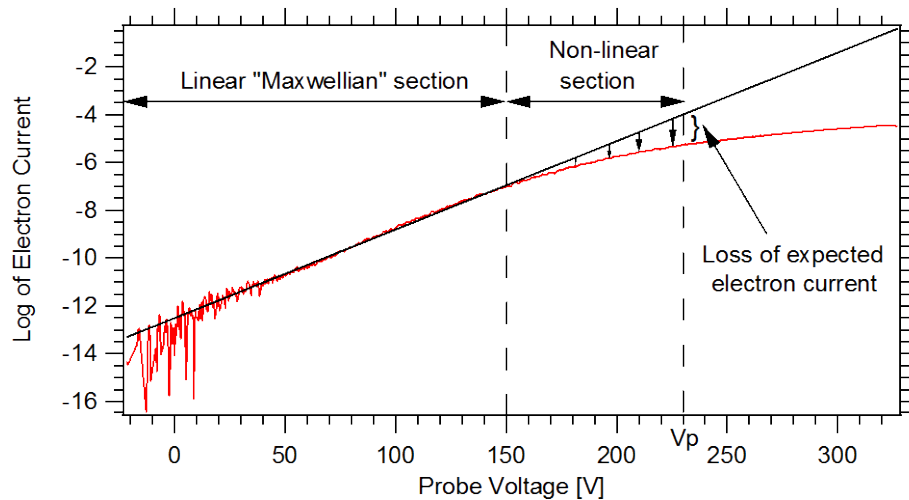


Figure 5-22. Example of a semi-log plot of an I-V characteristic taken within the acceleration zone inside the channel at 300 V and 20 mg/s. The transition region is composed of a linear and non-linear section. Electron current is less than expected near the plasma potential, where low-energy electrons should be collected.

5.4.2 Derivation of Potential Electron Distribution Functions

Measured EEDFs within the Hall thruster discharge channel have shown that the structure deviates from the assumed Maxwellian distribution function based on the measured electron temperature. In order to better understand the cause of this deviation, several energy distribution functions are derived and compared to the measured EEDFs.

These distributions are based on physical mechanisms that are expected to occur within the channel. Five functions are presented here: a generalized Maxwellian distribution, a Druyvesteyn distribution, a Maxwellian with an energy shift, a Maxwellian with a velocity shift, and an anisotropic Maxwellian distribution.

The Maxwellian distribution is expected when collisions between particles in a stationary gas occur often enough that an equilibrium energy distribution is fully reached. Due to its frequent use, it will not be derived here but merely presented in general form:

$$f(\varepsilon)d\varepsilon = AT_e^{-3/2}\varepsilon^{1/2} \exp\left(-\frac{\varepsilon}{T_e}\right)d\varepsilon, \quad (5-6)$$

where A and T_e are left as fitting parameters.

The Druyvesteyn distribution [73] is expected when particles within a steady electric field undergo elastic collisions with the neutral background. As such, this distribution is encountered frequently in low-pressure plasma discharges; due to its frequent use, it will not be derived here but only presented in general form:

$$f(\varepsilon)d\varepsilon = AT_e^{-3/2}\varepsilon^{1/2} \exp\left(-B\left(\frac{\varepsilon}{T_e}\right)^2\right)d\varepsilon, \quad (5-7)$$

where A , T_e , and B are left as fitting parameters.

The large radial electric fields measured near the channel wall in this work could produce an energy shift in an otherwise Maxwellian distribution if the electrons climb the potential hill without collisions to reach the wall. If this shift is in the z direction (this is chosen to simplify the resulting calculation, and does not necessarily correlate with the axial direction of the thruster coordinate system), then

$$v_{z_0}^2 = v_z^2 + (\Delta v)^2, \quad (5-8)$$

Since the number of particles with velocity v_0 should be the same number of particles with velocity v after the energy shift, then $f(v_0)dv_0 = f(v)dv$ in the z direction. Using $f(v_0)$ as a Maxwellian velocity distribution, this makes the velocity distribution with an energy shift

$$f(v_x, v_y, v_z)dv_x dv_y dv_z = \left(\frac{m}{2\pi kT}\right)^{3/2} \exp\left(-\frac{m(\Delta v)^2}{2kT}\right) \exp\left(-\frac{m}{2kT}(v_x^2 + v_y^2 + v_z^2)\right) \frac{v_z}{(v_z^2 + (\Delta v)^2)^{1/2}} dv_x dv_y dv_z. \quad (5-9)$$

Converting to spherical coordinates and integrating over all angles gives the speed distribution function

$$f(U)dU = 2\pi \left(\frac{m}{2\pi kT} \right)^{3/2} \exp\left(-\frac{m(\Delta v)^2}{2kT}\right) U \exp\left(-\frac{mU^2}{2kT}\right) \left((U^2 + (\Delta v)^2)^{1/2} - \Delta v \right) dU. \quad (5-10)$$

Given the energy $\varepsilon = \frac{1}{2}mU^2$, and defining $\Delta\varepsilon = \frac{1}{2}m(\Delta v)^2$, the final energy distribution function is

$$f(\varepsilon)d\varepsilon = \frac{1}{\sqrt{\pi}} \frac{1}{kT} \exp\left(-\frac{\varepsilon + \Delta\varepsilon}{kT}\right) \left(\left(\frac{\varepsilon + \Delta\varepsilon}{kT} \right)^{1/2} - \left(\frac{\Delta\varepsilon}{kT} \right)^{1/2} \right) d\varepsilon. \quad (5-11)$$

Putting this function in general form and converting to units of eV gives

$$f(\varepsilon)d\varepsilon = \frac{A}{T_e} \exp\left(-\frac{\varepsilon + \Delta\varepsilon}{T_e}\right) \left(\left(\frac{\varepsilon + \Delta\varepsilon}{T_e} \right)^{1/2} - \left(\frac{\Delta\varepsilon}{T_e} \right)^{1/2} \right) d\varepsilon, \quad (5-12)$$

where A , T_e , and $\Delta\varepsilon$ are left as fitting parameters.

Electron movement can be highly complex due to the electric and magnetic fields within the Hall thruster channel. One aspect of this movement can be drift velocities of the guiding center of gyroscopic motion. If this drift velocity, Δv , is in the z direction, then the velocity distribution function can be written as

$$f(v_x, v_y, v_z) dv_x dv_y dv_z = \left(\frac{m}{2\pi kT} \right)^{3/2} \exp\left(-\frac{m}{2kT} (v_x^2 + v_y^2 + (v_z + \Delta v)^2)\right) dv_x dv_y dv_z. \quad (5-13)$$

Converting to spherical coordinates and integrating over all angles gives the speed distribution:

$$f(U)dU = \frac{2}{\Delta v} \left(\frac{m}{2\pi kT} \right)^{1/2} \exp\left(-\frac{m(\Delta v)^2}{2kT}\right) U \exp\left(-\frac{mU^2}{2kT}\right) \sinh\left(\frac{mU\Delta v}{kT}\right) dU. \quad (5-14)$$

Given the energy $\varepsilon = \frac{1}{2}mU^2$, and defining $\Delta\varepsilon = \frac{1}{2}m(\Delta v)^2$, the final energy distribution function is

$$f(\varepsilon)d\varepsilon = \left(\frac{1}{\pi kT \Delta\varepsilon} \right)^{1/2} \exp\left(-\frac{\varepsilon + \Delta\varepsilon}{kT}\right) \sinh\left(2 \frac{(\varepsilon \Delta\varepsilon)^{1/2}}{kT}\right) d\varepsilon. \quad (5-15)$$

Putting this function in general form and converting to units of eV gives

$$f(\varepsilon)d\varepsilon = A \left(\frac{1}{T_e \Delta\varepsilon} \right)^{1/2} \exp\left(-\frac{\varepsilon + \Delta\varepsilon}{T_e}\right) \sinh\left(2 \frac{(\varepsilon \Delta\varepsilon)^{1/2}}{T_e}\right) d\varepsilon, \quad (5-16)$$

where A , T_e , and $\Delta\varepsilon$ are left as fitting parameters.

Since electrons within the discharge gain their energy from the axial electric field, the temperature normal to the magnetic field lines is typically higher than the temperature parallel to them, leading to anisotropy of the energy distribution function [9,68]. In order to maintain a relatively simple analytical form while still investigating the effects of anisotropy, it is assumed that

$$T_{\perp} = \zeta T_{\parallel}, \quad (5-17)$$

where ζ is a proportionality constant. If the z direction is taken to be parallel to the magnetic field, then the velocity distribution function is

$$f(v_x, v_y, v_z) dv_x dv_y dv_z = \left(\frac{m}{2\pi k T_{\parallel}} \right)^{1/2} \left(\frac{m}{2\pi k T_{\perp}} \right) \exp\left(-\frac{mv_z^2}{2kT_{\parallel}} - \frac{m(v_y^2 + v_x^2)}{2kT_{\perp}} \right) dv_x dv_y dv_z. \quad (5-18)$$

Using Eq. (5-17) to eliminate the temperature normal to the field lines, the velocity distribution function becomes

$$f(v_x, v_y, v_z) dv_x dv_y dv_z = \frac{1}{\zeta} \left(\frac{m}{2\pi k T_{\parallel}} \right)^{3/2} \exp\left(-\frac{m}{2kT_{\parallel}} \left(v_z^2 \left(1 - \frac{1}{\zeta} \right) + \frac{1}{\zeta} (v_x^2 + v_y^2 + v_z^2) \right) \right) dv_x dv_y dv_z. \quad (5-19)$$

Converting to spherical coordinates and integrating over all angles gives the speed distribution:

$$f(U) dU = \frac{2}{\zeta \alpha} \left(\frac{m}{2kT_{\parallel}} \right)^{3/2} U^2 \exp\left(-\frac{mU^2}{2k\zeta T_{\parallel}} \right) erf(\alpha) dU, \quad (5-20)$$

where α is defined by

$$\alpha^2 = \frac{mU^2}{2kT_{\parallel}} \left(1 - \frac{1}{\zeta} \right). \quad (5-21)$$

Given the energy $\varepsilon = \frac{1}{2}mU^2$, the final energy distribution function becomes

$$f(\varepsilon) d\varepsilon = \frac{1}{\zeta \left(1 - \frac{1}{\zeta} \right)^{1/2}} \frac{1}{kT_{\parallel}} \exp\left(-\frac{\varepsilon}{k\zeta T_{\parallel}} \right) erf\left(\left(\frac{\varepsilon}{kT_{\parallel}} \left(1 - \frac{1}{\zeta} \right) \right)^{1/2} \right) d\varepsilon. \quad (5-22)$$

Putting this function in general form and converting to units of eV gives

$$f(\varepsilon)d\varepsilon = \frac{A}{\zeta\left(1-\frac{1}{\zeta}\right)^{1/2}} \frac{1}{T_{\parallel}} \exp\left(-\frac{\varepsilon}{\zeta T_{\parallel}}\right) \operatorname{erf}\left(\left(\frac{\varepsilon}{T_{\parallel}}\left(1-\frac{1}{\zeta}\right)\right)^{1/2}\right) d\varepsilon, \quad (5-23)$$

where A , T_{\parallel} , and ζ are left as fitting parameters.

Figure 5-23 compares the structure of these five distributions: pure Maxwellian, Druyvesteyn, Maxwellian with energy shift, Maxwellian with velocity shift, and Maxwellian with anisotropy. The distributions are normalized such that the integral over all energies is unity, and are plotted as a function of non-dimensionalized energy. For the distributions shown in Figure 5-23, $B=1$ for the Druyvesteyn distribution, $T_{\parallel} = T_e$ and $\zeta = 3$ for the Maxwellian with anisotropy, and $\Delta\varepsilon = 2T_e$ for the Maxwellians with energy shift and velocity shift. In the following section, these fits will be used to determine the source of the measured EEDF structure, and resulting implications will be discussed.

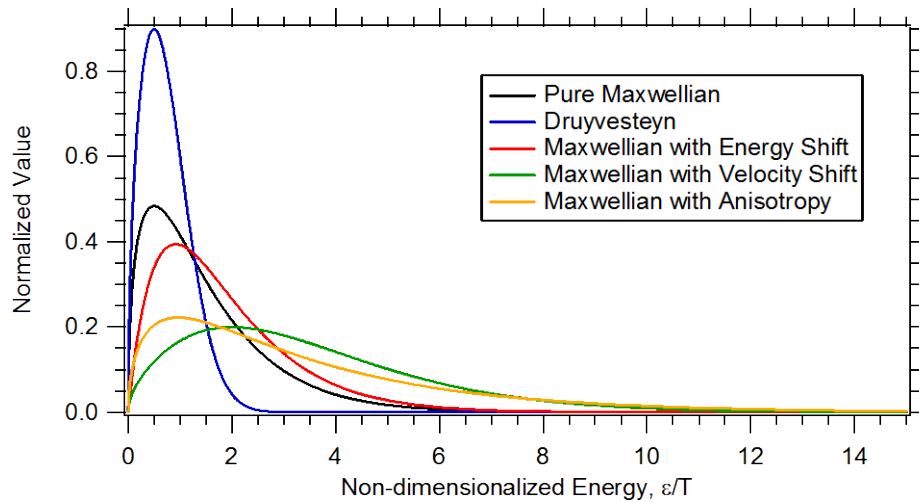


Figure 5-23. Comparison of various potential electron distribution functions within the channel of a Hall thruster. Distributions are normalized such that their integrals are unity.

5.4.3 Implications of the Measured EEDF Structure

Distribution functions discussed in Section 5.4.2 were fit to measured EEDFs along the channel walls in order to determine the source of the observed non-Maxwellian structure. The Maxwellian distribution with a velocity shift was found to best fit the observed distributions. Figure 5-24 and Figure 5-25 show comparisons of the measured EEDF to the curve fit of a Maxwellian with a velocity shift at two axial locations along the inner wall, under nominal operating conditions of 300 V and 20 mg/s anode flow rate.

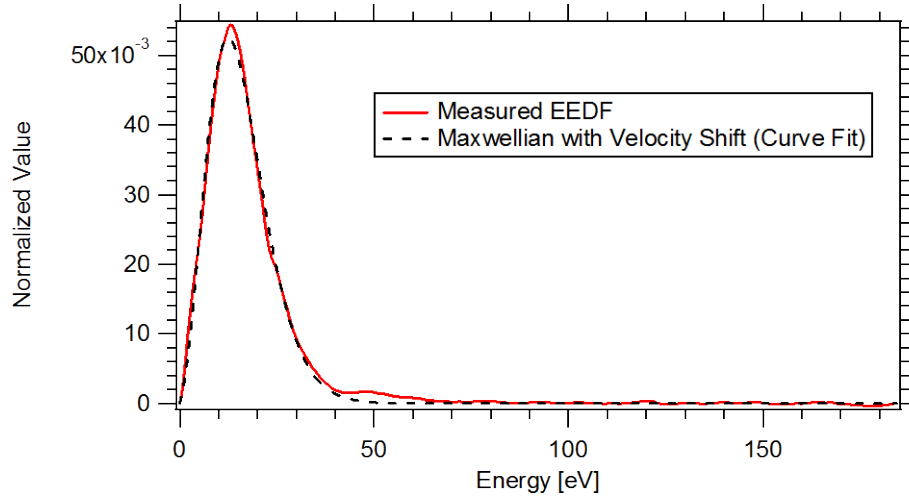


Figure 5-24. Comparison of the measured EEDF to the curve fit of a Maxwellian with velocity shift, at $z = -0.143$ channel lengths along the inner wall, under nominal operating conditions of 300 V and 20 mg/s.

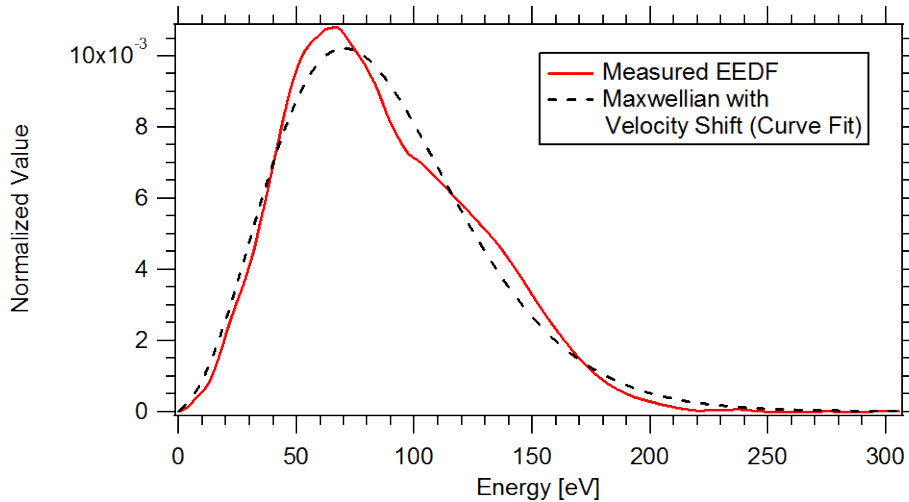


Figure 5-25. Comparison of the measured EEDF to the curve fit of a Maxwellian with velocity shift, at $z = -0.048$ channel lengths along the inner wall, under nominal operating conditions of 300 V and 20 mg/s.

It is evident that this distribution provides an excellent fit to observed EEDFs along the channel wall. However, since the electron temperature was left as a fit parameter, it was found that the corresponding values to the curve fit do not match well with measured values. Table 5-4 compares the measured electron temperature to those found using the Maxwellian with velocity shift. The corresponding velocity shift fit parameter is included for completeness. It is evident that while the measured and calculated values of electron temperature share the same trend with axial location, the values determined from the curve fit are significantly lower. This indicates that the large

energies seen in the measured EEDFs are primarily due to large drift velocities of the electrons, and that the population may be much colder than observed using simple Langmuir probe theory. Since the measured electron temperature came from only a portion of the transition region of the Langmuir probe characteristic, it is possible that the high-energy tail of the electron population mimics a Maxwellian distribution at higher temperatures.

Table 5-4. Comparison of measured values of electron temperature to values determined by the EEDF through distribution curve fitting using a Maxwellian with a velocity shift. The corresponding velocity shift is included for completeness.

Location	Measured T_e [eV]	Distribution Curve Fit Parameters	
		T_e [eV]	Velocity Shift [m/s]
Inner wall, $z = -0.143$	9.7	2.1	2.1×10^6
Inner wall, $z = -0.095$	26	4.4	2.6×10^6
Inner wall, $z = -0.071$	36	18	5.0×10^6
Inner wall, $z = -0.048$	35	11	5.0×10^6
Inner wall, $z = -0.024$	26	8.1	4.8×10^6
Outer wall, $z = -0.143$	14	2.4	2.2×10^6
Outer wall, $z = -0.095$	35	6.5	2.8×10^6
Outer wall, $z = -0.071$	27	9.8	5.0×10^6
Outer wall, $z = -0.048$	21	8.9	4.4×10^6
Outer wall, $z = -0.024$	28	7.0	4.4×10^6

The corresponding velocity shifts seen in Table 5-4 could be due to numerous physical phenomena in the Hall thruster discharge channel. Table 5-5 gives a few examples of the possible electron velocity drifts [49] within the channel, along with representative values calculated near the thruster exit plane. These values were found to be consistent with those calculated by Linnell within the NASA-173Mv1 [11]. Many of these drifts are variations of the generalized drift that occurs when a force acts perpendicular to an applied magnetic field:

$$\vec{v}_d = \frac{\vec{F} \times \vec{B}}{eB^2}. \quad (5-24)$$

The well-known $E \times B$ drift, responsible for the electron Hall current within the discharge, is an azimuthal drift velocity primarily created by the axial electric field and

radial magnetic field. Gradient “grad B” drift and curvature drift are created due to the non-uniformity and curvature of the magnetic field, respectively. Finally, polarization drift is caused by a slowly-varying electric field within a static magnetic field. For this calculation, the electric field was assumed to oscillate between the steady state value and zero on a timescale determined by the breathing mode frequency, which is approximately 10 kHz. This is considered an upper bound on the possibility of an oscillating axial electric field; even with this assumption, the polarization drift velocity is shown to be negligible in Hall thrusters.

Table 5-5. Possible sources of drift velocity for electrons within the Hall thruster channel and calculated typical values.

Type of Drift	Typical Values [m/s]
$E \times B$ drift	$1.3 \times 10^6 - 8.6 \times 10^6$
Gradient (Grad B) drift	9.5×10^3
Curvature drift	9.5×10^3
Polarization drift	6.5

It is evident from Table 5-5 that the only drift velocity of the correct order magnitude to explain the EEDF structure is the $E \times B$ drift. The values reported take into account the drift caused by axial electric and radial magnetic fields, as well as radial electric and axial magnetic fields close to the wall. Regardless, this drift is expected to occur in the azimuthal direction, making it unlikely that it was detected by the internal wall-mounted probes. While it is possible that components of the drift velocity occur in the radial direction, further studies are required to verify this finding.

Due to the radical differences between the results from the measured EEDFs and traditionally-determined electron temperatures, along with the inherent uncertainty associated with the EEDF measurement, remaining analyses will not attempt to take into account the reduced electron temperature and drift velocity implied by the EEDF structure. While these measurements are promising, further investigations are warranted to fully understand the energy distribution among electrons within the channel.

5.5 Summary

This chapter presented the measured plasma potential, electron temperature, and ion number density along the inner and outer channel walls near the thruster exit plane at 300 V and 20 mg/s anode flow rate. Comparison of these results to prior internal measurements [13] show that the plasma accelerates further upstream when close to the wall. This difference in acceleration zone location creates significant radial electric fields close to the walls that are of similar magnitude to the axially-generated electric fields. The cause of this phenomenon appears to be large plasma density gradients between the walls and channel centerline. The electron temperature was found to peak near the beginning of the acceleration zone, at a value of approximately a tenth of the discharge voltage, consistent with prior measurements.

Measured electron energy distribution functions (EEDFs) along the channel walls indicate a structure that is not consistent with the assumed Maxwellian distribution and the measured electron temperature. It was found that the EEDF most closely resembles a drifting Maxwellian distribution, with a much lower electron temperature and a drift velocity on the order of the local $E \times B$ velocity. This deviation from a Maxwellian distribution was found to be very significant within the acceleration zone of the discharge. The measured distribution functions indicate that simple measurements of electron temperature may provide artificially high values, with most of the electron energy coming from a large drift velocity.

Chapter 6

Thruster Simulations Using HPHall-2

This chapter details pertinent computational results of the 6-kW Hall thruster operating at nominal conditions of 300 V and 20 mg/s anode flow rate. The simulation program used is the hybrid-PIC Hall thruster code HPHall-2, heavily modified by the Jet Propulsion Laboratory (JPL). A brief summary of HPHall-2 is first provided, followed by axial profiles of various plasma parameters. Plasma potential, electron temperature, and ion number density are compared between channel centerline and the inner and outer walls in an effort to characterize the near-wall plasma, similar to Chapter 5. The computational results are then compared to experimental data taken with the internal wall-mounted probes. This was done to validate the simulation and experimental results, as well as better understand the source of the trends observed in Chapter 5.

6.1 General Overview of Hybrid-PIC code

HPHall-2 is a hybrid-PIC program capable of simulating the internal and near-field plasma physics of Hall thrusters as well as calculating performance and erosion characteristics under various geometries and operating conditions. The original program, HPHall, was developed by Fife [74] in the late 1990s during his time at the Massachusetts Institute of Technology (MIT) and later at the Air Force Research Laboratory (AFRL). Numerous improvements were made by Parra et al. [75] in 2006, producing a new version of the code called HPHall-2. Since then, JPL has made additional improvements to the plasma-wall physics, handling of multiply-charged species, and electron mobility models, and has built an entirely new erosion submodel [27,67,69,76,77].

HPHall-2 is a two-dimensional code in cylindrical (r-z) geometry, as any variations in the azimuthal direction are neglected. Heavy species (ions and neutrals) are

handled using particle-in-cell (PIC) methods, while the electrons are treated as a fluid. The magnetic field configuration is assumed to be static and is imported into the program prior to any computational run. Figure 6-1 shows a typical domain space and mesh within HPHall-2. The entire channel along with a portion of the near-field plume is included in the simulation domain. The mesh size is made larger than a Debye length, such that quasi-neutrality may be invoked in the entire domain. While this significantly reduces computational expense, it prevents HPHall-2 from simulating the sheaths formed along the channel walls, which are inherently non-neutral.

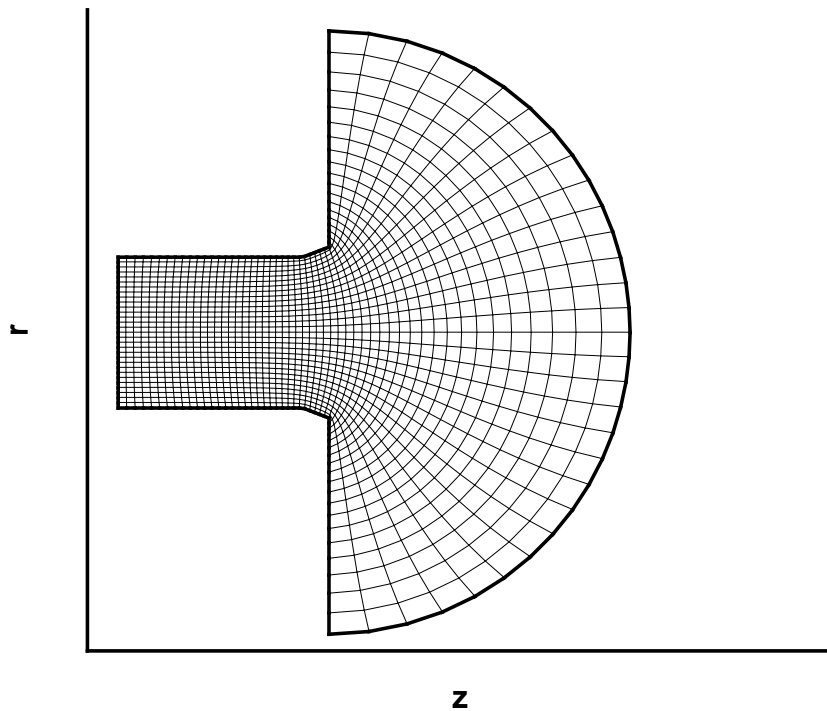


Figure 6-1. Example of a typical domain space and mesh within HPHall-2, including the channel and near-field plume.

Simplifying models are used along magnetic field lines that allow the code to effectively solve the governing equations in a quasi-one-dimensional manner. Due to the high plasma conductivity along magnetic field lines compared to across them, these lines are assumed to be isothermal for electrons; Boltzmann's relation (see Eq. (5-1)) is then used to relate the particle density to the electric potential along each field line. Thus, Ohm's law and current continuity only have to be solved between magnetic field lines.

Heavy particles are handled using the computational cycle shown in Figure 6-2. The electron equations are solved on the computational grid on a much faster time scale

than the heavy species. The equations of motion are used with the electric and magnetic fields at time t to move the heavy particles over the time step Δt . The species' densities and velocities are then weighted to the grid using a standard bilinear weighting scheme. The field equations are then solved on the grid using the species' densities and velocities and weighted back to the particle positions, such that the particles may be tracked through the next time step. Particle positions and velocities are solved using a standard leap-frog method where the velocities are solved every half time step (see Eq. (4-9)).

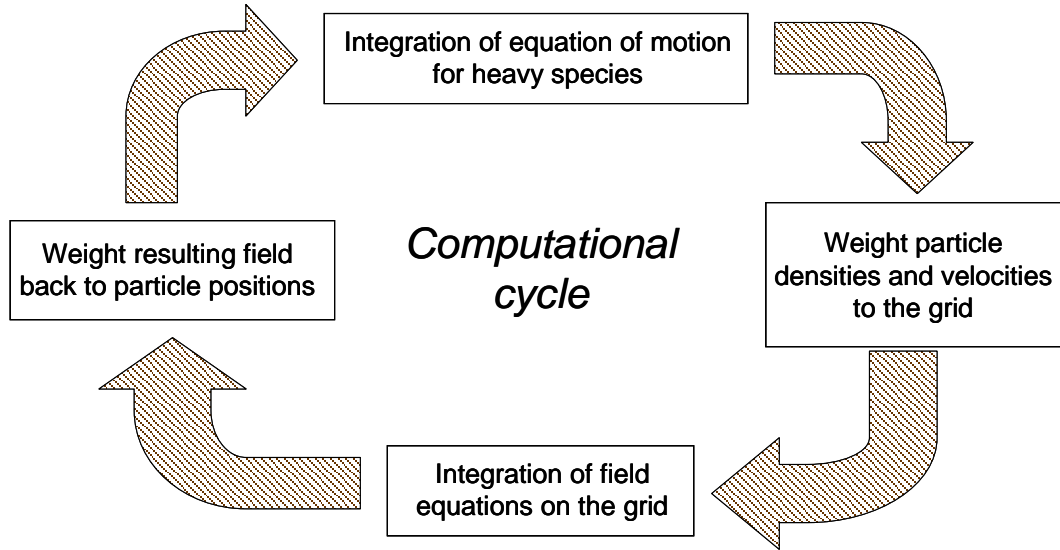


Figure 6-2. Computational cycle used to track heavy particle species within HPHall-2.

Due to the quasi-neutral assumption, sheaths along the wall cannot be resolved and are solved for analytically. The sheath potential is modeled using the Hobbs and Wesson solution of space-charge-limited emission, discussed in Section 4.5.3. Since ion motion is determined by the electric fields, the Bohm sheath criterion cannot be guaranteed at the wall boundaries on a coarse grid. Parra et al. solved this problem by employing a Bohm-condition forcing algorithm within HPHall-2 [75], which was later modified by Hofer et al. [69]. This algorithm determines the plasma number density at the wall boundary by dividing the calculated ion flux normal to the wall by the local Bohm velocity:

$$n_e|_{wall} = \frac{\Gamma_i|_{wall}}{v_{Bohm}} = \frac{\Gamma_i|_{wall}}{\sqrt{eT_e/M_i}}. \quad (6-1)$$

This allows ions to approach the wall at the Bohm velocity and has been shown to work well even on coarse meshes.

6.2 Baseline Simulation Results

HPHall-2 was used to simulate the steady-state plasma properties within the channel of the 6-kW Hall thruster under nominal operating conditions of 300 V and 20 mg/s anode flow rate. A three-region electron mobility model developed by Hofer et al. [27] was used within the simulation, and charge-exchange (CEX) collisions between ions and neutrals were neglected. The grid geometry was altered to match the chamfer present in the erosion rings used in the experimental study. A neutrals-only simulation was first run for 20,000 iterations with a time step $\Delta t = 5 \times 10^{-8}$ s in order to fill the channel with neutrals before any plasma was generated. The plasma was then “turned on” for 10,000 more iterations to simulate thruster startup. Finally, the plasma was left on for an additional 20,000 iterations with full collisionality to obtain the steady-state plasma solution. Table 6-1 compares resulting performance values between simulation and experiment, showing excellent agreement between the two.

Table 6-1. Comparison of measured and simulated values of performance at the nominal operating condition.

Discharge Property	Measured Value	Simulated Value
Discharge Voltage [V]	300	300
Anode Flow Rate [mg/s]	20	20
Discharge Current [A]	20.1	20.1
Thrust [mN]	385	388
Anode Efficiency	0.614	0.624

6.2.1 Plasma Potential

Axial profiles of the plasma potential at channel centerline and along each channel wall are shown in Figure 6-3. At all locations, the acceleration zone begins within the last 10% of the channel; acceleration occurs slightly upstream along the walls compared to channel centerline. Despite the difference in acceleration zone location, the maximum axial electric fields are roughly the same across the channel. Furthermore, the plasma potential always remains lower along the walls compared to channel centerline;

this indicates the presence of radial electric fields directed towards the wall, which would tend to defocus the ion beam. Figure 6-4 shows the complete plasma potential contour map, along with overlaid ion velocity vectors within the channel. It is evident that equipotentials tend to curve upstream close to the walls; thus, while the ion beam is primarily axial for most of the channel, the ions defocus close to the wall and obtain significant radial velocities. This defocusing effect would heavily influence the ion power to the wall as well as local erosion rates near the thruster exit plane.

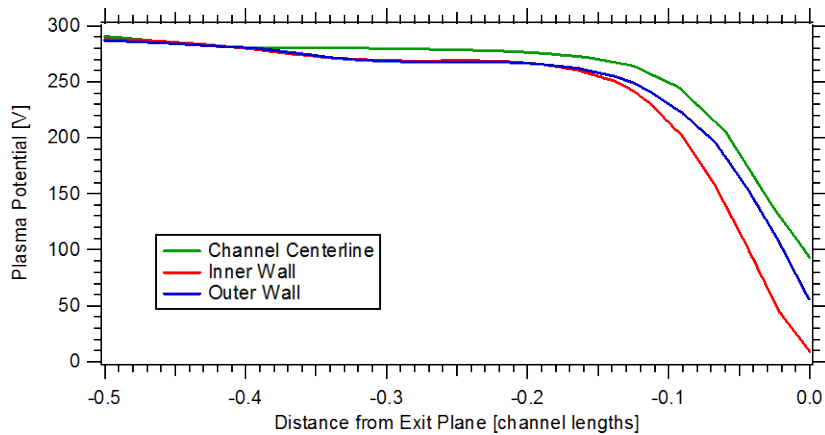


Figure 6-3. Comparison of axial profiles of plasma potential at channel centerline and along the channel walls. The acceleration zone occurs slightly upstream along the walls compared to channel centerline.

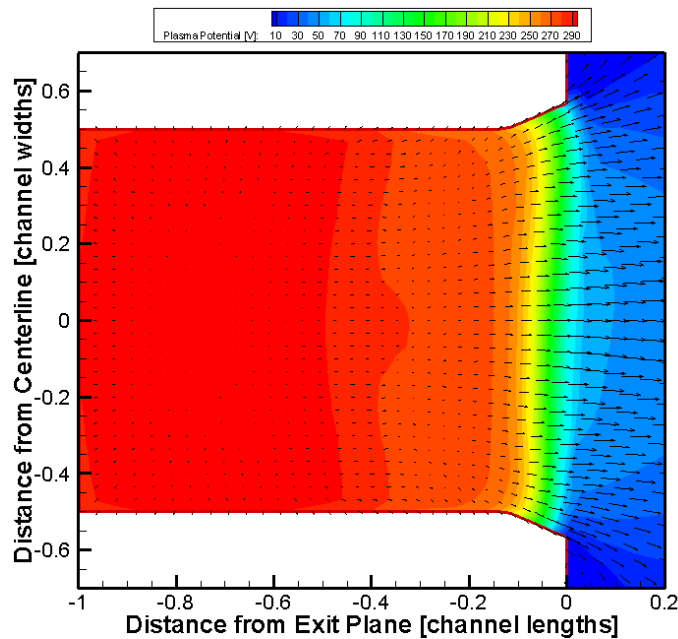


Figure 6-4. Contour map of plasma potential within the thruster channel. Ion velocity vectors are overlaid on the map to indicate how the electric fields affect the ion motion. Significant radial velocities exist near the wall where radial electric fields defocus the beam.

It is interesting to note that despite the use of the Boltzmann relation in HPHall-2, the equipotential lines have the opposite curvature to those of the plasma lens topology within the thruster channel. Based on Eq. (5-1), significant deviation of equipotentials from magnetic field lines would only occur in the presence of large differences in plasma density, or a large electron temperature with small differences in plasma density. While the electron temperature can approach large values near the thruster exit plane, it will be shown in Section 6.2.3 that large radial gradients in plasma density are the likely cause of the defocusing electric field near the channel walls.

6.2.2 Electron Temperature

Axial profiles of electron temperature within the channel are shown in Figure 6-5. Electron temperature peaks in the region where the acceleration zone begins, close to the thruster exit plane. The peak electron temperature within the channel was found to be roughly 10% of the discharge voltage, consistent with prior internal measurements [10,11,13]. While the plasma is hotter along centerline for most of the channel, electron temperature peaks at nearly the same value and location near the exit plane. This trend is due to the isothermal assumption along magnetic field lines. Figure 6-6 shows the full contour map of electron temperature within the channel. Due to the plasma lens curvature of the magnetic field lines, the electron temperature along the wall will typically be lower than at centerline at a given axial location since it connects to a location further upstream along channel centerline where the plasma is colder. Near the exit plane, however, the magnetic field lines are nearly radial; thus, electron temperature is much more consistent across the channel.

The concentration of high electron temperature near the thruster exit plane can have a significant impact on various plasma properties in this region. For instance, based on the sheath potential model described in Section 4.5.3, these high electron temperatures can push the wall sheaths into a space-charge-limited regime due to prolific secondary electron emission. In this regime, sheath potentials are reduced to one electron temperature; thus, the sheaths lose much of their insulating capability, and electron wall losses significantly increase. Furthermore, based on the Boltzmann relation (see Eq. (5-1)), a high electron temperature can cause large deviations of equipotentials from magnetic field lines even if there are only small changes in plasma density; however, this

deviation was observed to occur over a larger axial range than the region of high electron temperature. Thus, it is likely that the elevated electron temperatures near the exit plane are only partly responsible for the defocusing electric fields observed in Section 6.2.1.

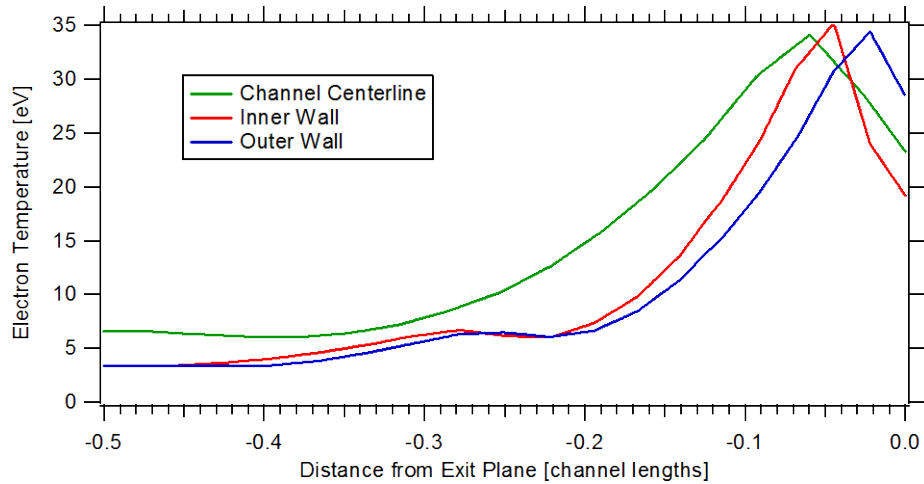


Figure 6-5. Axial profiles of electron temperature at channel centerline and along the walls of the 6-kW Hall thruster. While the plasma is hotter at channel centerline for most of the channel, the maximum electron temperature occurs at roughly the same axial location near the exit plane.

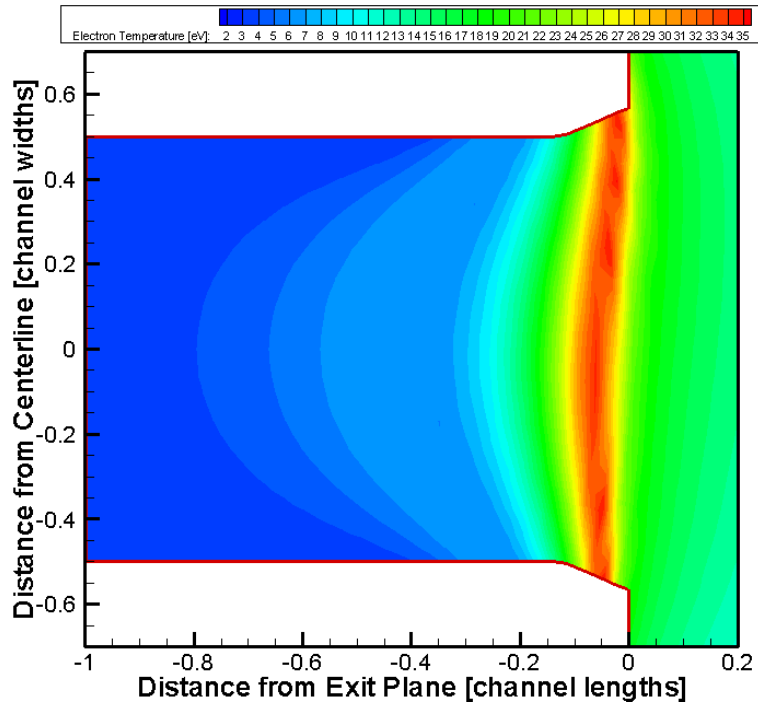


Figure 6-6. Contour map of electron temperature within the channel. Lines of constant electron temperature follow magnetic field lines, while maximum electron temperature occurs near the exit plane where the magnetic field lines are nearly radial.

6.2.3 Ion Number Density

Axial profiles of the ion number density at channel centerline and along the walls are shown in Figure 6-7. Since HPHall-2 tracks singly-ionized and doubly-ionized xenon separately, the two values were added to obtain the total ion number density. Several features are immediately evident from the axial profiles. First, the ion densities along the channel wall are significantly lower than at channel centerline, with peak values differing by a factor of four (inner wall) to six (outer wall). This large difference in density is the primary reason for the deviation of equipotentials from magnetic field lines observed in Section 6.2.1. The disparity is significant enough to defocus the ion beam near the walls despite the plasma lens magnetic field topology.

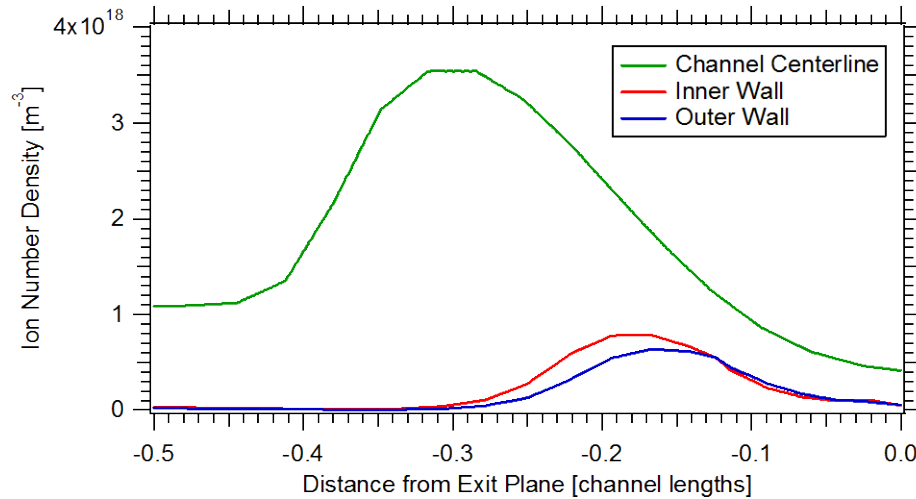


Figure 6-7. Axial profiles of ion number density at channel centerline and along the walls of the 6-kW Hall thruster. The plasma density is substantially lower close to the walls, and peak density occurs downstream of the peak location along channel centerline.

It is also evident that the peak ion density along the walls occurs further downstream than the peak along channel centerline. Figure 6-8 shows the ion number density map within the channel, which indicates that most of the plasma is contained within the center half of the channel (away from the walls) until the plasma density reaches a maximum; downstream of this point, significant ionization begins to occur near the walls. A possible reason for this difference in location is the isothermal behavior of the magnetic field lines. With the plasma lens topology, electrons near the wall gain sufficient energy to ionize xenon downstream of where electrons gain this energy at centerline. For example, the axial location where electrons first reach a temperature of 12.1 eV (first ionization potential of xenon) is $z = -0.234$ channel lengths along channel

centerline, while along the inner wall it is $z = -0.154$ channel lengths and along the outer wall it is $z = -0.139$ channel lengths. These locations roughly coincide with the locations of maximum plasma density.

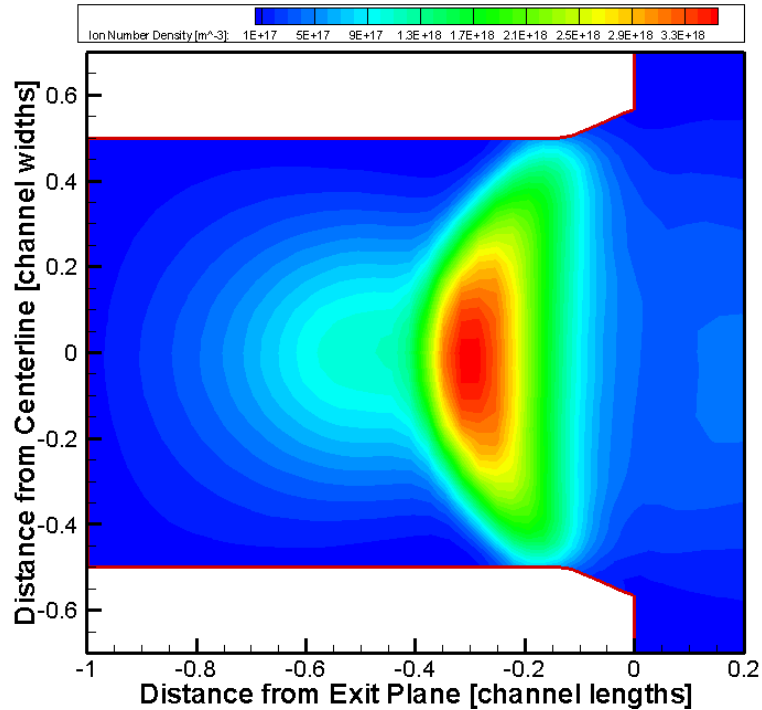


Figure 6-8. Contour map of the ion number density within the channel of the 6-kW Hall thruster. Ion density is 4-6X lower along the walls, with maximum densities occurring significantly downstream of the peak density along channel centerline.

Lastly, it is interesting to note that the peak ion density is slightly higher and occurs further upstream along the inner wall compared to the outer wall. This is due to the elevated electron temperatures along the inner wall upstream of the acceleration zone. Figure 6-9 shows a contour map of the local ionization rate within the channel, indicating higher rates occurring along the inner wall compared to the outer wall. Since the neutral number density was not found to vary significantly between inner and outer walls, the elevated ionization rates are attributed to higher electron temperatures along the inner wall occurring further upstream than along the outer wall. Thus, electrons along the inner wall have sufficient energy to ionize xenon over a wider axial range than along the outer wall, resulting in a higher ion number density. This is likely due to the slight asymmetry of the 6-kW Hall thruster magnetic field topology near the exit plane. The asymmetry would in turn create differences in locations of axial electric fields and the joule heating

of electrons, resulting in different electron temperature profiles along the inner and outer channel walls.

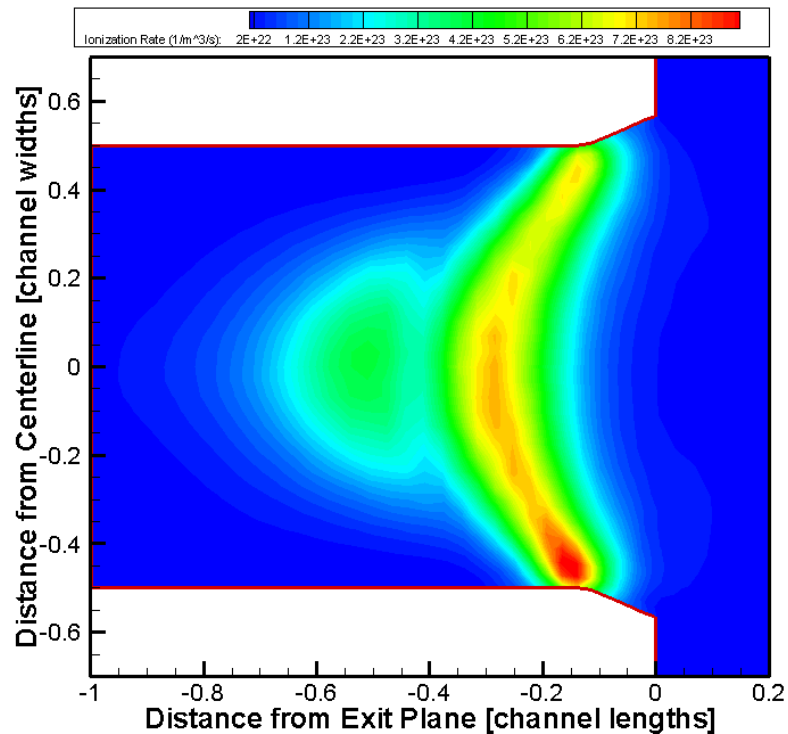


Figure 6-9. Contour map of the local ionization rate within the channel of the 6-kW Hall thruster. Elevated rates were found to occur along the inner wall compared to the outer wall.

6.3 Comparison to Experimental Data

Axial profiles of plasma potential, electron temperature, and ion number density along the channel walls from HPHall-2 are compared to those obtained experimentally using internal wall-mounted probes. Figure 6-10 shows the simulated and measured axial profiles of plasma potential along the channel walls near the thruster exit plane. Prior to the acceleration zone, there is a 30 V drop in plasma potential not observed in the experimental data. This is due to the importance of ion diffusion far upstream of the acceleration zone that is not captured in HPHall-2 since ions are modeled using particle-in-cell methods [27,78]. Despite this discrepancy, the location of the acceleration zone between simulated and measured values is in excellent agreement. The maximum axial electric field strength, 50-60 V/mm, is also consistent between simulation and experiment. It is interesting to note that the asymmetry between inner and outer walls is reversed in the simulation results compared to experiment; the acceleration zone along

the inner wall is further upstream in the HPHall-2 results, but is further downstream in the experimental data.

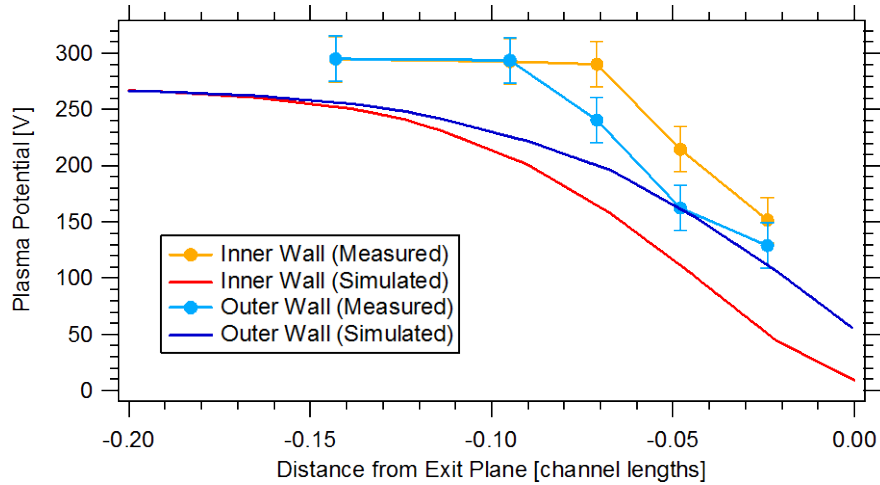


Figure 6-10. Comparison of measured and simulated axial profiles of plasma potential along the channel walls of the 6-kW Hall thruster. The location of the acceleration zone and the electric field strength are in good agreement.

Further insight into the asymmetry can be found by comparing the observed erosion profiles of the 6-kW Hall thruster after approximately 334 hours of operation. Figure 6-11 shows the measured radial recession along the inner and outer channel walls near the thruster exit plane. It is evident that increased erosion is measured along the outer wall. This is consistent with the measured plasma potential profiles, where the ions accelerate further upstream along the outer wall. This would expose the outer wall to higher ion energies compared to the inner wall, resulting in higher erosion rates.

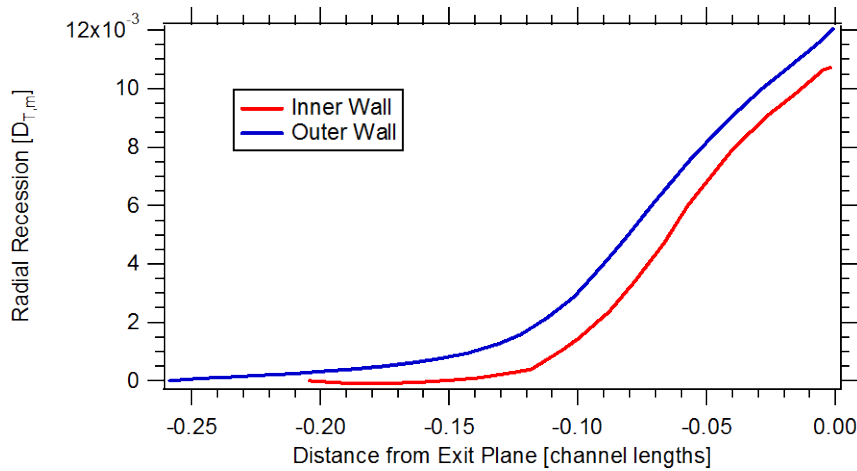


Figure 6-11. Comparison of the measured radial recession along the inner and outer channel walls of the 6-kW Hall thruster after 334 hours of operation. Increased erosion is observed along the outer wall, consistent with measured plasma potential profiles.

The reason for the shift in acceleration zone between the inner and outer walls is the slight asymmetry found in the 6-kW Hall thruster's magnetic field topology. Figure 6-12 compares the simulated radial magnetic field profiles along the inner and outer channel walls. While very similar, it is evident that the radial magnetic field along the inner walls peaks further downstream from the outer wall peak. The strength of the radial magnetic field is tied to the resistivity of the plasma; a higher radial magnetic field will result in a higher resistivity and an increase in axial electric field to sustain the discharge and enforce current continuity (through Ohm's law). The observed asymmetry in the magnetic field profiles is therefore consistent with the acceleration zone occurring further upstream along the outer wall. This asymmetry, however, occurs over only 2% of the channel length, and is therefore not highly significant.

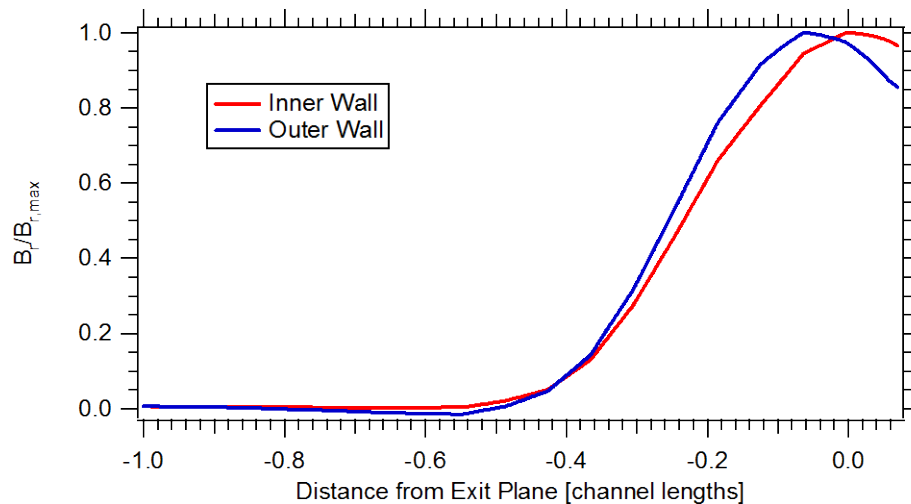


Figure 6-12. Comparison of simulated radial magnetic field profiles along the inner and outer channel walls of the 6-kW Hall thruster. The peak radial magnetic field occurs further upstream along the outer wall compared to the inner wall, consistent with plasma potential measurements.

Figure 6-13 shows the measured and simulated axial profiles of electron temperature along the channel walls near the thruster exit plane. The maximum electron temperature, approximately 10% of the discharge voltage, is consistent between simulation and experimental, as well as prior measurements [10,11,13]. The location of the peak electron temperature, however, occurs further upstream in the experimental data. This discrepancy was found to occur along channel centerline as well, by approximately 5% of the channel length. While this difference is not very large, the excellent agreement in plasma potential profiles may indicate that electron energy losses are present within the simulation that are not observed in the experiment. These losses would occur near the

beginning of the acceleration zone and reduce the local electron temperature, pushing the peak temperature further downstream.

It is worth noting that once again the asymmetry between inner and outer channel walls is reversed between simulation and experiment; the peak electron temperature along the inner wall occurs further upstream in the simulation, while further downstream in the experimental results. This discrepancy occurs over 2% of the discharge channel, and is thus not highly significant. However, these trends are consistent with the observed trends in plasma potential, both in the HPHall-2 and experimental results.

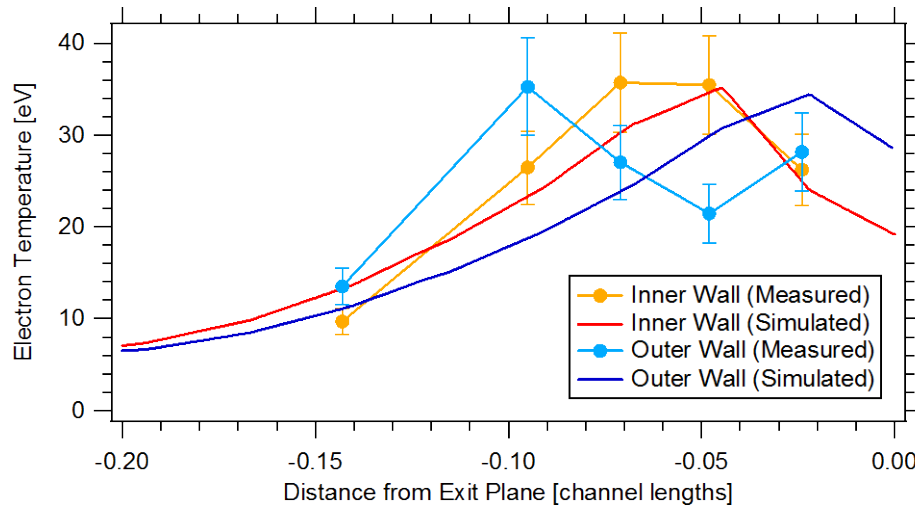


Figure 6-13. Comparison of measured and simulated axial profiles of electron temperature along the channel walls of the 6-kW Hall thruster. While maximum observed temperatures are in good agreement, their axial locations occur slightly upstream in the experimental data.

Figure 6-14 shows the measured and simulated axial profiles of ion number density along the channel walls near the thruster exit plane. The number density from HPHall-2 was calculated from the sum of the singly- and doubly-ionized xenon densities, while the measured number density took into account that ions could enter the sheath supersonically. Before the acceleration zone is reached, the measured ion density is significantly higher than that predicted by HPHall-2; better agreement is obtained near the thruster exit plane. It is difficult to determine agreement with the ion density peak location, since the experimental data only shows a monotonic decrease in density; however, this monotonic decrease is consistent with the simulation results. Furthermore, both experiment and simulation show that the maximum ion density along the inner wall is 1.5-2 times higher than along the outer wall; this difference becomes negligible as the exit plane is approached.

The significant difference between simulation and experiment may be partly due to the non-uniformity in plasma potential found in the HPHall-2 results upstream of the acceleration zone. This non-uniformity was not observed experimentally, yet a 10 V drop occurs in the simulation results between channel centerline and the walls. Using the Boltzmann equation (Eq. (5-1)) and an electron temperature of 10 eV, this plasma potential difference corresponds to a 3X drop in number density. The high number densities observed in experiment will have a significant impact on the measured ion power deposition to the walls, as well as predicted erosion rates.

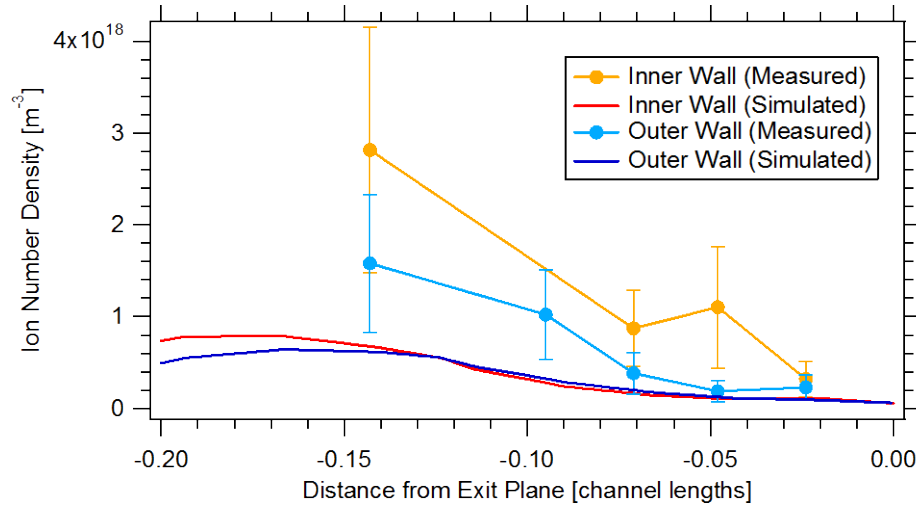


Figure 6-14. Comparison of measured and simulated axial profiles of ion number density along the channel walls of the 6-kW Hall thruster. Peak values are much higher in experiment than simulation, while better agreement is obtained within the acceleration zone close to the exit plane.

6.4 Summary

This chapter presented simulation results of the 6-kW Hall thruster at 300 V and 20 mg/s using the hybrid-PIC code HPHall-2. The results confirm the presence of strong axial electric fields near the channel walls caused by significant plasma density gradients. These electric fields tend to defocus ions and accelerate them towards the channel walls, which will strongly influence the resulting incident ion power to the walls as well as local erosion rates.

While the measured and simulated axial profiles of plasma potential and electron temperature are in good agreement, the measured ion number densities are significantly higher than predicted by the simulation. Better agreement is found near the thruster exit

plane after the plasma has begun to accelerate, but differences in the ionization zone approach a factor of five. It is still unclear why the simulated number densities are so much lower; uncertainties in the internal wall-mounted probe area may contribute to a higher calculated ion number density, but not enough to fully account for the differences between measured and simulated values.

Chapter 7

Incident Power Deposition onto Channel Walls

This chapter describes the calculated incident ion power to the inner and outer channel walls of the 6-kW Hall thruster using internal wall-mounted probes. The overall power deposited to the channel walls has been shown to be a significant energy loss mechanism in Hall thrusters [18,79]. Furthermore, it has been argued by Kim [80] that the incident ion power density to the wall is directly proportional to the local erosion rate. Thus, it is important for performance and lifetime to characterize the ion energy, current density, and incident power as a function of axial position along the wall as well as thruster operating condition.

Axial profiles of incident ion current density, beam and sheath ion energies, and incident ion power are first provided along the inner and outer channel walls at 150 V and 300 V, 20 mg/s anode flow rate. These quantities are then spatially integrated or averaged to obtain global trends over several operating conditions spanning a wide range of discharge voltages, anode flow rates, and discharge powers. Fitting functions are described that allow spatial extrapolation of relevant quantities outside the limited interrogation zone. The presented characteristics within the channel are then correlated to beam current and divergence measured in the near-field plume. Finally, the calculated electron power to the walls and related energy analysis within the channel are briefly discussed.

7.1 Axial Profiles along the Channel Walls

7.1.1 Incident Ion Current Density

The incident ion current density to the inner and outer walls was calculated using the ion saturation current measured by internal flush probes. The saturation current was determined using methods outlined in Section 4.2.4 that account for sheath expansion

around the probe. Figure 7-1 and Figure 7-2 show the axial profiles of incident ion current density along the inner and outer channel walls at 150 V and 300 V, and 20 mg/s anode flow rate. The current density at $z = -0.095$ channel lengths along the inner wall is omitted due to signs of leakage current that significantly affected the measurement. For both walls, the peak current density is of the same order magnitude as the average current density exiting the thruster (discharge current divided by annular channel area). Furthermore, the incident current to the wall drops as the exit plane is approached.

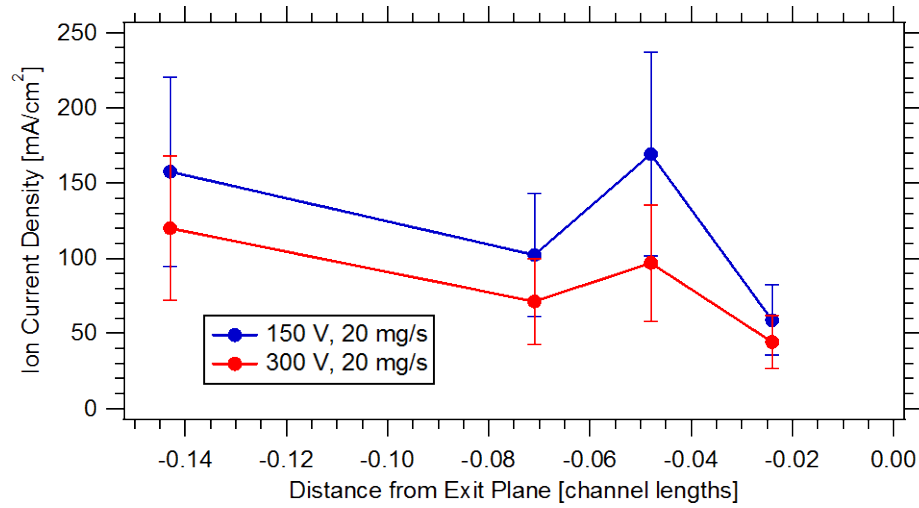


Figure 7-1. Axial profiles of incident ion current density along the inner channel wall at operating conditions of 150 V and 300 V, 20 mg/s. More ion current appears to reach the wall at 150 V, until the exit plane is approached where the incident currents are more equal.

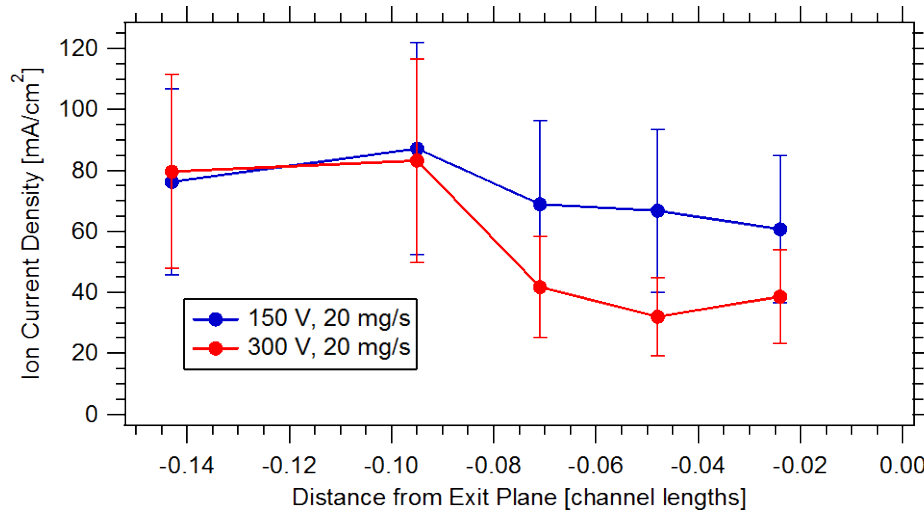


Figure 7-2. Axial profiles of incident ion current density along the outer channel wall at operating conditions of 150 V and 300 V, 20 mg/s. The incident current is roughly equal until the ions begin accelerating at 300 V, at which point the current hitting the walls is reduced.

Along the outer channel wall, the sudden drop in current at $z = -0.095$ channel lengths at 300 V is attributed to ions accelerating out of the channel; plasma potential profiles presented in Section 5.3.1 show the acceleration zone beginning at this location. The gain in axial-directed energy would reduce the residence time in the channel, and thus the time to be accelerated in the radial direction towards the wall. This trend, however, is not visible along the inner wall; this could be due to fewer available data points, as well as the fact that the acceleration zone at 300 V was found to begin further downstream along the inner wall compared to the outer wall (see Figure 5-9).

At nearly all locations, incident ion current was found to be higher at 150 V. Part of this trend is due to the acceleration zone occurring further downstream at low-voltage operation. Due to the weaker axial electric fields at 150 V, the increased current to the walls could also be caused by a naturally more divergent ion beam; this trend will be further discussed in Section 7.3, where internal data is correlated with ion current density measurements taken in the near-field plume.

Lastly, more ion current was measured along the inner wall compared to the outer wall. While this difference is largely diminished as the exit plane is approached, before the acceleration zone the incident current along the inner wall could exceed that along the outer wall by as much as a factor of two. This could be due in part to the acceleration zone occurring further downstream along the inner wall compared to the outer wall; thus, the drop in current density associated with acceleration would be shifted as well. However, HPHall-2 simulations presented in Chapter 6 showed elevated number densities along the inner wall at 300 V due to higher ionization rates; this could also increase the incident ion current density to the inner wall. Slightly elevated number densities (10-20% higher) were also present along the bulk plasma inner bound compared to the outer bound in prior internal measurements taken by Reid [13], although these data were limited to 0.1 channels widths away from the channel walls. Due to the dependence on current density, this asymmetry along the wall will also be seen in the calculated incident ion power density.

7.1.2 Sheath and Beam Energies

The incident ion energy at the channel walls is attained through voltage drops occurring within the acceleration zone of the thruster (beam energy) as well as the sheath

layer (sheath energy). The sheath energy is calculated using the measured electron temperature and methods outlined in Section 4.5.3. The beam energy is calculated by assuming ions fall from anode potential to the local plasma potential. This is justified since measurements in this work as well as prior internal measurements by Reid [13] show that the primary ionization zone occurs at a plasma potential that is within 5 – 10 V of the anode potential. Thus, the beam energy is set equal to the anode potential less the measured local plasma potential. Considering uncertainties in the plasma potential (for beam energy) and the calculated sheath potential, the uncertainty in the total ion energy is approximately $\pm 20\%$.

Figure 7-3 and Figure 7-4 show the calculated axial profiles of beam, sheath, and total ion energy incident along the inner and outer channel walls at 300 V, 20 mg/s anode flow rate. It is evident that, as expected, the total energy upstream of the acceleration zone is composed almost entirely of sheath energy. It is interesting to note that, within the interrogation zone, the sheath energy remains relatively fixed at 30 -50 eV. This is due to the secondary electron emission characteristics of the ceramic wall (see Section 4.5). For this reason, the total energy never exceeds 50 eV upstream of the acceleration zone. Once the ions begin gaining beam energy, the total energy rises significantly; over 200 eV of ion energy is expected to impact both walls at the exit plane.

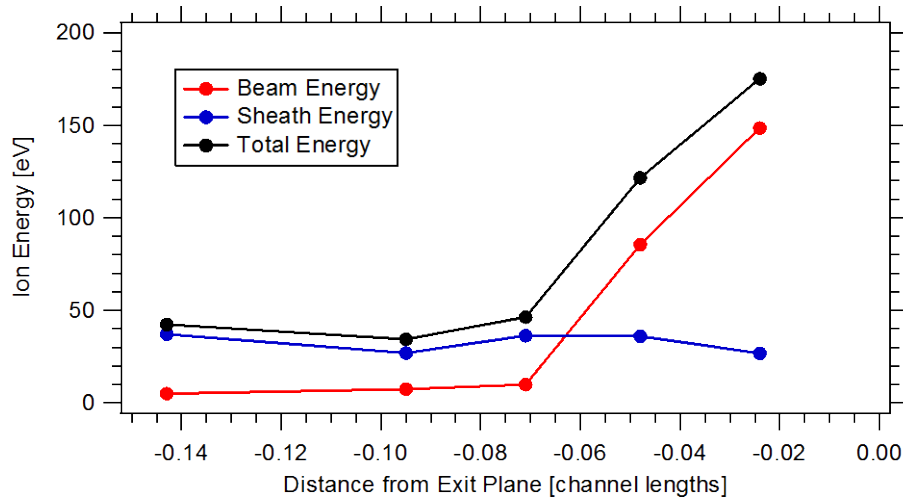


Figure 7-3. Axial profiles of sheath, beam and total ion energy along the inner wall near the exit plane at 300 V, 20 mg/s. The sheath energy is the primary component of ion energy for the majority of the channel, until the acceleration zone is reached. Uncertainty bars are omitted for clarity.

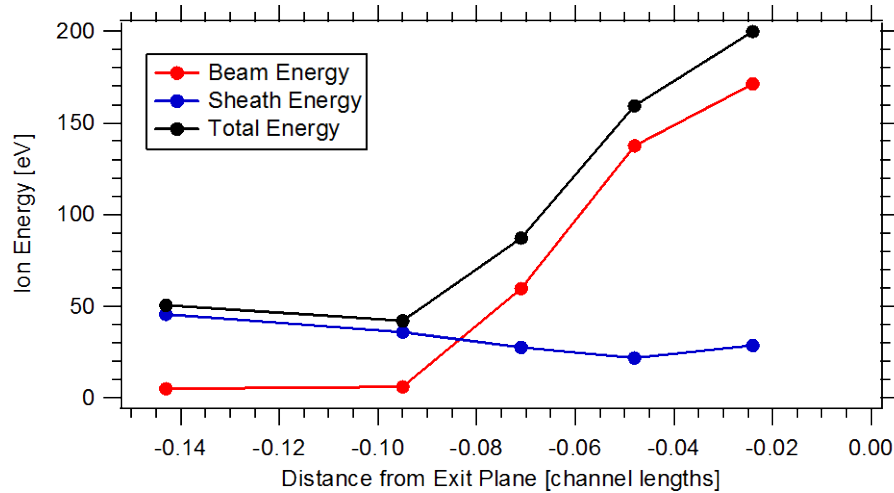


Figure 7-4. Axial profiles of sheath, beam and total ion energy along the outer wall near the exit plane at 300 V, 20 mg/s. The sheath energy is the primary component of ion energy until the acceleration zone is reached. Uncertainty bars are omitted for clarity.

The axial profiles of ion energy can have significant implications towards sputtering models and channel wall erosion. After approximately 334 hours of operation, the 6-kW Hall thruster showed negligible erosion along the inner wall occurring upstream of $z = -0.12$ channel lengths, with slightly more erosion occurring along the outer wall. While the thruster was only operated under nominal conditions for one-third of this duration, the correlation between the acceleration zone and the region of noticeable erosion is significant. This trend and related implications will be further discussed in Chapter 8.

Figure 7-5 and Figure 7-6 show the calculated beam, sheath and total ion energy axial profiles along the inner and outer walls near the exit plane at 150 V, 20 mg/s anode flow rate. The sheath energy is the primary component of ion energy for almost the entire channel; the beam energy does not become significant until the last 2% of the channel. As with operation at 300 V, the sheath energy is limited to approximately 50 eV due to the secondary electron emission characteristics of the ceramic wall. Despite the downstream shift in acceleration zone at lower voltage, total ion energies still approach about two-thirds of the discharge voltage at the exit plane.

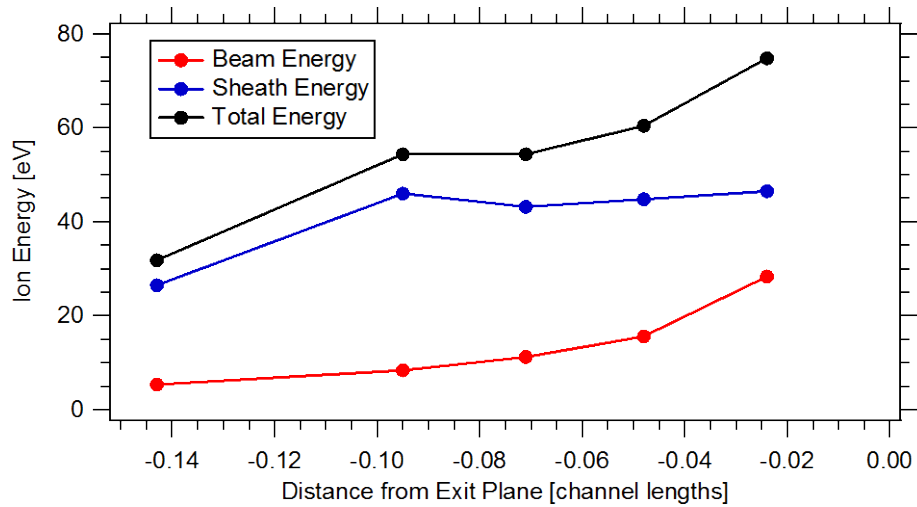


Figure 7-5. Axial profiles of sheath, beam and total ion energy along the inner wall near the exit plane at 150 V, 20 mg/s. The sheath energy remains the dominant component until the exit plane is reached. Uncertainty bars are omitted for clarity.

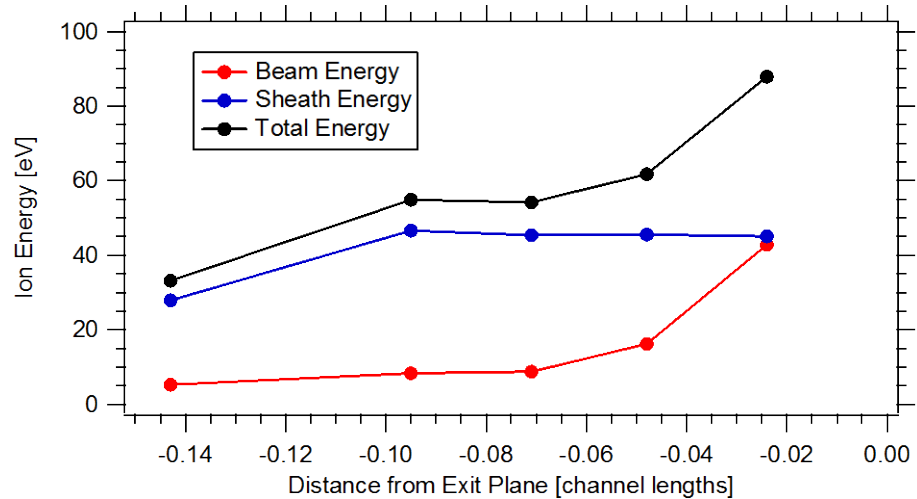


Figure 7-6. Axial profiles of beam, sheath and total ion energy along the outer wall near the exit plane at 150 V, 20 mg/s. The sheath energy remains the dominant component for almost the entire channel. Uncertainty bars omitted for clarity.

The contribution of beam and sheath energies to the total ion energy is better illustrated in Figure 7-7 and Figure 7-8. Due to similarities between walls, only the results for the outer wall are presented here. Deep in the channel, the sheath energy composes 80-90% of the total energy; as the exit plane is approached this trend is reversed, and the beam energy becomes the dominant source of total ion energy. These trends are consistent with simulation results of the BPT-4000 using HPHall-2 [69]. As expected, the location where the beam energy begins to dominate is determined by the location of the acceleration zone. At 300 V, the beam energy exceeds the sheath energy

for the last 8% of the channel. At 150 V, where the acceleration zone occurs further downstream, the beam energy does not exceed the sheath energy until the last 2% of the channel.

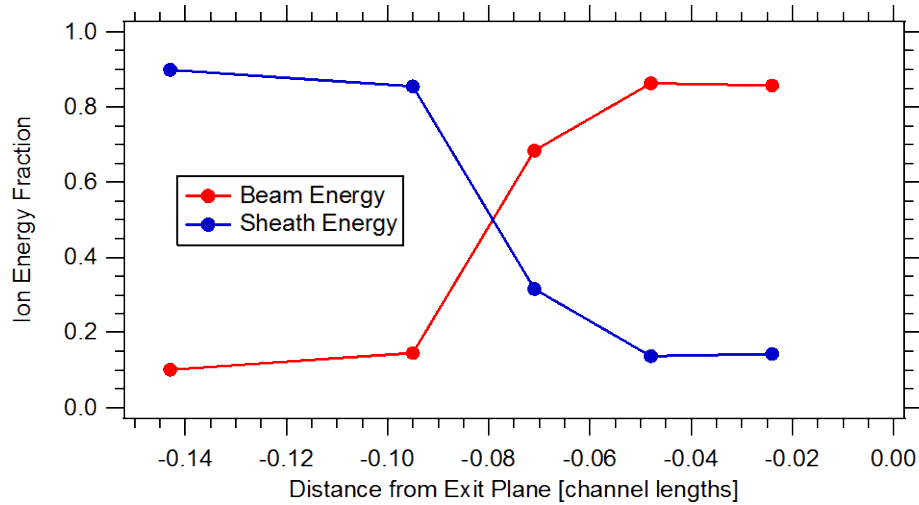


Figure 7-7. Axial profiles of the relative contributions of beam and sheath energies to the total ion energy along the outer wall at 300 V, 20 mg/s. Beam energy does not exceed the sheath energy contribution until the last 8% of the channel.

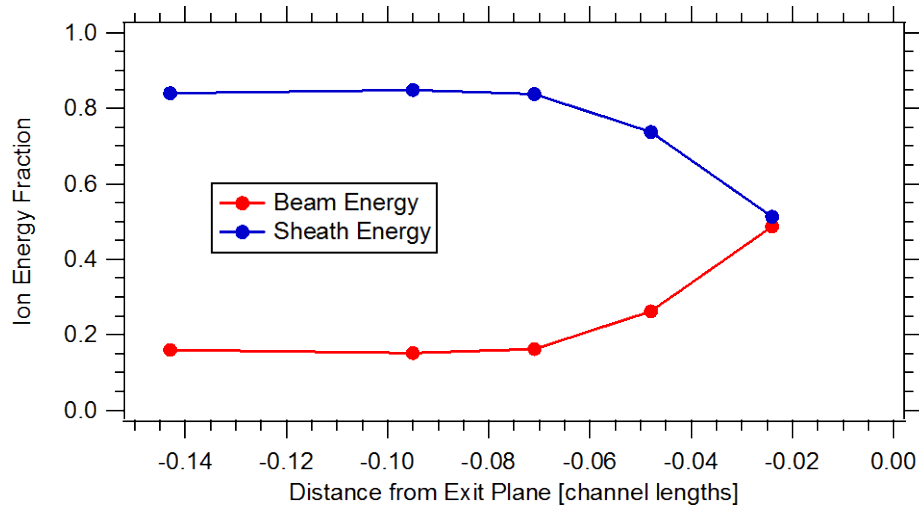


Figure 7-8. Axial profiles of the relative contributions of beam and sheath energies to the total ion energy along the outer wall at 150 V, 20 mg/s. Beam energy does not begin to exceed the sheath energy contribution until the last 2% of the channel.

The above profiles are important to characterize due to their impact on not only the incident energy but also the incident angle of approaching ions, both of which affect the sputtering yield of wall material. Furthermore, the correlation between the acceleration zone and the region of noticeable erosion indicates a high level of

dependence between the ion energy and sputter yield. The resulting trends will be used to infer more about the necessary sputtering yield function in Chapter 8.

7.1.3 Incident Ion Power Density

The incident ion power density is equal to the flux of ions to the wall multiplied by the energy each ion carries. Assuming that all the ions approaching the wall obtain the total energy calculated in Section 7.1.2, then this is simply the incident ion current density multiplied by the sum of the sheath and beam voltages. This assumption is justified due to prior LIF measurements taken within the channel which show a negligible fraction of ions with low energies in the acceleration zone [81]; thus, almost all the ions have been accelerated through the beam voltage near the wall. The combined uncertainty, from the calculated ion current density and energy, is estimated at $\pm 60\%$.

Figure 7-9 and Figure 7-10 show the calculated axial profiles of incident ion power density along the inner and outer channel walls at 150 and 300 V, 20 mg/s anode flow rate. The data at $z = -0.095$ channel lengths along the inner wall is not presented due to the probe showing signs of leakage current; thus, the measured ion current density was found to be significantly affected. The trend of the power density is a combination of the decrease in ion current density and increase in ion energy as the exit plane is approached. In general, the ion energy increases more rapidly than the current density decreases, resulting in a rise of power density as the exit plane is approached.

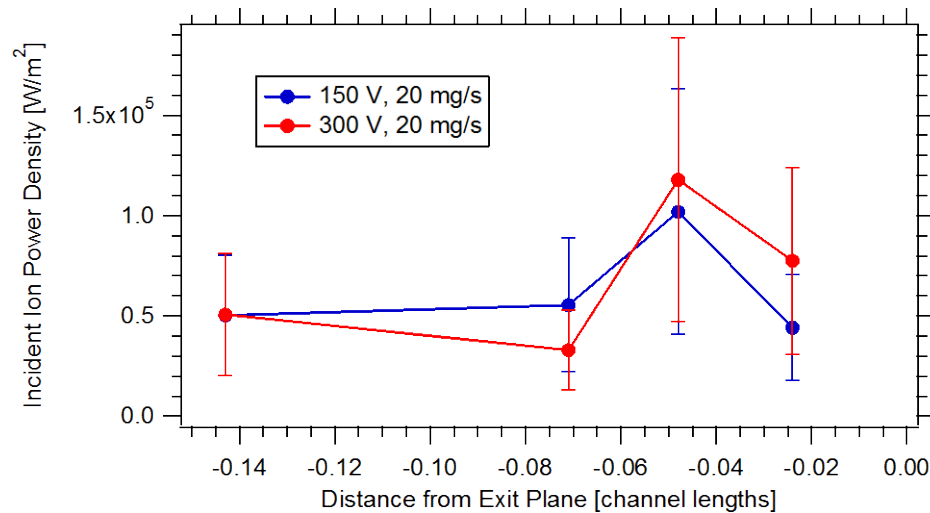


Figure 7-9. Axial profiles of incident ion power density along the inner wall near the exit plane at 150 and 300 V, 20 mg/s. In general, the power density increases as the exit plane is approached, with more power at 300 V.

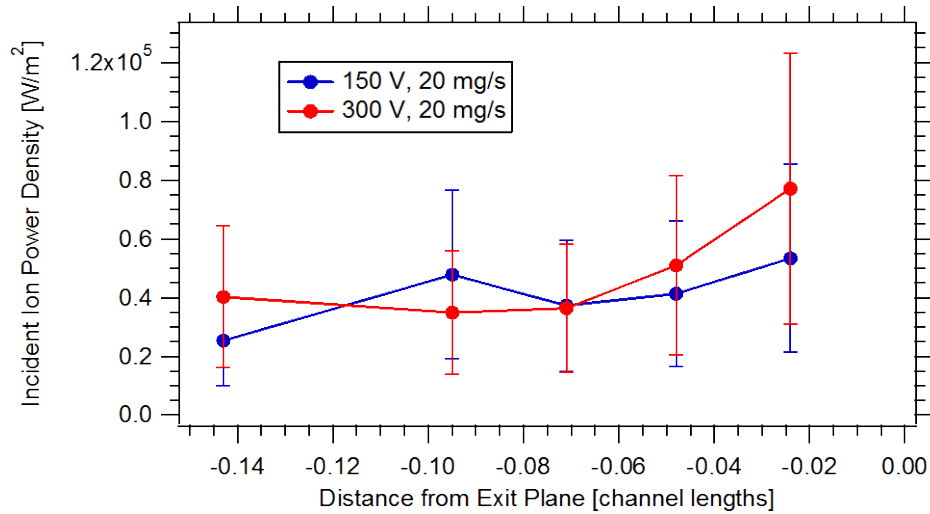


Figure 7-10. Axial profiles of incident ion power density along the outer wall near the exit plane at 150 and 300 V, 20 mg/s. The power density appears to increase as the exit plane is approached, with more power at 300 V.

While the incident power is roughly the same between 150 and 300 V upstream of the acceleration zone, increased power was calculated at 300 V near the thruster exit plane. Despite the discharge power being different by a factor of two, the sheath energies and incident ion current densities were found to be similar prior to ion acceleration, thus leading to similar power densities. However, the significantly higher beam energies present at 300 V near the exit plane result in a higher power density.

The drop in incident ion power along the inner wall from $z = -0.048$ to $z = -0.024$ channel lengths is caused by a drop in ion current to the wall. Since the ion energies near the exit plane are comparable between the inner and outer wall, and this trend is not seen along the outer wall, it is possible that this drop is due to uncertainty in the collection area due to probe degradation (see Section 5.1.2). This would cause uncertainty in the ion current density as well as the incident power density. However, with the exception of data at $z = -0.048$ channel lengths along the inner wall, the calculated power densities are comparable between the inner and outer channel walls. This rough similarity is expected due to the symmetric magnetic field topology used at all tested operating conditions.

7.2 Integrated and Averaged Quantities within the Channel

In order to quantify the incident ion power across a wide range of operating conditions, the power density is integrated along both channel walls to obtain the total incident ion power within the channel:

$$P_{ion} = 2\pi \left(\int_{inner\ wall} j_i \varepsilon_i r ds + \int_{outer\ wall} j_i \varepsilon_i r ds \right), \quad (7-1)$$

where j_i is the ion current density, ε_i is the incident ion energy, r is the local radius of the wall from thruster centerline, and s is the length coordinate along the wall. The incident ion power will also be investigated by decomposing the overall power into the total ion current to the walls and the average incident ion energy:

$$P_{ion} = I_{walls} \bar{\varepsilon}_i = 2\pi \left(\int_{inner\ wall} j_i r ds + \int_{outer\ wall} j_i r ds \right) \bar{\varepsilon}_i. \quad (7-2)$$

The list of the operating conditions that will be presented, which span a wide range of discharge voltages, flow rates, and discharge powers, can be found in Section 5.1. Bulk properties within the channel will first be limited to the interrogation zone near the exit plane using only the data points measured from the internal wall-mounted probes. Methods will then be described on extrapolating this data set to estimate values within the entire channel. These extrapolated values will then be used to determine the overall incident ion power properties within the channel.

7.2.1 Properties within Interrogation Zone

Figure 7-11 shows the integrated incident ion power to the channel walls within the interrogation zone of the 6-kW Hall thruster. In general, the power to the walls increases fairly linearly with discharge power, as expected. The line fit to the data corresponds to ion power that is 5.6% of the discharge power. Despite the linear trend, elevated values of incident ion power were calculated at a discharge voltage of 150 V, regardless of anode flow rate. Furthermore, the nominal operating condition of 300 V, 20 mg/s anode flow rate yielded less ion power than expected from the linear trend, only 4.3%. This can also be seen in Figure 7-12, which gives the percent discharge power that is incident on the channel walls from the ion flux. While the ensemble average is just over 6%, values over 8% were calculated at 150 V, 10 and 20 mg/s anode flow rate;

however, once the flow rate reached 30 mg/s the percentage dropped to just above 6%. In order to determine the cause of these trends, the incident power is decomposed into the total ion current to the walls and the average incident ion energy.

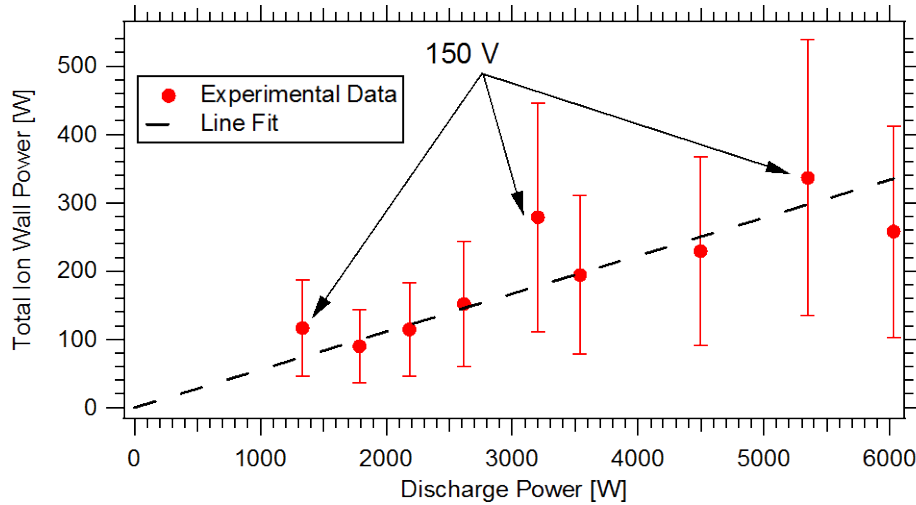


Figure 7-11. Total ion power to the walls within the interrogation zone. While the ion power is fairly linear with discharge power, elevated values were found at 150 V.

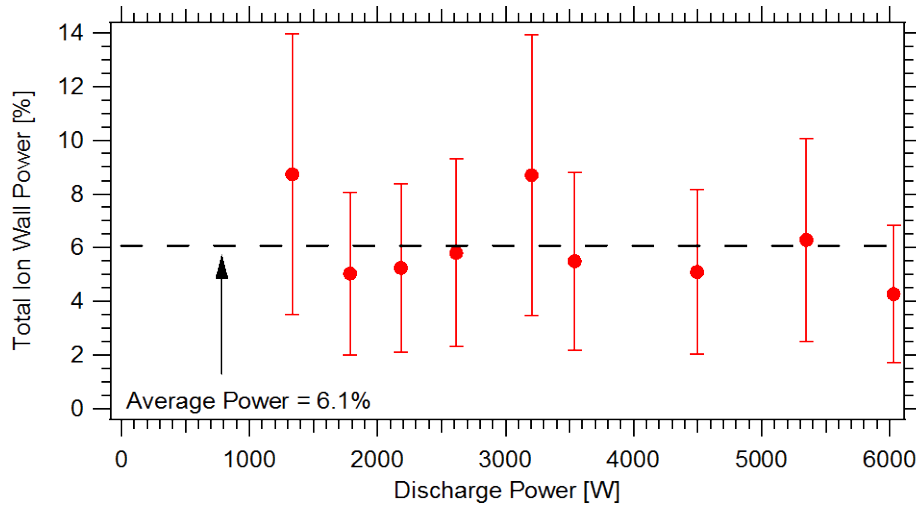


Figure 7-12. Percent of discharge power that is incident on walls from ion flux. Average power over all operating conditions tested is roughly 6%. Values over 8% were calculated at 150 V, 10 and 20 mg/s.

Figure 7-13 shows the integrated ion current to both channel walls within the interrogation zone. As expected, more current is incident upon the walls at higher flow rates, primarily due to the higher number of ions created. The incident ion current was found to decrease with increasing discharge voltage at all flow rates tested. This can be better seen in Figure 7-14, which non-dimensionalizes the incident ion current by the

beam current to minimize the dependence on flow rate. Beam current was determined from prior studies [13] as well as measurements in this work using near-field Faraday probes. Due to the $\pm 10\%$ uncertainty in measured beam current, the relative uncertainty for the non-dimensionalized incident ion current is $\pm 50\%$. Values dropped from over 30% to 10% across the range of voltages tested.

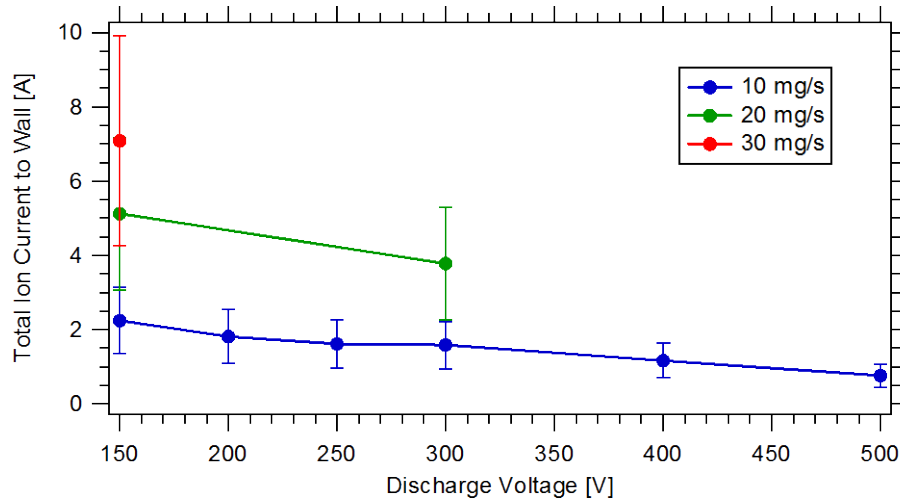


Figure 7-13. Integrated ion current to the channel walls within the interrogation zone. Total ion current appears to increase with anode flow rate and decrease with discharge voltage.

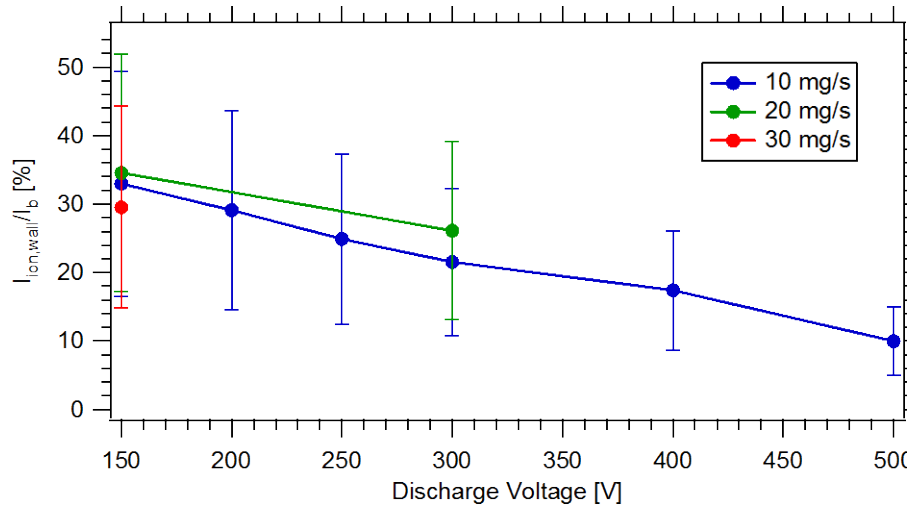


Figure 7-14. Total ion current to the channel walls within the interrogation zone, non-dimensionalized by the measured beam current. The decreasing trend with discharge voltage is much more defined, and is present at all flow rates.

The large ion currents to the wall at low voltages can be attributed to higher divergences within the channel created by relatively large radial electric fields. The correlation between this “internal” divergence and plume divergence is further investigated in Section 7.3.3. The elevated values of incident ion current at least partially

explain the reason for the higher incident ion powers observed at 150 V. However, the overall trend of decreasing current with discharge voltage may be the result of the acceleration zone moving upstream with increasing discharge voltage. Since the values above are limited to the interrogation zone, the internal wall-mounted probes could be measuring lower currents because the peak ion current density moves upstream with the acceleration zone. Thus, especially at higher discharge voltages, this peak may not be captured by the probes and would create a deceptively low incident ion current measurement. For this reason, the data set is extrapolated to the entire channel in Section 7.2.3 to better characterize the overall ion power to the wall.

Figure 7-15 shows the average incident ion energy along the channel walls within the interrogation zone. As expected, the average energy increases with discharge voltage due to the corresponding increases in beam energy. At low voltages where beam energies are low, average energies are approximately 50 eV; this corresponds to typical sheath energies found at these voltages. At higher voltages, the average energy near the exit plane can reach hundreds of eV.

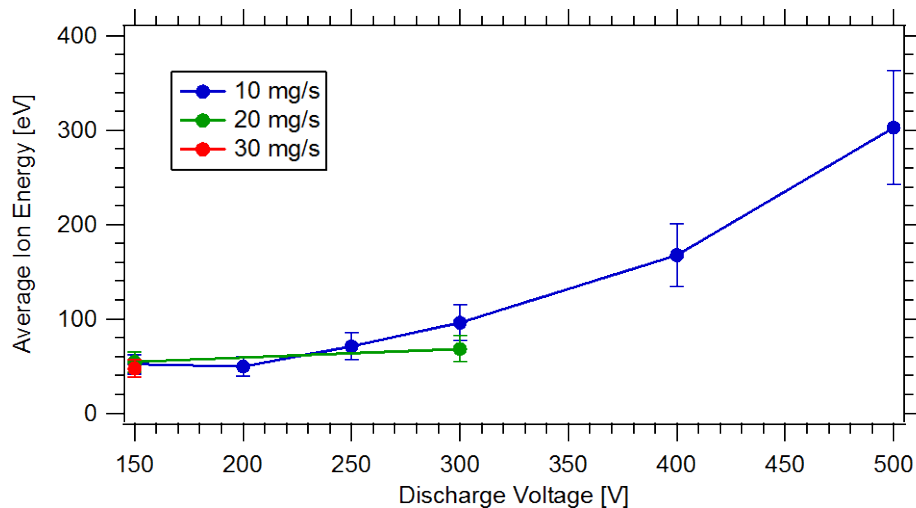


Figure 7-15. Averaged incident ion energy along the channel walls within the interrogation zone. As expected, the average energy increases with discharge voltage as the channel becomes exposed to higher beam energies.

In order to eliminate the dependence of the average incident energy on increased beam energies, the incident energy is non-dimensionalized by the discharge voltage. Figure 7-16 shows that despite this non-dimensionalization, the average incident ion energy is still found to increase with discharge voltage. However, at lower voltages, the average incident energy actually decreases before rising. This trend is caused by two

competing effects. The first is an increase in relative beam energy with discharge voltage. As the discharge voltage is increased, the acceleration zone recedes further into the channel; thus, within the interrogation zone, the ions have fallen through a larger portion of the total acceleration voltage and the walls are exposed to higher beam energies. The second effect is an increase in relative sheath energy at reduced voltages. The electron temperature within Hall thrusters has been shown to roughly scale with discharge voltage up to several hundred volts [8,10,11,13]. Based on the sheath model described in Section 4.5.3, while the sheath energy typically increases with electron temperature, the *relative* sheath energy maximizes at temperatures below 20 eV; that is, sheath energies are several electron temperatures when the electron temperature is low, but only one electron temperature when the electron temperature is high. Thus, at lower discharge voltages, the electron temperature will be lower and will correspond to higher relative sheath energies. These two competing effects create a minimum in the relative incident ion energy at moderate discharge voltages.

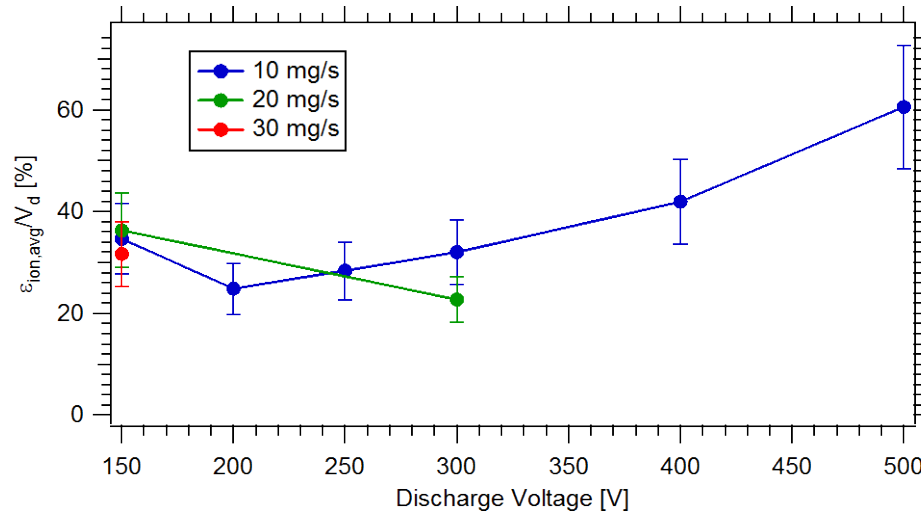


Figure 7-16. Averaged incident ion energy along the channel walls, non-dimensionalized by the discharge voltage. In general, the energy increases with discharge voltage, but decreases at lower voltages.

While the above trends are important towards understanding incident ion power near the exit plane where channel wall erosion is significant, limited insight can be gained without extending the data set to the entire channel. For this reason, extrapolation schemes are presented that allow estimates of total incident power to be made.

7.2.2 Extrapolation of Properties to Entire Channel

In order to extrapolate calculations of the total incident ion power to the entire channel, complete axial profiles of plasma potential (to calculate beam energy), electron temperature (to calculate sheath energy) and ion current density are required. Methods of performing this extrapolation and their validation are provided below.

7.2.2.1 Plasma and Floating Potentials

Prior internal measurements on the 6-kW Hall thruster [13] have shown that the axial profiles of plasma and floating potential follow a general “S” shape which is characteristic of a sigmoid function:

$$f(z) = A + \frac{B}{1 + \exp\left(\frac{C - z}{D}\right)}, \quad (7-3)$$

where A , B , C and D are fitting parameters. Figure 7-17 compares measured axial profiles of plasma and floating potential taken by Reid [13] along channel centerline to the corresponding sigmoid fits within the channel. In general, the sigmoid function agrees well with the experimental data; the slight deviation of floating potential near the exit plane is attributed to the irregular bump in the measured profile, and does not occur in the data of this work. It should be noted that these profiles are limited to the channel and does not include the plume; it was found that the downstream portion of the plasma potential is better described by exponential decay. For this particular work, however, only the profile within the channel needs to be sufficiently extrapolated.

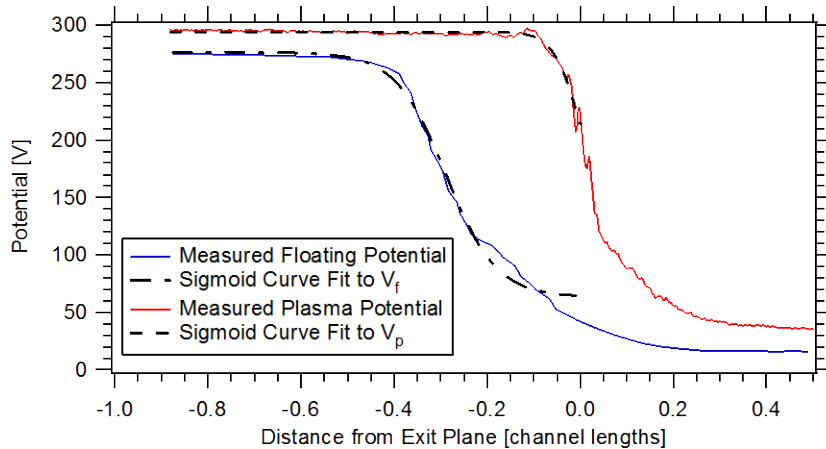


Figure 7-17. Sigmoid curve fits to floating and plasma potential axial profiles along channel centerline within the channel, under nominal conditions of 300 V and 20 mg/s anode flow rate. Data taken from Ref. [13].

In order for the sigmoid fit to be properly applied to the present data set, boundary conditions must be determined that allow the function to reach the proper plateaus. Since the measured plasma potential prior to the acceleration zone was found to be within 5 – 10 V of the anode potential, the plasma potential is set equal to anode potential at the location of the anode. Furthermore, the far-field plasma potential is typically 20 – 30 V above cathode potential [13], so the plasma potential is set to 25 V one channel diameter downstream of the thruster exit plane.

Floating potential boundary conditions are based off the plasma potential boundary conditions and a difference proportional to the local electron temperature. Based off prior internal measurements [13], the electron temperature at the anode and one channel diameter downstream of the exit plane is set to 5 eV. The average difference between measured plasma and floating potentials in this study was found to be 4.6 electron temperatures; thus the floating potential boundary conditions are set to 23 V below the plasma potential boundary conditions.

Figure 7-18 compares measured plasma and floating potentials along the outer channel wall to extrapolated sigmoid fits at 300 V, 20 mg/s anode flow rate. The sigmoid function appears to fit the experimental data very well, and thus allows for determination of plasma and floating potentials within the entire channel. The plasma potential may be used to determine the incident ion beam energy along the wall; as will be discussed in the following section, the floating potential will be used to determine the electron temperature, and thus the sheath energy, along the wall.

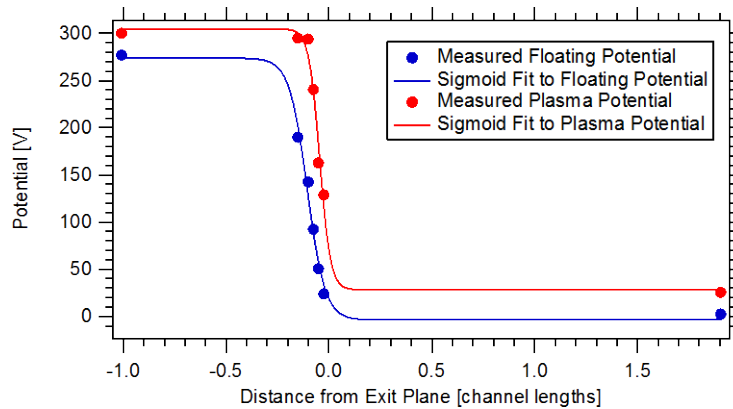


Figure 7-18. Comparison of measured plasma and floating potentials along the outer channel wall and extrapolated sigmoid fits to the entire channel, at 300 V and 20 mg/s anode flow rate. Boundary points at the anode and in the plume are based off prior measurements. Uncertainty bars omitted for clarity.

7.2.2.2 Electron Temperature

Based on the sheath model described in Section 4.5.3, the sheath energy may be calculated from the local electron temperature. Since fitting functions are difficult to apply in this case due to the uncertainty in magnitude and axial location of maximum electron temperature, the extrapolated plasma and floating potential profiles (see Section 7.2.2.1) are used to determine the electron temperature profile within the channel. Using the data from ten internal wall-mounted probes across nine operating conditions, the average difference between plasma and floating potentials along the channel wall was found to be 4.6 electron temperatures, very close to the ideal value of 5.3. The distribution of these values yielded a near-Gaussian profile with a standard deviation of approximately 20% of the mean value of 4.6. Since this deviation is close to the uncertainty in measured electron temperature, it was deemed acceptable to use for all operating conditions. Thus, the extrapolated floating potential was subtracted from the extrapolated plasma potential and divided by 4.6 to obtain the full axial profile of electron temperature within the channel.

Figure 7-19 compares the measured electron temperature along the outer wall to the extrapolated profile at 300 V, 20 mg/s anode flow rate. The extrapolated profile shows reasonable agreement with the experimental data, and accurately reproduces the location and magnitude of maximum electron temperature. Furthermore, the extrapolated profile was found to resemble a Gaussian distribution, which is consistent with prior internal measurements (see Section 7.2.2.3). Thus, this technique allows the determination of electron temperature and sheath energy along the entire channel wall.

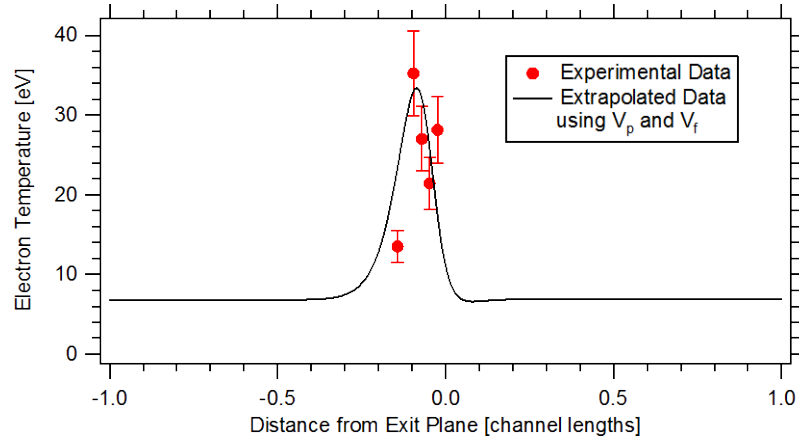


Figure 7-19. Comparison of measured electron temperature along the outer channel wall to the extrapolated axial profile within the channel, at 300 V and 20 mg/s anode flow rate. The extrapolated profile shows reasonable agreement with experimental data, and accurately reproduces the location and magnitude of maximum electron temperature.

7.2.2.3 Ion Current Density

Extrapolation of the ion current density profile is considerably more difficult than previous quantities due to the apparent lack of a general structure, uncertainty in the magnitude and location of maximum current density, and scarcity of prior internal measurements that span a larger axial range. However, a generalized functional form can be recovered by using observations of prior as well as present measurements. For most of the channel, the incident ion current should be equal to the Bohm current since negligible axial acceleration has occurred. Thus,

$$j_i = en_i \sqrt{\frac{eT_e}{M_i}} \propto n_i \sqrt{T_e}. \quad (7-4)$$

Prior internal measurements by Reid [13] can then be used to determine functional forms of ion number density and electron temperature. It was found that the electron temperature profile within the channel most closely resembles a Gaussian function, while the ion density profile most closely follows a Lorentzian profile. Figure 7-20 compares the functional fits to the measured profiles along the bulk plasma outer bound (10% of the channel width away from the outer wall), which shows reasonable agreement between the two.

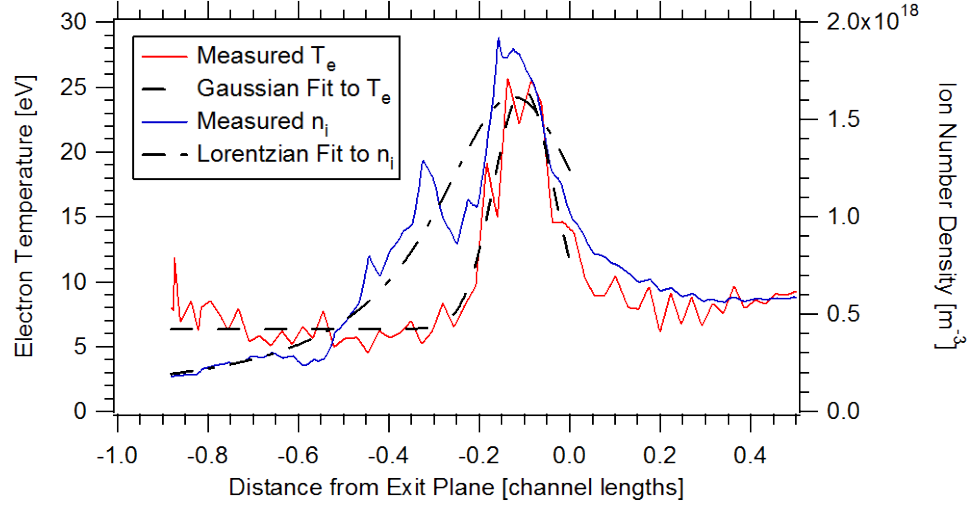


Figure 7-20. Comparison of functional fits to measured axial profiles of electron temperature and ion number density along the bulk plasma outer bound at 300 V and 20 mg/s anode flow rate. Data taken from Ref. [13]. The electron temperature was found to closely follow a Gaussian profile, while the ion number density most closely resembled a Lorentzian profile.

Following Eq. (7-4), the ion current density profile within the channel can be approximated as the product of Gaussian and Lorentzian functions:

$$f(z) = \frac{A \exp\left(-\frac{(z - z_0)^2}{B}\right)}{(z - z_0)^2 + C}, \quad (7-5)$$

where A , B , C and z_0 are fitting parameters. To simplify the equation and fitting process, the location of maximum number density and electron temperature were assumed to be the same; since these values typically both peak around the beginning of the acceleration zone, this was deemed a reasonable assumption. Furthermore, the function was forced to approach zero at positive and negative infinity based on physical reasoning. Boundary conditions at the anode and one channel diameter downstream were set to zero. While this is not strictly true, the low values of ion density and electron temperature at these extreme locations make this a reasonable approximation. Figure 7-21 compares the experimental values of ion current density to the functional fit along the outer channel wall at 300 V, 20 mg/s anode flow rate. Reasonable agreement is found between the two, indicating that this technique can be used to determine the incident ion current density along the entire channel wall.

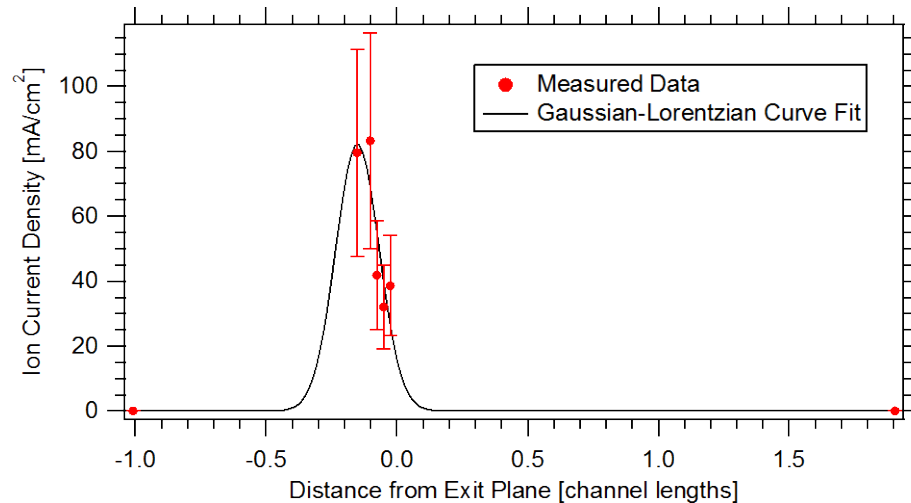


Figure 7-21. Comparison of measured and extrapolated ion current density to the outer channel wall, at 300 V and 20 mg/s anode flow rate. The functional fit is in reasonable agreement with the experimental data.

While the above technique is a reasonable method of extrapolation, it remains sensitive to the location of maximum current density. The present data indicates that this maximum occurs close to the beginning of the acceleration zone; since the entire acceleration zone was captured under most operating conditions, the maximum measured current density was typically taken as the maximum current density in the channel. However, at higher discharge voltages this is no longer the case. In particular, at 500 V significant acceleration had occurred upstream of the interrogation zone. Therefore, an artificial data point was created based off the extrapolated plasma potential profile as well as ion current density measurements at the other operating conditions. Since the maximum measured current density did not significantly change with increasing voltage, this data point was calculated as a reasonable estimate of the location and magnitude of the maximum current density at 500 V.

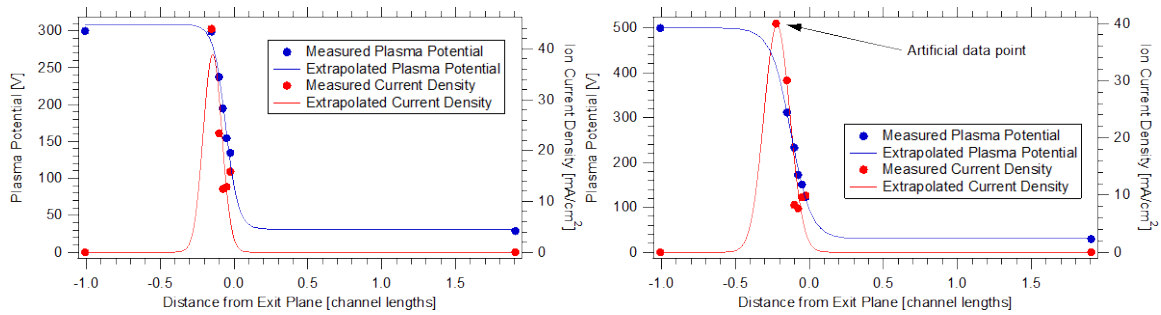


Figure 7-22. Extrapolated plasma potential and ion current density profiles at 300 V and 10 mg/s (left) as well as at 500 V and 10 mg/s (right). In order to ensure the peak current density was captured at 500 V, an artificial data point was created based on the magnitude of the peak at other operating conditions as well as the relative location of this peak along the plasma potential profile. Uncertainty bounds are omitted for clarity.

7.2.3 Estimated Values over Entire Channel Length

The methods outlined in Section 7.2.2 were used to determine the incident ion power characteristics over the length of the entire channel. Figure 7-23 shows the total incident ion power to the channel walls as a function of discharge power. In general, there is an increase in wall power with discharge power; the linear fit corresponds to 10.9% of the discharge power being incident on the walls through ion flux. However, nearly no actual points lie on this line, and elevated values were found at 150 and 500 V. The remaining operating conditions have less than 10% of the discharge power incident on the walls. This is better seen in Figure 7-24, which plots this percentage as a function of discharge power. The average wall power over all operating conditions was found to be over 11%, with elevated powers occurring at 150 V, 10 and 20 mg/s anode flow rate, as well as at 500 V. Similar to Section 7.2.1, further insight into these trends can be found by decomposing the ion power into the total ion current to the walls and the average incident ion energy.

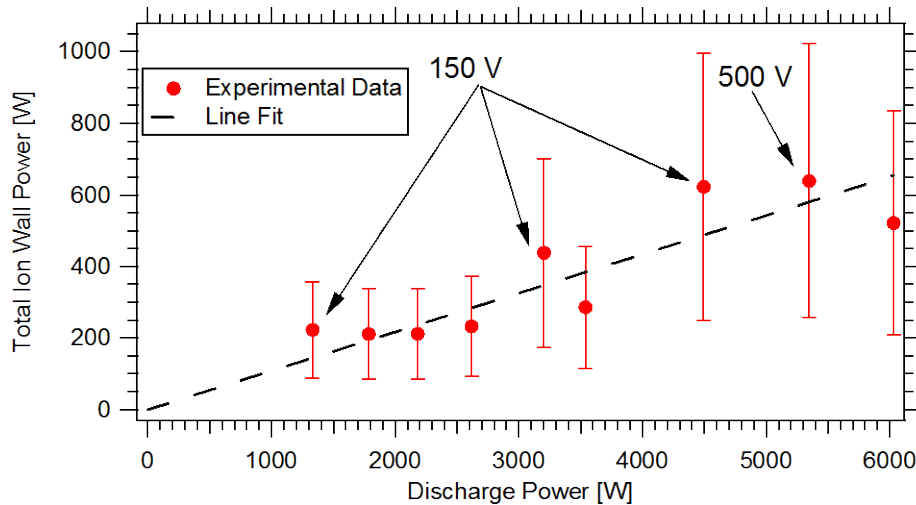


Figure 7-23. Total incident ion power to the walls within the channel. While there is a general increase in wall power with discharge power, elevated values were found at 150 and 500 V.

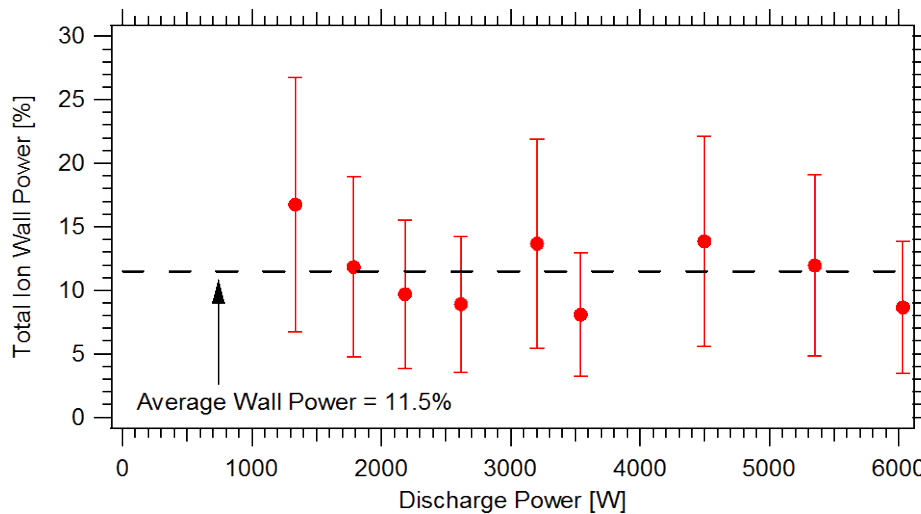


Figure 7-24. Percent of discharge power incident on the channel walls via ion flux. Elevated values are found primarily at 150 V, 10 and 20 mg/s, as well as at 500 V. Average ion power over all operating conditions is 11.5%.

The total integrated ion current to the channel walls is shown in Figure 7-25. As expected, the total current to the wall increases with flow rate due to the increased number of ions created. The ion current to the walls can be sizeable, approaching 20 A at 150 V, 30 mg/s anode flow rate. In general, it appears that the ion current drops as discharge voltage increases; however, the total ion current increases from 400 to 500 V, and hardly changes when going from 150 to 300 V at 20 mg/s anode flow rate. This can be better seen in Figure 7-26 which non-dimensionalizes the total ion current to the wall

by the ion beam current, determined from prior [13] and present (see Section 7.3) measurements within the near-field plume.

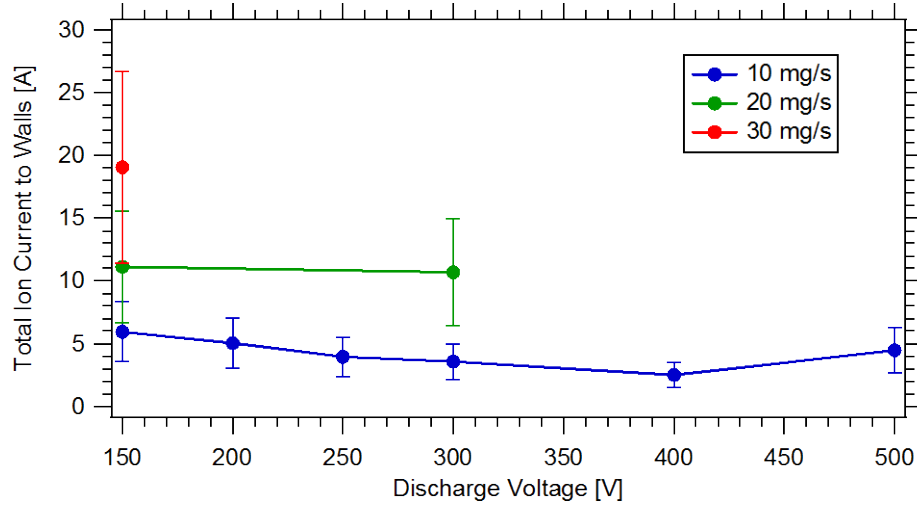


Figure 7-25. Total integrated ion current to the channel walls as a function of discharge voltage. As expected, total wall current increases with mass flow rate. In general, wall current drops with increased voltage, but appears to increase at 500 V.

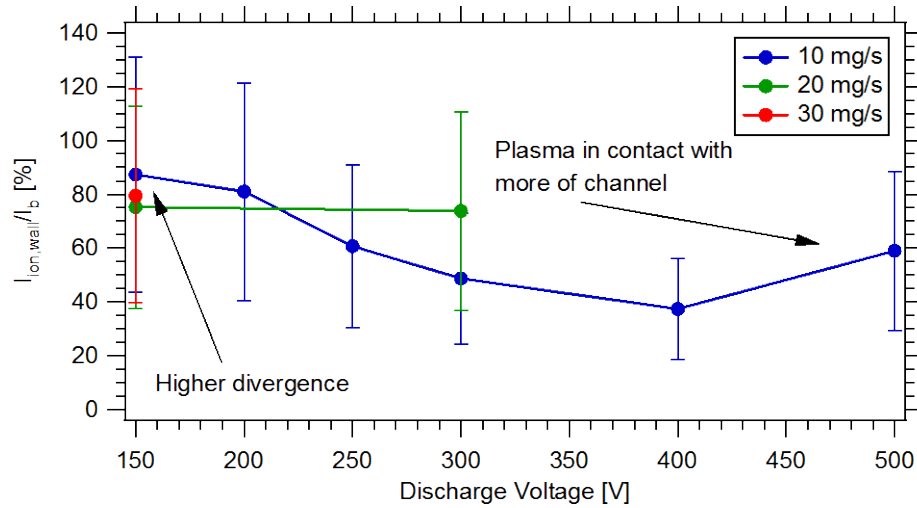


Figure 7-26. Total ion current to the channel walls non-dimensionalized by ion beam current. In general, elevated values are found at low voltage due to high divergence and at high voltage due to recession of the acceleration zone.

The observed trends are likely the cause of two competing effects. The first is high divergence of ions within the channel at low discharge voltage due to relatively strong radial electric fields. This will cause more ions to hit the wall, leading to elevated ion currents. This divergence will be correlated to measured near-field plume properties in Section 7.3.3. The second effect is the recession of the acceleration zone deeper into the channel at increased discharge voltages. As this layer recedes, more plasma is created

deeper in the channel, thus exposing more of the channel wall to ion flux. This will also increase the total ion current to the wall, and is the reason for elevated values at 500 V; this trend was not found when the integrated ion current was restricted to the interrogation zone. Thus, these two competing effects cause a minimum in the total ion current to the walls at moderate discharge voltages.

Figure 7-27 shows the average incident ion energy over the entire channel of the 6-kW Hall thruster. As expected, the incident ion energy increases with discharge voltage due to larger beam and sheath energies at higher discharge voltages. Despite being averaged over the entire channel, ion energies still exceed 100 eV at 400 and 500 V, and drop no lower than 40 eV at 150 V. In order to eliminate the dependence of elevated energies due to increased discharge voltage, the average ion energy is non-dimensionalized and plotted again in Figure 7-28.

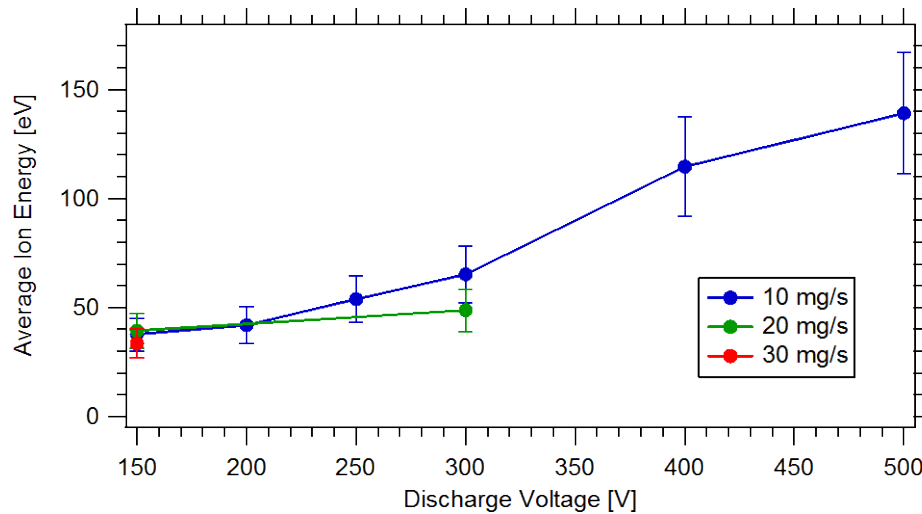


Figure 7-27. Average incident ion energy along the channel walls as a function of discharge voltage. As expected, the average energy increases with discharge voltage, exceeding 100 eV at 400 and 500 V.

With the exception of 300 V, 20 mg/s anode flow rate, the average incident ion energy remains between 20 and 30% of the discharge voltage. A clear minimum is found at moderate discharge voltages, similar to the result found in Section 7.2.1. The cause of this minimum is due to higher sheath energies at low voltage and higher beam energies at high voltage. Due to secondary electron emission effects, the lower temperatures typically found in low voltage discharges correspond to higher *relative* sheath energies; that is, sheath voltages that are several electron temperatures in magnitude. At higher voltages, the relative sheath energies are low; but the acceleration zone recedes further

into the channel, exposing more of the channel to high relative beam energies. For these reasons, the incident ion power (relative to the discharge power) is minimized at moderate voltages.

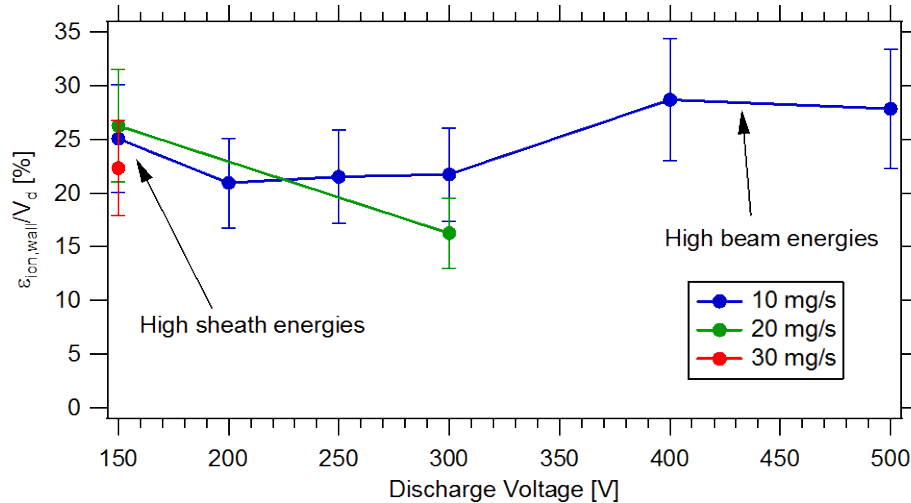


Figure 7-28. Average ion energy to the channel walls non-dimensionalized by discharge voltage. A minimum occurring at moderate voltages is caused by high sheath energies at low voltage and elevated beam energies at high voltage.

7.3 Correlation with Near-field Ion Current Density Measurements

Ion current density measurements were taken in the near-field plume of the 6-kW Hall thruster in order to correlate properties within the channel to those observed immediately downstream of the thruster exit plane. Calculated ion beam currents and plume divergences will first be discussed and compared to prior measurements at the nominal operating condition of 300 V, 20 mg/s anode flow rate. These values will then be used along with internal wall-mounted probe data to define an “internal divergence” that is compared to the calculated plume divergence.

7.3.1 Ion Beam Current

The total ion beam current was calculated at various axial locations downstream of the exit plane using methods described in Section 3.8. Figure 7-29 shows the calculated ion beam current at various distances from the thruster exit plane at 300 V, 20 mg/s. Values were found to be very consistent from 0.3 to over 1 mean thruster diameter ($D_{T,m}$) from the exit plane. As the probe moves deeper into the plume, the ion beam exiting the thruster begins to merge into a single beam centered at thruster centerline

instead of channel centerline; when this occurs, the near-field analysis techniques break down and the calculated beam current drops precipitously.

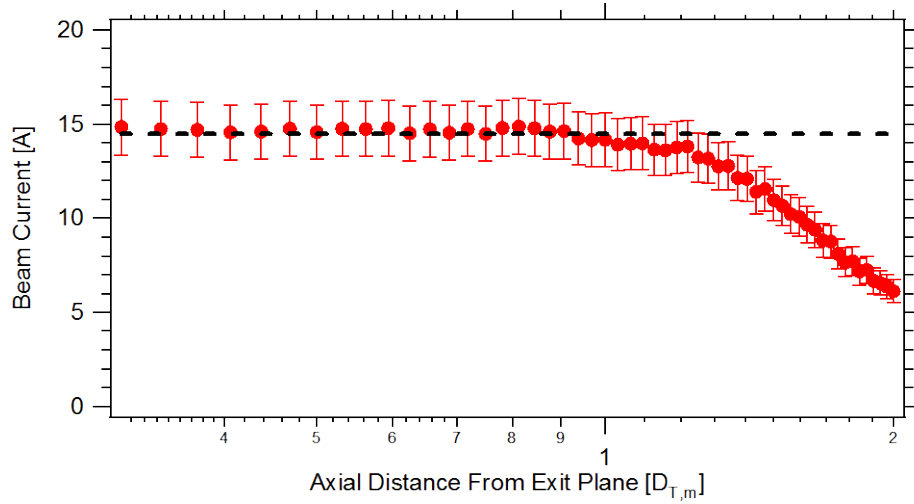


Figure 7-29. Calculated ion beam current as a function of distance from the thruster exit plane, at 300 V and 20 mg/s. Values are very consistent from 0.3 to over 1 mean channel diameter. Horizontal line corresponds to reported beam current value.

Calculated beam currents as well as the corresponding current utilization efficiencies are given in Table 7-1. Values with asterisks denote data taken from prior near-field studies performed by Reid [13]. In general, it appears that the current utilization increases with voltage and decreases with anode flow rate.

Table 7-1. List of calculated beam currents and current utilization efficiencies for the operating conditions in this work. Values with asterisks denote data taken from Reid [13].

Operating Condition	Beam Current [A]	Current Utilization Efficiency
150 V, 10 mg/s	6.80*	0.739*
200 V, 10 mg/s	6.23	0.700
250 V, 10 mg/s	6.48	0.739
300 V, 10 mg/s	7.35*	0.812*
400 V, 10 mg/s	6.66	0.739
500 V, 10 mg/s	7.58	0.830
150 V, 20 mg/s	14.8*	0.692*
300 V, 20 mg/s	14.5 (15.8*)	0.719 (0.777*)
150 V, 30 mg/s	24.0*	0.675*

These trends can be seen across the data taken by Reid as well as data taken within this work, but the two separate data sets do not match up well. It is evident that Reid consistently measured higher beam currents than those found in this study. This can

readily be seen by comparing the two data sets at 300 V, 20 mg/s anode flow rate, although these two measurements agree within the quoted uncertainty bounds. Figure 7-30 compares the radial profile of measured ion current density between Reid and this work at 300 V, 20 mg/s anode flow rate, $0.3 D_{T,m}$ (mean thruster diameters) downstream of the exit plane. While there is excellent agreement around the channel (centered at $0.5 D_{T,m}$), Reid measured elevated current densities at locations far off-axis and around thruster centerline. These regions are expected to largely contain slow-moving ions either from the cathode (at centerline) or within the facility background (far off-axis). It is likely that Reid measured more slow-moving ions due to the exposed edge and rear of the Faraday probe, which were insulated with ceramabond in this study. However, significant differences tended to only occur outside the radial range used to determine beam current and plume divergence. Therefore, since the difference between the two measurements in the analyzed region is within the uncertainty bounds, no attempts were made to correct them.

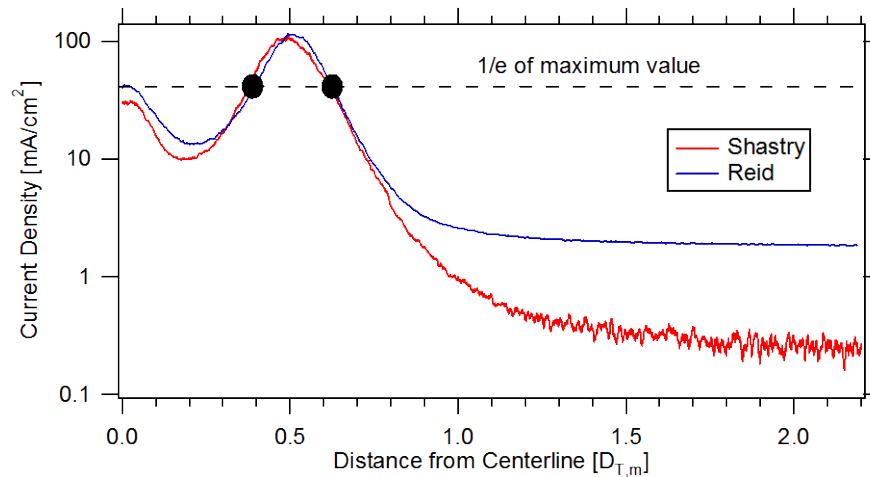


Figure 7-30. Comparison of ion current density radial profiles taken by Reid and in this study, $0.3 D_{T,m}$ downstream of the exit plane at 300 V, 20 mg/s. Elevated current densities are found by Reid far off axis and near thruster centerline.

7.3.2 Plume Divergence

The plume divergence angle was calculated from near-field current density measurements using analysis techniques described in Section 3.8. Figure 7-31 shows the calculated divergence angle at various axial locations downstream of the exit plane at 300 V, 20 mg/s anode flow rate. As found by Reid [13], the calculated divergence angle in the near-field plume is consistent over a certain axial range, usually around $1 D_{T,m}$. This

range corresponds to the locations that are far enough downstream where the point source approximation is valid, but upstream of where the plume merges into a single beam. This range was found to be highly dependent on operating condition, and can be relatively small in extent if the plume divergence is large.

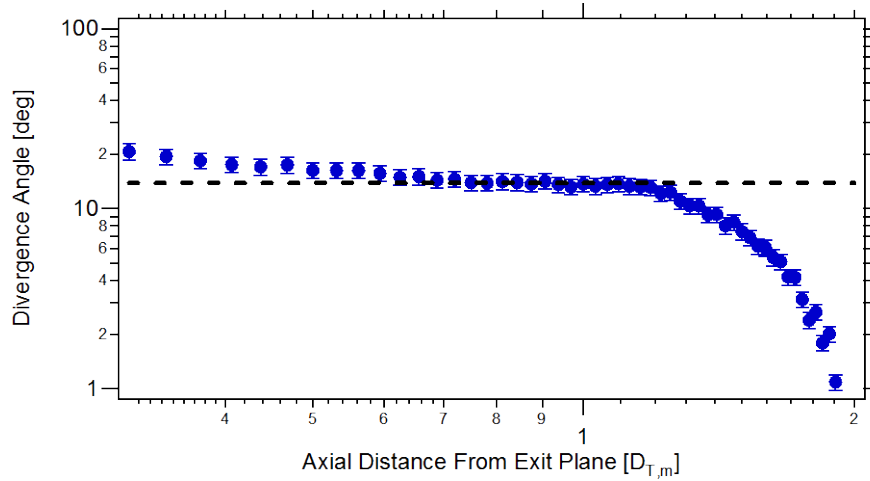


Figure 7-31. Calculated divergence angle at various axial locations downstream of the thruster exit plane at 300 V, 20 mg/s. Horizontal line corresponds to reported divergence angle.

Table 7-2 gives the calculated plume divergence angles and corresponding divergence efficiencies based off the near-field Faraday probe measurements. Values with asterisks correspond to data taken from Reid [13]. In general, better focusing is found at higher voltages and higher anode flow rates.

Table 7-2. List of calculated plume divergences and divergence efficiencies from near-field ion current density measurements. Values with asterisks correspond to data from Reid [13].

Operating Condition	Plume Divergence Angle [deg]	Divergence Efficiency
150 V, 10 mg/s	27*	0.794*
200 V, 10 mg/s	17	0.915
250 V, 10 mg/s	16	0.924
300 V, 10 mg/s	20*	0.883*
400 V, 10 mg/s	15	0.933
500 V, 10 mg/s	19	0.894
150 V, 20 mg/s	28*	0.780*
300 V, 20 mg/s	14 (16*)	0.941 (0.921*)
150 V, 30 mg/s	25*	0.821*

As observed with the beam current measurements, higher values of plume divergence were measured by Reid than in this study. The probable cause is identical to the reason for elevated beam currents: more slow-moving ions appear to have been collected near the thruster centerline and far off-axis, resulting in a wider current density distribution (see Section 7.3.1). However, the error is within the uncertainty bounds for both measurements, therefore no effort was made to correct it.

It is interesting to note that while beam focusing improved at higher discharge voltages, a higher divergence angle was measured at 500 V. This can easily be seen in the ion current density contours in Figure 7-32 and Figure 7-33, which show that the plume is much more collimated at 400 V. While the reason for this is still unclear, it will be shown in the following section that the increased divergence is correlated with increased ion currents to the walls within the channel. Despite this sudden increase in divergence at 500 V, a similar rise in beam current was found; the current utilization efficiency rose from 0.739 to 0.830 when increasing discharge voltage from 400 to 500 V. The combined effect (within these two efficiencies) is a net increase in efficiency at 500 V, which is consistent with thrust stand measurements.

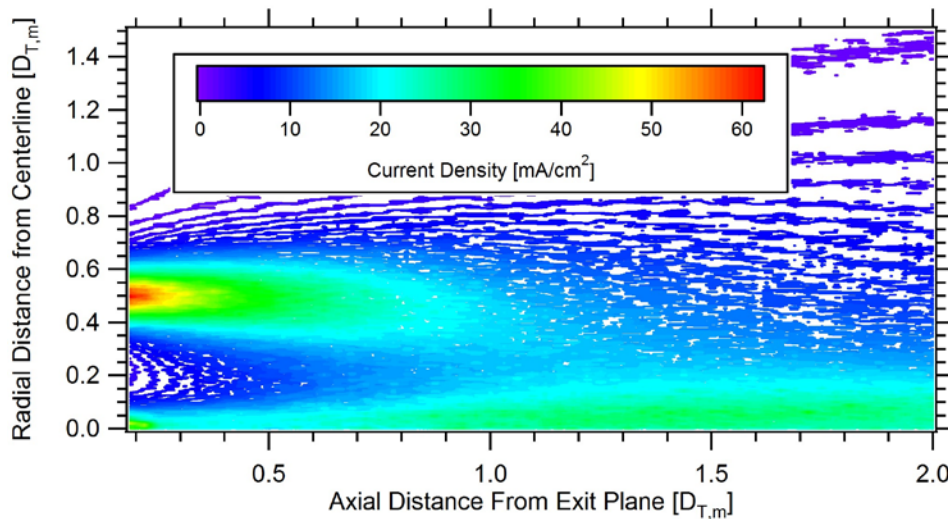


Figure 7-32. Ion current density contour map at 400 V, 10 mg/s anode flow rate. The ion beam exiting the channel is highly collimated, and merging towards thruster centerline does not occur upstream of $1 D_{T,m}$ from the exit plane.

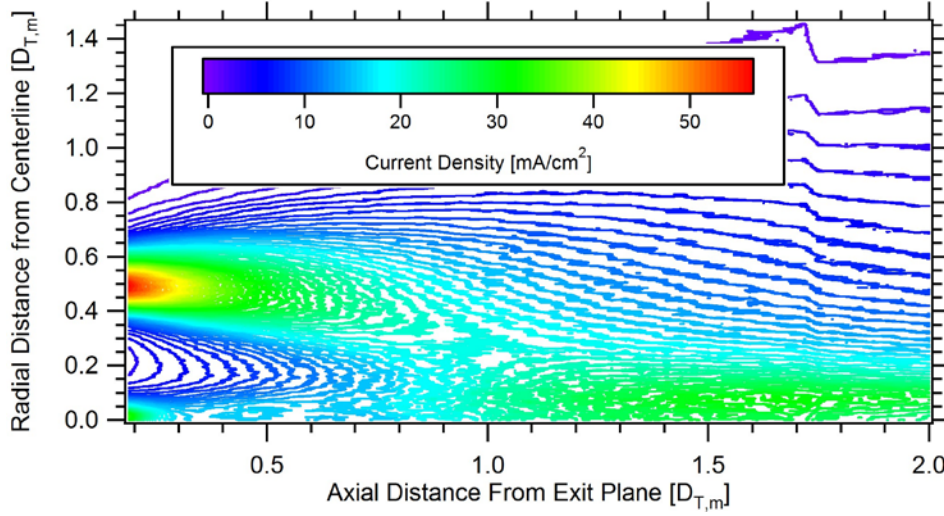


Figure 7-33. Ion current density contour map at 500 V, 10 mg/s anode mass flow rate. The ion beam exiting the channel is more divergent, and begins to merge towards thruster centerline upstream of 1 $D_{T,m}$.

7.3.3 Comparison between Internal and Near-field Measurements

The ion beam current and plume divergence calculated from Faraday probe measurements are used to correlate near-field properties to those within the channel. The plume divergence angle is a measure of how much the ion beam in the plume is axially-directed, as only the axial momentum produces net thrust. Thus, using far-field measurements, the divergence half angle is defined as [82]

$$\theta_d = \cos^{-1}\left(\frac{I_{axial}}{I_b}\right). \quad (7-6)$$

Equivalently, the plume divergence is a measure of how quickly (with axial distance) the ion beam spreads out in the radial direction, leading to the analysis techniques described in Section 3.8 for near-field measurements. A similar definition can be defined within the channel, referred to as “internal divergence.” The internal divergence is a measure of how much of the total ion current created actually leaves the channel to produce thrust; thus, this quantity is also a measure of the ion flux loss to the walls. Since most of the ion beam leaving the channel is axial and most of the ion current to the walls is radial, the internal divergence is analogous to the plume divergence. The internal divergence angle can be defined as

$$\psi = \cos^{-1}\left(\frac{I_b}{I_{total}}\right) = \tan^{-1}\left(\frac{I_{walls}}{I_b}\right). \quad (7-7)$$

The measured ion beam current from the near-field Faraday probe and the total integrated ion current to the channel walls from the internal wall-mounted probes are used to determine the internal divergence angle at each operating condition.

Figure 7-34 compares the calculated internal and plume divergence angles at all nine operating conditions within this study. A rough linear correlation is found between the two angles, with a non-zero internal divergence occurring at zero plume divergence. This is physically reasonable, since a perfectly collimated ion beam in the plume would still hit the walls within the channel due to the Bohm ion flux and accelerating sheath potentials. The linear fit corresponds to 0.7 degrees of internal divergence for every degree of plume divergence, with an offset of 20 degrees.

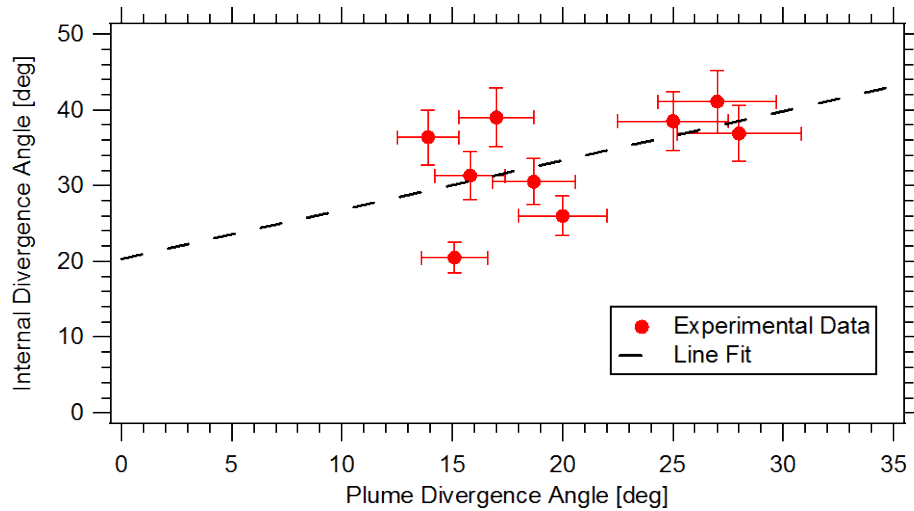


Figure 7-34. Comparison of internal and plume divergence angles for the nine operating conditions tested in this study. A rough linear correlation is found between the two angles.

Perfect correlation between the internal and plume divergence angles is not expected. While both angles depend upon the relative strengths of radial and axial electric fields, the behavior of the radial electric field as well as the geometry are fundamentally different within the channel compared to the plume. Despite this difference, it is interesting to note that a rough correlation still exists and that the increase in plume divergence and internal divergence is close to 1:1.

7.4 Energy Analysis and Comparison to Prior Measurements

The power carried by ions to the channel walls is very important in the context of efficiency since the heating of the wall by the plasma can represent a significant energy

loss. Thermal imaging studies of various thrusters by Mazouffre et al. [79,83] has shown that the power deposited into the channel walls is on the order of 10% of the discharge power. Using the estimated incident ion power along the channel walls, comparisons can be made between the calculated power deposition in this study and prior measurements.

While the average incident ion power to the channel walls was found to be approximately 11%, not all of this energy is absorbed by the surface. The ion energy accommodation factor, which is the fraction of incident energy absorbed by the surface, depends on how well the energy is coupled to the surface matrix. Studies performed by Kim et al. [84] has shown that the ion accommodation factor is less than unity for ion energies as high as 400 eV. Figure 7-35 shows the ion accommodation factors measured by Kim for four different materials; excellent linear behavior is observed within the energy range tested. From Section 7.2.3, the average incident ion energy varied from 40 to 140 eV, depending on discharge voltage. Given the linear extrapolation for boron nitride, this corresponds to ion accommodation factors of 0.55 to 0.61. Since under most operating conditions the average ion energy remained between 40 and 60 eV, an accommodation factor of 0.55 is chosen for this study.

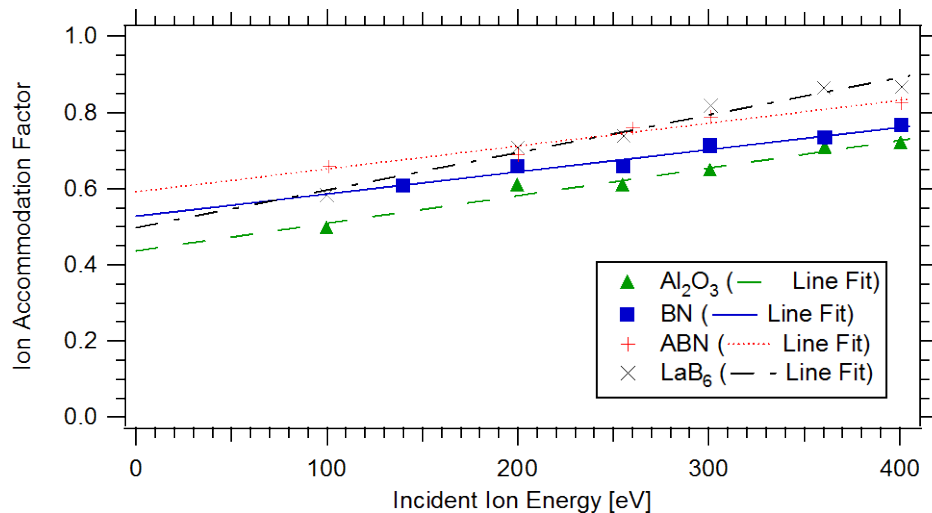


Figure 7-35. Measured ion accommodation factors at various incident ion energies for four different materials. Excellent linear behavior is observed within the energy range tested. Data taken from Kim et al. [84].

Given the above ion accommodation factor and estimated overall incident ion power presented in Section 7.2.3, ion power deposition varied from 4.4% to 9.2% of the discharge power, with an average of 6.3% being deposited to the channel walls. This

value is in excellent agreement with the 6.5% measured by Mazouffre [79,83] using calibrated thermal imaging on a similar-power Hall thruster, the PPSX000-ML. It has been noted by Mazouffre that satisfactory agreement was found between thermal imaging and internal wall-mounted probe studies by Kim [21] on the PPS®1350-G.

While the above analysis is promising in terms of quantifying the energy loss to the channel walls, it neglects the contributions of electrons; Mazouffre's thermal imaging studies do not differentiate between ion and electron power, while the internal wall-mounted probes only calculate the ion power deposition. The agreement between the two studies indicates that the electron contribution to the wall power deposition is likely small. Indeed, Mazouffre states that the trends observed in power losses to the walls indicate a mechanism driven by ion bombardment. However, calculations indicate that the electron power to the wall is significant, mainly due to the effects of secondary electron emission. The current balance to a floating wall is

$$j_i - j_e + j_{se} = 0, \quad (7-8)$$

where j_i is the incident ion current density, j_e is the incident electron current density, and j_{se} is the emitted secondary electron current density from the wall. Substituting in the equation for the secondary electron emission coefficient,

$$\delta_w = \frac{j_{se}}{j_e}, \quad (7-9)$$

a relation between the incident ion and electron currents can be found:

$$j_e = \frac{j_i}{1 - \delta_w}. \quad (7-10)$$

With each electron that impacts the wall carrying an average of $2T_e$ of energy, the incident electron power to the wall can be calculated:

$$P_{electron} = 4\pi \int_{walls} \frac{j_i(s)T_e(s)}{1 - \delta_w(T_e)} r ds. \quad (7-11)$$

Because the secondary electron emission coefficient can be near unity for a sizeable portion of the channel (see Section 4.5.3 for details on secondary electron emission from boron nitride), the incident electron current can become over an order of magnitude higher than the incident ion current. Figure 7-36 shows how the incident electron current changes as a function of electron temperature for boron nitride. Due to the secondary electron emission properties of the wall, the electron current can rise from

5X the ion current to near 60X the ion current over a short range of temperatures. The temperature at which this onset of the charge-saturated regime (CSR) in the sheath occurs can significantly impact the resulting electron power to the wall.

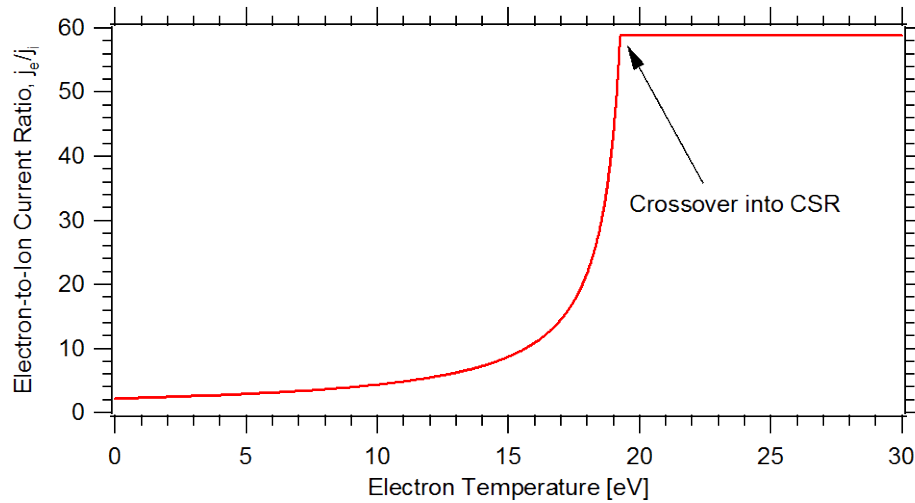


Figure 7-36. Dependence of the electron-to-ion current ratio to the channel wall on local electron temperature. The secondary electron emission characteristics of the wall can increase this ratio from 5 to almost 60 over a short range of temperatures.

Figure 7-37 shows the calculated axial profiles of incident ion power density, electron power density, and electron temperature along the outer wall at 300 V, 20 mg/s anode flow rate. The axial range where the local electron temperature exceeds the crossover energy (19.3 eV for boron nitride) is shown with dotted lines. Within this range, the sheath enters the CSR and the electron power approaches two orders of magnitude higher than the incident ion power. This rise in electron power is driven by the increase in incident electron current due to the prolific secondary electron emission from the channel wall. These trends are consistent with the computational analysis performed by Ahedo [85].

The electron power properties can change drastically depending on the crossover energy and the axial range where temperatures exceed this energy. Figure 7-38 shows the calculated electron power to the walls at 300 V and 20 mg/s, as a function of the crossover temperature and SEE coefficient at zero incident energy. It is evident that the electron power substantially drops once the crossover temperature exceeds the maximum observed temperature in the discharge. Thus, the calculation of incident electron power is sensitive to uncertainties in the measured electron temperature as well as the secondary electron emission coefficient. Indeed, a direct calculation yields large electron currents

that result in incident electron powers greater than the discharge power. While electron accommodation factors, radiative losses, and energy carried by secondary electrons can reduce the amount of power absorbed by the walls, the calculated incident electron power seems unphysical. It is possible that the SEE coefficients have large uncertainty due to the variation in experimentally determined values [6].

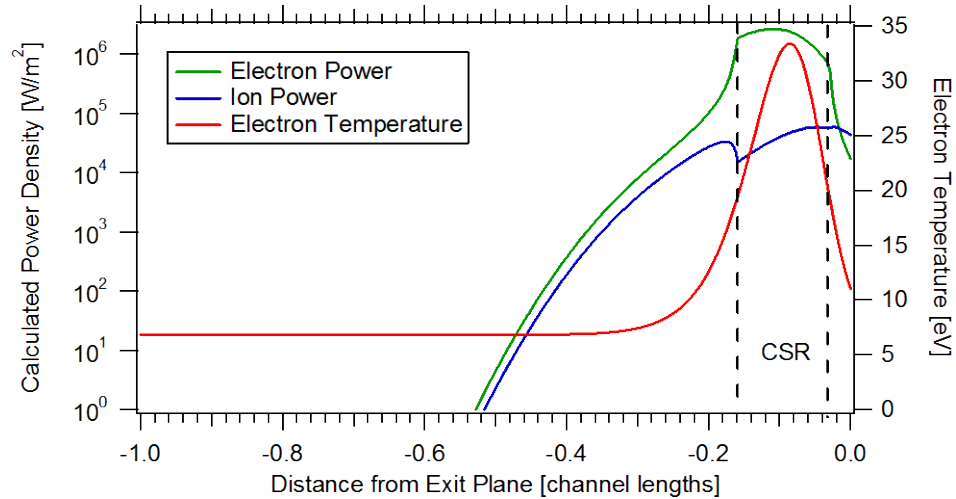


Figure 7-37. Calculated axial profiles of incident ion power density, electron power density, and electron temperature along the outer wall at 300 V, 20 mg/s. Around the region where the sheath enters the charge-saturated regime (CSR), the electron power density rises to nearly two orders of magnitude higher than the ion power density.

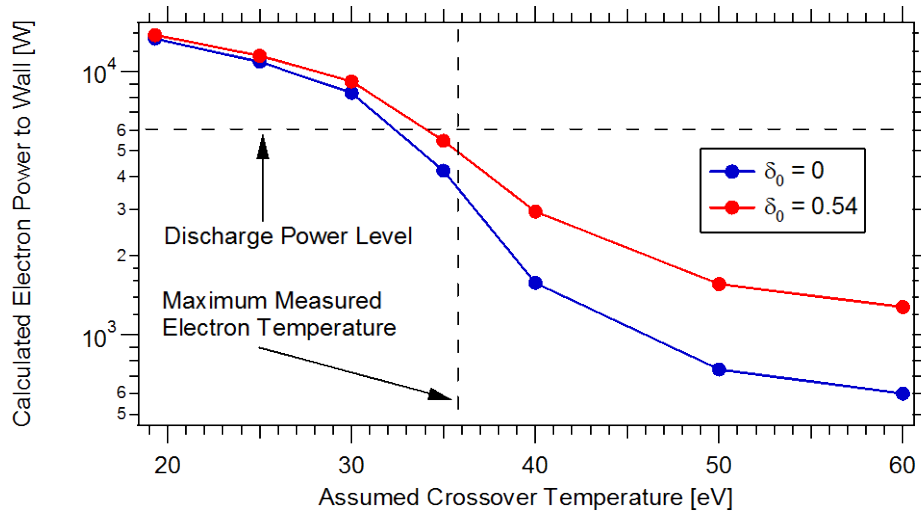


Figure 7-38. Variation of calculated electron power to the channel walls at 300 V, 20 mg/s, depending on the electron temperature at which crossover occurs (onset of CSR), as well as the SEE coefficient at zero incident energy, δ_0 . The calculated electron power drops significantly once the crossover temperature exceeds the maximum observed temperature in the discharge.

It is also possible that the measured incident ion current densities have large errors due to the observed probe degradation after data collection was completed (see

Section 5.1.2). However, previous internal studies by Kim [19,21] have also shown that the incident ion current to the channel walls is of the same order as the ion beam current. Therefore, it is highly unlikely that the uncertainty in the ion current density measurement can account for the elevated incident electron power. Thus, the role of secondary electron emission is found to considerably affect not only the sheath potential but the incident electron current to the wall. Further study is required to fully understand the impact of secondary electron emission on channel wall losses and related thruster efficiency.

7.5 Summary

This chapter presented the calculated incident ion power characteristics as a function of distance from the anode as well as operating condition. In general, the incident ion power to the channel walls increases as the exit plane is approached. This is due to the increasing beam energy as the ions pass through the acceleration zone, as the incident ion current density to the walls drops as the plasma accelerates out of the channel.

Integration of the incident ion power to the channel walls shows that the total ion power scales roughly linearly with discharge power, with elevated values found at 150 V and 500 V discharge voltage. The data taken with the internal wall-mounted probes was extrapolated to the entire channel length using fitting functions validated from prior internal measurements [13]. Average ion power to the channel walls was found to be approximately 11% of the discharge power, with 6.3% of this power actually being absorbed in the walls. Elevated values at 150 V were found to be caused by large relative sheath energies and high internal divergence, while elevated values at 500 V were found to be caused by large relative beam energies and a higher fraction of the walls being exposed to high-density plasma.

Calculation of the electron power to the channel walls was found to be non-trivial due to the strong influence of the assumed secondary electron emission (SEE) characteristics of the wall. The current model for SEE predicts a substantial portion of the channel to contain space-charge-limited sheaths, which inflates the overall electron

power to unreasonable values. Further investigation is required to fully characterize the influence of SEE on the plasma discharge in Hall thrusters.

Chapter 8

Sputtering Yield Estimates and Implications

This chapter details calculations of channel wall erosion rates using the experimental data from internal wall-mounted probes. The measured incident ion current density and ion energy are used with sputtering models to determine local erosion rates along the channel walls. These rates can then be compared to the observed erosion profile to determine any necessary changes to the sputtering model.

A brief overview is first given of currently used sputtering models as a function of incident ion energy and angle. Analysis techniques are then described that allow determination of the incident ion angle from internal wall-mounted probe data, to be used in the sputtering models. Local erosion rates are then calculated along the wall and compared to the experimentally observed erosion profiles of the 6-kW Hall thruster. Finally, modifications to the sputtering model are suggested based on the observed discrepancies between calculated and measured erosion profiles.

8.1 Sputtering Yield Overview and Present Models

The sputtering yield of channel wall material from ion bombardment is an important property that can significantly affect Hall thruster lifetime. Furthermore, the sputtering yield function is a critical parameter in any lifetime prediction code, as it ultimately determines the wall recession rate over time. In general, the amount of sputtered material is a function of incident ion species, energy, and angle, as well as properties of the wall material itself (see Figure 8-1). Due to its importance, several studies have been performed to determine the sputter yield as a function of ion energy and incidence angle; these studies have focused primarily on xenon ion bombardment for several ceramic materials typically used in Hall thrusters [86-91]. Unfortunately, these measurements have been found to be difficult, and little agreement is found across

studies. The dependence of these measurements on surface properties, fabrication processes, temperature, and moisture absorption further complicate the ability to compare values across studies.

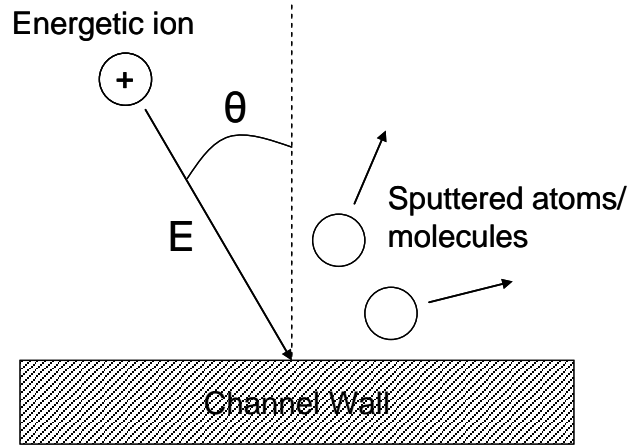


Figure 8-1. Diagram illustrating the dependence of sputtering yield on incident ion energy, E , and incidence angle, θ , for a given ion species and wall material.

In this study, the sputtering yield function is assumed to be the product of two functions for a given ion species and wall material:

$$Y(E, \theta) = Y_E(E)Y_\theta(\theta), \quad (8-1)$$

where Y is the total sputtering yield, Y_E is the energy-dependent sputter yield at normal incidence, and Y_θ is the angle-dependent sputter yield. This separation of variables is how sputtering is modeled in HPHall-2 [69,76] and is validated by measurements from Garnier et al. [87] that show the normalized angular dependence is largely independent of ion energy.

Measured sputtering yields for boron nitride, the wall material used in the 6-kW Hall thruster, are somewhat limited in the literature. However, recent measurements taken by Rubin et al. [86] provide the sputtering yield dependence of boron nitride on xenon ion energy (including energies below 100 eV) and angle of incidence. These data are also selected due to the use of a quartz-crystal microbalance (QCM), which provides higher-fidelity measurements than other experimental techniques. The experimental data will be fit to various proposed functions to determine a satisfactory sputtering yield model to be used in this study. This model, as well as the model used in HPHall-2, will

then be utilized with the internal wall-mounted probe data to predict erosion rates within the 6-kW Hall thruster.

8.1.1 Energy-dependent Sputter Yield

Various functions have been proposed in the literature to describe the sputter yield as a function of ion energy at normal incidence. These functions largely vary by how they model the sputtering at low ion energies (below 100 eV), which is critical in Hall thruster erosion calculations since most ion energies lie between 50 and 200 eV. Garnier et al. [87] observed that the sputtering yield is linear with ion energy, although ion energies below 350 eV were not tested. Abgaryan et al. [91] suggested a simple power law fit to better model sputtering at low energies. Gamero-Castaño and Katz suggested a simplified model [76] of the semi-empirical law proposed by Yamamura and Tawara for monatomic solids at normal incidence [92]:

$$Y_E(E) = A\sqrt{E}\left(1 - \sqrt{\frac{E_{th}}{E}}\right)^{2.5}, \quad (8-2)$$

where A and E_{th} are fitting parameters; E_{th} corresponds to the minimum threshold energy for sputtering to occur. This model is currently used within HPHall-2 [69], with $A = 0.0023$ and $E_{th} = 5.1$ eV used for boron nitride. Finally, a function was developed by Bohdanský [22] to better fit sputtering yields of polycrystalline monatomic solids at lower impact energies:

$$Y_E(E) = A\left[1 - \left(\frac{E_{th}}{E}\right)^{\frac{2}{3}}\right]\left[1 - \frac{E_{th}}{E}\right]^2, \quad (8-3)$$

where A and E_{th} are fitting parameters. This model was found by Rubin to best fit experimental data taken with the QCM [86].

Figure 8-2 shows the comparison between the experimental data and the various proposed fitting functions. While all the models fit the data adequately, they differ substantially at energies below 60 eV. The power law fit predicts sputtering occurring at all energies, while the linear fit and Bohdanský fit both predict energy thresholds around 45 eV. The HPHall-2 fit also predicts an energy threshold, but closer to 30 eV. Due to the lack of data, it is difficult, if not impossible, to determine the function that more accurately describes the sputtering yield. Therefore, the simplest model, the linear fit,

will be chosen as the energy-dependent model for sputtering yield. This model was also chosen due to the excellent agreement with the experimental data.

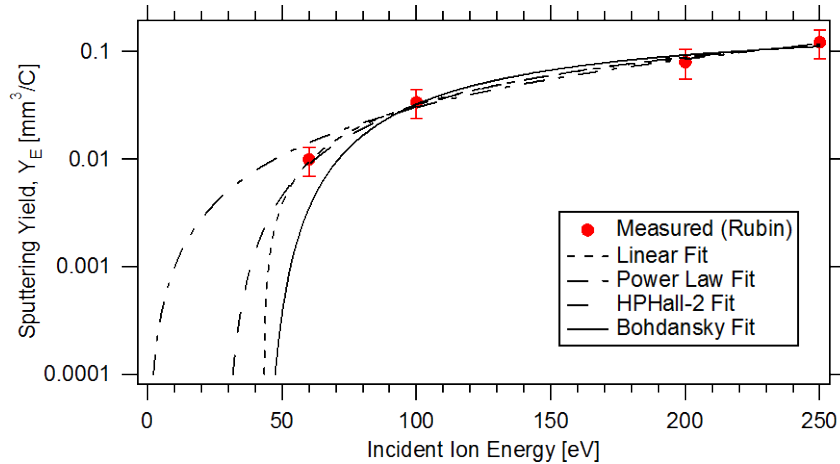


Figure 8-2. Comparison of various fitting functions to experimentally measured values by Rubin et al. While all functions adequately fit the data, the linear and HPHall-2 fits match the best.

Figure 8-3 compares the proposed linear fit model to that presently used in HPHall-2. Two features are immediately evident: the threshold energy in the HPHall-2 model is much lower than in the linear fit model, and the predicted yields are much higher in the linear fit model for energies over 60 eV. This disparity in yield magnitude is also found between Rubin’s data and other studies [86]; presently there is no concrete explanation for the difference. Both the linear fit model based on Rubin’s data and the HPHall-2 model will be used to predict erosion rates in the 6-kW Hall thruster using data from the internal wall-mounted probes.

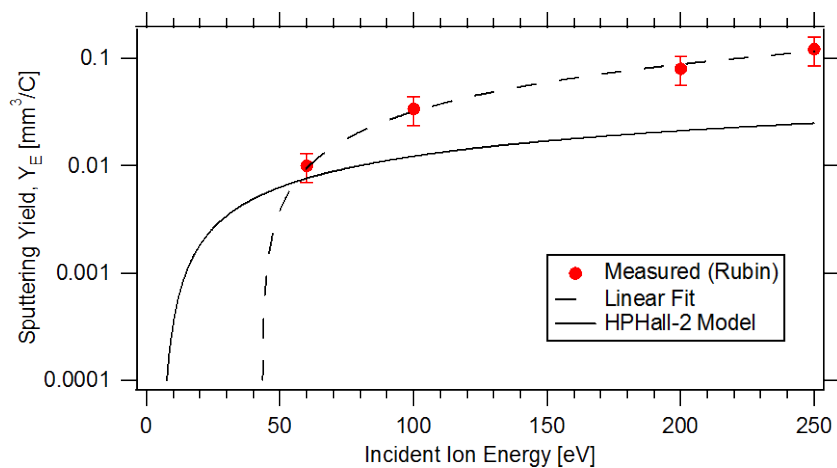


Figure 8-3. Comparison of the linear fit model to the energy-dependent sputtering yield used in HPHall-2. The values measured by Rubin are much higher than those predicted by HPHall-2, as well as previously measured yields.

8.1.2 Angle-dependent Sputter Yield

Proposed functions to describe the angle-dependent sputter yield are relatively scarce in the literature. Rubin et al. found the model developed by Yamamura [93] to adequately fit the experimental data, while Garnier et al. used third-order polynomial fits [87]. The model presently used in HPHall-2 is that proposed by Pencil et al. [94]:

$$Y_{\theta}(\theta) = 1 + c_0 [1 - \cos(c_1 \theta)]^k, \quad (8-4)$$

where c_0 , c_1 , and k are fitting parameters; presently $c_0 = 0.52663$, $c_1 = 2.60506$, and $k = 1.53462$ in HPHall-2 for boron nitride. This function was also found to fit well to experimental data from Garnier [87]. Due to the lack of experimental data from Rubin above 45° , proper fits could not be completed; however, it will be shown in Section 8.2 that the observed incidence angles do not greatly exceed 45° . Therefore, a curve fit using Eq. (8-4) on data from Rubin is deemed adequate as the angle-dependent sputter yield model in this study.

Figure 8-4 compares the cosine fit to Rubin's data to the model presently used in HPHall-2. The experimental data from Rubin predicts only a weak dependence on incidence angle, at least up to 45° . Previous studies show a significant rise in yield at angles between 60° and 80° [87,90], similar to the model in HPHall-2. Both models will be used to predict the erosion rates in the 6-kW Hall thruster using data from the internal wall-mounted probes.

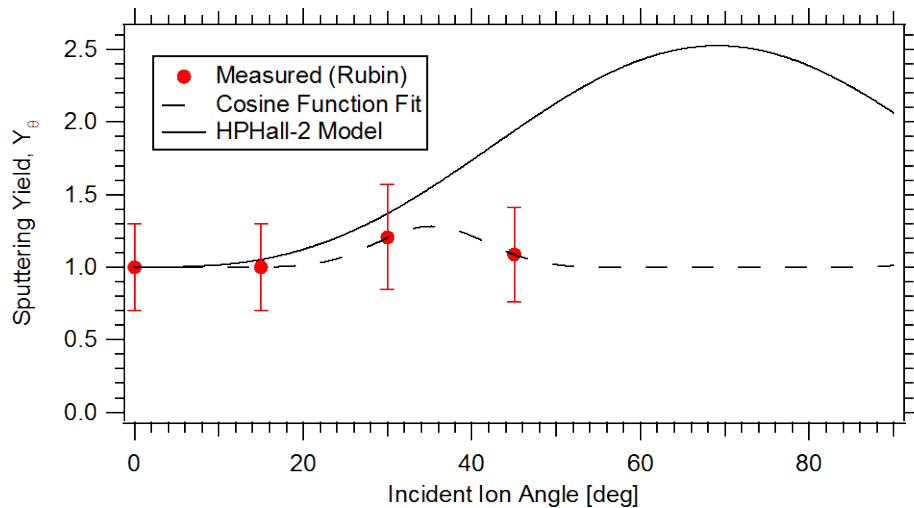


Figure 8-4. Comparison of the proposed cosine fit to Rubin's data for angle-dependent sputter yield and that presently used in HPHall-2. The experimental data from Rubin predicts a much weaker dependence on sputtering angle.

8.2 Determination of Incident Ion Angles

The angle of incidence for ions approaching the channel wall can significantly affect the resulting sputter yield. Thus, it is important to quantify this angle in order to obtain a more accurate calculation of the local sputtering yield and resulting wall recession rate. For planar Langmuir probes, the presence of ion beams can be detected and their energy estimated [48]. This energy can then be used to determine the angle of incidence upon the sheath relative to the wall surface.

When a planar Langmuir probe is biased sufficiently high above the local plasma potential, the ion beam approaching the probe can no longer overcome the potential hill and is repelled. When this occurs, the beam creates a stagnation point within the sheath, which forms a large space charge layer. This layer causes the sheath to “bulge” out, greatly increasing the sheath boundary and associated collection area (see Figure 8-5). This phenomenon is manifested in the Langmuir probe I-V characteristic as a large increase in collected electron current.

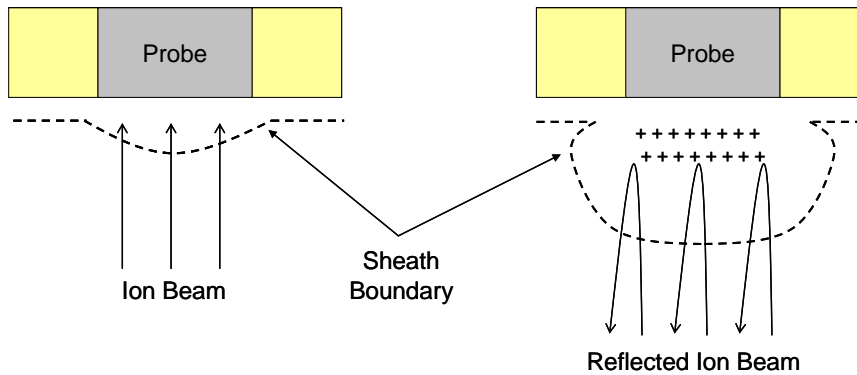


Figure 8-5. Diagram illustrating the effects of an ion beam on the sheath around a planar Langmuir probe. When the probe bias is sufficiently high, the ion beam is repelled. This creates a large space charge layer in the sheath that causes it to bulge out and collect many more electrons.

While the presence of magnetic fields can suppress this phenomenon [48], the effect was still found to manifest itself in the second derivative of the probe characteristic (see Figure 8-6). The rise in electron current creates an associated peak in the second derivative occurring at a probe voltage higher than the local plasma potential. The voltage at which this peak maximized was taken as the ion beam’s most probable energy normal to the surface, as this is the energy that can overcome the potential hill created by the probe.

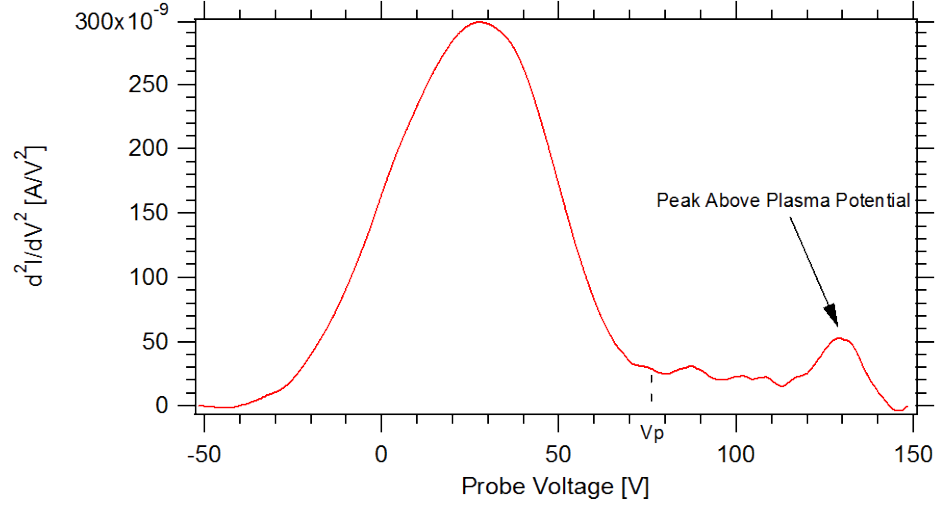


Figure 8-6. Representative second derivative of a probe I-V characteristic. The peak occurring at a voltage above the plasma potential is evidence of an ion beam.

Thus, the beam energy normal to the surface can be determined from the difference between the peak location and the local plasma potential:

$$\varepsilon_{\perp} = e(V_{peak} - V_p). \quad (8-5)$$

Assuming that ions accelerate electrostatically from anode potential to the local plasma potential without collisions, the total ion beam energy is

$$\varepsilon_{total} = e(V_{anode} - V_p). \quad (8-6)$$

Care must be taken to reference the same potential for all these values, such as the cathode potential. Given these two energies, the associated velocities can be calculated and used to determine the angle of incidence with respect to the surface:

$$\theta_0 = \cos^{-1} \left(\left(\frac{\varepsilon_{\perp}}{\varepsilon_{total}} \right)^{1/2} \right). \quad (8-7)$$

It should be noted, however, that θ_0 is the angle of incidence *upon the sheath surface*. In order to determine the angle of incidence upon the channel wall, θ , the calculated sheath energy must be used. Assuming the sheath energy is imparted normal to the surface, and using conservation of energy, the velocities perpendicular and parallel to the wall may be calculated and used to determine the angle of incidence at the wall surface:

$$v_{\perp}^2|_{wall} = v_{\perp}^2|_{sheath} + \frac{2e|V_{sheath}|}{M_i},$$

$$v_{\parallel}^2|_{wall} = v_{\parallel}^2|_{sheath} = \frac{2\mathcal{E}_{total}}{M_i} (\sin(\theta_0))^2, \quad (8-8)$$

$$\theta = \tan^{-1} \left(\frac{v_{\parallel}}{v_{\perp}} \right)_{wall}.$$

Figure 8-7 illustrates the relationship between the various variables used to determine the ion incidence angle at the channel wall.

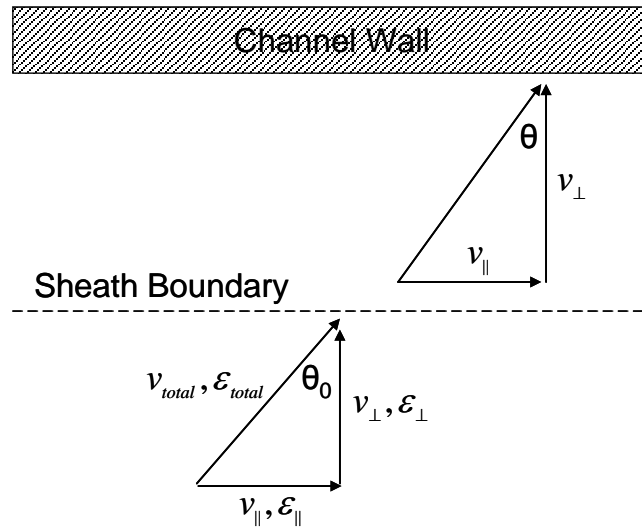


Figure 8-7. Diagram illustrating the various variables used to determine the ion incidence angle at the channel wall.

Table 8-1 gives the calculated incidence angles along the inner and outer channel walls at nominal conditions of 300 V, 20 mg/s anode flow rate. Probe locations are given in units of channel lengths from the exit plane. If no ion beam was detected in the data, which typically occurred upstream of the acceleration zone where the directed ion energy is small, the incidence angle was assumed to be normal to the wall (0°). The incidence angle was found to increase only slightly as the exit plane is approached and the ions gain more energy from the axial electric field. It should be noted that due to the linear chamfer present in the erosion rings, the values reported in Table 8-1 do not always represent the angle with respect to the thruster “r” axis. Indeed, due to the chamfer, the calculated incidence ion angles represent ion trajectories to the wall in excess of 60° with respect to the thruster firing axis (“z” axis). These angles are likely the result of the

strong radial electric fields present near the channel walls, a feature discussed in Chapter 5 and Chapter 6.

Table 8-1. List of calculated incidence angles along the inner and outer channel walls at 300 V, 20 mg/s. Probe locations are given in units of channel lengths from the exit plane. Incidence angles increase slightly as the exit plane is approached.

Probe Location	Along Inner Wall [deg]	Along Outer Wall [deg]
$z = -0.143$	0	0
$z = -0.095$	0	0
$z = -0.071$	0	34
$z = -0.048$	47	38
$z = -0.024$	48	44

8.3 Calculated Erosion Rates and Profiles

The sputtering models described in Section 8.1 are used with the calculated ion current densities, energies, and incidence angles from internal wall-mounted probe data to predict the local erosion rates of the channel wall in the 6-kW Hall thruster. The wall recession rate can be calculated as

$$\frac{dr}{dt} = j_i Y(E, \theta) = j_i Y_E(E) Y_\theta(\theta). \quad (8-9)$$

Uncertainty propagation analysis on $Y_\theta(\theta)$, given an uncertainty in the measured incidence angle of $\pm 10^\circ$, gives an uncertainty for both models of $\pm 20\%$. In addition to the $\pm 40\%$ uncertainty in ion current density and $\pm 20\%$ uncertainty in $Y_E(E)$ (since the function is roughly linear with ion energy), there is an estimated $\pm 80\%$ uncertainty in the calculated recession rate. Due to similarities in the data, only values along the outer wall will be presented.

Comparison of predicted erosion rates to those experimentally observed is complicated due to the numerous conditions the thruster was operated under during the first few hundred hours of lifetime. Operating conditions of 300 V, 10 and 20 mg/s anode flow rate represent approximately 60% of the total operating time, while the remaining 40% is divided between several different operating conditions between 150 and 600 V, and 10 and 30 mg/s anode flow rate. Approximately 20% of the operating time is at 150 V, where ion energies at the wall are much lower and less erosion is

expected. Much of the remaining time occurs at 300 V, 30 mg/s anode flow rate, and 600 V, 10 mg/s anode flow rate, where erosion rates are expected to be higher. In order to simplify the analysis, the thruster was assumed to operate the full 334 operational hours at 300 V, 10 and 20 mg/s. The thruster was run for an equal amount of time for each of these operating conditions, so the 334 hours was divided evenly between the two. Also, the wall recession rate was assumed to occur purely in the radial direction. While the wall recedes strictly in the direction normal to the surface, the small operating time limits this error to within 10%.

Figure 8-8 shows the predicted erosion rates using the sputtering model in HPHall-2 given the data from 300 V, 10 mg/s anode flow rate and 300 V, 20 mg/s anode flow rate. The expected local erosion rates based off the measured erosion profile is shown for comparison. At all locations, the model predicts a much higher erosion rate than what is observed. The general profile shape of much higher erosion at the exit plane is consistent across all calculations.

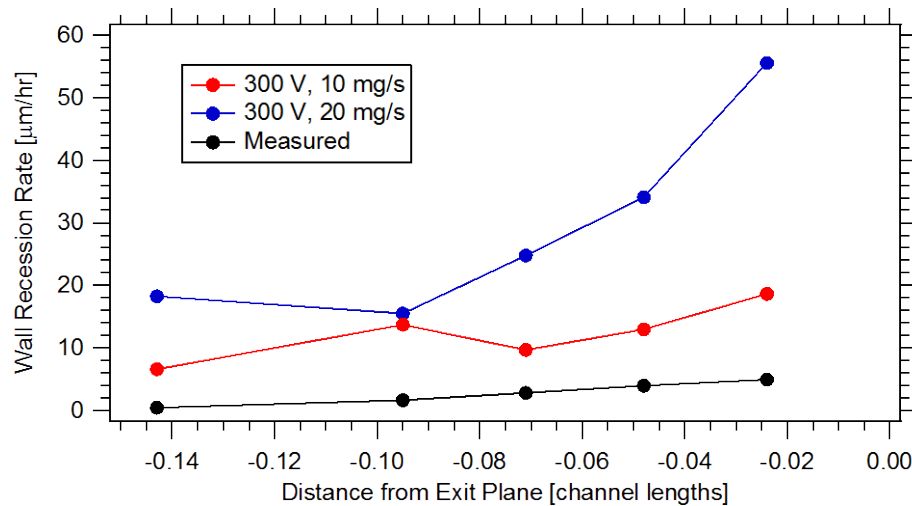


Figure 8-8. Comparison of predicted erosion rates using the HPHall-2 sputtering model, based off data from 300 V, 10 mg/s and 300 V, 20 mg/s, to those expected based off the measured erosion profile. The model predicts much higher erosion rates at all locations, but matches the expected profile shape. Uncertainty bounds are omitted for clarity.

Figure 8-9 shows predicted erosion rates using the model derived from Rubin’s experimentally determined sputtering yields [86], referred to as the “Rubin-based model.” Yields were calculated at 300 V, 10 mg/s anode flow rate and 300 V, 20 mg/s anode flow rate, and compared to the expected erosion rates based off the measured erosion profile. As with the HPHall-2 model, the Rubin-based model predicts much higher erosion rates

than what is experimentally observed. However, the Rubin-based model more accurately predicts the low erosion rates far back in the channel; this is due to the higher threshold energy of 43 eV.

Due to the large difference between predicted and observed erosion rates, it is possible that redeposition of wall material, not accounted for in this analysis, could reduce the local erosion rates to the values that are experimentally observed. Furthermore, the lack of erosion deep inside the channel despite large ion current densities could be due to redeposition from the opposing wall, since incidence angles are normal to the surface. However, studies by Rubin [86] on the angular distribution of sputtered material show a hemispherical distribution even at normal incidence; that is, there is a significant fraction of material sputtered at non-normal angles from the surface. This makes it unlikely that redeposition prevents net erosion deep in the channel. It is more likely that typical ion energies in this region do not meet a minimum energy threshold for sputtering to occur. Furthermore, numerical studies by Sullivan et al. [95] show that the deposition rates at moderate voltages do not exceed 20% of the peak erosion rates. Thus, redeposition is likely not the cause of the large differences between predicted and observed erosion rates.

The uncertainties associated with the sputtering yield model could also explain the difference between predicted and observed values. It has been mentioned previously that the measured values by Rubin et al. [86] are much higher than those measured in previous studies. Based on expected differences between the amount of sputtered material and the amount of material condensable on the QCM, the total reported sputtering yields were higher than the condensable yields by over 50%. Due to these uncertainties, the data from the internal wall-mounted probes are used instead to estimate the energy-dependent sputtering yield required to match observed profiles, presented in the following section.

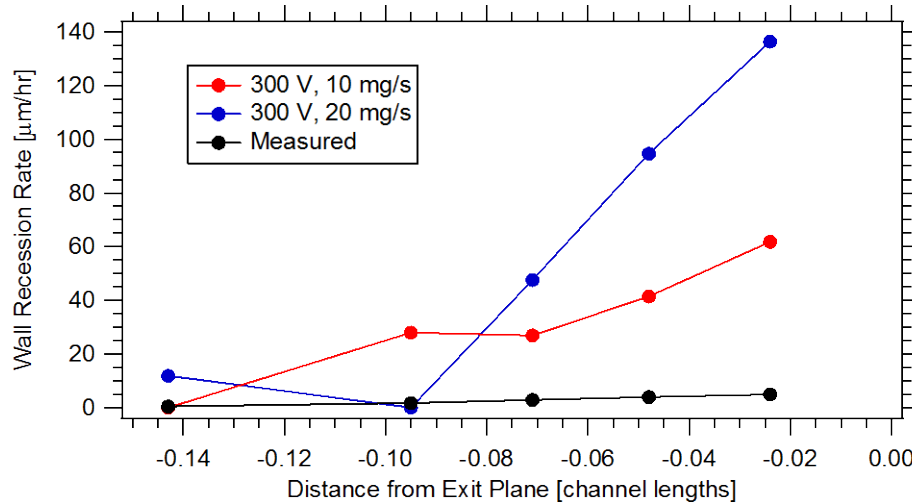


Figure 8-9. Comparison of predicted erosion rates using the Rubin-based sputtering model, based off data from 300 V, 10 mg/s and 300 V, 20 mg/s, to those expected based off the measured erosion profile. While the Rubin-based model more accurately predicts the very low erosion rates far back in the channel, the predicted erosion rates are much higher near the exit plane than those predicted by the HPHall-2 model. Uncertainty bounds are omitted for clarity.

8.4 Calculated Sputtering Yield Functions

Due to the uncertainty associated with the sputtering yield function, the ion current densities, energies, and incidence angles from internal wall-mounted probe data are used to determine the required energy-dependent sputtering yield to match observed erosion rates in the 6-kW Hall thruster. Equation (8-9) is used to determine Y_E along the outer channel wall at operating conditions of 300 V, 10 mg/s anode flow rate and 300 V, 20 mg/s anode flow rate. Since the functions for Y_θ differed between the HPHall-2 model and the Rubin-based model, both were used to obtain estimates of the energy-dependent sputter yield.

Figure 8-10 shows the calculated energy-dependent sputtering yield using the HPHall-2 model for angle-dependent sputter yield. Values calculated from 300 V, 20 mg/s anode flow rate and 300 V, 10 mg/s anode flow rate were also averaged based on their relative amount of charge delivered to the surface in order to represent a more accurate sputtering yield. Using Eq. (8-9), the recession rate is equal to

$$\frac{dr}{dt} = j_{i,avg} Y_{E,avg}(E) Y_{\theta,avg}(\theta). \quad (8-10)$$

Assuming that the recession rate is approximately equal in time for each operating condition,

$$\Delta r \approx j_{i,avg} Y_{E,avg}(E) Y_{\theta,avg}(\theta) \Delta t = \sum_m j_{i,m} Y_{E,m}(E) Y_{\theta,m}(\theta) \Delta t_m. \quad (8-11)$$

where m is summed over all operating conditions. Solving for the average sputtering yield:

$$Y_{E,avg}(E) = \sum_m \frac{j_{i,m}}{j_{i,avg}} Y_{E,m}(E) \frac{Y_{\theta,m}(\theta)}{Y_{\theta,avg}(\theta)} \frac{\Delta t_m}{\Delta t}. \quad (8-12)$$

Since the sputter yield is only a weak function of incident angle over the observed range of values, the ratio of $Y_{\theta,m}/Y_{\theta,avg}$ is set equal to unity for simplicity. Using charge conservation, it can be shown that the average incident current density is equal to

$$j_{i,avg} = \sum_m j_{i,m} \frac{\Delta t_m}{\Delta t}. \quad (8-13)$$

Thus, the averaged sputter yield is weighted based on the relative incident current densities and durations of operation. The average incident ion energy is calculated in a similar manner.

The calculated sputter yield is very low at energies below 50 eV, with typical values on the order of 4×10^{-3} mm³/C at energies of 200 eV. Figure 8-11 shows the calculated energy dependent sputter yield using the Rubin-based model for angle-dependent sputter yield. Results between the two models are very similar; it is evident that the sputter yield has a much weaker dependence on angle than energy, at least for incidence angles less than 45°.

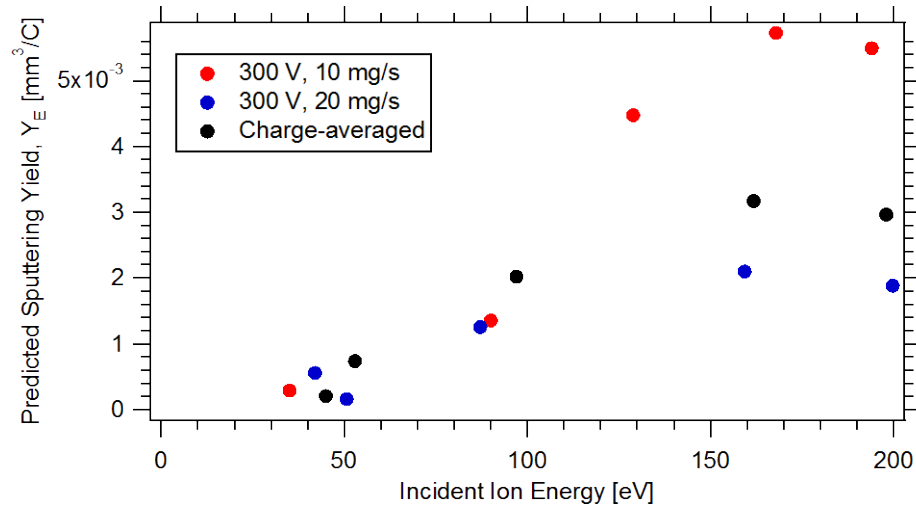


Figure 8-10. Calculated energy-dependent sputter yields using the HPHall-2 model for angle-dependent sputtering yield, given data at 300 V, 10 mg/s and 300 V, 20 mg/s. The data was also weight-averaged by the relative amounts of total charge for each operating condition to represent a more accurate sputtering yield.

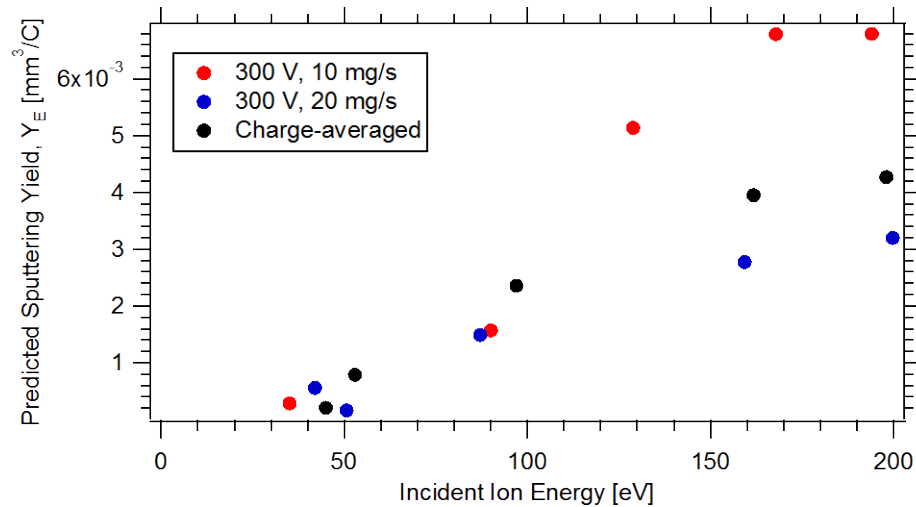


Figure 8-11. Calculated energy-dependent sputter yields using the Rubin-based model for angle-dependent sputtering yield, given data at 300 V, 10 mg/s and 300 V, 20 mg/s. The data was also weight-averaged by the relative amounts of total charge for each operating condition to represent a more accurate sputtering yield.

Figure 8-12 shows the charge-averaged energy-dependent sputtering yields using both the HPHall-2 and Rubin-based angle-dependent sputtering yield equations. Of all the energy-dependent models discussed in Section 8.1.1, the Bohdanský model in Eq. (8-3) best fits the data. The corresponding threshold energies are 27.1 ± 1.4 eV for the Rubin-based model and 23.9 ± 3.1 eV for the HPHall-2 model. This is consistent with the low erosion rates observed deep in the channel despite the presence of large ion current densities and energies in excess of 30 eV.

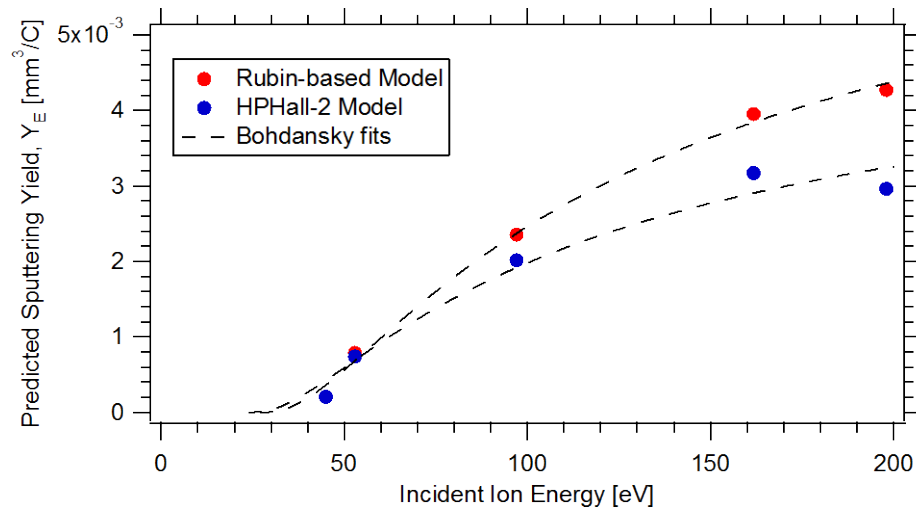


Figure 8-12. Comparison of calculated charge-averaged energy-dependent sputter yields using HPHall-2 and Rubin-based angle-dependent sputtering yields. Curve fits using the Bohdanský model are also included, showing excellent agreement.

The sputtering models shown in Figure 8-12 can not strictly be used due to the numerous simplifying assumptions involved in their calculation. However, a few valuable features can be taken from the data and used to better sputtering yield functions used in lifetime models. These features and their validation are discussed in the following section.

8.5 Suggested Features of Sputtering Yield Model

Despite the simplifying assumptions of the sputtering yield calculations in Sections 8.3 and 8.4, a few important features of the derived energy-dependent sputtering yield can be used to improve the functions used in lifetime prediction models.

1. **Energy thresholds greater than 25 eV.** Despite large measured ion current densities upstream of the acceleration zone, very little erosion is observed. Since sheath energies in this region are typically 30 – 50 eV, the expected energy threshold for sputtering to occur should be in this vicinity. The energy thresholds predicted by the calculated sputtering yields were 25 – 30 eV, while that predicted by Rubin’s experimental data [86] was 43 eV, given the fitting function proposed by Bohdanský [22].
2. **Sputtering yields at normal incidence on the order of 3×10^{-3} mm³/C for ion energies of 100 eV.** In order to match observed erosion profiles, the required sputter yield at normal incidence was on the order of a few thousandths of a mm³/C. This value is likely an underestimate due to the assumption that the thruster was run for a full 334 hours at 300 V, 10 and 20 mg/s, even though it was only run for 60% of that time at those operating conditions. Furthermore, the uncertainty associated with the measured ion current densities would also underestimate the calculated sputter yield. The typical values in the HPHall-2 model, as well as prior sputtering yield studies (excluding that of Rubin et al. [86]) appear to be the correct order of magnitude.
3. **A dependence on ion energy that resembles the function proposed by Bohdanský.** The functional form of the calculated energy-dependent sputter yield appears to have excellent agreement with the function proposed by

Bohdansky. This function was also found by Rubin to match well with experimental data taken with the QCM [86]. Characteristics of this function include a slow rise in sputtering yield at energies near the energy threshold, followed by a sharp rise at moderate energies (~ 100 eV), and a more gradual rise at high energies (> 200 eV). The slow initial rise in sputtering yield likely contributes to the low erosion rates observed when only sheath energies (< 50 eV) are present.

The above recommendations represent only minor modifications to the model presently used in HPHall-2. However, the change in behavior at low ion energies due to the higher threshold energy and use of the Bohdansky function will likely affect erosion profiles deeper in the channel where sheath energies dominate the sputtering yield. These modifications should improve the ability to predict erosion rates within present Hall thruster lifetime prediction codes.

8.6 Summary

This chapter investigated the predictive capability of present sputtering models by comparing calculated erosion rates using the internal wall-mounted probe data to those that were experimentally observed in the 6-kW Hall thruster. Models based on data taken by Rubin et al. [86] as well as the present model used in HPHall-2 [69] appears to predict much higher erosion rates than those inferred from the measured erosion of the thruster.

The data from the internal wall-mounted probes were also used to calculate the sputtering yields required to reproduce the measured erosion profiles. This energy-dependent sputtering yield was found to resemble the model proposed by Bohdansky [22] with an energy threshold of at least 25 eV for sputtering to occur. This threshold is consistent with the lack of significant erosion observed upstream of the acceleration zone, despite large measured ion currents to the walls; sheath energies are expected to be limited to 50 eV. This sputtering model represents minor modifications to the present model in HPHall-2, and should improve the predictive capabilities of such Hall thruster codes and lifetime models.

Chapter 9

Conclusions

9.1 Dissertation Summary

The primary purpose of the work presented in this dissertation is to experimentally characterize the interaction between the plasma and the channel walls of a Hall thruster. This includes measurements of various plasma properties that are relevant towards energy losses to the channel walls as well as erosion of the wall, which is known to be a life-limiting mechanism for these devices. A rigorous experimental study of the near-wall region was required to better understand these plasma-wall interactions and how they affect thruster performance and lifetime. These measurements also help to validate and refine ongoing modeling efforts that seek to reduce expensive life tests currently required to qualify flight articles.

Internal wall-mounted Langmuir probes were instrumented along the inner and outer channel walls of a 6-kW Hall thruster near the exit plane. Studies were first performed to characterize the behavior of data from flush-mounted Langmuir probes, including ion saturation current, plasma potential, and sheath potential. These studies have improved the fidelity and accuracy of data analysis techniques over the use of traditional Langmuir probe theory. Techniques were also described that allow the determination of incident angles of ions upon the sheath surface, an important quantity in the sputtering of wall material and thruster lifetime.

Comparison of plasma properties along the channel wall to internal measurements taken by Reid [13] show that the acceleration of the plasma near the wall begins further upstream than within the rest of the channel. This tends to create large radial electric fields that defocus the ion beam and direct the flow towards the channel walls. Large radial gradients in plasma number density were found to be cause of these defocusing

fields, despite the use of a plasma lens magnetic field topology. These features have been accurately reproduced in the hybrid-PIC simulation program HPHall-2.

Measured sheath potentials along the channel walls have indicated the presence of a high-energy electron population with energies greater than four electron temperatures. Furthermore, local measurements of the electron energy distribution function have shown that the electrons near the wall resemble a drifting Maxwellian distribution, with a drift velocity on the order of the $E \times B$ velocity. These findings are evidence of thermalization processes present in the channel that are able to replenish the high-energy population of electrons. The presence of thermalization validates the significance of secondary electron emission in determining the sheath potential, as described by the Hobbs and Wesson solution [42] and used in the hybrid-PIC code HPHall-2.

Calculations of the incident ion power to the channel walls have shown that this power scales roughly linearly with discharge power. However, elevated values were found at voltages below 200 V as well as above 400 V. At these voltages, increased ion current to the wall as well as higher ion energies were measured. At low voltages, a high ion beam divergence was attributed to the increase in ion current, while large relative sheath energies were found to be the cause of the elevated ion energies. At high voltages, increased wall surface area exposed to the plasma was found to increase the overall ion current to the wall, while higher beam energies caused the rise in ion energy.

Analysis of the required sputtering yield of wall material to reproduce observed profiles has shown several necessary features. Despite the presence of large ion currents to the wall upstream of the acceleration zone, little to no erosion is observed. Thus, it is likely that the energy threshold for sputtering is higher than typical sheath energies, around 25-30 eV. Also, the sputtering dependence on energy was found to resemble the model proposed by Bohdanský [22], which includes a slow rise in sputtering at lower energies (below 50 eV). Inclusion of these features in erosion models should improve their lifetime prediction capabilities of Hall thrusters.

9.2 Recommendations for Future Work

The research contained within this dissertation has not only improved the implementation and data analysis of internal wall-mounted probes, but has contributed

towards the understanding of plasma-wall interactions and how they affect thruster performance and lifetime. However, several interesting features observed in this work deserve further study that was beyond the scope of this dissertation.

While magnetic field effects on probe characteristics were found to be largely negligible, ion flow parallel to the probe surface was found to significantly affect the measured floating potential and electron temperature. In this particular study, the ion beam was never found to flow parallel to the channel surface; however, as the wall continues to erode, it is possible that the flow angle with respect to the surface could change. Therefore, a deeper characterization of how this condition affects flush-mounted Langmuir probe data would improve the use of this diagnostic in Hall thrusters.

Measured electron energy distribution functions indicated a Maxwellian electron population with a velocity drift on the order of the $E \times B$ velocity. However, this velocity is expected to be in the azimuthal direction, and thus likely could not be detected by the internal wall-mounted probes. Further measurements of distribution functions within the channel are necessary to verify this finding, and provide additional insight into the possible drift velocity and implications on measured electron temperatures within the channel. High-speed Langmuir probe measurement techniques [39] currently being developed would allow for rapid collection of high-fidelity, time-resolved distribution functions within the channel. These measurements would greatly enhance the understanding of electron dynamics and plasma-wall interactions in Hall thrusters.

While the presence of thermalization provided evidence of the strong dependence of sheath potentials on secondary electron emission, the use of this model to estimate electron losses to the channel walls gave unphysical results. This calculation is very sensitive to the secondary electron emission characteristics of the wall, including the crossover energy used. Since the secondary electron emission properties of the wall material significantly affect sheath properties and electron power losses, an in-depth investigation is warranted to fully characterize these properties for various materials used in Hall thrusters. In particular, probing of the sheath would help in verifying the presence of a space-charge-saturated regime. Dependence of these properties on material temperature, up to values typically observed in Hall thruster channel walls (> 600 K) [83], is also warranted. Deeper understanding of secondary electron emission in Hall

thrusters will not only refine ongoing modeling efforts but also improve Hall thruster design for longer lifetimes and enhanced performance.

Appendix A

6-kW Hall Thruster Performance Data

Table A-1. Thruster performance values for the 6-kW Hall thruster at all presented operating conditions.

V_d [V]	V_{cg} [V]	I_d [V]	P_d [W]	\dot{m}_a [mg/s]	\dot{m}_c [mg/s]	IM [A]	OM [A]	P_{mag} [W]	Thrust [mN]	η_a	Pressure [torr-xe]
150	-12.6	8.90	1335	10	0.7	2.10	1.88	14	110	0.453	5.0×10^{-6}
150	-9.0	21.4	3210	20	1.4	2.58	2.33	18	250	0.487	8.8×10^{-6}
150	-8.5	35.7	5355	30	2.1	2.79	2.50	27	388	0.469	1.2×10^{-5}
200	-13.0	8.93	1786	10	0.7	2.10	1.88	13	138	0.533	5.0×10^{-6}
250	-13.2	8.73	2198	10	0.7	2.20	1.96	15	159	0.575	5.0×10^{-6}
300	-13.6	8.72	2619	10	0.7	2.39	2.14	17	180	0.619	5.0×10^{-6}
300	-10.3	20.1	6030	20	1.4	2.99	2.70	29	385	0.614	8.8×10^{-6}
400	-14.1	8.85	3540	10	0.7	3.19	2.86	33	213	0.641	5.0×10^{-6}
500	-14.4	8.99	4495	10	0.7	4.19	3.75	58	245	0.668	5.0×10^{-6}

Appendix B

Additional Internal Wall-mounted Probe Data

Table B-1. Measured values along the channel walls at 150 V and 10 mg/s anode flow rate.

Position	V_f [V]	V_p [V]	T_e [eV]	j_i [A/m ²]
Inner wall, $z = -0.143$	106	145	9.0	691
Inner wall, $z = -0.095$	--	143	18.6	--
Inner wall, $z = -0.071$	66	143	17.5	440
Inner wall, $z = -0.048$	52	140	16.0	752
Inner wall, $z = -0.024$	37	124	14.1	281
Outer wall, $z = -0.143$	106	146	8.8	345
Outer wall, $z = -0.095$	81	144	14.4	360
Outer wall, $z = -0.071$	69	145	16.3	320
Outer wall, $z = -0.048$	53	140	12.6	285
Outer wall, $z = -0.024$	39	118	13.8	285

Table B-2. Calculated values along the channel walls at 150 V and 10 mg/s anode flow rate.

Position	$n_{i,Bohm}$ [m ⁻³]	$n_{i,Beam}$ [m ⁻³]	ϵ_{sheath} [eV]	ϵ_{beam} [eV]	p_{ion} [W/m ²]	θ [deg]
Inner wall, $z = -0.143$	1.7×10^{18}	--	35	4.7	2.8×10^4	0
Inner wall, $z = -0.095$	--	--	34	6.7	--	0
Inner wall, $z = -0.071$	7.7×10^{17}	--	42	7.3	2.1×10^4	0
Inner wall, $z = -0.048$	1.4×10^{18}	--	46	10	4.2×10^4	0
Inner wall, $z = -0.024$	5.5×10^{17}	--	46	26	2.0×10^4	0
Outer wall, $z = -0.143$	8.5×10^{17}	--	35	4.2	1.3×10^4	0
Outer wall, $z = -0.095$	6.9×10^{17}	--	46	5.7	1.9×10^4	0
Outer wall, $z = -0.071$	5.8×10^{17}	--	46	5.4	1.6×10^4	0
Outer wall, $z = -0.048$	5.9×10^{17}	--	44	9.6	1.5×10^4	0
Outer wall, $z = -0.024$	5.6×10^{17}	--	46	32	2.2×10^4	0

Table B-3. Measured values along the channel walls at 150 V and 20 mg/s anode flow rate.

Position	V_f [V]	V_p [V]	T_e [eV]	j_i [A/m ²]
Inner wall, $z = -0.143$	114	145	6.4	1578
Inner wall, $z = -0.095$	--	142	16.1	--
Inner wall, $z = -0.071$	65	139	17.2	1022
Inner wall, $z = -0.048$	47	134	16.7	1694
Inner wall, $z = -0.024$	28	122	14.8	590
Outer wall, $z = -0.143$	111	145	6.9	763
Outer wall, $z = -0.095$	79	142	14.8	871
Outer wall, $z = -0.071$	63	141	16.5	689
Outer wall, $z = -0.048$	44	134	13.6	668
Outer wall, $z = -0.024$	31	107	13.2	607

Table B-4. Calculated values along the channel walls at 150 V and 20 mg/s anode flow rate.

Position	$n_{i,Bohm}$ [m ⁻³]	$n_{i,Beam}$ [m ⁻³]	ϵ_{sheath} [eV]	ϵ_{beam} [eV]	P_{ion} [W/m ²]	θ [deg]
Inner wall, $z = -0.143$	4.5×10^{18}	--	27	5.3	5.0×10^4	0
Inner wall, $z = -0.095$	--	--	46	8.4	--	0
Inner wall, $z = -0.071$	1.8×10^{18}	--	43	11	5.6×10^4	0
Inner wall, $z = -0.048$	3.0×10^{18}	--	45	16	1.0×10^5	0
Inner wall, $z = -0.024$	1.1×10^{18}	--	47	28	4.4×10^4	0
Outer wall, $z = -0.143$	2.1×10^{18}	--	28	5.3	2.5×10^4	0
Outer wall, $z = -0.095$	1.7×10^{18}	--	47	8.3	4.8×10^4	0
Outer wall, $z = -0.071$	1.2×10^{18}	--	45	8.8	3.7×10^4	0
Outer wall, $z = -0.048$	1.3×10^{18}	--	46	16	4.1×10^4	0
Outer wall, $z = -0.024$	1.2×10^{18}	--	45	43	5.3×10^4	0

Table B-5. Measured values along the channel walls at 150 V and 30 mg/s anode flow rate.

Position	V_f [V]	V_p [V]	T_e [eV]	j_i [A/m ²]
Inner wall, $z = -0.143$	114	146	6.7	2258
Inner wall, $z = -0.095$	--	144	22.9	--
Inner wall, $z = -0.071$	51	141	17.5	1212
Inner wall, $z = -0.048$	38	140	18.5	2100
Inner wall, $z = -0.024$	23	125	18.1	1107
Outer wall, $z = -0.143$	105	145	7.3	1364
Outer wall, $z = -0.095$	63	143	16.2	1189
Outer wall, $z = -0.071$	48	142	17.6	948
Outer wall, $z = -0.048$	34	134	16.2	907
Outer wall, $z = -0.024$	19	115	19.8	862

Table B-6. Calculated values along the channel walls at 150 V and 30 mg/s anode flow rate.

Position	$n_{i,Bohm}$ [m^{-3}]	$n_{i,Beam}$ [m^{-3}]	ϵ_{sheath} [eV]	ϵ_{beam} [eV]	P_{ion} [W/m^2]	θ [deg]
Inner wall, $z = -0.143$	6.4×10^{18}	--	27	3.6	7.0×10^4	0
Inner wall, $z = -0.095$	--	--	23	6.4	--	0
Inner wall, $z = -0.071$	2.1×10^{18}	--	42	9.2	6.2×10^4	0
Inner wall, $z = -0.048$	3.6×10^{18}	--	35	11	9.5×10^4	0
Inner wall, $z = -0.024$	1.9×10^{18}	--	38	25	7.0×10^4	0
Outer wall, $z = -0.143$	3.7×10^{18}	--	30	5.1	4.7×10^4	0
Outer wall, $z = -0.095$	2.2×10^{18}	--	46	7.3	6.3×10^4	0
Outer wall, $z = -0.071$	1.7×10^{18}	--	42	7.7	4.7×10^4	0
Outer wall, $z = -0.048$	1.6×10^{18}	--	46	16	5.6×10^4	0
Outer wall, $z = -0.024$	1.4×10^{18}	--	20	35	4.7×10^4	0

Table B-7. Measured values along the channel walls at 200 V and 10 mg/s anode flow rate.

Position	V_f [V]	V_p [V]	T_e [eV]	j_i [A/m^2]
Inner wall, $z = -0.143$	123	196	13.3	727
Inner wall, $z = -0.095$	--	191	28.2	--
Inner wall, $z = -0.071$	56	186	22.9	287
Inner wall, $z = -0.048$	42	163	20.1	422
Inner wall, $z = -0.024$	27	109	20.2	211
Outer wall, $z = -0.143$	122	196	15.0	414
Outer wall, $z = -0.095$	81	192	23.1	304
Outer wall, $z = -0.071$	62	170	21.3	195
Outer wall, $z = -0.048$	43	136	17.8	215
Outer wall, $z = -0.024$	29	123	20.0	192

Table B-8. Calculated values along the channel walls at 200 V and 10 mg/s anode flow rate.

Position	$n_{i,Bohm}$ [m^{-3}]	$n_{i,Beam}$ [m^{-3}]	ϵ_{sheath} [eV]	ϵ_{beam} [eV]	P_{ion} [W/m^2]	θ [deg]
Inner wall, $z = -0.143$	1.5×10^{18}	--	45	3.7	3.6×10^4	0
Inner wall, $z = -0.095$	--	--	29	9.3	--	0
Inner wall, $z = -0.071$	4.4×10^{17}	--	23	15	1.1×10^4	0
Inner wall, $z = -0.048$	6.9×10^{17}	--	21	37	2.4×10^4	0
Inner wall, $z = -0.024$	3.4×10^{17}	1.5×10^{17}	21	92	2.4×10^4	35
Outer wall, $z = -0.143$	7.8×10^{17}	--	47	3.6	2.1×10^4	0
Outer wall, $z = -0.095$	4.6×10^{17}	--	24	8.4	9.7×10^3	0
Outer wall, $z = -0.071$	3.1×10^{17}	--	22	30	1.0×10^4	0
Outer wall, $z = -0.048$	3.7×10^{17}	2.3×10^{17}	40	64	2.2×10^4	39
Outer wall, $z = -0.024$	3.1×10^{17}	--	20	78	1.9×10^4	--

Table B-9. Measured values along the channel walls at 250 V and 10 mg/s anode flow rate.

Position	V_f [V]	V_p [V]	T_e [eV]	j_i [A/m ²]
Inner wall, $z = -0.143$	147	249	23.2	720
Inner wall, $z = -0.095$	--	217	33.8	--
Inner wall, $z = -0.071$	64	181	28.7	254
Inner wall, $z = -0.048$	49	157	20.2	309
Inner wall, $z = -0.024$	33	130	20.7	180
Outer wall, $z = -0.143$	136	249	27.1	430
Outer wall, $z = -0.095$	92	209	24.5	251
Outer wall, $z = -0.071$	69	177	21.8	153
Outer wall, $z = -0.048$	47	148	18.0	153
Outer wall, $z = -0.024$	29	129	23.9	180

Table B-10. Calculated values along the channel walls at 250 V and 10 mg/s anode flow rate.

Position	$n_{i,Bohm}$ [m ⁻³]	$n_{i,Beam}$ [m ⁻³]	ϵ_{sheath} [eV]	ϵ_{beam} [eV]	p_{ion} [W/m ²]	θ [deg]
Inner wall, $z = -0.143$	1.1×10^{18}	--	24	1.0	1.8×10^4	0
Inner wall, $z = -0.095$	--	--	34	33	--	0
Inner wall, $z = -0.071$	3.5×10^{17}	2.3×10^{17}	29	69	2.5×10^4	38
Inner wall, $z = -0.048$	5.0×10^{17}	3.5×10^{17}	21	93	3.5×10^4	53
Inner wall, $z = -0.024$	2.9×10^{17}	1.7×10^{17}	21	120	2.5×10^4	53
Outer wall, $z = -0.143$	6.0×10^{17}	--	28	1.1	1.2×10^4	0
Outer wall, $z = -0.095$	3.7×10^{17}	3.1×10^{17}	25	41	1.7×10^4	37
Outer wall, $z = -0.071$	2.4×10^{17}	1.3×10^{17}	22	73	1.5×10^4	39
Outer wall, $z = -0.048$	2.6×10^{17}	1.5×10^{17}	39	102	2.2×10^4	46
Outer wall, $z = -0.024$	2.7×10^{17}	1.6×10^{17}	24	121	2.6×10^4	51

Table B-11. Measured values along the channel walls at 300 V and 10 mg/s anode flow rate.

Position	V_f [V]	V_p [V]	T_e [eV]	j_i [A/m ²]
Inner wall, $z = -0.143$	176	300	33.8	786
Inner wall, $z = -0.095$	--	237	41.0	--
Inner wall, $z = -0.071$	73	193	31.8	225
Inner wall, $z = -0.048$	54	170	24.6	311
Inner wall, $z = -0.024$	34	141	26.1	189
Outer wall, $z = -0.143$	159	299	33.7	440
Outer wall, $z = -0.095$	107	238	27.2	234
Outer wall, $z = -0.071$	79	195	23.6	125
Outer wall, $z = -0.048$	55	155	22.1	129
Outer wall, $z = -0.024$	33	135	28.1	158

Table B-12. Calculated values along the channel walls at 300 V and 10 mg/s anode flow rate.

Position	$n_{i,Bohm}$ [m ⁻³]	$n_{i,Beam}$ [m ⁻³]	ϵ_{sheath} [eV]	ϵ_{beam} [eV]	P_{ion} [W/m ²]	θ [deg]
Inner wall, $z = -0.143$	9.9×10^{17}	--	34	-0.1	2.7×10^4	0
Inner wall, $z = -0.095$	--	--	42	63	--	32
Inner wall, $z = -0.071$	2.9×10^{17}	1.4×10^{17}	32	107	3.1×10^4	32
Inner wall, $z = -0.048$	4.6×10^{17}	--	25	130	4.8×10^4	--
Inner wall, $z = -0.024$	2.7×10^{17}	1.0×10^{17}	27	159	3.5×10^4	37
Outer wall, $z = -0.143$	5.5×10^{17}	--	34	0.9	1.5×10^4	0
Outer wall, $z = -0.095$	3.3×10^{17}	2.0×10^{17}	28	62	2.1×10^4	33
Outer wall, $z = -0.071$	1.9×10^{17}	7.7×10^{16}	24	105	1.6×10^4	32
Outer wall, $z = -0.048$	2.0×10^{17}	6.9×10^{16}	23	145	2.2×10^4	34
Outer wall, $z = -0.024$	2.2×10^{17}	8.2×10^{16}	29	166	3.1×10^4	36

Table B-13. Measured values along the channel walls at 300 V and 20 mg/s anode flow rate.

Position	V_f [V]	V_p [V]	T_e [eV]	j_i [A/m ²]
Inner wall, $z = -0.143$	237	295	9.7	1201
Inner wall, $z = -0.095$	--	293	26.5	--
Inner wall, $z = -0.071$	97	290	35.7	713
Inner wall, $z = -0.048$	61	215	35.5	968
Inner wall, $z = -0.024$	27	152	26.2	443
Outer wall, $z = -0.143$	190	295	13.5	796
Outer wall, $z = -0.095$	143	294	35.2	832
Outer wall, $z = -0.071$	92	240	27.0	418
Outer wall, $z = -0.048$	51	163	21.4	320
Outer wall, $z = -0.024$	24	129	28.1	386

Table B-14. Calculated values along the channel walls at 300 V and 20 mg/s anode flow rate.

Position	$n_{i,Bohm}$ [m ⁻³]	$n_{i,Beam}$ [m ⁻³]	ϵ_{sheath} [eV]	ϵ_{beam} [eV]	P_{ion} [W/m ²]	θ [deg]
Inner wall, $z = -0.143$	2.8×10^{18}	--	37	5.1	5.1×10^4	0
Inner wall, $z = -0.095$	--	--	27	7.5	--	0
Inner wall, $z = -0.071$	8.7×10^{17}	--	36	9.9	3.3×10^4	0
Inner wall, $z = -0.048$	1.2×10^{18}	1.1×10^{18}	36	85	1.2×10^5	47
Inner wall, $z = -0.024$	6.3×10^{17}	3.2×10^{17}	27	148	7.8×10^4	48
Outer wall, $z = -0.143$	1.6×10^{18}	--	46	5.1	4.0×10^4	0
Outer wall, $z = -0.095$	1.0×10^{18}	--	36	6.1	3.5×10^4	0
Outer wall, $z = -0.071$	5.9×10^{17}	3.8×10^{17}	28	60	3.6×10^4	34
Outer wall, $z = -0.048$	5.0×10^{17}	1.9×10^{17}	22	138	5.1×10^4	38
Outer wall, $z = -0.024$	5.3×10^{17}	2.3×10^{17}	29	171	7.7×10^4	44

Table B-15. Measured values along the channel walls at 400 V and 10 mg/s anode flow rate.

Position	V_f [V]	V_p [V]	T_e [eV]	j_i [A/m ²]
Inner wall, $z = -0.143$	208	348	27.8	544
Inner wall, $z = -0.095$	--	277	46.2	--
Inner wall, $z = -0.071$	75	218	37.5	169
Inner wall, $z = -0.048$	50	196	30.5	221
Inner wall, $z = -0.024$	36	170	32.4	124
Outer wall, $z = -0.143$	173	325	37.5	433
Outer wall, $z = -0.095$	101	264	33.	121
Outer wall, $z = -0.071$	69	201	29.6	96
Outer wall, $z = -0.048$	47	164	28.0	71
Outer wall, $z = -0.024$	7	161	43.4	159

Table B-16. Calculated values along the channel walls at 400 V and 10 mg/s anode flow rate.

Position	$n_{i,Bohm}$ [m ⁻³]	$n_{i,Beam}$ [m ⁻³]	ϵ_{sheath} [eV]	ϵ_{beam} [eV]	p_{ion} [W/m ²]	θ [deg]
Inner wall, $z = -0.143$	7.5×10^{17}	5.7×10^{17}	28	52	4.4×10^4	57
Inner wall, $z = -0.095$	--	--	47	123	--	45
Inner wall, $z = -0.071$	2.0×10^{17}	9.2×10^{16}	38	182	3.7×10^4	41
Inner wall, $z = -0.048$	2.9×10^{17}	1.1×10^{17}	31	204	5.2×10^4	40
Inner wall, $z = -0.024$	1.6×10^{17}	7.7×10^{16}	33	230	3.3×10^4	52
Outer wall, $z = -0.143$	5.2×10^{17}	3.2×10^{17}	38	75	4.9×10^4	49
Outer wall, $z = -0.095$	1.5×10^{17}	8.6×10^{16}	34	136	2.1×10^4	44
Outer wall, $z = -0.071$	1.3×10^{17}	4.3×10^{16}	30	199	2.2×10^4	33
Outer wall, $z = -0.048$	9.7×10^{16}	3.0×10^{16}	29	236	1.9×10^4	36
Outer wall, $z = -0.024$	1.8×10^{17}	1.0×10^{17}	44	239	4.5×10^4	52

Table B-17. Measured values along the channel walls at 500 V and 10 mg/s anode flow rate.

Position	V_f [V]	V_p [V]	T_e [eV]	j_i [A/m ²]
Inner wall, $z = -0.143$	188	289	34.2	355
Inner wall, $z = -0.095$	--	283	61.1	--
Inner wall, $z = -0.071$	66	158	21.7	61
Inner wall, $z = -0.048$	36	134	23.7	111
Inner wall, $z = -0.024$	27	132	27.5	87
Outer wall, $z = -0.143$	160	312	44.2	301
Outer wall, $z = -0.095$	85	233	34.6	83
Outer wall, $z = -0.071$	59	172	35.1	77
Outer wall, $z = -0.048$	20	151	43.9	96
Outer wall, $z = -0.024$	24	123	32.2	100

Table B-18. Calculated values along the channel walls at 500 V and 10 mg/s anode flow rate.

Position	$n_{i,Bohm}$ [m^{-3}]	$n_{i,Beam}$ [m^{-3}]	ϵ_{sheath} [eV]	ϵ_{beam} [eV]	p_{ion} [W/m^2]	θ [deg]
Inner wall, $z = -0.143$	4.4×10^{17}	1.8×10^{17}	35	211	8.7×10^4	63
Inner wall, $z = -0.095$	--	--	62	217	--	37
Inner wall, $z = -0.071$	9.5×10^{16}	2.1×10^{16}	22	342	2.2×10^4	36
Inner wall, $z = -0.048$	1.7×10^{17}	--	24	366	4.3×10^4	--
Inner wall, $z = -0.024$	1.2×10^{17}	2.8×10^{16}	28	368	3.4×10^4	32
Outer wall, $z = -0.143$	3.3×10^{17}	1.9×10^{17}	45	188	7.0×10^4	68
Outer wall, $z = -0.095$	1.0×10^{17}	3.3×10^{16}	35	267	2.5×10^4	35
Outer wall, $z = -0.071$	9.4×10^{16}	3.0×10^{16}	36	328	2.8×10^4	41
Outer wall, $z = -0.048$	1.1×10^{17}	3.6×10^{16}	45	349	3.8×10^4	40
Outer wall, $z = -0.024$	1.3×10^{17}	3.6×10^{16}	33	377	4.1×10^4	40

Appendix C

Additional Near-field Faraday Probe Data

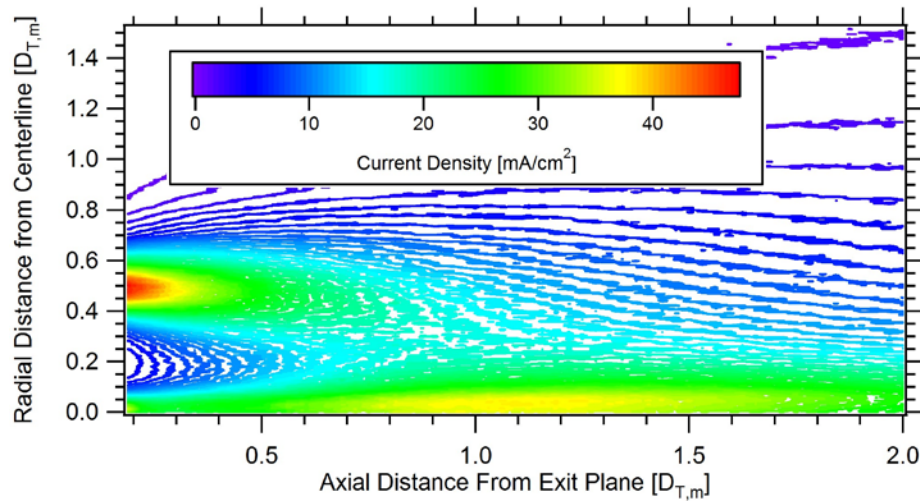


Figure C-1. Near-field ion current density contour map at 200 V and 10 mg/s anode flow rate.

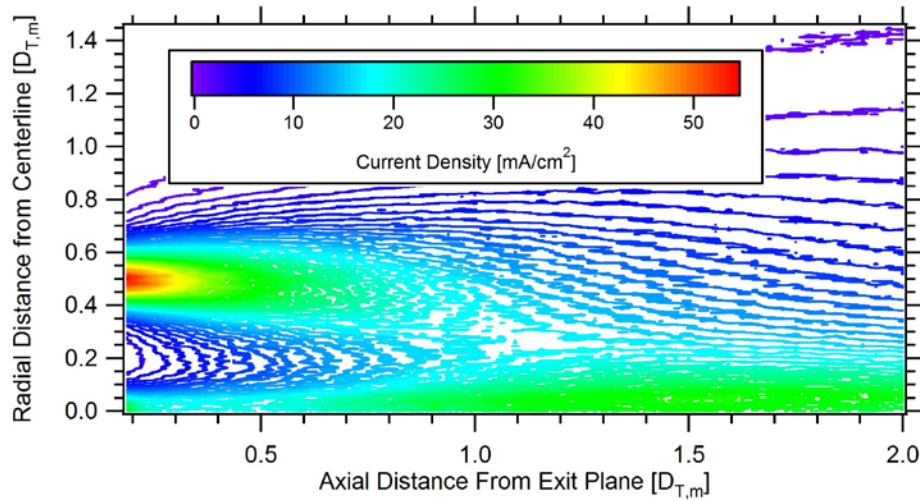


Figure C-2. Near-field ion current density contour map at 250 V and 10 mg/s anode flow rate.

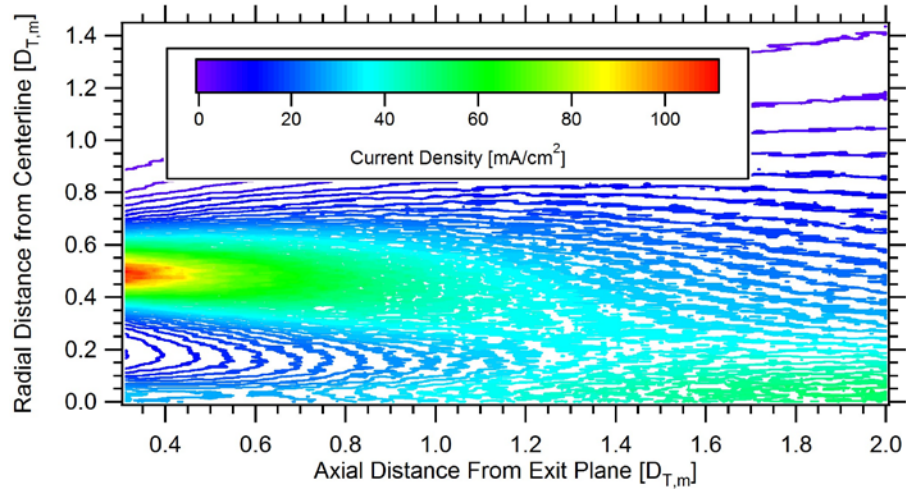


Figure C-3. Near-field ion current density contour map at 300 V and 20 mg/s anode flow rate.

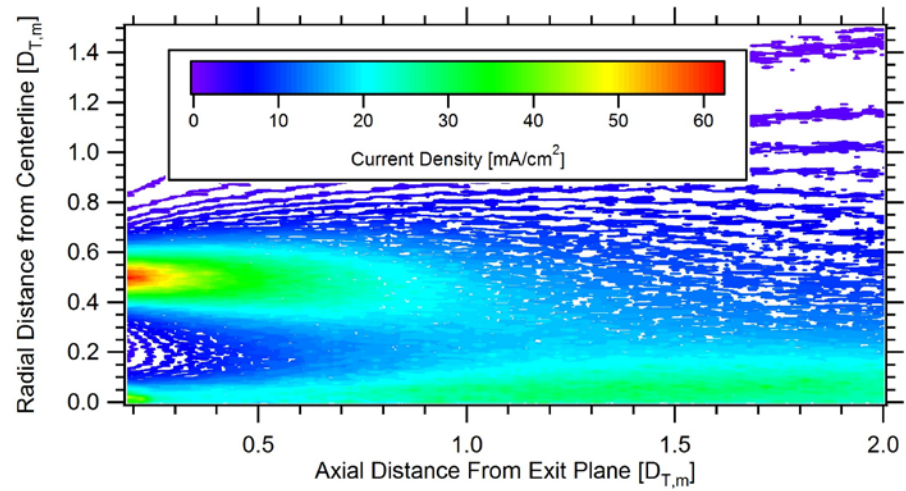


Figure C-4. Near-field ion current density contour map at 400 V and 10 mg/s anode flow rate.

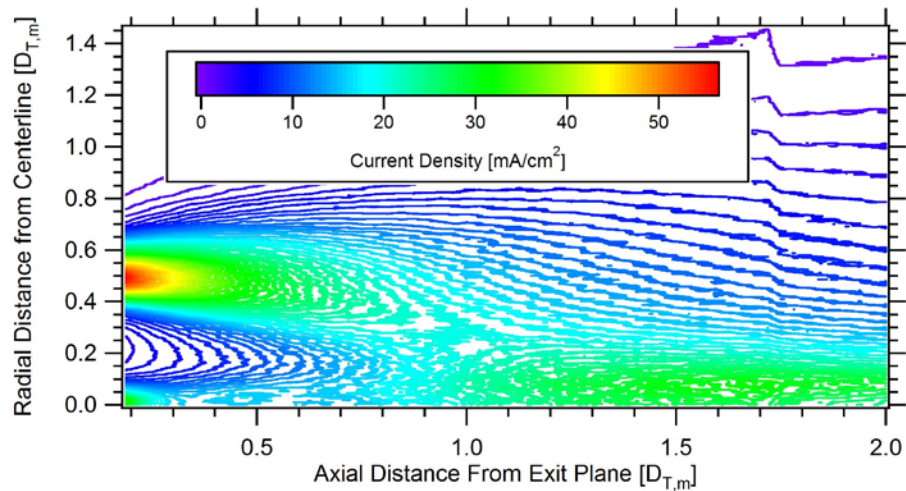


Figure C-5. Near-field ion current density contour map at 500 V and 10 mg/s anode flow rate.

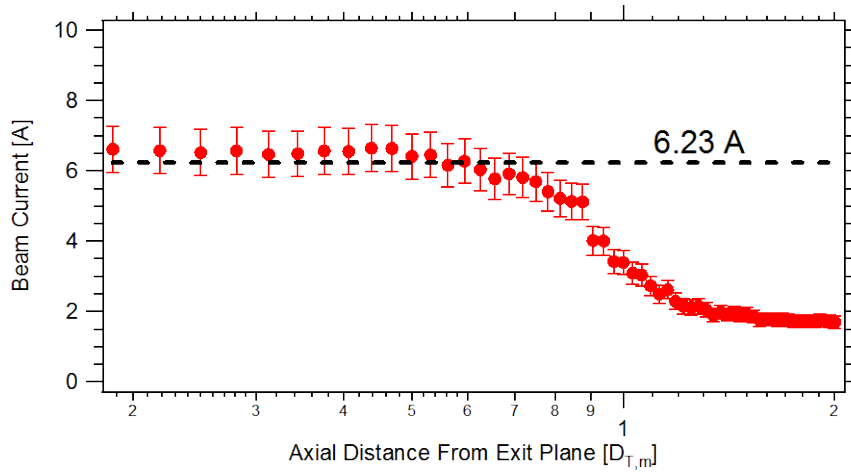


Figure C-6. Calculated ion beam current as a function of axial distance at 200 V and 10 mg/s anode flow rate.

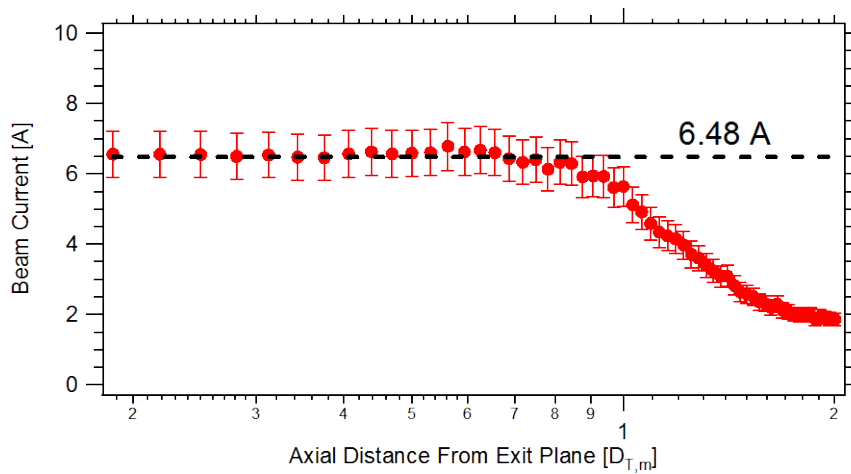


Figure C-7. Calculated ion beam current as a function of axial distance at 250 V and 10 mg/s anode flow rate.

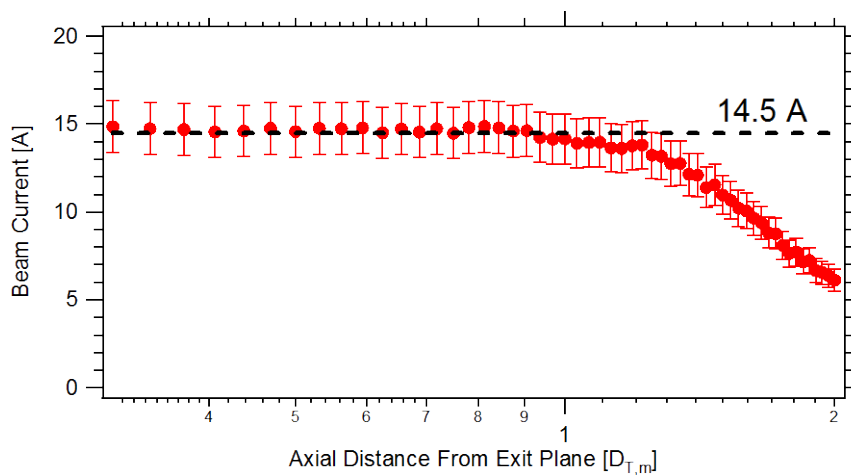


Figure C-8. Calculated ion beam current as a function of axial distance at 300 V and 20 mg/s anode flow rate.

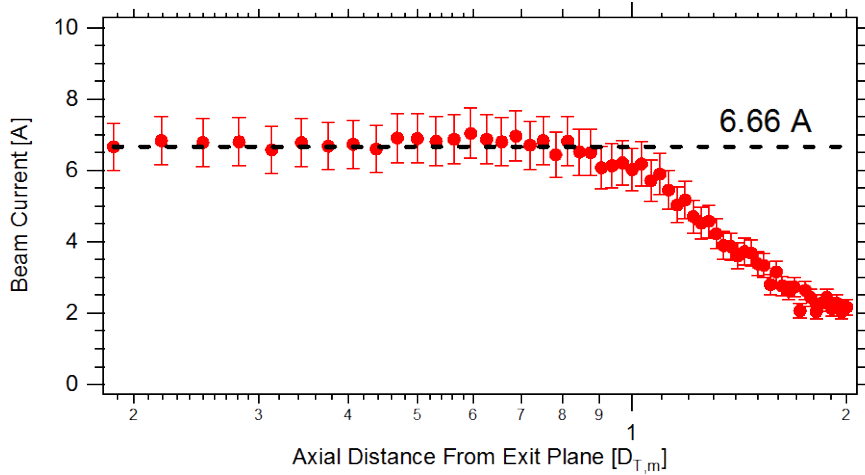


Figure C-9. Calculated ion beam current as a function of axial distance at 400 V and 10 mg/s anode flow rate.

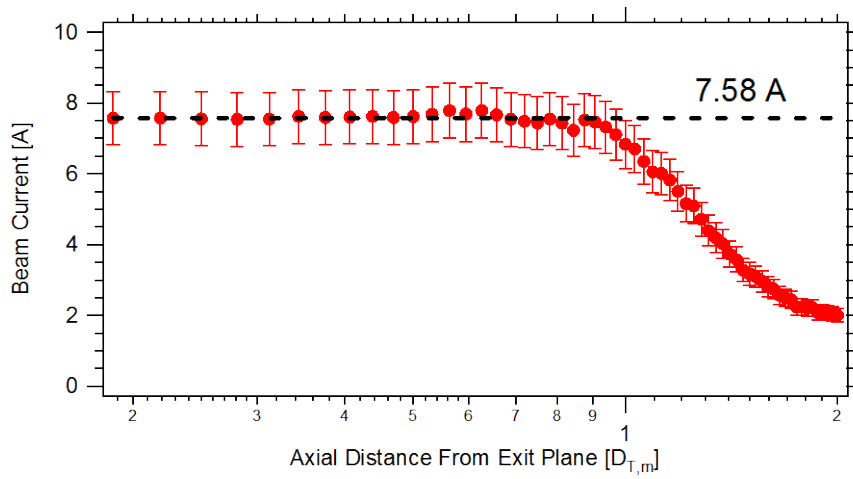


Figure C-10. Calculated ion beam current as a function of axial distance at 500 V and 10 mg/s anode flow rate.

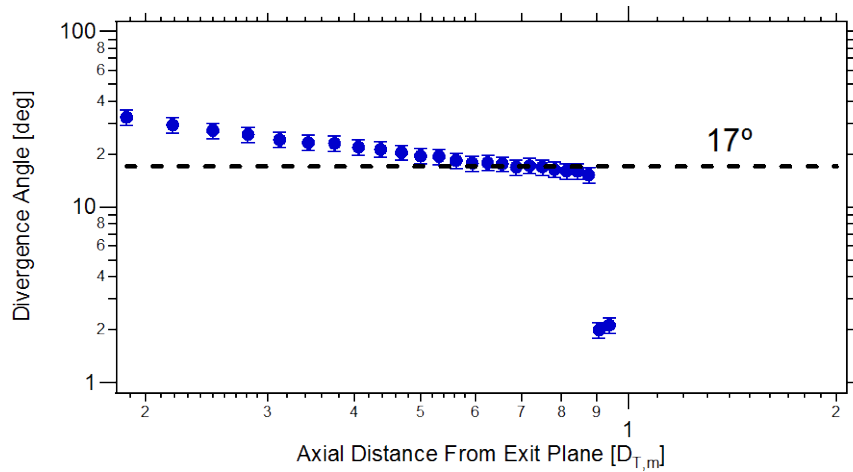


Figure C-11. Calculated plume divergence angle as a function of axial distance at 200 V and 10 mg/s anode flow rate.

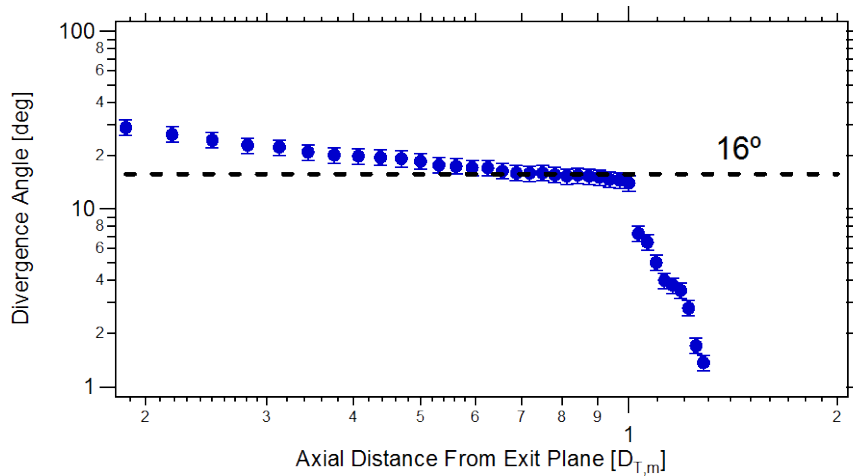


Figure C-12. Calculated plume divergence angle as a function of axial distance at 250 V and 10 mg/s anode flow rate.

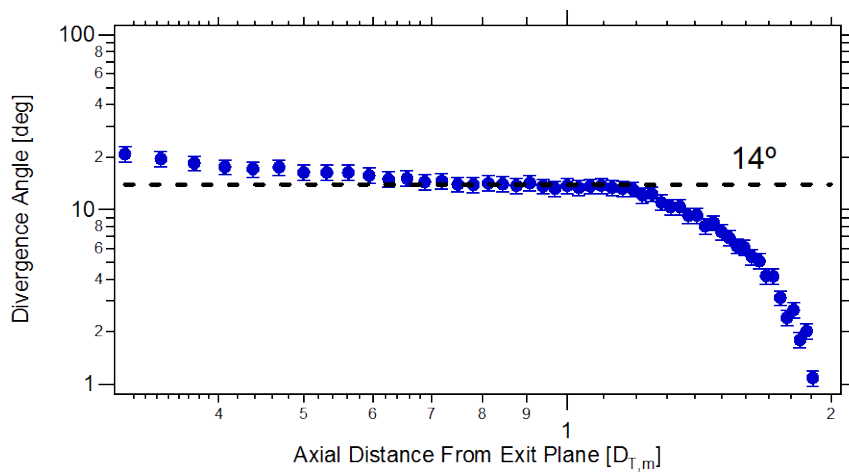


Figure C-13. Calculated plume divergence angle as a function of axial distance at 300 V and 20 mg/s anode flow rate.

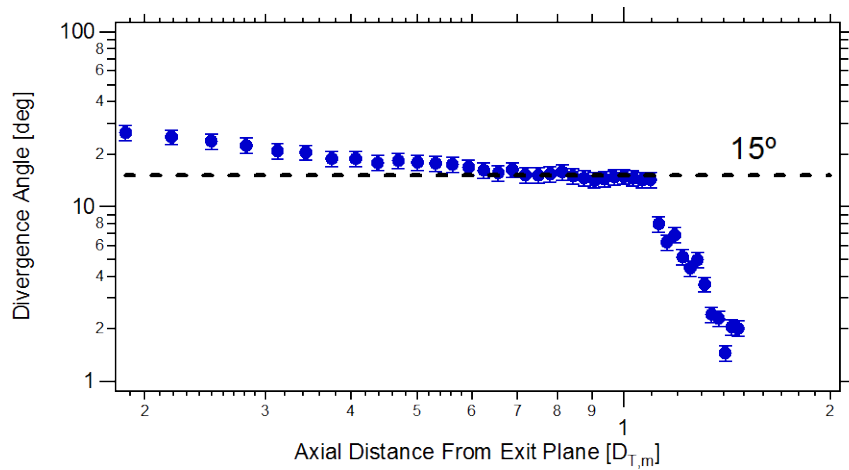


Figure C-14. Calculated plume divergence angle as a function of axial distance at 400 V and 10 mg/s anode flow rate.

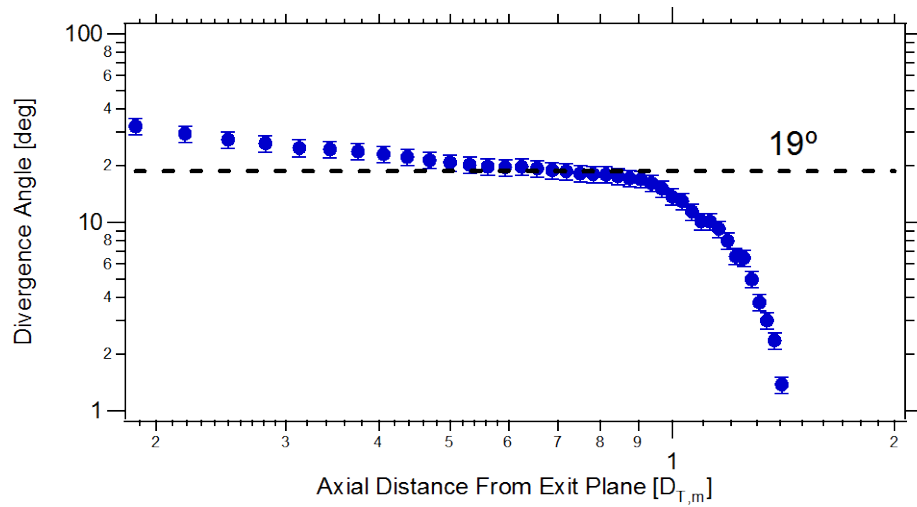


Figure C-15. Calculated plume divergence angle as a function of axial distance at 500 V and 10 mg/s anode flow rate.

Bibliography

- [1] Gnizdor, R., Kozubsky, K., Koryakin, A., Maslennikov, N., Pridannikov, S. et al., "SPT100 Life Test with Single Cathode up to Total Impulse Two Million Nsec," Presented at the 34th AIAA/ASME/SAE/ASEE Joint Propulsion Conference and Exhibit, AIAA-1998-3790, Cleveland, OH, July 13-15, 1998.
- [2] Cornu, N., Marchandise, F., Darnon, F., and Estublier, D., "The PPS®1350-G Qualification Demonstration: 10500 hrs on the Ground and 5000 hrs in Flight," Presented at the 43rd AIAA/ASME/SAE/ASEE Joint Propulsion Conference and Exhibit, AIAA-2007-5197, Cincinnati, OH, July 8-11, 2007.
- [3] Ahedo, E. and De Pablo, V., "Effects of electron secondary emission and partial thermalization on a Hall thruster plasma," Presented at the 42nd AIAA/ASME/SAE/ASEE Joint Propulsion Conference and Exhibit, AIAA-2006-4328, Sacramento, CA, July 9-12, 2006.
- [4] Ahedo, E. and Parra, F. I., "Partial trapping of secondary-electron emission in a Hall thruster plasma," *Physics of Plasmas* 12, 7, 073503-1 - 073503-7 (2005).
- [5] Barral, S., Makowski, K., Peradzynski, Z., Gascon, N., and Dudeck, M., "Wall material effects in stationary plasma thrusters. II. Near-wall and in-wall conductivity," *Physics of Plasmas* 10, 10, 4137-4152 (2003).
- [6] Dunaevsky, A., Raitses, Y., and Fisch, N. J., "Secondary electron emission from dielectric materials of a Hall thruster with segmented electrodes," *Physics of Plasmas* 10, 6, 2574-2577 (2003).
- [7] Gascon, N., Dudeck, M., and Barral, S., "Wall material effects in stationary plasma thrusters. I. Parametric studies of an SPT-100," *Physics of Plasmas* 10, 10, 4123-4136 (2003).
- [8] Raitses, Y., Smirnov, A., Staack, D., and Fisch, N. J., "Measurements of secondary electron emission effects in the Hall thruster discharge," *Physics of Plasmas* 13, 1, 014502-1 - 014502-4 (2006).
- [9] Sydorenko, D., Smolyakov, A., Kaganovich, I., and Raitses, Y., "Kinetic simulation of secondary electron emission effects in Hall thrusters," *Physics of Plasmas* 13, 1, 014501-1 - 014501-4 (2006).
- [10] Haas, J. M., "Low-Perturbation Interrogation of the Internal and Near-Field Plasma Structure of a Hall Thruster Using a High-Speed Probe Positioning System," Ph.D. Dissertation, Aerospace Engineering, University of Michigan, 2001.
- [11] Linnell, J. A., "An Evaluation of Krypton Propellant in Hall Thrusters," Ph.D. Dissertation, Aerospace Engineering, University of Michigan, 2007.
- [12] Raitses, Y., Staack, D., Smirnov, A., and Fisch, N. J., "Space charge saturated sheath regime and electron temperature saturation in Hall thrusters," *Physics of Plasmas* 12, 7, 073507-1 - 073507-10 (2005).

- [13] Reid, B. M., "The Influence of Neutral Flow Rate in the Operation of Hall Thrusters," Ph.D. Dissertation, Aerospace Engineering, University of Michigan, 2008.
- [14] Huang, W., Drenkow, B., and Gallimore, A. D., "Laser-Induced Fluorescence of Singly-Charged Xenon inside a 6-kW Hall Thruster," Presented at the 45th AIAA/ASME/SAE/ASEE Joint Propulsion Conference and Exhibit, AIAA-2009-5355, Denver, CO, August 2 - 5, 2009.
- [15] Azziz, Y., Warner, N. Z., Martinez-Sanchez, M., and Szabo, J. J., "High Voltage Plume Measurements and Internal Probing of the BHT-1000 Hall Thruster," Presented at the 40th AIAA/ASME/SAE/ASEE Joint Propulsion Conference and Exhibit, AIAA-2004-4097, Fort Lauderdale, FL, July 11-14, 2004.
- [16] Szabo, J. J., Warner, N. Z., and Martinez-Sanchez, M., "Instrumentation and Modeling of a High Isp Hall Thruster," Presented at the 38th AIAA/ASME/SAE/ASEE Joint Propulsion Conference and Exhibit, AIAA-2002-4248, Indianapolis, IN, July 7-10, 2002.
- [17] Warner, N. Z., "Performance Testing and Internal Probe Measurements of a High Specific Impulse Hall Thruster," Master's Thesis, Aeronautics and Astronautics, Massachusetts Institute of Technology, 2003.
- [18] Arkhipov, A. S., Kim, V., Sidorenko, E. K., and Khartov, S. A., "Analysis of Energy Balance in the Discharge of SPT Using Results of Its Integral Parameters and Plume Characteristics Measurements," Presented at the 31st International Electric Propulsion Conference, IEPC-2009-097, Ann Arbor, MI, September 20 - 24, 2009.
- [19] Kim, V., Grdlichko, D., Kozlov, V., Lazourenko, A., Popov, G. et al., "Local Plasma Parameter Measurements by Nearwall Probes Inside the SPT Accelerating Channel Under Thruster Operation with Kr," Presented at the 38th AIAA/ASME/SAE/ASEE Joint Propulsion Conference and Exhibit, AIAA-2002-4108, Indianapolis, IN, July 7-10, 2002.
- [20] Kim, V., Kozlov, V., Skrylnikov, A., Sidorenko, E. K., Murashko, V. M. et al., "Investigation of the SPT operation and discharge chamber wall erosion rate under increased discharge voltages," Presented at the 30th International Electric Propulsion Conference, IEPC-2007-151, Florence, Italy, September 17-20, 2007.
- [21] Kim, V., Kozlov, V., Skrylnikov, A., Umnitsin, L. N., Svitina, V. V. et al., "Investigation of the Local Plasma Parameters in the SPT Accelerating Channel Under Increased Discharge Voltages," Presented at the 29th International Electric Propulsion Conference, IEPC-2005-004, Princeton, NJ, October 31 - November 4, 2005.
- [22] Bohdansky, J., "A universal relation for the sputtering yield of monatomic solids at normal ion incidence," Nuclear Instruments and Methods in Physics Research Section B 2, 1-3, 587 - 591 (1984).
- [23] Goebel, D. M. and Katz, I., *Fundamentals of Electric Propulsion: Ion and Hall Thrusters*. (Pasadena, CA, 2008).
- [24] Hofer, R. R., "Development and Characterization of High-Efficiency, High-Specific Impulse Xenon Hall Thrusters," Ph.D. Dissertation, Aerospace Engineering, The University of Michigan, 2004.
- [25] Jahn, R. G., *Physics of Electric Propulsion*. (McGraw-Hill, Inc., New York, 1968).
- [26] Morozov, A. I., "Focussing of Cold Quasineutral Beams in Electromagnetic Fields," Soviet Physics - Doklady 10, 8, 775-777 (1966).

- [27] Hofer, R. R., Katz, I., Mikellides, I. G., Goebel, D. M., Jameson, K. K. et al., "Efficacy of Electron Mobility Models in Hybrid-PIC Hall Thruster Simulations," Presented at the 44th AIAA/ASME/SAE/ASEE Joint Propulsion Conference and Exhibit, AIAA-2008-4924, Hartford, CT, July 20-23, 2008.
- [28] Brown, D. L., "Investigation of Low Discharge Voltage Hall Thruster Characteristics and Evaluation of Loss Mechanisms," Ph.D. Dissertation, Aerospace Engineering, The University of Michigan, 2009.
- [29] Brown, D. L., Reid, B. M., Gallimore, A. D., Hofer, R. R., Haas, J. M. et al., "Performance Characterization and Design Verification of the H6 Laboratory Model Hall Thruster," Presented at the 54th JANNAF Propulsion Meeting, Denver, CO, 14-17 May, 2007.
- [30] Haas, J. M., Hofer, R. R., Brown, D. L., Reid, B. M., and Gallimore, A. D., "Design of the H6 Hall Thruster for High Thrust/Power Investigation," Presented at the 54th JANNAF Propulsion Meeting, Denver, CO, 14-17 May, 2007.
- [31] Hofer, R. R., Goebel, D. M., and Watkins, R. M., "Compact LaB₆ Hollow Cathode for the H6 Hall Thruster," Presented at the 54th JANNAF Propulsion Meeting, Denver, CO, 14-17 May, 2007.
- [32] Huang, W., Reid, B. M., Smith, T. B., and Gallimore, A. D., "Laser-Induced Fluorescence of Singly-Charged Xenon in a 6-kW Hall Thruster Plume," Presented at the 44th AIAA/ASME/SAE/ASEE Joint Propulsion Conference and Exhibit, AIAA-2008-5102, Hartford, CT, July 21 - 23, 2008.
- [33] Jameson, K. K., "Investigation of Hollow Cathode Effects on Total Thruster Efficiency in a 6 kW Hall Thruster," Ph.D. Dissertation, Aerospace Engineering, University of California Los Angeles, 2008.
- [34] Reid, B. M., Gallimore, A. D., Hofer, R. R., Li, Y., and Haas, J. M., "Anode Design and Verification for the H6 Hall Thruster," Presented at the 54th JANNAF Propulsion Meeting, Denver, CO, 14-17 May, 2007.
- [35] Hofer, R. R., Goebel, D. M., Snyder, J. S., and Sandler, I., "BPT-4000 Hall Thruster Extended Power Throttling Range Characterization for NASA Science Missions," Presented at the 31st International Electric Propulsion Conference, IEPC-2009-085, Ann Arbor, MI, September 20 -24, 2009.
- [36] Haag, T. W., "Design of a Thrust Stand for High Power Electric Propulsion Devices," Presented at the 25th AIAA/ASME/SAE/ASEE Joint Propulsion Conference, AIAA-1989-2829, Monterey, CA, July 10 -13, 1989.
- [37] Xu, K. G. and Walker, M. L. R., "High-power, null-type, inverted pendulum thrust stand," Review of Scientific Instruments 80, 5, 055103-1 - 055103-6 (2009).
- [38] Haas, J. M., Gallimore, A. D., Mcfall, K., and Spanjers, G., "Development of a High-Speed, Reciprocating Electrostatic Probe System for Hall Thruster Interrogation," Review of Scientific Instruments 71, 11, 4131-4138 (2000).
- [39] Lobbia, R. B. and Gallimore, A. D., "High-speed dual Langmuir probe," Review of Scientific Instruments 81, 7, 073503-1 - 073503-9 (2010).
- [40] Kemp, R. F. and J.M. Sellen, J., "Plasma Potential Measurements by Electron Emissive Probes," Review of Scientific Instruments 37, 4, 455-461 (1966).

- [41] Hershkowitz, N. and Cho, M. H., "Measurement of plasma potential using collecting and emitting probes," *The Journal of Vacuum Science and Technology A* 6, 3, 2054-2059 (1988).
- [42] Hobbs, G. D. and Wesson, J. A., "Heat flow through a Langmuir sheath in the presence of electron emission," *Plasma Physics* 9, 85-87 (1967).
- [43] Hofer, R. R. and Gallimore, A. D., "Recent Results from Internal and Very-Near-Field Plasma Diagnostics of a High Specific Impulse Hall Thruster," Presented at the 28th International Electric Propulsion Conference, IEPC-2003-037, Toulouse, France, March 17-21, 2003.
- [44] Jameson, K. K., Goebel, D. M., Hofer, R. R., and Watkins, R. M., "Cathode Couplings in Hall Thrusters," Presented at the 30th International Electric Propulsion Conference, IEPC-2007-278, Florence, Italy, September 17-20, 2007.
- [45] Hagstrum, H. D., "Auger Ejection of Electrons from Tungsten by Noble Gas Ions," *Physical Review* 96, 2, 325 - 335 (1954).
- [46] Hagstrum, H. D., "Auger Ejection of Electrons from Molybdenum by Noble Gas Ions," *Physical Review* 104, 3, 672 - 683 (1956).
- [47] Sheridan, T. E., "How big is a small Langmuir probe?," *Physics of Plasmas* 7, 7, 3084-3088 (2000).
- [48] Hershkowitz, N., in *Plasma Diagnostics: Discharge Parameters and Chemistry*, edited by Flamm, D. L. (Academic Press, Inc., 1989), pp. 113-181.
- [49] Lieberman, M. A. and Lichtenberg, A. J., *Principles of Plasma Discharges and Materials Processing*, Second ed. (John Wiley & Sons, Inc., Hoboken, NJ, 2005).
- [50] Riemann, K.-U., "The Bohm criterion and sheath formation," *Journal of Physics D: Applied Physics* 24, 493-518 (1991).
- [51] Bergmann, A., "Two-dimensional particle simulation of Langmuir probe sheaths with oblique magnetic field," *Physics of Plasmas* 1, 11, 3598-3606 (1994).
- [52] Bergmann, A., "Two-dimensional particle simulation of the current flow to a flush-mounted Langmuir probe in a strong oblique magnetic field," *Physics of Plasmas* 9, 8, 3413-3420 (2002).
- [53] Chung, P. M., Talbot, L., and Touryan, K. J., "Electric Probes in Stationary and Flowing Plasmas: Part 1. Collisionless and Transitional Probes," *AIAA Journal* 12, 2, 133-144 (1974).
- [54] Chung, P. M., Talbot, L., and Touryan, K. J., "Electric Probes in Stationary and Flowing Plasmas: Part 2. Continuum Probes," *AIAA Journal* 12, 2, 144-154 (1974).
- [55] Demidov, V. I., Ratynskaia, S. V., and Rypdal, K., "Electric probes for plasmas: The link between theory and instrument," *Review of Scientific Instruments* 73, 10, 3409-3439 (2002).
- [56] Johnson, J. D. and Holmes, A. J. T., "Edge effect correction for small planar Langmuir probes," *Review of Scientific Instruments* 61, 10, 2628-2631 (1990).
- [57] Laframboise, J. G., "Theory of Spherical and Cylindrical Langmuir Probes in a Collisionless, Maxwellian Plasma at Rest," Ph.D. Dissertation, Institute of Aerospace Studies, University of Toronto, 1966.

- [58] Weinlich, M. and Carlson, A., "Flush-mounted Langmuir probes in an oblique magnetic field," *Physics of Plasmas* 4, 6, 2151-2160 (1997).
- [59] Brophy, J. R., Katz, I., Polk, J. E., and Anderson, J. R., "Numerical Simulations of Ion Thruster Accelerator Grid Erosion," Presented at the 38th AIAA/ASME/SAE/ASEE Joint Propulsion Conference and Exhibit, AIAA-2002-4261, Indianapolis, IN, July 7-10, 2002.
- [60] Ahedo, E., "Structure of the plasma-wall interaction in an oblique magnetic field," *Physics of Plasmas* 4, 12, 4419-4430 (1997).
- [61] Ahedo, E., "Plasma-wall interaction in an oblique magnetic field: Model of the space-charge sheath for large potentials and small Debye lengths," *Physics of Plasmas* 6, 11, 4200-4207 (1999).
- [62] Ahedo, E. and Carralero, D., "Model of a source-driven plasma interacting with a wall in an oblique magnetic field," *Physics of Plasmas* 16, 4, 043506-1 - 043506-13 (2009).
- [63] Petry, R. L., "Secondary Electron Emission from Tungsten, Copper and Gold," *Physical Review* 28, 362-366 (1926).
- [64] Viel-Inguimbert, V., "Secondary Electron Emission of Ceramics Used in the Channel of SPT," Presented at the 28th International Electric Propulsion Conference, IEPC-2003-258, Toulouse, France, Mar. 17 - 23, 2003.
- [65] Barral, S., Jayet, Y., Mazouffre, S., Dudeck, M., Veron, E. et al., "Hall Effect Thruster with an AlN discharge channel," Presented at the 29th International Electric Propulsion Conference, IEPC-2005-152, Princeton, NJ, October 31 - November 4, 2005.
- [66] Kim, V., Kozlov, V., Skrylnikov, A., Veselovzorov, A., Hilleret, N. et al., "Investigation of Operation and Characteristics of Small SPT with Discharge Chamber Walls Made of Different Ceramics," Presented at the 39th AIAA/ASME/SAE/ASEE Joint Propulsion Conference and Exhibit, AIAA-2003-5002, Huntsville, AL, July 20-23, 2003.
- [67] Hofer, R. R., Mikellides, I. G., Katz, I., and Goebel, D. M., "Wall Sheath and Electron Mobility Modeling in Hybrid-PIC Hall Thruster Simulations," Presented at the 43rd AIAA/ASME/SAE/ASEE Joint Propulsion Conference and Exhibit, AIAA-2007-5267, Cincinnati, OH, July 8-11, 2007.
- [68] Kaganovich, I., Raitses, Y., Sydorenko, D., and Smolyakov, A., "Kinetic effects in a Hall thruster discharge," *Physics of Plasmas* 14, 5, 057104-1 - 057104-11 (2007).
- [69] Hofer, R. R., Mikellides, I. G., Katz, I., and Goebel, D. M., "BPT-4000 Hall Thruster Discharge Chamber Erosion Model Comparison with Qualification Life Test Data," Presented at the 30th International Electric Propulsion Conference, IEPC-2007-267, Florence, Italy, September 17-20, 2007.
- [70] King, L. B., "A (Re-) examination of electron motion in Hall thruster fields," Presented at the 29th International Electric Propulsion Conference, IEPC-2005-258, Princeton, NJ, October 31 - November 4, 2005.
- [71] Ngom, B. B., "Magnetic Field Simulation and Mapping Based on Zeeman-split Laser-induced Fluorescence Spectra of Xenon in the Discharge Channel of 5-6 kW Coaxial Stationary-Plasma Hall Thrusters," Ph.D. Dissertation, Aerospace Engineering, University of Michigan, 2009.
- [72] Druyvesteyn, M. J., "Z. Phys. 64, 781 (1930).

- [73] Bell, A. T., *Techniques and Applications of Plasma Chemistry*. (John Wiley & Sons, New York, 1974).
- [74] Fife, J. M., "Hybrid-PIC Modeling and Electrostatic Probe Survey of Hall Thrusters," Ph.D. Dissertation, Aeronautics and Astronautics, Massachusetts Institute of Technology, 1999.
- [75] Parra, F. I., Ahedo, E., Fife, J. M., and Martinez-Sanchez, M., "A two-dimensional hybrid model of the Hall thruster discharge," *Journal of Applied Physics* 100, 2, 023304-1 - 023304-11 (2006).
- [76] Gamero-Castaño, M. and Katz, I., "Estimation of Hall Thruster Erosion Using HPHall," Presented at the 29th International Electric Propulsion Conference, IEPC-2005-303, Princeton, NJ, October 31 - November 4, 2005.
- [77] Hofer, R. R., Katz, I., Mikellides, I. G., and Gamero-Castaño, M., "Heavy Particle Velocity and Electron Mobility Modeling in Hybrid-PIC Hall Thruster Simulations," Presented at the 42nd AIAA/ASME/SAE/ASEE Joint Propulsion Conference and Exhibit, AIAA-2006-4658, Sacramento, CA, July 9-12, 2006.
- [78] Mikellides, I. G., Katz, I., Hofer, R. R., and Goebel, D. M., "Hall-effect Thruster Simulations with 2-D Electron Transport and Hydrodynamic Ions," Presented at the 31st International Electric Propulsion Conference, IEPC-2009-114, Ann Arbor, MI, September 20 - 24, 2009.
- [79] Mazouffre, S., Dannenmayer, K., and Perez-Luna, J., "Examination of plasma-wall interactions in Hall effect thrusters by means of calibrated thermal imaging," *Journal of Applied Physics* 102, 2, 023304-1 - 023304-10 (2007).
- [80] Kim, V., "Main Physical Features and Processes Determining the Performance of Stationary Plasma Thrusters," *Journal of Propulsion and Power* 14, 5, 736-743 (1998).
- [81] Huang, W., Gallimore, A., and Smith, T. B., "Two-Axis Laser-Induced Fluorescence of Singly-Charged Xenon inside a 6-kW Hall Thruster," Presented at the 49th AIAA Aerospace Sciences Meeting, AIAA-2011-1015, Orlando, FL, Jan. 4 - 7, 2011.
- [82] Brown, D. L., Larson, C. W., Beal, B. E., and Gallimore, A., "Methodology and Historical Perspective of a Hall Thruster Efficiency Analysis," *Journal of Propulsion and Power* 25, 6, 1163 - 1177 (2009).
- [83] Mazouffre, S., Echegut, P., and Dudeck, M., "A calibrated infrared imaging study on the steady state thermal behaviour of Hall effect thrusters," *Plasma Sources Science and Technology* 16, 13-22 (2006).
- [84] Kim, V., Semenov, A., and Shkarban, I., "Investigation of the Accelerated Ions Energy Accommodation under their Impingement with Solid Surfaces," Presented at the 38th AIAA/ASME/SAE/ASEE Joint Propulsion Conference and Exhibit, AIAA-2002-4110, Indianapolis, IN, July 7 - 10, 2002.
- [85] Ahedo, E., "Presheath/sheath model with secondary electron emission from two parallel walls," *Physics of Plasmas* 9, 10, 4340 - 4347 (2002).
- [86] Rubin, B., Topper, J. L., and Yalin, A. P., "Total and differential sputter yields of boron nitride measured by quartz crystal microbalance," *Journal of Physics D: Applied Physics* 42, 205205, 1 - 11 (2009).

- [87] Garnier, Y., Viel, V., Roussel, J.-F., and Bernard, J., "Low-energy xenon ion sputtering of ceramics investigated for stationary plasma thrusters," *The Journal of Vacuum Science and Technology A* 17, 6, 3246 - 3254 (1999).
- [88] Yalin, A. P., Rubin, B., Domingue, S. R., Glueckert, Z., and Williams, J. D., "Differential Sputter Yields of Boron Nitride, Quartz, and Kapton Due to Low Energy Xe⁺ Bombardment," Presented at the 43rd AIAA/ASME/SAE/ASEE Joint Propulsion Conference and Exhibit, AIAA-2007-5314, Cincinnati, OH, July 8-11, 2007.
- [89] Kim, V., Kozlov, V., Semenov, A., and Shkarban, I., "Investigation of the Boron Nitride based Ceramics Sputtering Yield Under it's Bombardment by Xe and Kr ions," Presented at the 27th International Electric Propulsion Conference, IEPC-01-073, Pasadena, CA, October 15-19, 2001.
- [90] Yim, J. T., Falk, M. L., and Boyd, I. D., "Modeling low energy sputtering of hexagonal boron nitride by xenon ions," *Journal of Applied Physics* 104, 12, 123507-1 - 123507-6 (2008).
- [91] Abgaryan, V., Kaufman, H. R., Kim, V., Ovsyanko, D., Shkarban, I. et al., "Calculation Analysis of the Erosion of the Discharge Chamber Walls and Their Contamination During Prolonged SPT Operation," Presented at the 30th AIAA/ASME/SAE/ASEE Joint Propulsion Conference and Exhibit, AIAA-1994-2859, Indianapolis, IN, June 27 - 29, 1994.
- [92] Yamamura, Y. and Tawara, H., "Energy Dependence of Ion-Induced Sputtering Yields from Monatomic Solids at Normal Incidence," *Atomic Data and Nuclear Data Tables* 62, 2, 149-253 (1996).
- [93] Yamamura, Y., Itikawa, Y., and Itoh, N., *Angular dependence of sputtering yields of monatomic solids*. (IPPJ-AM 26, 1983).
- [94] Pencil, E. J., Randolph, T. M., and Manzella, D., "End-of-life Stationary Plasma Thruster far-field plume characterization," Presented at the 32nd AIAA/ASME/SAE/ASEE Joint Propulsion Conference and Exhibit, AIAA-96-2709, Lake Buena Vista, FL, July 1-3, 1996.
- [95] Sullivan, K., Fox, J., Martinez-Sanchez, M., and Batishchev, O., "Kinetic Study of Wall Effects in SPT Hall Thrusters," Presented at the 40th AIAA/ASME/SAE/ASEE Joint Propulsion Conference and Exhibit, AIAA-2004-3777, Fort Lauderdale, FL, July 11-14, 2004.